# Flow and Mass Transfer in Fibrous and Granular Porous Media

by

Branko Bijeljic

A thesis submitted for the degree of Doctor of Philosophy of the University of London

Department of Chemical Engineering and Chemical Technology
Imperial College of Science, Technology and Medicine
London SW7 2BY

October 2000

**For my family**

# ACKNOWLEDGEMENTS

This work has only been made possible with the help of many people.

I would first like to thank my supervisors, Professor Julia Higgins and Professor Paul Luckham for the guidance, encouragement and full independence that they have both given to me throughout my work.

Thanks must also go to Dr Thanasis Papathanasiou who offered me the chance to do the PhD in the first place. I am grateful to the ORS body for the award and to Dr Chris Lawrence for all of his support during the final year.

Special thanks go to the NMR group in Cavendish-Cambridge i.e. Professor Lynn Gladden, Mick, Andy and Mike for introducing me to the magic of NMRI velocimetry, which doesn't lie.

I am also grateful to the Polymer and Particle Technology groups. Joao, Tony, Nickie, Herve, Renata, Chatchai, Helen, Yi-Ying, Dimitra, Simon, Alberto, Andy, Cecil, Sarah, Rob, Jaochim from upstairs, Ricardo, Maria Elena, Mani, Roya and countless others from downstairs.

To my friend Nick Duggan and Mr Alan Barnes for their invaluable combined technical experience and for all of the help they gave me in the design and construction of the first Mass Transfer experiment

Thanks to Liz, who always managed to put up with my pestering in the library, Keith, Patricia, Chris. Also to Ian from the Aeronautics Department.

To my Parents and family, thank you for the unwavering support that you have given to me throughout my studies, this has helped me more than you'll ever know.

Finally, thank you to all of my friends who have been there to offer me a listening ear and/or a small spiritual beverage - I have appreciated both in equal measures.

# *Abstract*

The overall objective of the thesis is a fundamental experimental, computational and theoretical study of coupled flows in: (i) fibrous; and (ii) granular; heterogeneous porous media characterised by multiple length scales. Two general classes of static porous media are studied: (i) a porous medium surrounded by a free flow fluid region and (ii) two porous media of different porosities. The aim is to elucidate the local physics of the flow in these media and their potential interaction with local transport phenomena. In this context, two long-standing problems in porous media have been investigated:

(i) coupled flow in a fibrous porous medium and an adjacent free flow region. Local and global aspects of viscous flow over cylinder arrays (fibre lattices) bounded by a free flow region have been studied in Hele-Shaw cells using Magnetic Resonance Imaging (MRI) velocimetry. Specifically, macroscopic (square and semi-circular) and unit cell (square and hexagonal) geometries, pore size, porosity and number of the fibre lattices were varied, whilst, with respect to the free flow region, the width of the open channel was kept constant or varied in a simple or more complex way. Locally, the transitions of the fluid velocities are illuminated in two dimensions at either side of the channel-lattice interface. 'Entrance/Exit' local velocity enhancements (LVE) effects within the corner of rectangular single fibre lattices and 'edge' LVE effects in the lattice exteriors are observed and quantified. The presence of LVE in both examined directions are ascertained within the single semi-circular fibre lattices and an assembly of semi-circular fibre lattices. Remarkably, the flow enhancements originate from (and thus, in design, can be controlled by) the local configuration of the lattice-channel arrangement. The flow details found in the experimental part have been evaluated against the predictions of numerical models (lattice-Boltzmann model, Boundary element method). Experimentally observed LVE and global flow fields within the free flow and the lattice regions are qualitatively and quantitatively reconfirmed by the predictions of the lattice-Boltzmann model. These findings result in a broadening of knowledge and understanding of theoretical and design issues in coupled free flow and flow in a fibrous (or any) porous medium.

(ii) simultaneous flow and mass transfer through beds of saturated granular porous particles. The effect of coupled flow and mass transfer on the transient response of a fixed-bed porous granular

column has been studied at low to moderate particle Reynolds numbers - high particle Peclet numbers. From comparisons with the predictions of a macro-scale (centimetres) tanks-in-series model for packed beds of (a) impermeable and (b) porous particles, the effect of mass transfer from bed voidage to porous particles on column dynamics has been quantified. The principal mechanism responsible for the mass transfer was found to be intraparticle diffusion. Mass transfer limitations are shown to be of critical importance for the column dynamics at low Reynolds numbers ($Re \leq 5$). These findings have been compared with a large number of relevant experimental and theoretical studies on mass transfer in packed beds, resulting in a further contribution to understanding of mechanisms of dynamic transport phenomena in granular packed beds.

# TABLE OF CONTENTS

## CHAPTER 3



## CHAPTER 4

## CHAPTER 7



## CHAPTER 8

# *LIST OF FIGURES*

## *Chapter 2*



## *Chapter 3*

magnitude $M_0$) being tipped for an angle $\gamma B_1 t=\pi/2$ (solid line) or inverted for $\pi$ (dashed line) in the rotating frame; (d) if the nuclei are slightly off-resonance, they will precess with $|\omega|<|\omega_0|$, the effective longitudinal magnetic field $B_{eff}$ is the sum of the two components $B_1$ and $|\omega_0-\omega|/\gamma$. Hence, $M$ is attenuated and phase-shifted in the $x'y'$ plane. When the resonance condition holds ($|\omega|=|\omega_0|$), $B_{eff}$ reduces to $B_1$. *(Page 29)*

**Figure 3.3** The signal acquisition for nuclei which have a slightly different frequency from that subtracted in heterodyning. The real and imaginary part of the free induction decay signal is collected by turning the receiver coil in the x-y plane in the time domain (left) and then Fourier transformed to obtain the NMR spectrum in the frequency domain (right). *(Page 31)*

**Figure 3.4** Implementation of the spin-echo pulse sequence (e) with the manipulation of $M$ in the rotating frame: (a) application of an RF $90^0$ pulse in the $x'$ direction tips $M$ into the $x'y'$ plane; (b) the spin-isochromats A and B begin to dephase due to local magnetic field heterogeneities; (c) after a time $t_d$ a $180^0$ pulse is applied in the $y'$-direction, inverting the spin-ischromats A and B; (d) after another time $t_d$ elapsed the spin-isochromats will have refocused along $y'$ in the $x'y'$ plane. Hence, the maximum possible signal is acquired after the time $2t_d$, which is termed the spin echo time (*TE*). The time between two repetitions of the pulse sequences is called the repetition time (*TR*). *(Page 36)*

**Figure 3.5** NMR imaging of two beakers filled with different volumes of water. When a linear magnetic field gradient $G_x$ (right) is applied in addition to the external magnetic field $B_0$, the spin-isochromats in the two beakers will resonate, in accordance with their position, with different frequencies. This results in the two broad signals in the NMR spectrum whose intensities are a quantitative measure of the number of the liquid nuclei in the beakers. The separation between the peaks of the two signals, $\Delta\omega$, is proportional to the magnitude of the applied gradient and the distance between the beakers. When no gradient is applied (left), the NMR spectrum consists of one narrow signal centred at the Larmor frequency. The intensity of the signal is proportional to the number of the liquid nuclei in both beakers. *(Page 40)*

**Figure 3.6** The full pulse sequence used in the spin-warp imaging (a) and the corresponding $k$-space rastor analysis (b). The sample to be imaged is presented by the points in the $k$-space. The sequence begins by a simultaneous application of two mutually orthogonal magnetic field gradients $G_{1x}$ and $G_y$ (the line 1 in the $k$-space). Then the $180^0$ RF pulse is applied, traversing the $k$-space vector along the line 2. The signal is acquired by applying the second read gradient $G_{2x} = 2G_{1x}$, which 'frequency' encodes the spin-isochromats at both negative and positive $x$ points within a row in the $k$-space along the line 3. The sequence is then repeated, but with increments in the gradient $G_y$, which phase encodes the spin-isochromats at different rows of pixels. The position of the $k$-vector after one such increment is shown by the arrow 4. *(Page 42)*

**Figure 3.7** Spin-echo pulse imaging sequence with a $90^0$x RF pulse used with the slice gradient $G_z$ to selectively excite a region along the $z$-direction for acquisition of an image in the $xy$ plane. The slice gradient is reversed in the second lobe, following the application of the RF pulse, in order to refocus the phase shift induced by the same gradient in the first lobe. *(Page 44)*

## *Chapter 5*

## *Chapter 6*



## *Chapter 7*

## *Chapter 8*

## ***Chapter 9***

## *Appendix 1*

**Figure A1.1** Control volume $V$ located in a body bounded by a double-sided surface with the outward unit normal $\boldsymbol{n}$ defined. *(Page 206)*

## *Tables*

### *Chapter 8*

**Table 8.1.** Literature mass-transfer correlations for beds of spherical particles used for comparison with the data obtained in this study. *(Page 182)*

# Chapter 1

# General Concepts in Studies of Porous Media

This introductory Chapter briefly outlines basic definitions of porous media, and then identifies the main issues in porous media studies. The conceptual and mathematical approaches used to tackle the fundamental issues pertinent to this study of porous media are explained. As will be seen, the modelling principles of continuum mechanics (rather than statistical mechanics, which is another appropriate option) are highlighted. The Chapter ends with a description of the thesis structure.

## *1.1 Introduction to Porous Media*

Porous materials are encountered in many science and engineering fields including biomechanics, geophysics, hydraulics, soil mechanics, ground water hydrology, civil, aeronautical, agricultural, petroleum and chemical engineering. The term porous media encompasses a wide variety of substances; amongst the most significant are porous packings in the adsorption towers such as Berl saddles and Raschig rings, beds formed of granules or sand, porous rocks such as limestone or dolomite, fibrous aggregates such as cloth, filter paper and catalytic supports containing micro-pores.

The constituent parts of any porous medium domain are the solid matrix occupied by the solid phase and the void space occupied by a single or multiple fluid phase(s). When sufficiently large samples of the porous medium are taken at different locations within the porous medium domain, the solid phase will always be present in the sample.

A phase in a porous medium is a homogeneous part of a porous medium domain separated from other parts of the domain by a definite physical boundary or interface

or interphase boundary. A component is a part of a phase composed of an identifiable homogeneous chemical species, or of one assembly of species (ions, molecules) [1].

Flow and transfer of species through porous media play significant roles in heterogeneous catalysis, gel permeation chromatography, membrane separation processes, filtering of gases and liquids drying of bulk goods and many other processes [1-4].

The precondition for transport of extensive quantities (the quantities that are additive over volumes such as momentum or mass) through a single phase is the connectivity of that phase. A domain is said to be connected if any two points belonging to the domain can be connected by a curve that lies completely within it. Conversely, a non-connected domain is composed of a collection of disjoint domains, with disjoint boundaries [1].

The fact that only the interconnected void spaces can contribute to transport of matter across the porous medium is essential in studies of transport through porous media. In addition, the possibility of the existence of the pores that are interconnected only from one side with the fluid phase needs to be considered. These pores are called 'dead end ' or 'blind' pores and their contribution to transport is usually negligible.

In porous media the interconnected or non-connected fluid portions make up networks of channels, commonly referred to as pores. A fundamental porous media parameter, porosity (or voidage), is defined as the volume fraction of the porous sample that is occupied by pore or void space. The rest of the sample volume is occupied by the solid fraction. A fundamental porous media property, hydraulic conductivity, is characterised by resistance of the solid matrix to fluid flow (permeability) and fluidity of the fluid phase (reciprocal of kinematic viscosity).

A porous medium is heterogeneous with respect to its porosity (or its solid volume fraction), and therefore hydraulic conductivity and permeability if, at the length-scale examined, the porosity varies locally with space in the porous domain. A porous medium domain is anisotropic at a point with respect to a certain property (i.e.

hydraulic conductivity, permeability) if that property varies with direction at that point. A porous medium is static (or fixed) if its morphology does not change during the examined process that involves transport phenomena.

The fibrous and granular porous media investigated in this study are static. Both media are characterised by dual porosity, therefore being heterogeneous with respect to the porosity (and the permeability) and anisotropic with respect to the permeability at microscopic length scales.

## *1.2 Conceptual and Mathematical Approach in the Study of Fundamental Issues in Porous Media*

In fundamental research on porous media, the three main interrelated issues that need to be simultaneously examined are: transport phenomena; interfacial or interphase effects; and pore structure. In this study the emphasis has been placed on transport phenomena and interphase effects in dense porous particle assemblies. A better comprehension of transport phenomena in these systems is necessary in order to improve the design of many industrial processes, amongst which liquid composite moulding processes, heat and mass transfer operations in heat exchangers and hollow fibre reactors, filtration processes, flow in rock formations in petroleum reservoirs and reactor technology are the most pertinent to this study. These processes are commonly described by conceptual models consisting of heterogeneous fibrous (relevant to the first three processes referred to) or granular porous media (relevant to the last two processes referred to). The two types of porous media selected for studying are amongst the most typical choices for representing real porous systems, therefore serving as a good foundation for comprehensive studies of porous media.

Flow and transport of species in porous media are, in essence, dependent on the structure of the porous material, i.e. the geometry of solid phase boundaries. In some real systems (i.e. tube banks in a hollow fibre reactor or a heat exchanger), the surface geometry of the solid phase can be precisely mirrored in the model. This is the case

studied in the first part of the thesis, which concerns steady-state flow in a fibrous porous system with well-defined solid boundaries. This fact enables the determination of spatial distributions of state variables (velocity, pressure of the fluid phase) with the use of numerical mathematical models based on continuum mechanics. The solutions for the state variables can be found from the Navier-Stokes equations written for the fluid phase of the porous media domain at microscopic level. What is more, the specification of boundary conditions prevailing at the solid phase surfaces does not, in general, pose problems.

However, in many other porous systems (e.g. packed bed column) an exact description of the system is practically impossible due to the complexity of the solid phase boundaries. This fact renders any solution for extensive quantities at a microscopic level of the solid phase boundaries impractical and/or impossible. Instead, the analysis is done at the macroscopic level at which measurable, continuous and differentiable quantities are introduced. Now, the porous medium, rather than the fluid phase only, is considered as a continuum in which the macroscopic mass balance applies. This approach is used in the second part of this thesis that deals with transport phenomena in granular porous media in a packed bed column. The values for variables are space-averaged over a number of porous medium subdomains, i.e. fundamental unit cells, with well-defined solid phase boundaries. Yet, we must always be cognisant of the loss of information, inevitably occurring with the introduction of fixed ideal boundaries in the space averaging process. To overcome this problem, the conditions at the fluid-solid phase boundary are supplied in the form of a closure law. The exchange of extensive quantities between the adjacent subdomains is also described in terms of average quantities.

### *1.3 Organisation of the Thesis*

As described in the abstract, this thesis concerns the two fundamental problems in studies of heterogeneous porous media: (i) flow in a fibrous porous medium surrounded by a free flow fluid region and (ii) flow and mass transfer in a granular

porous medium of dual porosity. Accordingly, the thesis is divided into the two parts, although many of the ideas used in modelling the two porous media studied are conceptually similar. The references related to the first part are given in the end of Chapter 5, whilst the references related to the second part are given in the end of Chapter 8.

## Bibliography

[1] **Bear J.:** *Dynamics of Fluids in Porous Media.* New York: Dover Publications, Inc., 1st edition, (1988).

[2] **Bear J.; Bachmat Y.:** *Introduction to Modeling of Transport Phenomena in Porous Media.* Dordrecht. Boston. London. Kluver Academic Publishers, 1st edition, (1991).

[3] **Dullien, F.A.L.:** *Porous Media: Fluid Transport and Pore Structure.* San Diego: Academic Press Inc., 2nd edition, (1992).

[4] **Scheidegger, A.E.:** *The Physics of Flow Through Porous Media.* London: Oxford University Press, 2nd edition, (1960).

[5] **Muskat M.:** *The Flow of Homogeneous Fluids Through Porous Media.* McGraw-Hill Book Company Inc., 1st edition, (1946).

# PART I

## *Creeping Flow in a Fibrous Porous Medium of Dual Porosity*

# Chapter 2

# Flow in Fixed Beds of Fibrous Particles

The subject of investigation in the first part of the thesis is the flow field in a system comprised of a fibrous porous medium adjacent to a free flow region. In this Chapter, a description of this major class of porous media is given, together with its direct applications; the description of the relevant flow properties and the mechanisms governing physical phenomena that take place during flow in the examined porous medium. Further, the progress that has been made in this research field up to date is reviewed; the problems to be tackled in this investigation are addressed, including a brief modelling strategy for their solution.

## *2.1 Some Main Line Applications of Flow Studies in Fibrous Porous Media*

Flow through porous media consisting of a network of cylindrical fibres (lattices) can be found in many engineering applications such as liquid composite moulding, flow and mass transfer in hollow-fibre reactors and heat transfer in heat exchangers. In this section each of these applications will be reviewed briefly.

*Liquid composite moulding* (LCM) operations such as Resin Transfer Moulding (RTM) and Structural Reaction Injection Moulding (SRIM) have become increasingly popular during the past twenty years because of the potential for high volume production of fibre reinforced composite material components. The main development work is nowadays focused on the production of structural parts for the automotive, transportation and commercial and military aircraft industries [6,7].

The basic steps of RTM include five basic operations [8], as seen from Fig.(2.1):

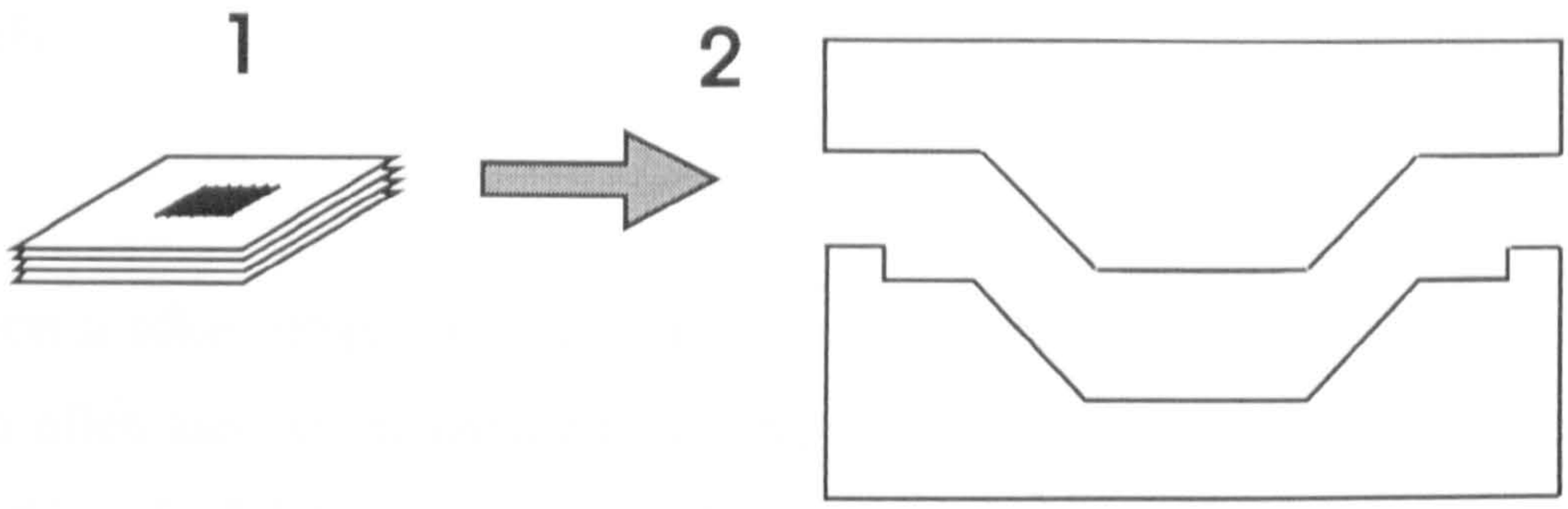


**Figure 2.1** Basic steps in resin transfer moulding processes.

The critical processing issues in RTM are pressure drop, the mould filling time and filling patterns [9,10], which are all related to the controllable injection pressure at the inlet. With a small inlet pressure, the mould will fill very slowly or not at all, which may result in premature resin cure with an unimpregnated preform section. At the opposite limit, with excessive pressure used, there may be a fibre wash, fibre displacement or the mould may leak or deform. Bearing in mind that pressure drop in the mould is (through the preform hydraulic conductivity) related to the mould fluid velocity, it is of great interest to have full descriptions of the local velocity fields in the mould. This knowledge will reduce the high number of costly trial and error experiments that are presently required to identify the best processing conditions for

the manufacturing of any new component, and therefore will speed up the design process.

The preform is often comprised of a number of fibre lattices (fibre bundles or tows are terms also often used in the literature of composite materials [11,12]), arranged in a desired fashion. Each lattice consists of a large number of individual fibres, as seen in Fig.(2.2).

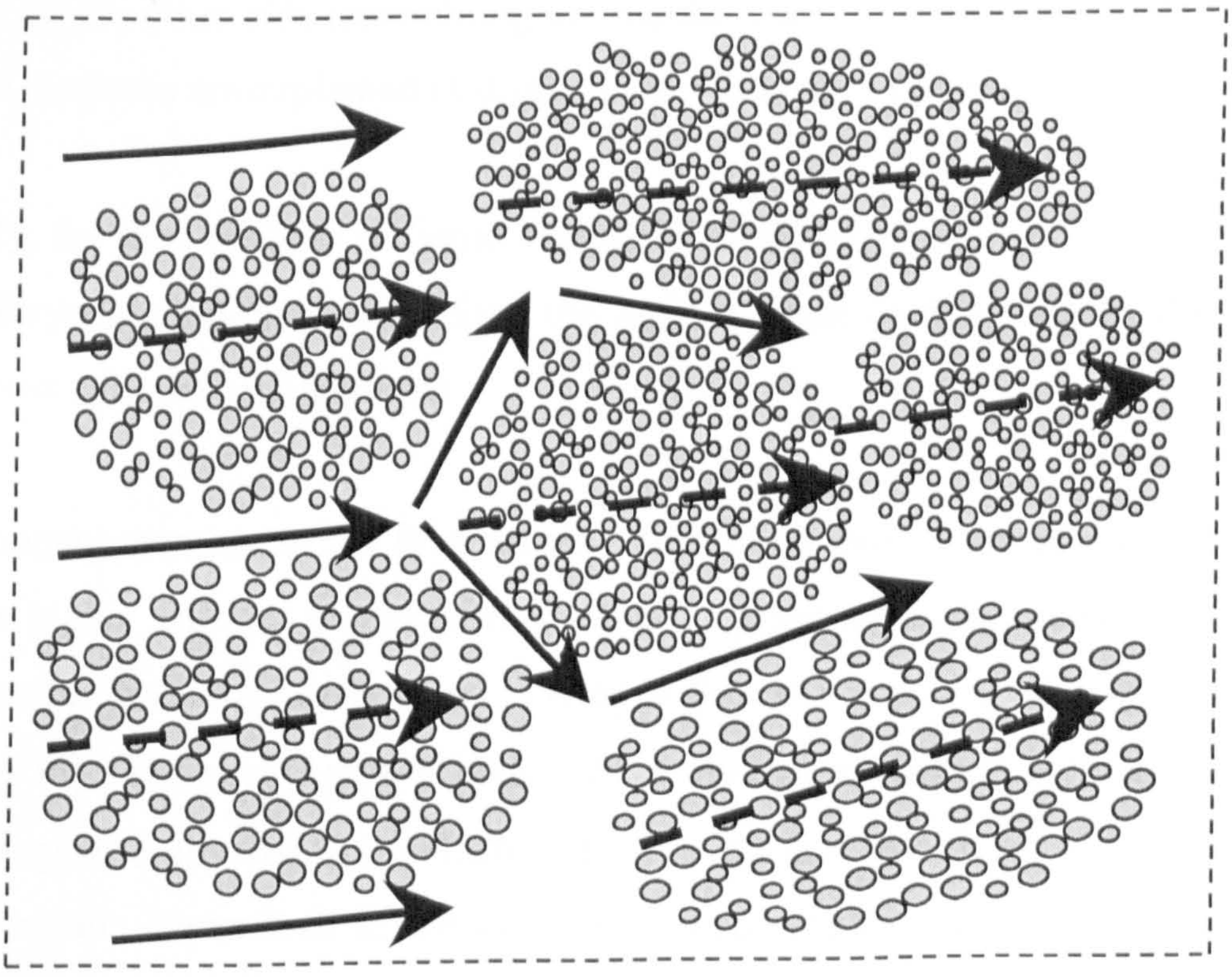

**Figure 2.2** An insert depicting the cross section of the middle part of a fibre preform during the injection step. Fluid flows through the fibre lattices (bundles, tows), as shown by the dotted lines and around them, as shown by the solid lines. The arrows indicate the flow direction.

From this description, it follows that the length-scales associated with the size of fibre lattices (termed the macro-scale in this study, centimetres) and with the size of fibres comprising each lattice (the micro-scale, a few hundred microns) can be defined. In accordance with the two defined length-scales, the resin injection step (4) includes two, simultaneously occurring, types of flow:

- the advancement of the bulk flow front through the interstitial spaces between the fibre lattices (see the solid lines in Fig.(2.2))
- the local flow within the fibre lattices, i.e. the fibre lattice impregnation (see the dotted lines in Fig.(2.2)).

In order to experimentally and mathematically simulate these types of flow in the heterogeneous fibrous porous media, it is logical to introduce a model system consisting of arrays of cylinders (resembling the fibre lattices), surrounded by an open region from one side (resembling the interstitial space between the fibre lattices) and the wall on the other side (resembling the mould wall) [13]. The flow cells designed for these purposes are explained in detail in the subsequent section.

Typically, the flow regimes in liquid composite moulding processes are in the region of low Reynolds numbers. Therefore, the main concern of this study is the viscous flow across cylinder arrangements.

As previously mentioned, the flow across arrays of cylinders surrounded by an open region is highly relevant in a number of other engineering applications, such as *flow and heat transfer in heat exchangers* [14,15] *or flow and mass transfer in hollow-fibre reactors* [16]. Heat exchangers or hollow-fibre reactors are commonly made up of in-line or staggered tube banks in which cross flow plays a significant role. Fluid flows across the tube banks and, at the same time, bypasses the tube banks through the interstitial space between the exchanger walls and the banks arrangement. This is, again, the physical problem of coupled free flow and flow through a fibrous porous medium.

Predictions of the overall performance of heat exchangers or hollow-fibre reactors are based on empirically-based correlations of pressure drop and heat or mass transfer coefficients. Important effects such as entrance/exit phenomena, bypassing, variable flow properties etc. are required to be readily accommodated in the theoretical models. In all these phenomena, local fluctuations of the pertinent variables (velocity, temperature, concentration) are present and dependent on geometry of the fibre arrangement. The main concern of the studies in fibrous porous media undertaken

here, are local aspects of flow in the free flow and the porous region including their interface. Obtaining accurate information of the local flow characteristics would aid designing the heat and mass transfer equipment.

## *2.2 Theoretical Background of Viscous Flow Studies in Saturated Fibrous Porous Media*

Viscous flow of an incompressible Newtonian fluid in saturated fibrous porous media has received significant experimental and theoretical attention in the scientific and engineering literature due to a vast number of applications, some of which are explained in the previous section. Traditionally, such flow has been described by a macroscopically averaged equation, which linearly relates the average fluid velocity in the porous medium, $\overline{u}$ , to the average pressure gradient ( $\frac{d\overline{p}}{dz}$ ) in the flow direction $z$:

$$\frac{d\overline{p}}{dz} = -\frac{\mu}{k}\overline{u}\,, \tag{2.1}$$

where the average fluid velocity in the porous medium is given as the ratio between the volumetric flowrate and the cross section area perpendicular to the flow direction $z$ and $\mu$ is the fluid dynamic viscosity. The average pressure, $\overline{p} = \overline{P} + \rho g h$, is the modified averaged fluid pressure, where $\overline{P}$ is the atmospheric pressure, $\rho$ is the fluid density, $g$ is the gravitational acceleration and $h$ is the height above a horizontal datum plane, which is at $\overline{P}$. The constant, $k$, is termed permeability of the porous medium and, through its mathematical reciprocal, expresses the magnitude of resistance of the solid matrix to flow.

Equation (2.1) was originally presented by Darcy (1856) [17], on empirical grounds, for a homogeneous fluid flow through a homogeneous, static and non-deformable porous medium, in which $k$ is a scalar. It is often stated as Darcy's law. In general, the permeability in Darcy's law is the direction dependent property of porous medium and therefore is mathematically described by a second order tensor. It is important to say that in Darcy's law, inertial effects are neglected. Hence its upper validity is limited to flows at low Reynolds numbers ($Re$<10).

Permeability of any porous medium including fibrous ones depends on the size, shape, concentration and the geometrical arrangements of the particles (i.e. fibres) that make up the solid matrix. Various modelling approaches have been employed to obtain the permeability constant in Darcy's law for porous media. For this purpose, a well established model was developed by Carman and Kozeny (1938) [18,19], in which functional dependence for permeability $k$ is given by:

$$k = f(\varepsilon, s, k_{cc}), \tag{2.2}$$

where $\varepsilon$ is porosity, s is the specific surface of porous medium particles and $k_{cc}$ is the porous medium constant named after Carman and Kozeny.

It is generally accepted that the Carman-Kozeny model well describes flow in isotropic porous media. However, its suitability for flow description in fibrous porous media, including the ones typically employed in RTM processes, is questionable [9,20]. The simplest shortcoming of the model is that it predicts a finite permeability in a physical situation when the fibres are closely packed together (expressed as the maximum fibre packing density) thus blocking any transverse flow. The representation of fibrous porous media with cylinder arrays better describes the physical systems pertinent to this study.

Flow across cylinder arrays has been mathematically modelled with the aid of analytical or numerical methods. Analytical methods have been used at low porosities (lubrication approach) and at high porosities (unit cell models). The experiments of flow in homogeneous fibrous porous media at high porosities are in a relatively good agreement with the models [20,21]. However, many real fibrous porous systems are heterogeneous. In RTM, for example, experiments by Sadiq *et al.* [10] indicated a notable difference in permeability between an ideal fibre bed made up of solid rods and a real fibre preform bed made up of fibre lattices, even though both beds had equal porosities. The difference in permeability was ascribed to the microstructural variations in the real fibre preform bed, which make such porous bed heterogeneous.

An open channel region adjacent to an arrangement of the cylinder arrays (the fibre lattices), as depicted in Fig.(2.3), is a logical starting point for a model for heterogeneities in the fibre preform.

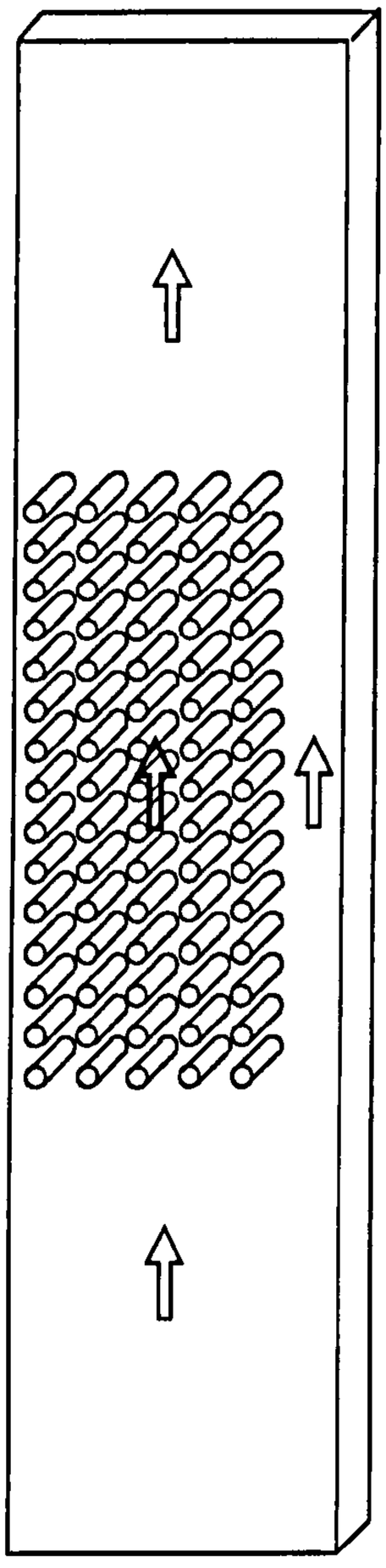

**Figure 2.3** A starting-point model dual porosity fibrous medium used to experimentally and theoretically simulate flow in a heterogeneous fibrous preform, or a heat exchanger or a hollow-fibre reactor.

Since many mould-filling processes in fibrous porous media deal with parts that have a shell-like geometry with very small thickness compared to the other dimensions of the part, the flow in the thickness direction can be neglected and therefore considered as two dimensional [22]. This line of thought has been followed in the design of experiments: the model systems are formed by cylindrical rods, macroscopically arranged in rectangular or circular fashion and confined inside a Hele-Shaw cell, as in Fig.(2.3).

In addition, it is worth recalling from Section (2.1) that identical flow patterns are expected to exist in flow across tube banks in heat exchangers or flow and mass transfer in hollow-fibre reactors. An accurate description of flow phenomena in these systems can be obtained from studying the model system with the simple configuration from Fig.(2.3), along with the more complex configurations to be explained in the subsequent section.

The open channel is designed to be narrow enough to force fluid through the array but wider than the distance between individual cylinders in the lattices. Evidently, the system may be deemed a heterogeneous porous medium with two different porosities and consequently permeabilities, depending on the length-scale considered. The first scale, encompassing the channel and the arrays, is characterised by a macro-scale porosity and the second scale, defined by the solid volume fraction of the cylinders forming the lattice, is associated with a micro-scale porosity. Therefore, the channel simulates the effect of a neighbouring medium with higher permeability on the velocity distributions within the fibre arrangements. The flow in this system must now be looked into at the two length-scales.

Two classical modelling concepts have been used to model coupled free flow in an open channel region - flow in a porous medium (including the fibrous one). The first is by Beavers and Joseph [23], who solved Stokes equations [24] for flow description in the open channel:

$$0 = -\nabla P + \mu \nabla^2 u \,, \tag{2.3}$$

in which the acceleration and the convective inertia terms in the Navier-Stokes equations (see Appendix 1) are neglected and therefore zero on the left-hand side of equation (2.3). This is a fair assumption for studying steady-state viscous flow. Within the porous medium, Beavers and Joseph applied Darcy's law. The two regions are matched by a slip boundary condition at the open region - porous matrix interface:

$$u_{ch} - \bar{u} = \frac{\sqrt{k}}{\alpha} \frac{du_{ch}}{dx} \quad \text{at} \quad x=0 \,, \tag{2.4}$$

where $u_{ch}$ denotes the fluid velocity within the channel, $\overline{u}$ stands for the mean (ensemble-averaged) Darcy velocity within the porous medium, $\alpha$ is a dimensionless constant which characterises the porous medium and can only be determined by experiment.

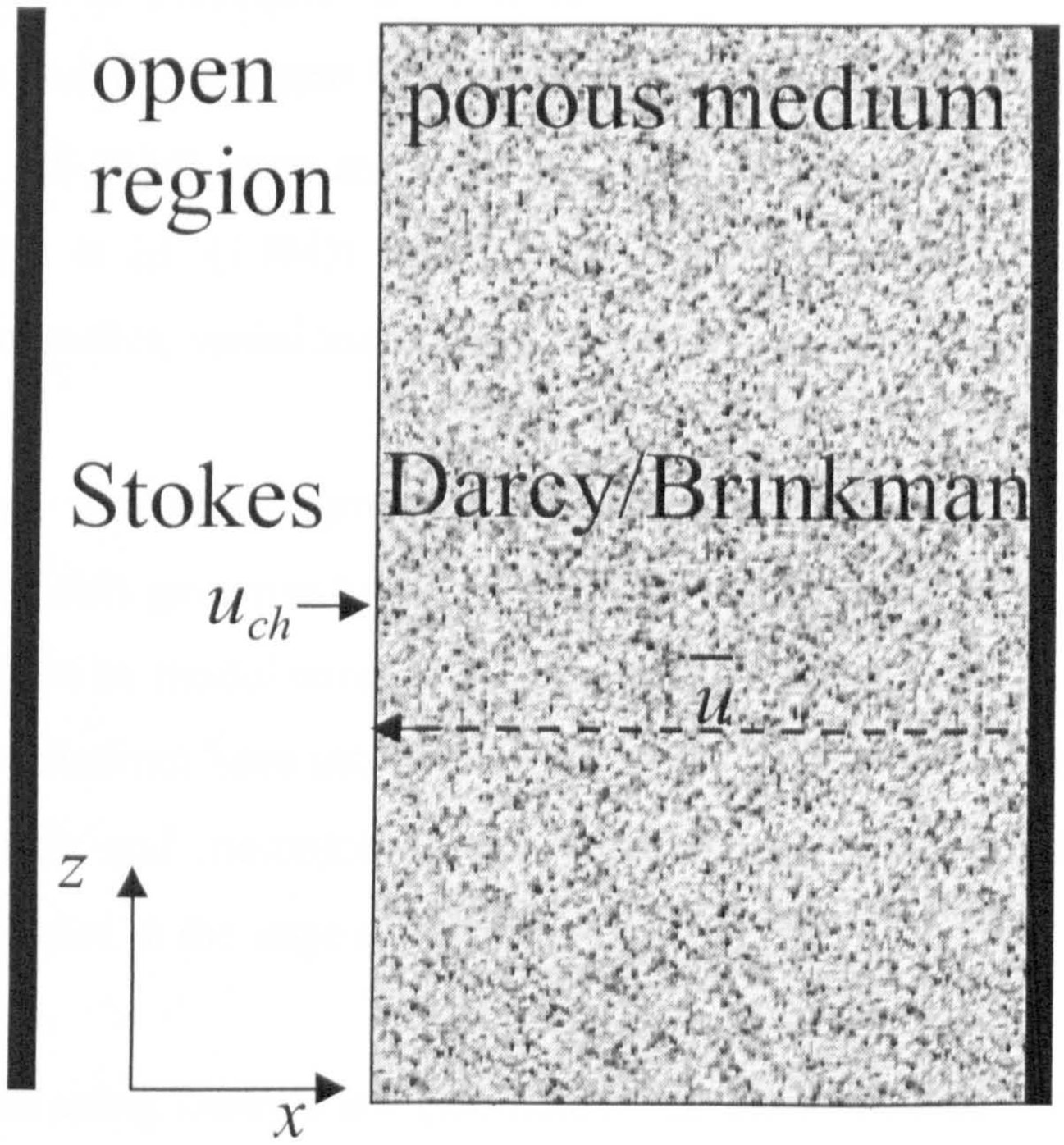


**Figure 2.4** Modelling concepts used in the theoretical description of coupled free flow in an open region and flow through a porous medium.

The velocity profile in the open channel is solved from Stokes equations with the slip boundary condition from equation (2.4) applied at the boundary with the porous medium and no-slip condition at the channel wall. The velocity profile just below the channel-porous medium interface is flat and the decay of longitudinal velocities in this region is not described.

The second modelling concept, again, describes the flow in the open channel by the Stokes equations. For the flow description in the porous medium, an equation, originally developed by Brinkman (1947) [25], is used. Brinkman, in an ad hoc manner, added to the Darcy's law equation a macroscopic viscous (or diffusion) term:

$$\frac{d\overline{p}}{dz} = -\frac{\mu}{k}\overline{u} + \tilde{\mu}\frac{d^2\overline{u}}{dx^2} \quad , \tag{2.5}$$

where $\tilde{\mu}$ denotes the effective fluid viscosity that can, in general, differ in value from the fluid viscosity $\mu$. In the Brinkman equation the velocity gradients act in the $x$ direction, which is perpendicular to fluid flow. The relationship between the two viscosities, $\mu$ and $\tilde{\mu}$, has been the subject of debate over the years and has not been resolved yet. [26-29] (Larson and Higdon (1986), Durlofski and Brady (1987), Nield (1991), Martys *et al.* (1994)). Specifically, in heterogeneous porous media with anisotropic properties, variations in the effective viscosity could be expected.

These milestone modelling approaches (Brinkman's equation and Beavers and Joseph slip velocity model) gave rise to a number of experimental, theoretical and numerical studies. Attempts to model coupled free flow in an open channel region - flow in a fibrous porous medium have included application of macroscopic Darcy's equation at both microscopic and macroscopic scales (Parnas and Phelan (1991) [30]). These flows were coupled in the large scale continuity equation.

The approaches using Darcy's law (including Beavers and Joseph, Parnas and Phelan) have a common drawback: that is the lack of information they provide at the micro-scale level in the porous medium. And exactly this can be an essential feature of coupled free flow - flow in a fibrous porous medium. It is well known that momentum transfer by shear (tangential stress) at the interface of the two media affects the velocity of the fluid just below the boundary, inside the porous medium. These considerations imply that the interrelation between the flow fields in an open channel region and in a fibrous porous medium need to be better understood. The micro- and macro-scale aspects of this type of flow are illuminated in this study.

Recent years have seen numerical methods as an often employed tool for flow description in heterogeneous fibrous porous media. The numerical methods have included the use of finite [31,32] and boundary element [26,33,34] methods, as well as, more recently, the lattice-Boltzmann method [35-37]. Their main advantage lies in providing the solutions for microscopic Stokes equations in both open channel and fibre lattice regions without artificially separating them, as it is the case with

modelling approaches that use Darcy's law and Brinkman equation. The application of numerical methods at microscopic level is facilitated when a system has well-defined solid boundaries, as the arrays of cylinders do in this study. As will be elaborated later, in Chapter 4, the solutions for flow in the fibrous media (as depicted in Fig.(2.3)) in the creeping flow regime obtained by Boundary Element Method (BEM) and lattice-Boltzmann model (LBM) were used for comparisons with the experimentally detected flow fields in the same media by Magnetic Resonance Imaging velocimetry.

## *2.3 Experimental Studies of Flow in Saturated Fibrous Porous Media*

Comprehensive reviews on experimental viscous flow studies in deterministic and random fibrous porous media have been published by Jackson and James (1986) [38] and Skartsis *et al.* (1992) [20]. Both authors point out that not many studies have been carried out in deterministic porous media.

Bergelin *et al.* (1950) [14] were the first to study flow in deterministic fibrous porous systems experimentally. They studied the flow of oil across tube banks of large diameter (9.53mm and 10.05mm) in a heat exchanger, for a wide range of Reynolds numbers. The range of solid volume fractions was from 0.503 to 0.580. Relevant to this work, they ascertained that Darcy's law was still valid in the Reynolds number range from 1 to 10.

An experimental study, interesting from a theoretical point of view, of the steady state flow at low Reynolds numbers ($Re$<1.914) in model fibrous porous media (in the absence of any open regions) was carried out by Yarlagadda and Yoganathan (1989) [39] using Laser Doppler Anemometry (LDA). Obtaining two velocity components and estimating the third component from the continuity equation, they inferred that the flow was dominated by viscous effects and observed no presence of mixing and inertial effects. The present study seeks to elucidate the influence of the aforementioned effects on the patterns of steady-state coupled flow across regular arrays of cylinders and a free flow region, in the creeping flow regime. In this context,

the Reynolds number based on the average superficial velocity and the size of the fibres is designed to be well below 1 in the experiment – of the order of $10^{-3}$.

Very few experiments on coupled viscous free flow and flow in a porous medium are reported in the literature. A well-known experimental study of coupled parallel flow in a porous medium and an open channel is that by Beavers and Joseph (1967) [23]. The flow description, leading to the establishment of the slip boundary condition at the interface, is based on the comparison of the total volumetric flowrates through the channel and the porous block in one case and the channel and the non-porous block in the other case. Therefore, the experimental data could only provide information on the global velocity field. The local velocity fields along an open-channel flow over regularly and randomly packed porous media were studied by Saleh *et al.* (1993) [40] using Particle Image Velocimetry (PIV). The characteristic length for the Reynolds number (typically $Re$=0.5) was the height of the open channel. The velocity components in two dimensions were obtained in the open channel and near the interface of the free flow and the porous medium regions, yet no data were reported for the local flow through the porous medium.

More recently, Gupte and Advani (1997) [41,42] studied viscous flow near the interface of a highly porous aligned fibre preform/mat and an open region by LDA in a Hele-Shaw cell. Their experimental findings show that the depth of the boundary layer zone inside the fibre preform/mat in which longitudinal velocities sharply decrease (from that in the open channel to the velocity within the fibre arrangements) is of the order of the thickness of the cell.

## *2.4 Objectives of Study of Flow in Fibrous Porous Media of Dual Porosity*

The theoretical and experimental reviews have implied that coupled viscous flow in a porous medium and an adjacent open region is a fundamental problem of substantial theoretical and experimental interest in porous media studies that has not been satisfactorily solved. In order to theoretically describe it, models commonly resolve the problem on the macroscopic scale using the average flow quantities in the porous

medium, which, especially near the interface, may significantly deviate from the mean values due to differences between the velocity fields in the free flow and porous regions. The local flow characteristics within the porous medium and free flow region may be profoundly different from the average flow characteristics. Therefore, knowledge of the local flow aspects is required to fully understand this class of flow in porous media.

Obtaining the local characteristics of the two-dimensional viscous flow field in the system where the porous medium is represented by fibre arrays placed in a Hele-Shaw cell is the primary aim of this investigation. The fibrous porous medium consists of ordered lattices of circular, finite-size cylinders and a low resistance open region (channel) on one side of the lattices. In particular, the velocity component which is transverse to the flow direction can have an important contribution to the total velocity field in these systems and is studied in both porous and the free flow regions.

As introduced in Section (2.2), at the channel-lattice interface a transition zone exists across which the velocity varies. Velocity variations in this 'screening effect' zone could be small, but the length of this zone at the either side of the interface is of importance. A full description of the flow field in the transition zone will give the answer on how far the screening effect propagates from the open channel to the fibre lattices, as well as, on the other side of the interface, what is the scale of the disturbance to flow from the fibre lattice on the open channel flow. Importantly, this study includes detection of the velocity fields in the regions ahead of (fore-region) and behind (aft region) the fibre lattices that may also affect the local velocity distribution within the lattices.

This is a comparative study that seeks to elucidate the effects of porosity, unit-cell geometry, macroscopic geometry and the fibre size within the fibre lattices on velocity patterns in coupled flow in fibrous media of dual porosity. Furthermore, the effects of variable width flow region for single lattices arrangements and the lattice assembly are examined. For this purpose, the flow cells with various macroscopic and

unit cell geometries and porosities of fibre lattices are designed. They are presented in Fig.(2.5).

The effect of porosity on the local velocity distributions within a fibre array is studied by comparing two macroscopically rectangular square unit cell fibre lattice geometries (the cells I and II in Fig.(2.5)) of different porosities (nominally $\varepsilon$=0.5 and $\varepsilon$=0.7 respectively) with different, relatively large, (3mm and 4mm respectively) cylinder diameters.

Macroscopically rectangular but hexagonal unit cell lattice (the cell III) of the same porosity and cylinder diameter as one of the square unit cell lattices (the cell I) was selected in order to examine the effect of fibre unit cell arrangement on local flow patterns.

Furthermore, the influence of macroscopic geometry of the fibre lattices and variable width of the free flow region on flow patterns in coupled flow in a fibrous medium of dual porosity is studied by designing semi-circular macroscopic arrangements of cylinder arrays of moderate porosities (the fibre lattices IV-VI). The effect of the cylinder diameter/gap between the cylinders is studied on the cell VI, which has the same porosity and the macroscopic geometry as the cell IV but reduced fibre diameter. Recalling from Fig.(2.2) that a fibre preform may be comprised of fibre lattices of various macroscopic and unit cell geometries, this selection of experimental cells is a logical step further in description of heterogeneities in fibrous porous media.

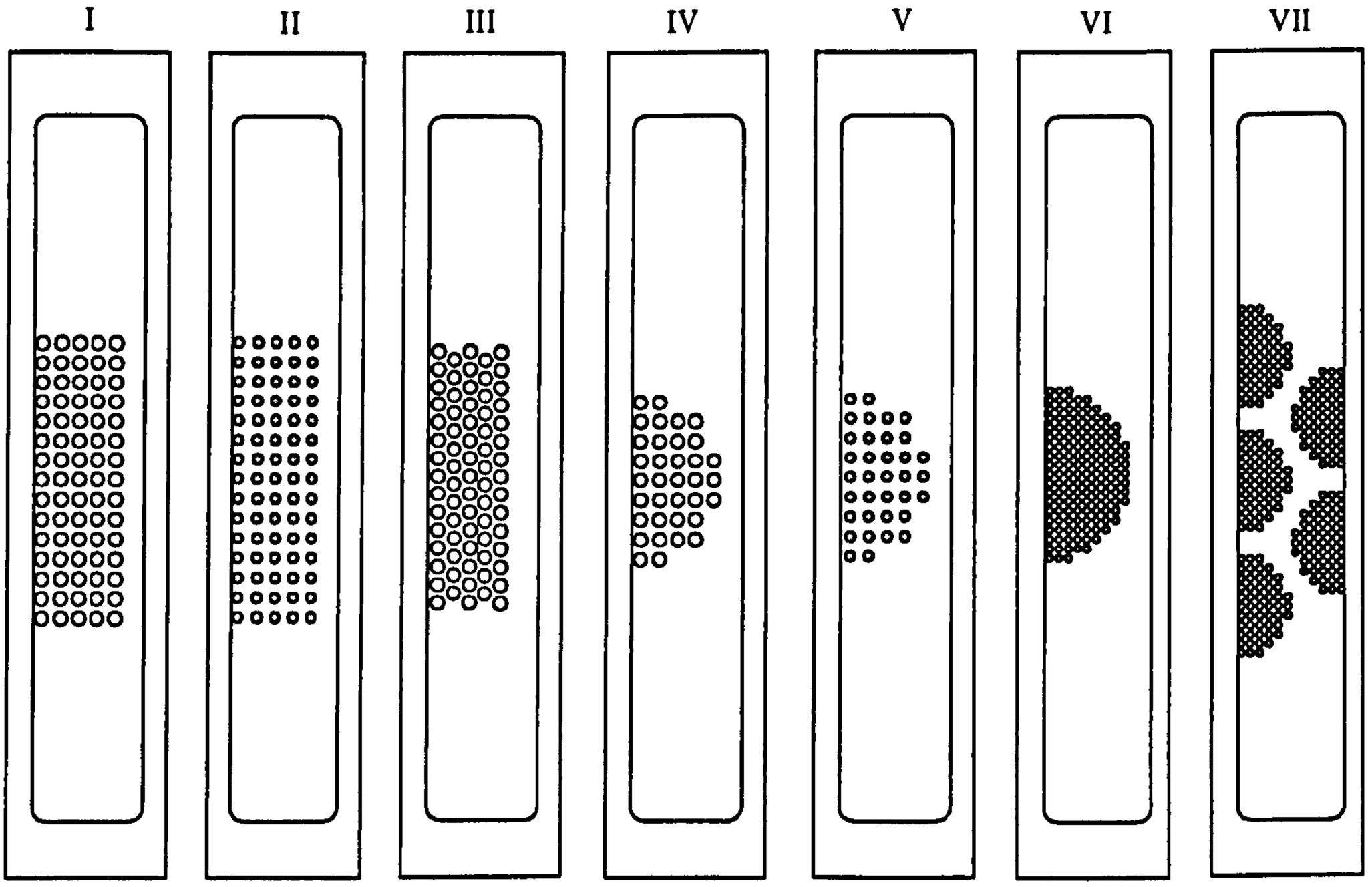


**Figure 2.5** The cross sections of flow cells with the fibre array configurations designed to study the effects of porosity, unit-cell geometry, macroscopic geometry and the fibre size on velocity patterns in coupled flow in fibrous media of dual porosity: cell I – macroscopically rectangular square unit cell lattice of porosity $\varepsilon$=0.5 and fibre diameter D=4mm; cell II – macroscopically rectangular square unit cell lattice, $\varepsilon$=0.7, D=3mm; cell III - macroscopically rectangular hexagonal unit cell lattice of porosity, $\varepsilon$=0.5, D=4mm; cell IV - macroscopically semi-circular square unit cell lattice, $\varepsilon$=0.5, D=4mm; cell V - macroscopically semi-circular square unit cell lattice, $\varepsilon$=0.7, D=3mm; cell VI - macroscopically semi-circular square unit cell lattice, $\varepsilon$=0.5, D=2mm. The effect of neighbouring lattices on flow field in dual porosity fibrous media is studied on the assembly of macroscopically semi-circular square unit cell lattices of porosity $\varepsilon$=0.5 arranged in the hexagonal order (cell VII). Fibre diameters in each lattice are D=2mm.

Finally, an arrangement of five fibre lattices, all having the same micro-scale porosities, and macroscopically arranged in a hexagonal fashion, is designed to illuminate the velocity patterns at both scales when an individual lattice is in the neighbourhood of the other fibre lattices. The free flow region in this configuration is of variable width but is designed to vary in a more complex fashion than in the examined cells with the semi-circular lattices. The geometry of the free flow region adjacent to the fibre lattice assembly is affected by the surface macroscopic irregularities of the neighbouring lattices, therefore enabling for more complex tortuous pathways of the fluid in the free flow region.

For the experimental detection of the two-dimensional steady-state viscous flow field in the investigated dual porosity fibrous medium, Magnetic Resonance Imaging (MRI) velocimetry [43] was used. For the purpose of monitoring the steady state flow, MRI measurements are well suited as they give accurate information on average flow properties over time. A considerable number of experimental studies of fluid flow in porous media have been carried out by other techniques such as Laser Dopler Anemometry (LDA) [44] and Particle Image Velocimetry (PIV) [45]. The most important advantages of MRI techniques lie in its non-invasiveness and its ability to provide images of a sample in all three dimensions with micron scale resolution. In addition, MRI techniques offer advantages in monitoring fluid transport in non-transparent systems, as they do not suffer from signal attenuation due to opacity or scattering at the fluid-solid interface.

Use of MRI in the study of velocity distributions in general three-dimensional flows has been well documented over the last decade. Porous systems studied using MRI range from hollow-fibre bioreactors [46], wall bounded flow through a cylindrical plug of porous material [47] to flow in packed beds [48]. Therefore, MRI is an appropriate experimental technique for studying of the two-dimensional flow field in a dual porosity fibrous medium. In the next Chapter, fundamentals of magnetic resonance will be outlined, along with basic principles of magnetic resonance imaging and velocimetry.

# Chapter 3

# Theory on Nuclear Magnetic Resonance (NMR) Imaging and Velocimetry

The physical phenomenon of Nuclear Magnetic Resonance (NMR) was discovered independently by Bloch *et al.* [49] and Purcell *et al.* [50] in 1946. Originally, the technique was predominantly used in chemistry for structural analysis at a molecular level. Two decades later, further major breakthroughs in the experimental field of NMR enabled the use of magnetic field gradients to: (a) monitor diffusion phenomena (Stejskal and Tanner,1965 [51]) and (b) spatially resolve nuclear spin density (Lauterbur,1973 [52] and Mansfield and Grannell, 1973,1975 [53,54]). Since then NMR has profoundly advanced in terms of both experimental techniques and the spectrometer hardware. Most recently, the work introduced by Callaghan (1991) [55] broadened NMR capabilities to monitoring velocities of moving nuclei. These fundamental developments made it possible to carry out research in many areas of chemical engineering such as catalysis, material science and transport phenomena (Gladden,1994) [56].

The great versatility of NMR lies in its ability to distinguish not only different nuclei and the molecules they form but also the spin relaxation characteristics, spatial position and motion of these nuclei. Experimentally, all these contrast-schemes may be used independently or as a combination to provide selective information. Furthermore, the NMR technique is a truly non-invasive method offering the advantage of studying non-transparent materials. Its main merits are: micron-scale resolution; fully three-dimensional spatial characterisation; fully quantitative data; no models required for the interpretation of the raw data.

In this chapter, the basic principles of NMR are described as well as its extension to the concepts of imaging and velocimetry. The fundamentals of NMR imaging and

velocimetry presented here are based on the book by Callaghan (1991) [55] and the review by Gladden (1994) [56].

## *3.1 Basic Principles of NMR*

### *3.1.1 Nuclear Spin and Magnetisation*

NMR techniques rely on the intrinsic spin properties of the nuclei. In the quantum mechanical description of nuclear spin (i.e. spin angular momentum), the concept of the spin states in which all the properties of the nucleus belong to a discrete set of possibilities is introduced. A nucleus can be regarded as a particle spinning on its axis (precessing), which implies that nucleus has the property of nuclear spin angular momentum, $\boldsymbol{P}$. In quantum mechanics, the angular momentum is proportional to any of a discrete set of values, $m_I$ (the magnetic quantum number), in the range $-I$, $-I+1$, $\ldots, I-1, I$:

$$P = \frac{h}{2\pi}[I(I+1)]^{\frac{1}{2}}, \tag{3.1}$$

where $I$ is an integer or half integer number called the angular momentum spin quantum number. The component of the angular momentum in the $z$-direction is given by:

$$P_z = \frac{h}{2\pi} I_z . \tag{3.2}$$

Furthermore, as the nucleus is charged its intrinsic spin gives rise to a tiny magnetic dipole moment, $\mu$. The magnetic dipole moment of an atomic nucleus is directly proportional to its spin angular momentum:

$$\mu = \gamma \boldsymbol{P}, \tag{3.3}$$

where the constant of proportionality, $\gamma$, is called the gyromagnetic ratio of the nucleus. Therefore, the magnetic moment is an intrinsic property of a given nucleus.

In this study all imaging was performed on $^1$H (proton) nuclei, for which $I$=½. Hence, the magnetic quantum number for proton nuclei can take up two discrete values ($m_I$= ± ½) and the spin nuclei are differentiated into the two states. In the absence of an external static magnetic field, the two spin states have the same energy, i.e. the energy levels are degenerate, as illustrated in Fig.(3.1a). When an external magnetic field $\boldsymbol{B}_0$ is applied to a collection of spin ½ ($I$=½) nuclei, the degeneracy of the nuclei spin energy is lifted. The nuclei populate themselves between the two states with different energy, namely $\alpha$ ($m_I$=+½) and $\beta$ ($m_I$ =-½), as depicted in Fig.(3.1b). This separation of spin states in a magnetic field is referred to as the nuclear Zeeman effect.

Any nucleus can alter its magnetic spin quantum number by either absorbing or emitting energy. The interaction energy between the magnetic dipole and a static magnetic field $\boldsymbol{B}_0$ (of magnitude $B_0$) is mathematically described by a Hamiltonian ($H$), and given by:

$$H = -\mu \cdot \boldsymbol{B}_0 = -\gamma \frac{h}{2\pi} I_z B_0 \quad , \tag{3.4}$$

The difference in the interaction energy between the spin states is then:

$$\Delta H = \pm \hbar \gamma B_0 \Delta I_z = \pm h\nu = \pm \hbar \omega_0 \quad , \tag{3.5}$$

where $\hbar = \frac{h}{2\pi}$ is the Planck's constant. For the $^1$H nucleus, the energy separation between the two spin states ($\alpha$) and ($\beta$) is $\hbar \gamma B_0 = \hbar \omega_0$.

The individual magnetic moments do not align perfectly with $\boldsymbol{B}_0$. Rather, as illustrated in (Fig.(3.1c) they precess in a conical fashion about $\boldsymbol{B}_0$ with a uniform angular frequency called the Larmor frequency $\omega_0$:

$$\omega_0 = \gamma B_0 \quad . \tag{3.6}$$

For protons $\gamma$=2.67519•$10^8$ rad $s^{-1}T^{-1}$ and the magnetic field used in this study $B_0$=4.7T, the linear precession frequency corresponding to the Larmor frequency ( $\nu_0 = \frac{\omega_0}{2\pi}$) is therefore 200.1MHz.

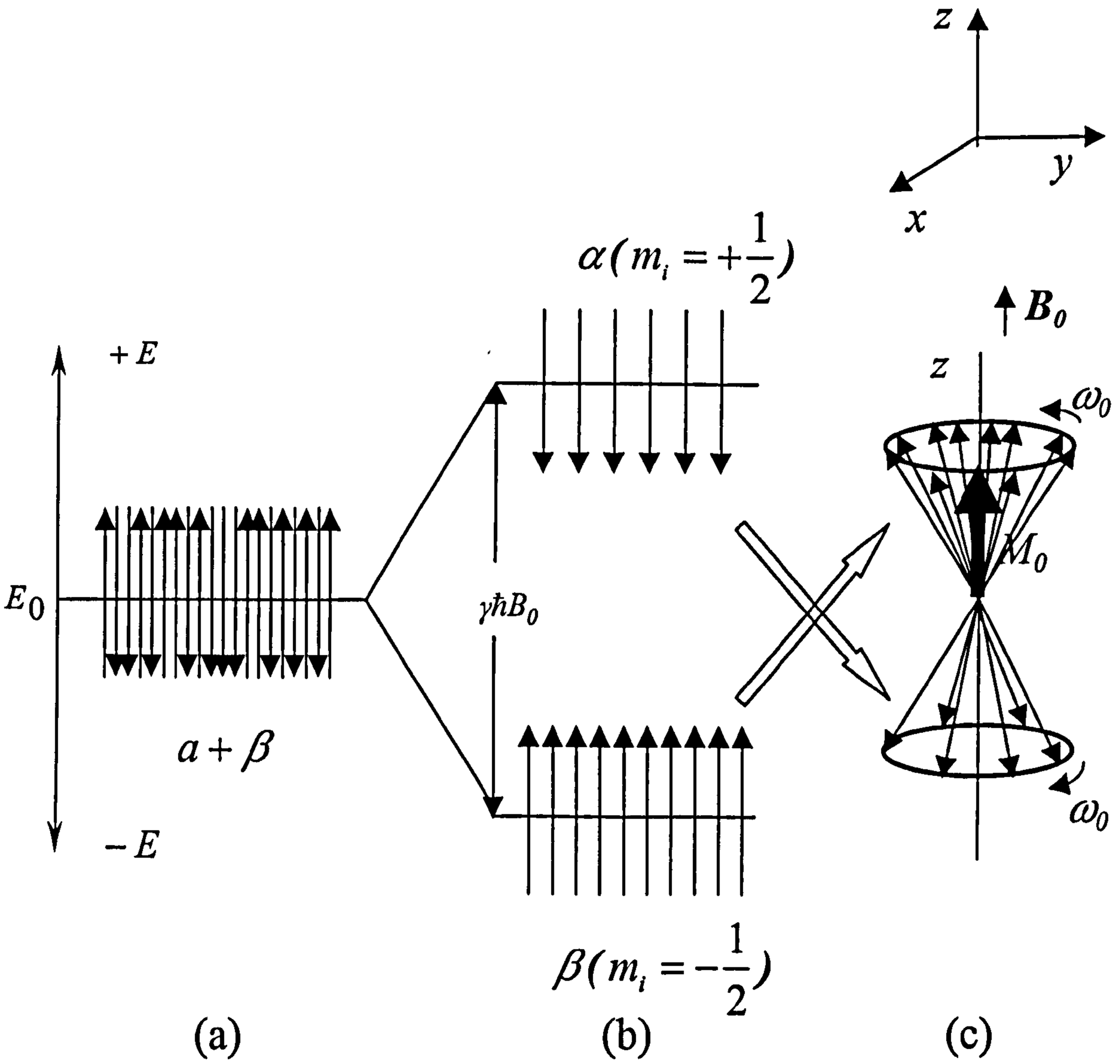


**Figure 3.1** Illustration of the Zeeman effect: (a) in the absence of an external magnetic field $B_0$, $^1$H nuclei spins are populated in the two spin states that have the same energy. (b) in the presence of $B_0$, $^1$H nuclei spins are split into the two states of different energy and populations $\alpha$ ($m_i$ =+1/2) and $\beta$ ($m_i$=-1/2). (c) the exaggerated pictorial representation of the magnetic moments of the spin nuclei in $\alpha$ and $\beta$, precessing about $B_0$ with the same characteristic (Larmor) frequency $\omega_0$, but in the opposite directions, which results in a formation of the net magnetisation vector along the $z$-axis, $M_0$. The magnitude of $M_0$ is $M_0$.

thermal equilibrium there will always be more nuclei in the lower energy state ($\beta$) than in the upper state of energy ($\alpha$). This difference in populations of the two states is given by a Boltzmann distribution:

$$\frac{N_\beta}{N_\alpha} = e^{-\frac{\Delta H}{kT}} \quad , \tag{3.7}$$

where $k$ is the Boltzmann constant, $T$ is the temperature of the sample and $N_\alpha$ and $N_\beta$ are the numbers of spin nuclei in $\alpha$ and $\beta$.

The vector sum of all individual magnetic moments of the spin nuclei yields a total magnetic moment or magnetisation vector ($M$). At equilibrium, the bulk magnetisation of the sample along the $z$-axis has a magnitude $M_0$ (Fig.(3.1c)):

$$M_0 = N_\alpha \gamma P_{z\alpha} + N_\beta \gamma P_{z\beta} = \frac{h}{8\pi} \frac{\Delta H}{kT} \gamma N \,, \tag{3.8}$$

where $N = N_\alpha + N_\beta$ is the total number of spin nuclei in the sample.

This equation shows that at equilibrium, as a result of increased population in the lower energy state, there will be a net magnetisation aligned in the direction of the magnetic field. The fact that the number of observed spins ($N$) directly determine the net magnetisation ($M_0$) makes NMR a quantitative technique.

For $^1$H nuclei at the room temperature and $B_0$ of 4.7T used in this study, it can be shown from equation (3.7) that a fraction of nuclei of $10^{-5}$ is detectable in the experiment. This means that in a small volume of glycerol, which was used in the flow studies, the number of observed $^1$H nuclei is large (one millilitre of glycerol contains approximately $10^{22}$ $^1$H nuclei, thus the detectable number is $10^{17}$). Hence, the net magnetisation can be viewed as a bulk property of the 'ensemble' of spins and in classical terms.

### *3.1.2 The Rotating Frame and Spin Excitation*

NMR is based on the manipulation and detection of the macroscopic net magnetisation vector, which describes the behaviour of a collection of nuclei in a magnetic field $\boldsymbol{B}_0$. From classical mechanics, this macroscopic quantity, $\boldsymbol{M}$, obeys:

$$\frac{d\,\boldsymbol{M}}{dt} = \boldsymbol{M} \times \gamma \boldsymbol{B}_0 \quad . \tag{3.9}$$

The solution of equation (3.9) implies that $\boldsymbol{M}$ precesses about $\boldsymbol{B}_0$ at constant angular frequency $\omega_0=\gamma B_0$, where $B_0$ is the magnitude of $\boldsymbol{B}_0$. In the laboratory frame of reference, *xyz*, this is illustrated in Fig.(3.2a).

After placing the sample in a magnetic field, the next step in conducting NMR experiments is excitation of the spin system. Excitation is achieved by irradiation of the sample with electromagnetic radiation in the radio-frequency (RF) range of an appropriate frequency, $\omega_1$. This is done with a current applied to a coil surrounding the sample, thus generating an oscillating magnetic field $\boldsymbol{B}_1$ perpendicular to $\boldsymbol{B}_0$. When the nuclei absorb photons from this radiation, $\boldsymbol{M}$ simultaneously precesses about the static field $\boldsymbol{B}_0$ and the RF field $\boldsymbol{B}_1$.

In order to simplify the analysis of the behaviour of $\boldsymbol{M}$, a new frame of reference, $x'y'z'$, which rotates about the $z$ or $\boldsymbol{B}_0$ axis of the laboratory frame of reference at the Larmor frequency $\omega_0$, is introduced. To an observer moving with the rotating frame at a frequency $\omega_0$, $\boldsymbol{M}$ appears stationary, as depicted in Fig.(3.2b).

In the equilibrium state, the magnitude of the longitudinal component of $\boldsymbol{M}$ along the $z$-axis, $M_z$, is equal to $M_0$. When, during the spin excitation, the resonance condition is satisfied, the frequency of $\boldsymbol{B}_1$ is equal to the Larmor frequency ($\omega_1=\omega_0$) and $\boldsymbol{M}$ precesses only about $\boldsymbol{B}_1$, but not about $\boldsymbol{B}_0$, The application of RF pulses of adequate amplitude ($B_1$) and duration ($t$), causes $\boldsymbol{M}$ to be accurately rotated into the transverse

plane (termed $90^0$ RF pulse) or inverted (termed $180^0$ RF pulse) in the rotating frame of reference, as shown in Fig.(3.2c).

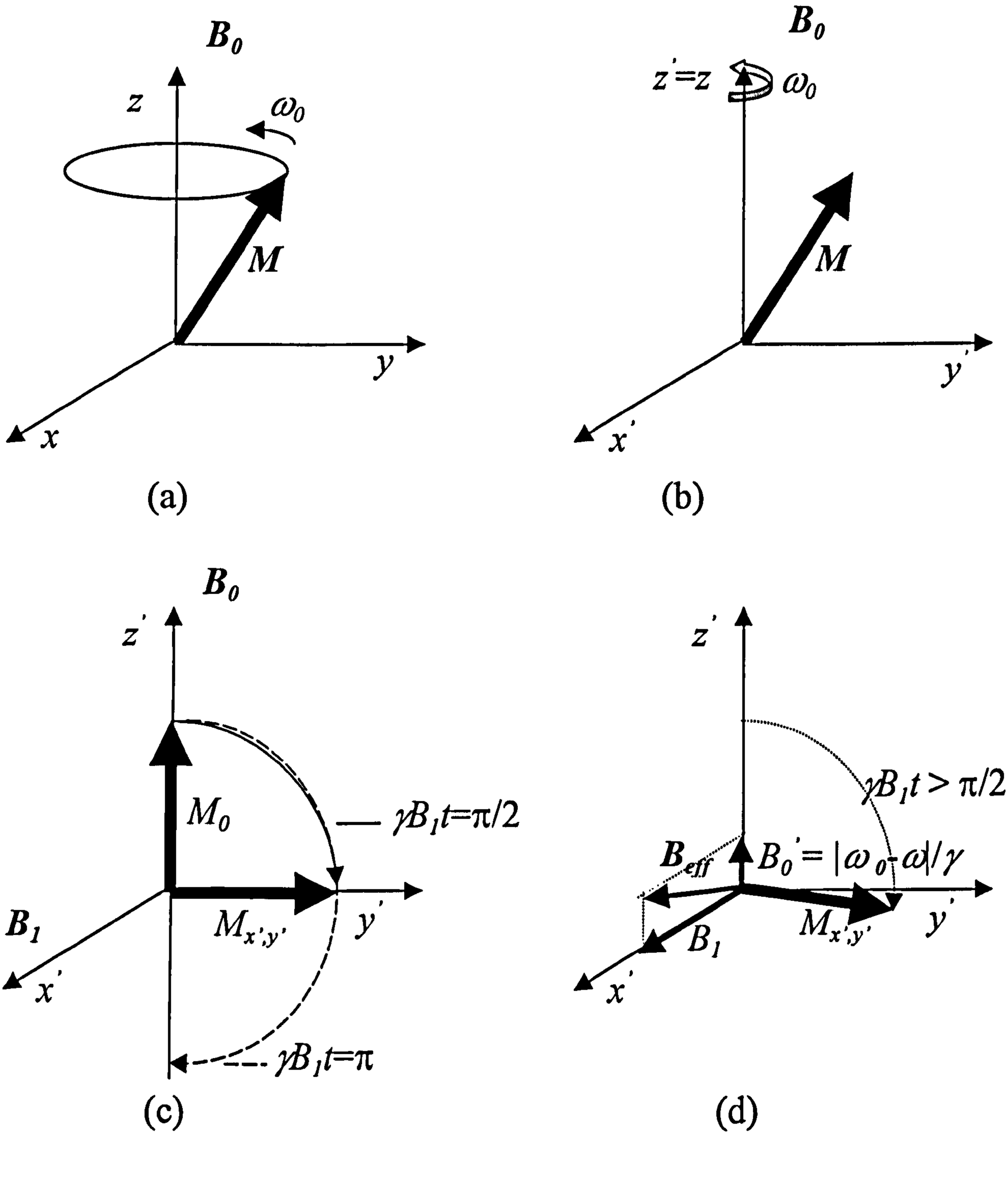


**Figure 3.2** (a) precession of $M$ in a non-equilibrium state at Larmor frequency ($\omega_0$) about $B_0$ in the laboratory frame $xyz$; (b) in the frame $x'y'z'$ rotating at $\omega_0$ about the $z$ axis $M$ is stationary; (c) the application of an RF pulse of appropriate magnitude $B_1$ and duration $t$ results in $M$ (of magnitude $M_0$) being tipped for an angle $\gamma B_1 t=\pi/2$ (solid line) or inverted for $\pi$ (dashed line) in the rotating frame; (d) if the nuclei are slightly off-resonance, they will precess with $|\omega| < |\omega_0|$, the effective longitudinal magnetic field $B_{eff}$ is the sum of the two components $B_1$ and $|\omega_0 - \omega|/\gamma$. Hence, $M$ is attenuated and phase-shifted in the $x'y'$ plane. When the resonance condition holds ($|\omega| = |\omega_0|$), $B_{eff}$ reduces to $B_1$.

On the other hand, when the resonance condition does not hold, the nuclei have a different $\omega_0$ from the applied frequency of $\boldsymbol{B}_1$. This results in $\boldsymbol{M}$ precessesing about both $\boldsymbol{B}_0'$ with magnitude $B_0' = |\omega_0 - \omega|/\gamma$ along the $z'$ axis and $\boldsymbol{B}_1$ along the $x'$ axis in the rotating frame of reference. Consequently, the transverse component of $\boldsymbol{M}$ for such off-resonance nuclei following a $90^0$ pulse, will be both phase-shifted and attenuated in comparison with for $\boldsymbol{M}$ for on-resonance nuclei.

The excitation bandwidth of the RF pulse ($\Delta\nu_1$) has to be broad enough to cover the spectral width ($\Delta\nu_{SW}$) of the linear precession frequencies of all the spins we wish to observe. The required bandwidth is achieved by selecting the pulse duration ($t$), bearing in mind that $\nu$ relates to the pulse duration as $1/t$. The pulses with large excitation bandwidths are referred to as non-selective or hard pulses.

The aim of the experiment may be to excite only a certain nuclear spins with a characteristic chemical shift or the nuclear spins within some specified geometric layer of the sample. In these cases the pulses are applied for much longer times giving much narrower bandwidths for resonant frequency. They are termed 'soft' pulses and their use will be explained in more detail in further text.

### *3.1.3 Signal Detection*

Once the application of an RF pulse is completed, the coil is switched off. After the irradiation stops, spin system begins to lose its energy by photon emission through a number of processes termed relaxation processes, therefore returning to thermodynamic equilibrium. The coil surrounding the sample is then switched on again, now to detect an oscillatory e.m.f. signal of the current, $S(t)$, induced by the decay of magnetisation, which is governed by the relaxation processes. When the signal intensity is plotted versus time it shows a regular decay, referred to as the Free Induction Decay (FID). Then the Larmor frequency is subtracted from the acquired signal in a process termed heterodyning. Finally, the resultant time-domain signal is Fourier transformed to yield the frequency domain response $A(\nu)$:

$$A(v) = \int_{-\infty}^{\infty} S(t)\exp(+i2\pi vt)dt. \qquad (3.10)$$

The real and imaginary part of the FID signal with the corresponding Fourier transforms for nuclei which have a slightly different frequency from that subtracted in heterodyning are shown in Fig.(3.3).

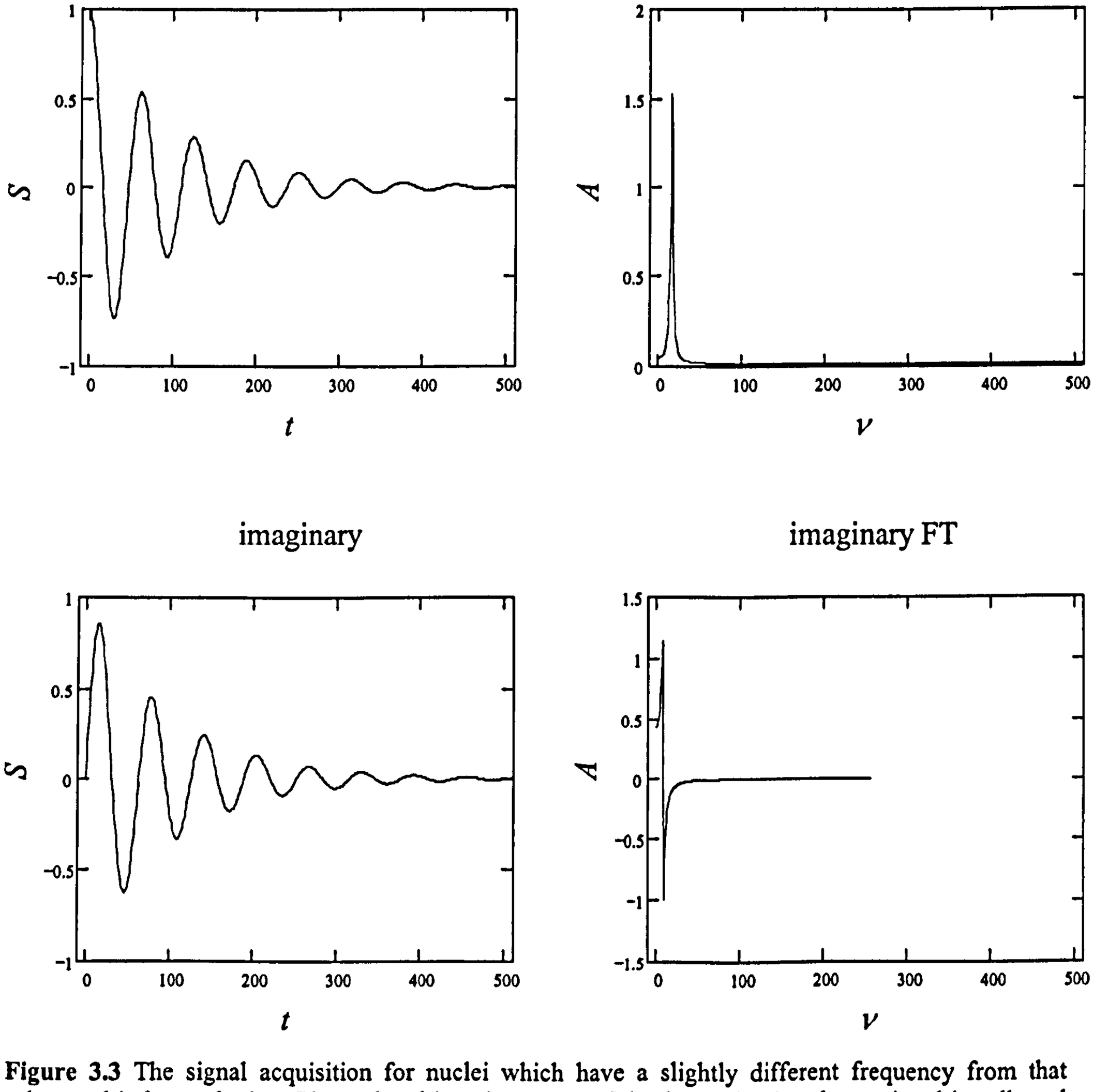


**Figure 3.3** The signal acquisition for nuclei which have a slightly different frequency from that subtracted in heterodyning. The real and imaginary part of the free induction decay signal is collected by turning the receiver coil in the x-y plane in the time domain (left) and then Fourier transformed to obtain the NMR spectrum in the frequency domain (right).

### *3.1.4 Relaxation Processes*

As previously mentioned, after the irradiation ceases the system returns to the thermodynamic equilibrium by forfeiting the excess energy in a process known as relaxation. The return to equilibrium occurs simultaneously through the spin interaction with the surroundings (termed spin-lattice relaxation) or the mutual spin interaction (termed spin-spin relaxation).

#### *3.1.4.1 Spin-Lattice Relaxation*

Once the nuclei are perturbed from thermal equilibrium, the longitudinal component of $\boldsymbol{M}$ in the rotating frame of reference, $M_z$, no longer lies parallel to the $\boldsymbol{B_0}$ field (taken to be in the $z$ direction). The excess energy of the nuclei acquired from the RF pulse is exchanged with the surrounding thermal reservoir ('lattice') via photon transmission and the nuclei system returns to the equilibrium. The removal of this energy to the surrounding system is known as spin-lattice relaxation. Spin-lattice relaxation is governed by the rate at which $M_z$ returns to its equilibrium state, parallel to $\boldsymbol{B_0}$, and is restored to its initial value, $M_0$, along the $z$-axis. This process is described by the following equation:

$$\frac{dM_z}{dt} = -\frac{(M_z - M_0)}{T_1}, \tag{3.11}$$

with the solution:

$$M_z(t) = M_z(0)\exp(-t/T_1) + M_0[1-\exp(-t/T_1)]. \tag{3.12}$$

In the above equations $T_1$ is termed the spin-lattice or longitudinal relaxation time, $M_z(0)$ refers to the $z$-component of the magnetisation vector at time $t$=0 and $M_0$ is the magnetisation at thermal equilibrium. The value of $T_1$ depends on the type of the nucleus, the location of the nucleus within a molecule and the physical state of the

sample. In solids, the rate of molecular tumbling is slow compared to liquids, so that the ability of the 'lattice' to absorb energy is more limited. This, in turn, results in larger values of $T_1$ for solids in comparison with liquids. The methods for determining longitudinal relaxation time, $T_1$, can be found in Fukushima and Roeder (1981) [57].

The value of $T_1$ is very important in experimental considerations. In NMR experiments a pulse sequence for the spin excitation is repeated many times. Between each two applications of RF pulses (which is characterised by the recycle delay time, *TR*) the spin-nuclei system must be left for sufficiently long time, so that it relaxes back to the thermal equilibrium. As can be calculated from equation (3.12), a period of $5T_1$ is required for 99% of $M_0$ to be restored in the *z*-direction, following excitation. If the recycle delay time is shorter than $5T_1$ the recovery of magnetisation $M_z$ along the *z*-axis to the value $M_0$ would not be completed and such an attenuated signal would no longer represent the number of spin nuclei within the sample. This in turn means that the signal would no longer be quantitative. In the worst case, the difference in populations between the spin states may become so small that acquiring the subsequent radiant power by RF signals will render the populations equalised. Such a spin nuclei system is said to be saturated and no further net absorption is possible. Therefore, it is often advantageous to reduce $T_1$ in the experiments. This can be done by adding (doping) small amounts of paramagnetic species to the sample. In some cases, when the $T_1$ within the sample is constant, the signal attenuation within the sample is constant too, so shorter recycle delays can be used. Broadly speaking, the total experimental time is often optimised as the best compromise between the values of the recycle delay time and the relaxation time $T_1$.

### *3.1.4.2 Spin-Spin Relaxation*

Although one can presuppose that the time constant $T_1$, describing the life time of longitudinal magnetisation, could also be adequate for describing the rate at which transverse magnetisation occurs this is not the case. The transverse magnetisation is governed by an intrinsically different mechanism and is characterised by a time constant $T_2$.

The following description is based on the analysis of the behaviour of the volume segments of the sample consisting of a large number of the nuclei experiencing exactly the same external magnetic field. These volume segments of the sample have the well defined contribution to magnetisation and are termed spin-isochromats.

Following the application of an RF pulse, the excited spins of different nuclei can mutually interact, thus causing the relaxation of $\boldsymbol{M}$ in the transverse plane in the rotating frame of reference. This process is known as transverse relaxation and results in a loss of phase coherence of the nuclei, which return to a random arrangement around the $z$-axis. The transverse relaxation process among spins occurs at the time-scale defined by the spin-spin relaxation time $T_2$ and is governed by the equations:

$$\frac{dM_x}{dt} = -\frac{M_x}{T_2}; \quad \frac{dM_y}{dt} = -\frac{M_y}{T_2}. \tag{3.13}$$

The components of magnetisation in the transverse plane are denoted as $M_x$ and $M_y$ The loss of phase coherence in the $T_2$ relaxation process is irreversible and does not cause removal of the spins energy. The value for $T_2$ depends on the mobility of the molecules within the sample. Faster molecular tumblings will average out more of local magnetic field heterogeneities occurring with the gradual loss of phase coherence of the spin nuclei, which will result in larger $T_2$ times.

In a real experiment, the loss of phase coherence can also be caused by other factors, in particular local heterogeneities of the magnetic field $\boldsymbol{B_0}$. In a spatially non-homogeneous magnetic field $\boldsymbol{B_0}$, the spin-isochromats in different areas of the sample will experience a different $\boldsymbol{B_0}$ and resonate at different Larmor frequencies, $\Delta\omega=\gamma\Delta B_0$. Upon excitation, after time $t$, the spin-isochromats will have a phase difference of $\Delta\omega t$ and therefore will lose phase coherence due to these $\boldsymbol{B_0}$ heterogeneities. This effect is reversible and is characterised by the time constant $T_2'$. The time constants $T_2$ and $T_2'$ are added to yield the total apparent relaxation time $T_2^*$ of the system:

$$\frac{1}{T_2^*} = \frac{1}{T_2} + \frac{1}{T_2'}. \tag{3.14}$$

In a simple 'pulse-acquire' experiment, the influence of both $T_2$ and $T_2'$ effects exist and the decay of the FID signal is characterised by the time $T_2^*$. Since the effects of $T_2'$ are not reversed, the apparent decay of the FID signal is more rapid than the one observed from $T_2$ processes alone. In the spectrum, the influence of $T_2'$ is reflected in a broader resonance spectrum lineshape, as compared to the lineshape obtained from the $T_2$ process alone. For liquids with a single resonant frequency, the $T_2^*$ weighed spectrum is approximately Lorentzian in shape and the linear frequency spectral width $\Delta\nu_{FWHM}$ at half its maximum height (FWHM) is:

$$\Delta\nu_{FWHM} = \frac{1}{\pi T_2^*}. \tag{3.15}$$

In a well-shimmed (homogeneous) magnetic field, the spectral linewidth of liquids can be often below 1Hz. In porous media, differences in magnetic susceptibilities between the liquid and solid phase produce magnetic field hetrogeneities at the phase boundaries. Consequently, the relaxation rate is faster and the spectrum lineshape is broadened to the range of $10^2$-$10^4$ Hz. In experiments, such large bandwidths can act as a drawback causing a loss in spectral resolution in NMR microscopy and spatial resolution in magnetic resonance imaging (MRI).

Equation (3.15) shows that the value for $T_2^*$ can be directly obtained from an FID. The value for $T_2$, the irreversible component of $T_2^*$, can be determined by a spin-echo experiment.

### *3.1.4.3 The Spin Echo*

The pulse sequence of a spin echo experiment along with the analysis of the change of the magnetisation vector in the rotating frame is shown in Fig.(3.4).

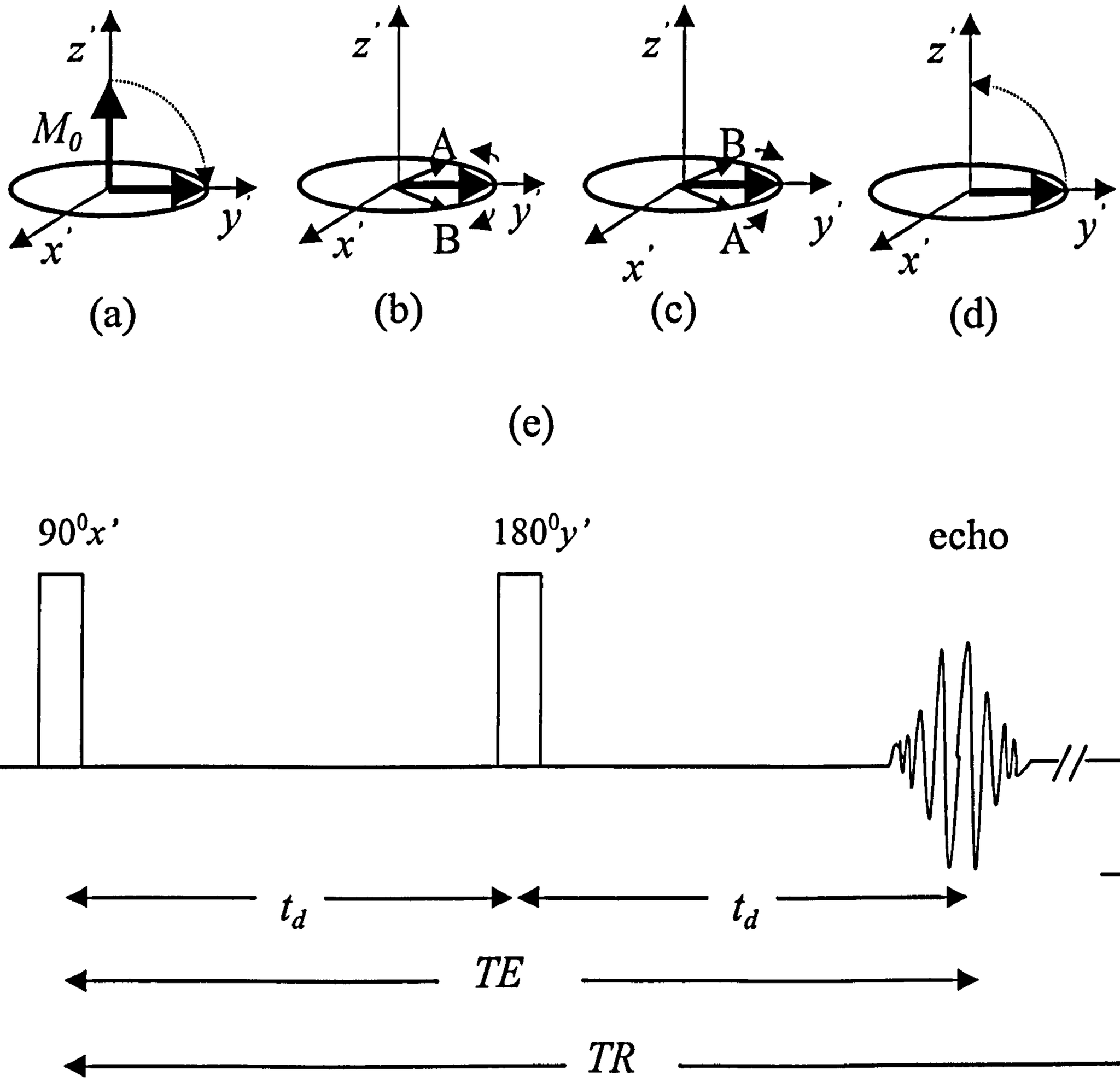


**Figure 3.4** Implementation of the spin-echo pulse sequence (e) with the manipulation of $M$ in the rotating frame: (a) application of an RF $90^0$ pulse in the $x'$ direction tips $M$ into the $x'y'$ plane; (b) the spin-isochromats A and B begin to dephase due to local magnetic field heterogeneities; (c) after a time $t_d$ a $180^0$ pulse is applied in the $y'$-direction, inverting the spin-ischromats A and B; (d) after another time $t_d$ elapsed the spin-isochromats will have refocused along $y'$ in the $x'y'$ plane. Hence, the maximum possible signal is acquired after the time $2t_d$, which is termed the spin echo time ($TE$). The time between two repetitions of the pulse sequences is called the repetition time ($TR$).

In the beginning of the experiment, the sample is immersed in the static magnetic field $B_0$ and the magnetisation vector is aligned with the field lying along the $z'$-direction with a value of $M_0$. Then a 90 degree RF pulse is applied along the $x'$-direction, tipping $M$ in the $x'y'$ plane. Due to the static magnetic field inhomogeneities and/or the

variations in the magnetic field in the sample, the spin isochromats begin to slowly lose coherence or 'dephase'. The frequency with which they resonate will deviate from the Larmor frequency, according to the change in the magnetic field strength. If the magnetic field is greater, the isochromats gain positive phase shift in the rotating frame and vice versa. The aim of the spin echo experiment is to make these effects of the magnetic field inhomogeneities reversible. This is attained by applying the RF field $B_1$ again to produce a $180^0$ pulse about the y-axis at a time $t=t_d$. This application results in inverting relative positions of the spin isochromats for exactly the same phase shift. As the spin isochromats still precess with their former deviated frequency, during the time $2t_d$ they are precisely rephased (refocused). This refocusing process is termed spin echo. During the time $2t_d$ (termed the spin echo time, $TE$) the maximum signal (or echo) will have decayed due to intrinsic $T_2$ relaxation processes but the loss of the phase coherence (hence loss of the signal) due to $T_2'$ processes will have been recovered.

Provided the spins have not moved to the regions with different field strengths the value for $T_2$ can be estimated from the equation:

$$M_y = M_0 \exp(\frac{-2t_d}{T_2}). \tag{3.16}$$

The importance of the spin echo sequence comes forward when the decay of the magnetisation in the $x'y'$ plane is too rapid (very short $T_2^*$) that makes it impossible to complete the required sequence of spin manipulations in the experiment. Elimination of the effects of $T_2'$ relaxation and acquiring the signal with only $T_2$ relaxation brings vital advantages in signal-to-noise ratio. For liquids in porous media $T_2$ values are usually in the range of 10-1500ms whilst $T_2^*$ is commonly below 1ms. Since the echo times of a typical image sequence are greater than 1ms, the advantages gained by using a spin echo are obvious.

As a good alternative to the spin echo, especially when relatively long pulse sequences are required, the stimulated echo can be used. After the first $90^0$ RF pulse, instead of applying a $180^0$ RF signal as in the spin echo, a $90^0$ RF signal is used in order to 'store' the transverse magnetisation information along the $z$-axis during the

application. After the required sequence is applied, another $90^0$ RF pulse is used to tip magnetisation back into the $x'y'$ plane where it can be detected. Without going into detail, it is worth mentioning that this storage of information allows the use of longer pulse sequences. The constraints are that $T_1$ must be much greater that $T_2$ (this condition holds for liquids in porous media) and that there is an unavoidable loss of the intensity of the excited signal.

### *3.1.5 Chemical Shift*

In molecules, nuclei are surrounded by the magnetic fields produced by electron clouds of different structures, which contribute to the total magnetic field experienced by the nuclei. Thus, the total magnetic field experienced by the identical nuclei within the same molecule at different locations or in different molecules may slightly vary, which, in turn, causes a small deviation in the magnitude of their respective Larmor frequencies, $\omega_0$. In the NMR spectrum, this is seen as a displacement of the position of the resonant signal. This phenomenon is known as the chemical shift and has to be included in the experimental considerations.

## *3.2 Spatially Resolved NMR (NMR Imaging)*

### *3.2.1 Magnetic field Gradients*

In NMR experiments, it is always desirable to have as homogeneous an external magnetic field $\boldsymbol{B_0}$ as possible and to neutralise the effect of local magnetic field heterogeneities in the sample on the signal (i.e. by using spin-echo experiment). However, in spatially resolved NMR, a sample experiences the magnetic field which is intentionally varied along required directions. This is achieved by adding to $\boldsymbol{B_0}$ a

small linear magnetic gradient, $G$. If the gradient $G$ is applied along the $z$-direction the resultant magnetic field $B$ varies as:

$$\frac{\partial B}{\partial z} = G_z = const.. \tag{3.17}$$

Dependent on their location within the sample, the nuclei experience different magnetic field and hence precess with different Larmor frequency given by:

$$\omega(r) = \gamma(B_0 + G \cdot r), \tag{3.18}$$

where $r$ is the position of the vector spin.

Spatial information is therefore obtained by 'frequency encoding' the FID signal. The signal acquired in this way is, again, a quantitative measure of the number of the nuclei within the sample but also distinguishes the nuclei according to their position.

This is illustrated in Fig.(3.5) which shows a comparison of the signals obtained by monitoring two beakers containing different volumes of water without and with the use of a unidirectional magnetic field gradient, $G_x$. In the latter case, the NMR image shows two broad resonant lines, which will be separated in accordance with the size of the applied magnetic field gradient, $G_x$, and the distance between the beakers, $\Delta x$. The sum of the signal intensities of the two resonant lines obtained with the use of the gradient is equal to the signal intensity of the resonant line gained without application of the gradient, and this is a quantitative measure of the number of nuclei within each beaker.

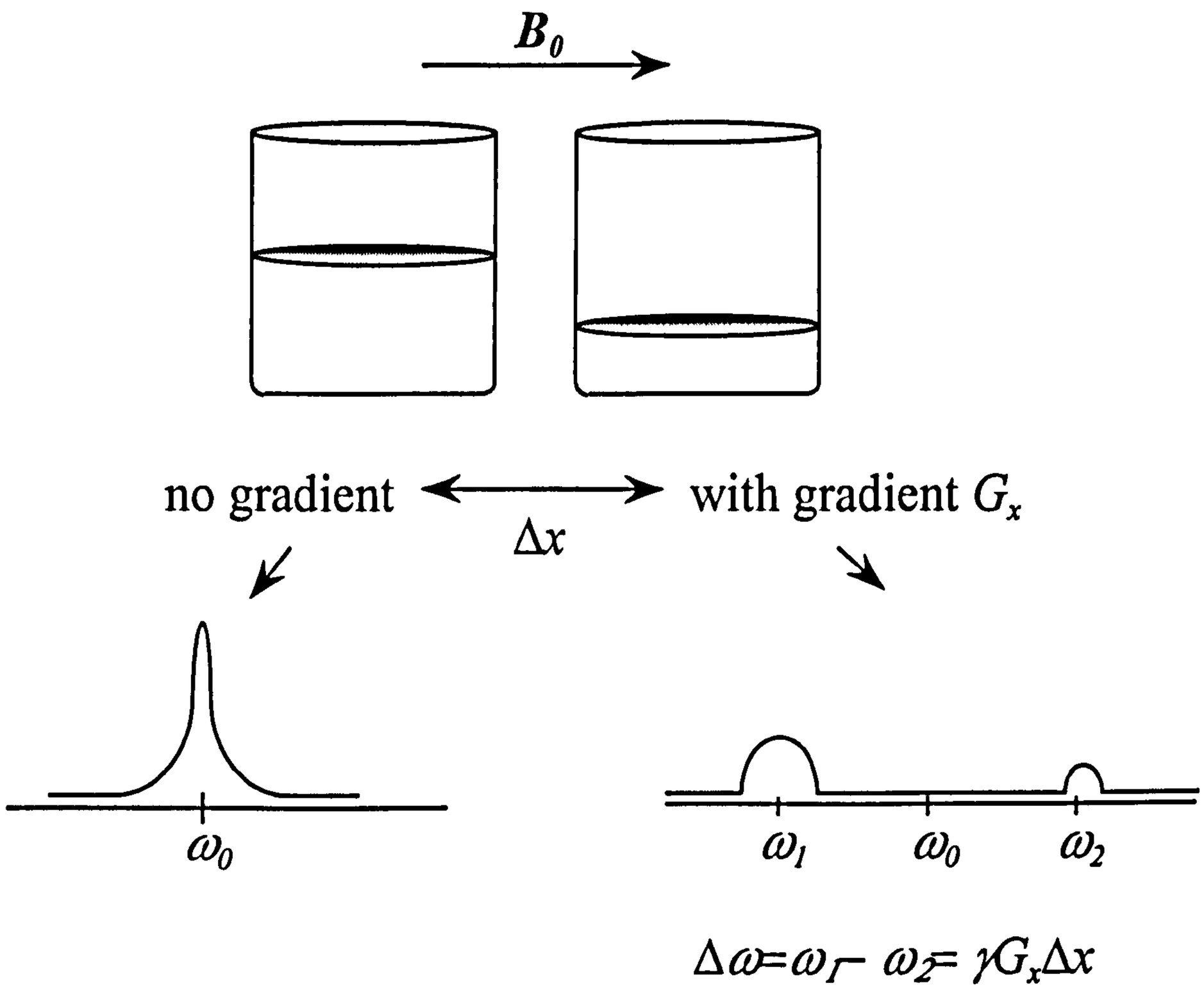


**Figure 3.5** NMR imaging of two beakers filled with different volumes of water. When a linear magnetic field gradient $G_x$ (right) is applied in addition to the external magnetic field $B_0$, the spin-isochromats in the two beakers will resonate, in accordance with their position, with different frequencies. This results in the two broad signals in the NMR spectrum whose intensities are a quantitative measure of the number of the liquid nuclei in the beakers. The separation between the peaks of the two signals, $\Delta\omega$, is proportional to the magnitude of the applied gradient and the distance between the beakers. When no gradient is applied (left), the NMR spectrum consists of one narrow signal centred at the Larmor frequency. The intensity of the signal is proportional to the number of the liquid nuclei in both beakers.

### *3.2.2 Extension to two-dimensional (2D) and tree-dimensional (3D) Imaging*

The magnetic field gradients can be applied in any desired direction. In general three-dimensional case the signal $dS$, in an element of volume $dV$, is proportional to the spin density distribution, $\rho(r)$ and the gradient vector strength, $G$. In complex notation this is written as:

$$dS(G,t) = \rho(r)\exp[i(\gamma B_0 + \gamma G\cdot r)t]\,dV\,, \tag{3.19}$$

where the relaxation effects are ignored. In the rotating frame $\gamma B_0$ disappears, and equation (3.19), when integrated for the total signal amplitude $S$, is reduced to:

$$S(G,t) = \iiint \rho(r)\exp[i(\gamma G\cdot r)t]\,d\,r\,, \tag{3.20}$$

where $dr$ represents a volume integration. In order to make the analysis suitable for the use of Fourier transform, the concept of $k$-space was introduced by Mansfield (Mansfield *et al.* 1973) [53]. In this concept, the reciprocal space vector $k$ is defined as:

$$k = (2\pi)^{-1}\gamma G t\,. \tag{3.21}$$

Equation (3.20) now becomes:

$$S(k,t) = \iiint \rho(r)\exp[i(2\pi k\cdot r)]\,d\,r\,. \tag{3.22}$$

The inverse Fourier transform of equation (3.22) yields the spin density distribution in all three spatial coordinates:

$$\rho(r) = \iiint S(k)\exp[-i(2\pi k\cdot r)]\,d\,k\,. \tag{3.23}$$

Measurements of the spin density distribution are obtained by sampling $k$ variable in all of reciprocal space. This is achieved by applying constant magnetic field gradients oriented in three orthogonal directions within the magnet. Any component of $k$-vector ($k_x$, $k_y$, $k_z$) can be varied by changing the gradient strengths $G$ ($G_x$, $G_y$, $G_z$), or the time ($t_x$, $t_y$, $t_z$) for which the gradients are applied in each spatial direction.

The most common 2D imaging sequence termed spin-warp imaging (Edelstein et al., 1980) [58] is presented in Fig.(3.6a), along with the $k$-space 'rastor' analysis in Fig.(3.6b). All the points shown in the $k$-space must be sampled. Prior to the applications of any gradients, the sample is at the origin of the rastor.

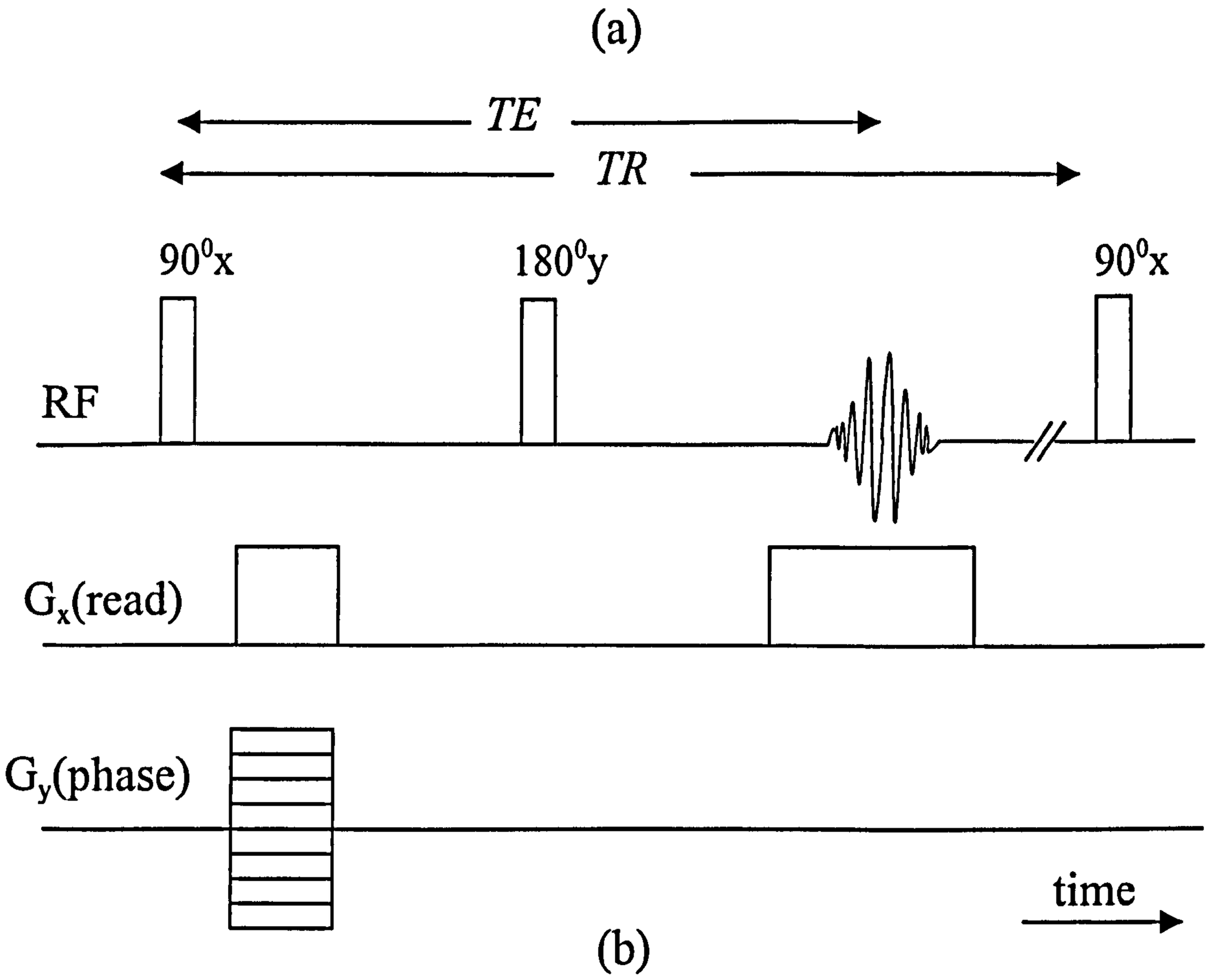


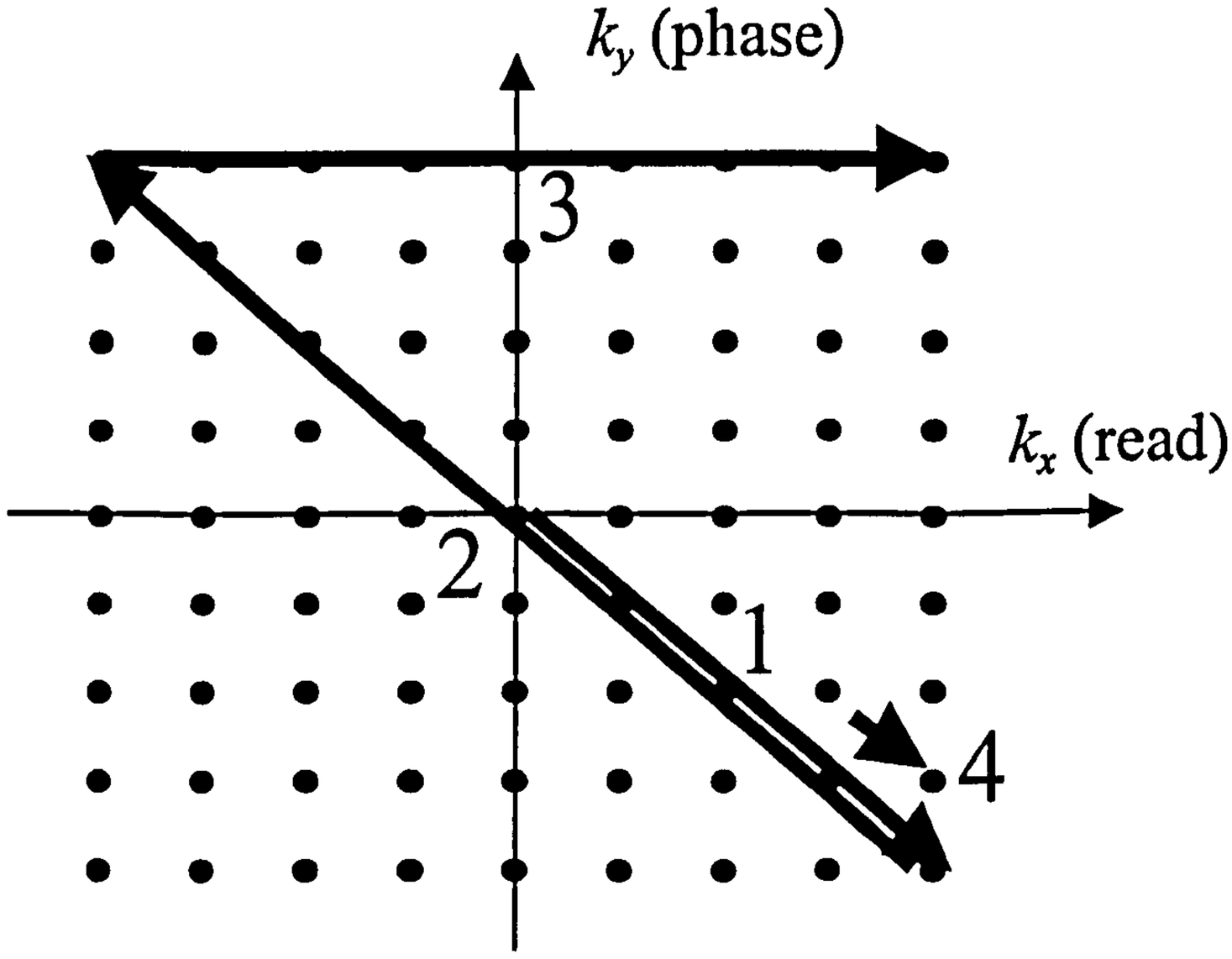


**Figure 3.6** The full pulse sequence used in the spin-warp imaging (a) and the corresponding ***k***-space rastor analysis (b). The sample to be imaged is presented by the points in the ***k***-space. The sequence begins by a simultaneous application of two mutually orthogonal magnetic field gradients $G_{1x}$ and $G_y$ (the line 1 in the ***k***-space). Then the $180^0$ RF pulse is applied, traversing the ***k***-space vector along the line 2. The signal is acquired by applying the second read gradient $G_{2x} = 2G_{1x}$, which 'frequency' encodes the spin-isochromats at both negative and positive $x$ points within a row in the ***k***-space along the line 3. The sequence is then repeated, but with increments in the gradient $G_y$, which phase encodes the spin-isochromats at different rows of pixels. The position of the ***k***-vector after one such increment is shown by the arrow 4.

After the initial excitation with a $90^0$ RF pulse, two mutually orthogonal magnetic field gradients $G_{lx}$ and $G_y$ are simultaneously applied. In the ***k***-space rastor this is seen as the change in the position of the ***k***-vector to a positive $k_x$ value along the line 1. As the negative $k_x$ values are also desired, the $180^0$ RF pulse is applied to invert the phase of the observed spin-isochromats, which results in the ***k***-vector traversing the path along the line 2 to a negative $k_x$ value. The signal is then acquired by applying a second gradient in the $x$ (read) direction $G_{2x}$, which has the magnitude twice as much as the first read gradient $G_{lx}$. Thus, the second read gradient encodes the spin isochromats consecutively within each data point in an entire row of the ***k***-space according to their frequency, $\omega_x=\gamma x G_x t_x$. As seen in the rastor, both positive and negative $k_x$ points are now acquired along the line 3. The pulse sequence is then repeated, but with an increment in the value for the phase gradient, $G_y$, which positions the ***k***-vector in the subsequent row in the ***k***-space (the arrow marked with 4). Hence, the role of the phase gradient is to label the spin isochromats consecutively from different rows by changing their phase, $\phi_y=\gamma y G_y t_y$. The data matrix then consists of X times Y points (pixels) indexed by $\gamma G_x t_x$ for each row and $\gamma G_y t_y$ for each column. The overall echo signal is:

$$S(k_x,k_y)=\iint \rho(x,y)\exp(-i2\pi(k_x x+k_y y))dxdy \quad , \qquad (3.24)$$

from which the spin-density image is obtained by the two-dimensional Fourier transformation.

If a three-dimensional image of the sample is required, an additional phase gradient, mutually orthogonal to the frequency gradient and the first phase gradient, is applied.

### *3.2.3 Selective Excitation*

The 2D imaging sequence described above yield a 2D image without spatial resolution in the direction perpendicular to the image plane, $z$. The image is a projection of spin density along the third orthogonal direction. If the aim of the experiment is to study the nuclear spins within some specified geometric layer of the

sample ('slice'), the RF irradiation can be made restricted to these spins. The slice selection is achieved by simultaneously applying a narrow band RF field and gradient field $G_z$. The narrow band RF field is produced with the application of soft pulses (Section 3.1.2). A typical spin-echo pulse sequence used for slice selection is shown in Fig.(3.7). The slice-selection gradient is reversed, following the application of the RF pulse, in order to reverse the dephasing of the precession of the spin-isochromats within the slice that occurs during the application of the RF pulse. As a result of that, all spin isochromats have the same phase at the end of the gradient pulse.

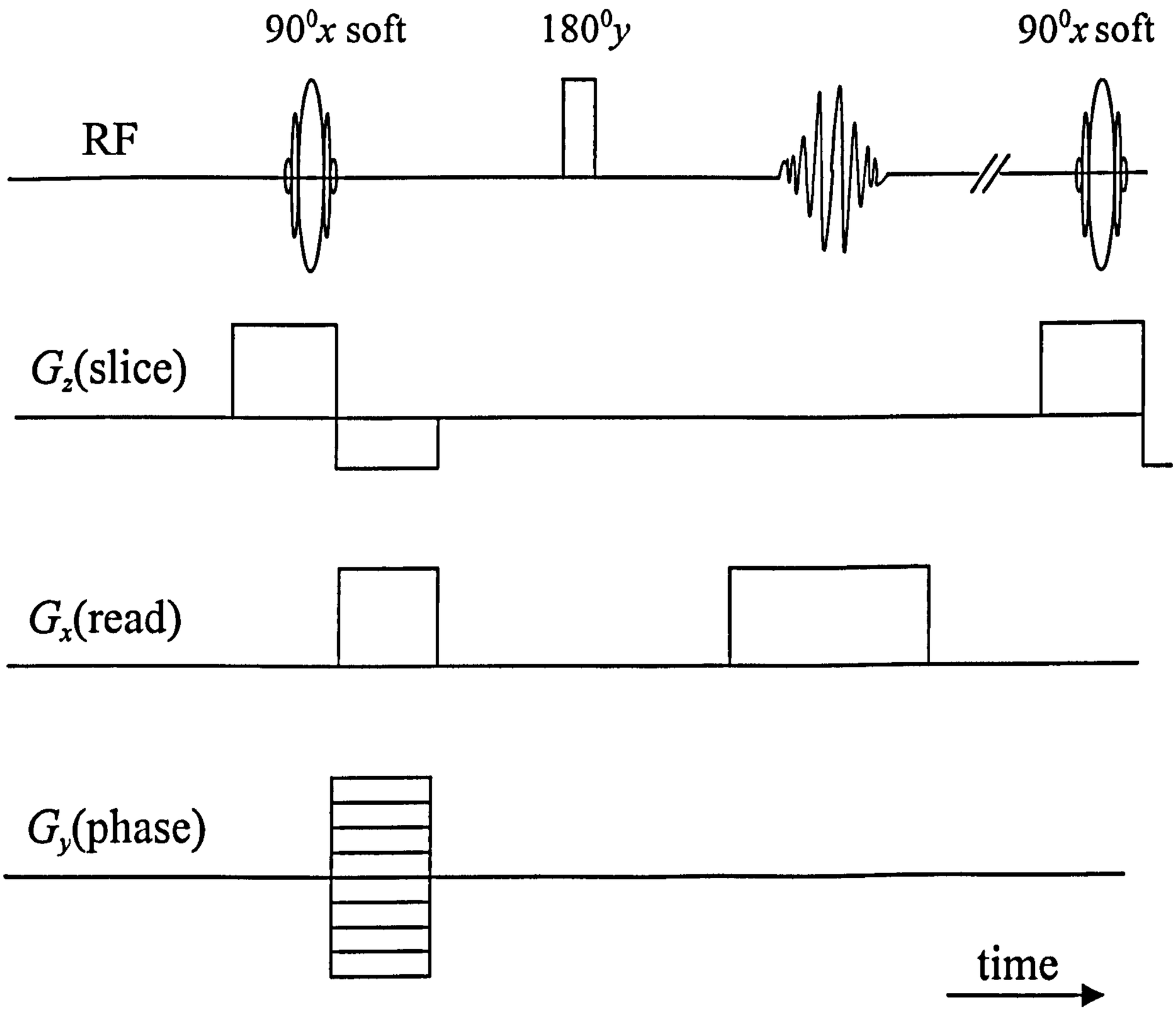


**Figure 3.7** Spin-echo pulse imaging sequence with a $90^0$x RF pulse used with the slice gradient $G_z$ to selectively excite a region along the $z$-direction for acquisition of an image in the $xy$ plane. The slice gradient is reversed in the second lobe, following the application of the RF pulse, in order to refocus the phase shift induced by the same gradient in the first lobe.

The applied gradient field $G_z$ causes spins to precess at different frequencies, depending on their spatial position along $G_z$. The simultaneous application of an RF pulse allows only the spins which resonate within the frequency bandwidth ($\Delta\omega$) of the pulse) to be excited. These are the spins within the examined slice. The region which is excited, $\Delta z$, is given by:

$$\Delta z = \frac{\Delta\omega}{\gamma G_z}. \tag{3.25}$$

The frequency profile of such soft pulses is equal to the Fourier transform of the modulation of the pulse over time (Callaghan, 1991) [55]. A common choice for the soft pulse is a Gaussian shape pulse.

## *3.3 NMR Velocimetry*

### *3.3.1 Measurement of motion with NMR*

In a sample, molecular motion may occur due to diffusion (random molecular motion) or convection (translational bulk motion of molecular assemblies). In the cases where the self-diffusion coefficient of the investigated liquid is sufficiently low that the nuclei ensembles do not move to the neighbouring pixels during the experiment, the NMRI measurements of molecular motion are reduced to monitoring translational velocity. In order to understand how velocities may be measured by using the phase shift acquired by spin-isochromats (spin-isochromats are defined in Section (3.1.4.2)) between successive image acquisition, the basic pulse sequence is shown in Fig.(3.8). The lower half of the diagram shown in Fig.(3.8) depicts a pipe containing a fluid.

Here a magnetic field gradient in the $z$ direction, which follows the application of the 90-degree RF excitation pulse encodes the nuclear spins with a phase offset dependent on their position in the $z$ direction. This is shown by vectors (here labelled 1-5) representing the phase offset of the magnetisation vector of volume elements of spins

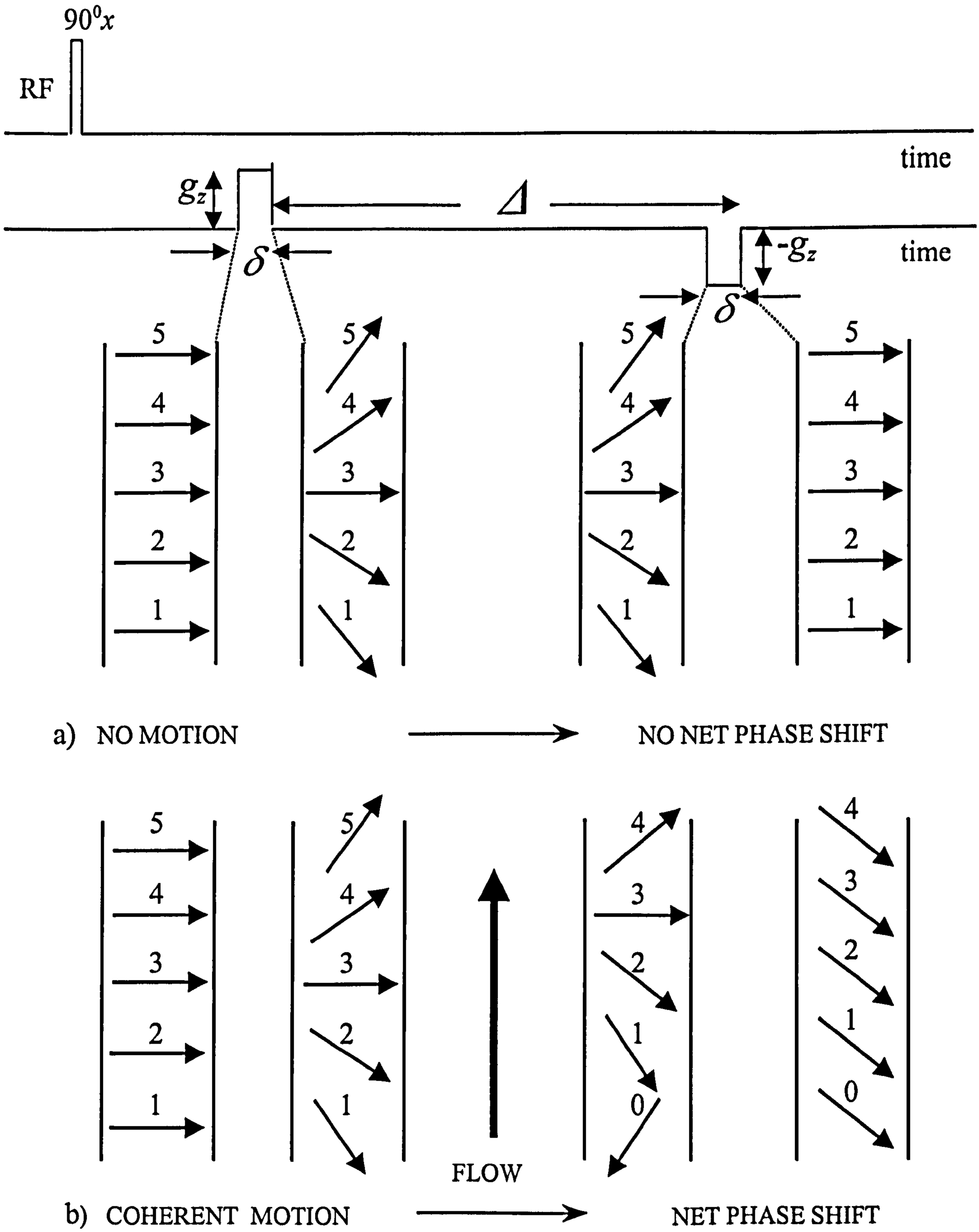


**Figure 3.8** Principles of velocity imaging used in monitoring 2D flow field: when the motion occurs (*b*), application of two velocity encoding gradients in the *z* direction ($g_z$, $-g_z$) of identical magnitude and opposite polarity results in the net phase shift of the spin-isochromats (arrows 1-5). For static systems (*a*) the phase shift is zero. Duration of the velocity encoding gradients pulses is given by time $\delta$. The time between the application of the two velocity encoding gradients is called observation time and denoted $\Delta$.

at different positions along $z$; these vectors represent the behaviour of spin-isochromats.

Consider first the case where no motion of the fluid in the pipe occurs. Application of a magnetic field gradient (often referred to as a velocity encoding gradient) in the $z$ direction will then cause the groups of transverse magnetisation to dephase by an amount given by:

$$\phi = \gamma g_z \delta r_z \quad , \tag{3.26}$$

where $g_z$ is the magnitude of the gradient pulse, $\delta$ is the time for which the pulse is applied and $r_z$ is the spatial location along $z$ of an individual spin-isochromat. The system is then left for a time $\Delta$. Once $\Delta$ has elapsed, a velocity encoding gradient equal in magnitude but of opposite polarity, $-g_z$, is applied to the system. Because no motion of the spin-isochromats has occurred during $\Delta$, they receive an equal and opposite phase offset at this point, hence isochromats 1-5 will refocus at the end of the second velocity encoding gradient pulse i.e.:

$$\Sigma\phi = \gamma g_z \delta r_{z1} - \gamma g_z \delta r_{z2} = 0 \ . \tag{3.27}$$

Therefore, for the case of no motion, i.e. $r_{z1} - r_{z2} = 0$, there is no net phase shift. If, on the other hand, motion occurs during $\Delta$, Fig.(3.8) shows that the vector groups 1-5 will refocus with a net phase shift, $\phi_s$ given by:

$$\phi_s = \gamma g_z \delta \Delta u_z \tag{3.28}$$

where $u_z$ is the superficial velocity of the vector groups in the $z$ direction and thus:

$$u_z = \frac{r_{z1} - r_{z2}}{\Delta} \ . \tag{3.29}$$

In addition to the bulk flow, during the time interval $\Delta$ between the application of the two velocity encoding gradients, molecules within spin-isochromats undergo diffusive motion, which will cause the nuclei to acquire an additional phase shift. Since the nature of this motion is random, the distribution of the phase shifts incurred for each spin within the molecules will take on a Gaussian distribution. This directly results in

an additional dephasing of the spin-isochromats, and thus an attenuation of the echo-signal. Therefore, when the effects of flow and diffusion are combined, the signal is given by:

$$E(g_z) = exp(i\gamma\delta g_z \Delta - \gamma^2\delta^2 g_z^2 D(\Delta - \frac{\delta}{3})), \qquad (3.30)$$

where $D$ is the self-diffusion coefficient of the fluid examined.

This approach in which the bulk velocity is related to the phase shift of a spin-echo signal and diffusion is related to the attenuation of the spin-echo signal was extended by Callaghan (1988, 1991) to simultaneously measure both effects on fluid motion. The technique was termed dynamic NMR microscopy.

NMR microscopy probes at the scale which contains a large number of molecules i.e. molecular ensembles. The function describing the motion of these molecular ensembles is an averaged propagator, $\overline{P}_s$ (Callaghan, 1991) [55]. This propagator defines the probability that a spin, anywhere in the sample, has moved its position by displacement $R=r'-r$ in a time $\Delta$, as depicted in Fig.(3.9).

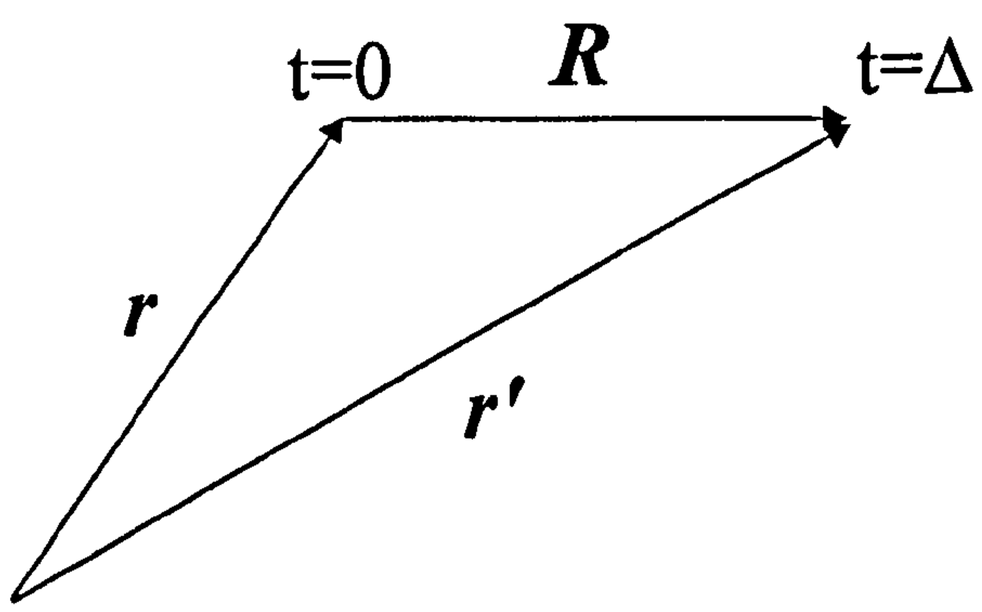


**Figure 3.9:** In dynamic NMR microscopy an averaged propagator $\overline{P}_s(R,\Delta)$ is introduced as a measure of probability of the particle displacement from $r$ to $r'$ over time $\Delta$.

The echo signal intensity, $E_\Delta(q)$, is obtained by averaging the dephasing due to the velocity encoding gradient $g$ over all possible molecular positions:

$$E_{\Delta}(q) = \int \overline{P}_s(R,\Delta) exp(i2\pi q R) d R, \qquad (3.31)$$

where $q = \frac{1}{2\pi}\gamma g \delta$ is a dynamic reciprocal space vector. $E_{\Delta}(q)$ has to be normalised to the reference value when $q$=0, $E_{\Delta}(0)$. When the applied velocity encoding gradient width is narrow and the motion occurs due to translational flow and diffusion, the solution of equation (3.31), obtained by using inverse Fourier transform, is [55]:

$$E_{\Delta}(q) = exp(i2\pi q u \Delta) exp(-4\pi^2 q^2 D\Delta), \qquad (3.32)$$

where $u$ is the velocity in the direction of $q$ and $D$ is the self-diffusion coefficient. In dynamic experiments, the information obtained by application of spatially encoding gradients is combined with the information obtained by application of velocity encoding gradients so that the overall signal is:

$$S(k,q) = \int E_{\Delta}(q)\rho(r) exp(i2\pi k \cdot r) d r \qquad (3.33)$$

For various $k$, using the Fourier transformation in $k$-space, a complex pair of planar images, weighed by $E_{\Delta}(q)$, is obtained for each $q$. From multiple $q$-contrasted slices, using the Fourier transformation in $q$-space, the averaged propagator $\overline{P}_s(R,\Delta)$ is obtained from equation (3.31) between corresponding voxels in the two-dimensional matrices. Hence, the velocity information is obtained in the third dimension, which is referred to as the velocity domain ($Z$). A typical averaged propagator $\overline{P}_s(R,\Delta)$ for a single voxel in the velocity domain $Z$ is shown in Fig.(3.10). The values for unidirectional velocity $u$ and diffusion coefficient $D$ can be directly calculated from equations given by Callaghan and Xia (1991) [43]:

$$u = \frac{2\pi k_u n_d}{N_{ar}\gamma g_m \delta\Delta} \quad , \quad D = \frac{3.56(n_D k_{FWHM})^2}{\gamma^2\delta^2 g_m^2 N_{ar}{}^2 \Delta} \qquad (3.34)$$

where $u$ is the magnitude of $u$ in the direction of $g$, $N_{ar}$ is the digital array size in transformation, $g_m$ is the maximum value of $g$, $k_u$ is the position of the peak centre of $\overline{P}_s$ in $Z$, $k_{FWHM}$ is the full width-half maximum of peak of $\overline{P}_s$ in $Z$ and $n_d$ is the number of increments in $g$ used in the experiment.

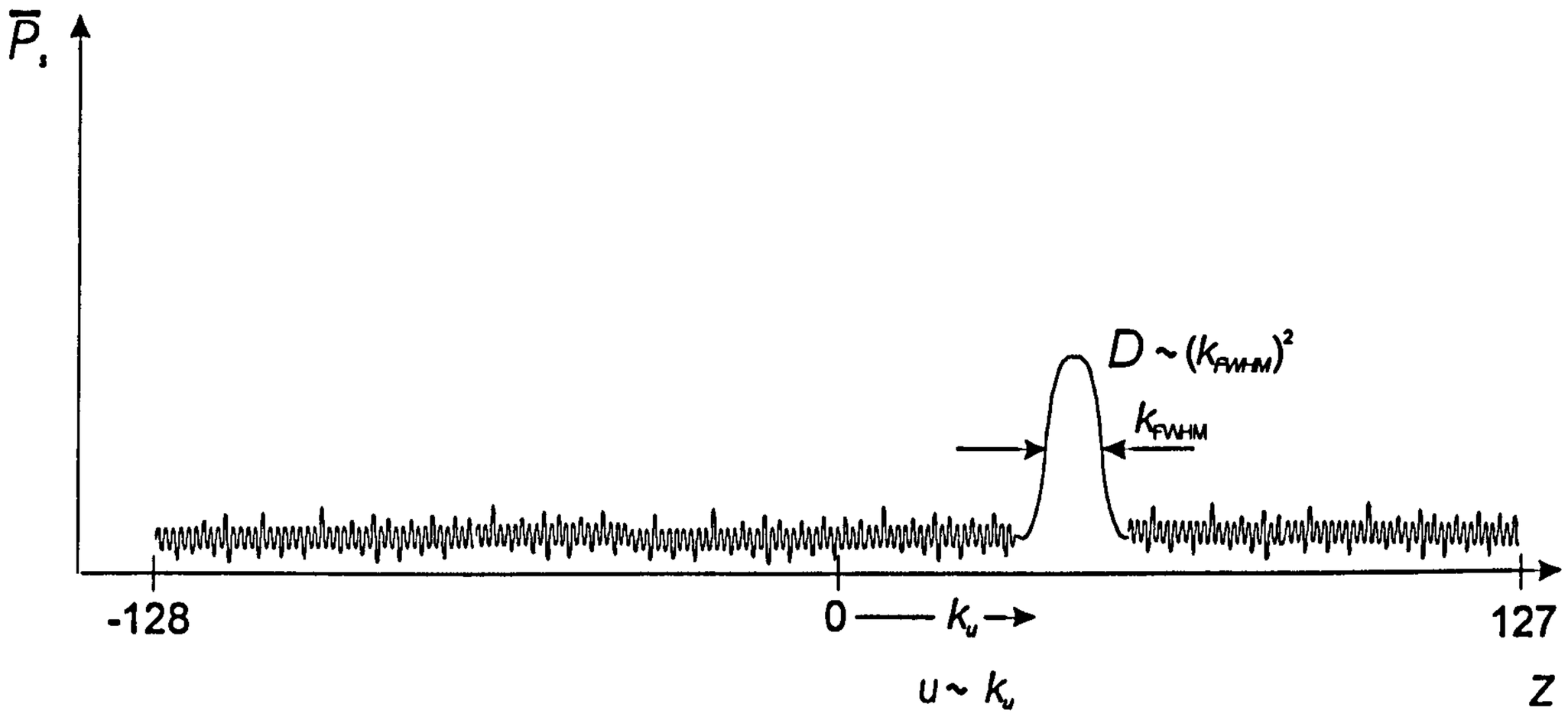


**Figure 3.10** Signal intensity in the form of an averaged propagator $\overline{P}_s(R, \Delta)$ for a single voxel in the velocity domain Z. The unidirectional velocity $u$ is proportional to the position of the peak centre of $\overline{P}_s$, $k_u$, whereas diffusion coefficient D is related to the full width-half maximum of peak, $k_{FWHM}$ of $\overline{P}_s$ in Z.

### *3.3.2 Practical Considerations*

Problems that can be encountered in single phase flow studies in porous media include the local variations in supposedly homogeneous magnetic field. These local magnetic field heterogeneities can occur due to chemical shift effects and/or differences in magnetic susceptibilities at the solid-liquid interface.

Identical nuclei (proton nuclei in this study) in different molecules or within the same molecule at different locations experience different electron environment, which cause a deviation in Larmor frequency of the nuclei. The signal positions for each group of nuclei (protons) is then displaced in the NMR spectrum. The spectrum takes the form of the signals superimposed on one another, but shifted in the read direction by respective chemical shifts. Obviously, this can distort the images in the read direction.

The values for magnetic susceptibilities are discontinuous at the solid-fluid interfaces thus producing local heterogeneities in the magnetic field $B_o$. This will produce an additional dephasing of proton spins in these regions with a consequential loss of signal and a shorter apparent value of the spin-spin relaxation time, $T_2^*$. In addition, the susceptibility gradients at the interface can distort the images severely.

The most important consequence of chemical shifts effects and differences in magnetic susceptibilities is the broadening of the NMR signal in the frequency spectrum. Therefore, care must be taken that the total acquisition bandwidth ($\Delta\nu$) used in imaging divided by the number of voxels in the read direction is greater than the frequency width due to chemical shifts and magnetic susceptibility differences. This is achieved by increasing magnetic field gradients used for imaging so that the effects of susceptibility gradients and chemical shift are negated.

## *3.4 Notation*

| | |
|---|---|
| $A(\nu)$ | spectral response |
| $B_0$ | static magnetic field |
| $B_1$ | r.f. induced magnetic field |
| $D$ | diffusion coefficient |
| $E$ | echo signal intensity |
| $G$ | magnetic field gradient |
| $I$ | spin quantum number |
| $M$ | bulk magnetic moment |
| $M_0$ | bulk magnetic moment at equilibrium |
| $N$ | total number of spins |
| $N_a$ | number of spins in the state |
| $N_b$ | number of spins in the state |
| $N_{ar}$ | number of pixels |
| $V$ | volume |
| $P$ | nuclear spin angular momentum |
| $\overline{P}_s$ | averaged propagator describing the motion of molecular ensembles |
| $R$ | motion vector |
| $S$ | signal intensity |
| $T_1$ | spin-lattice relaxation time constant |

$T_2$ spin-spin relaxation time constant

$T_2'$ reversible transverse relaxation time constant

$T_2^*$ FID decay constant or total transverse relaxation time constant

$TR$ time between experimental repetitions

$TE$ spin-echo time

$Z$ velocity domain

$g$ velocity encoding gradient

$g_m$ maximum phase encoding gradient strength

$h$ Planck's constant

$k$ reciprocal space vector

$k_u$ position of the peak centre of $\overline{P}_s$ in the Z-velocity domain

$k_{FWHM}$ full width-half maximum of peak of $\overline{P}_s$ in the Z-velocity domain

$n_d$ number of increments in $g$

$m$ nuclear angular momentum spin state

$q$ dynamic reciprocal space vector

$r_{z1}$, $r_{z2}$ displacements of the space vector on the $z$ direction

$r$ space vector

$r'$ space vector

$t$ time

$t_d$ time between the two pulses in PGSE experiment

$u$ velocity

x spatial directions

y spatial directions

z spatial directions

$\alpha$ upper energy spin state for $^1$H nucleus

$\beta$ lower energy spin state for $^1$H nucleus

$\delta$ time between the two flow gradients in PGSE experiment

$\Delta$ application time of the gradient

$\phi_s$ phase shift of the spin-isochromats

$\gamma$ nuclear gyromagnetic ratio

$\mu$ magnetic dipole moment

$\nu$ nuclei spin linear frequency

$\Delta\nu_1$ excitation bandwidth of the RF pulse

$\Delta\nu_{SW}$ spectral width of the linear precession frequencies of the spins observed

$\Delta\nu_{FWHM}$ spectral width of the linear precession frequencies at half the maximum height of the signal

$\rho$ spin density function

$\omega_0$ Larmor frequency

*Subscripts*

$x$ x spatial co-ordinate

$y$ y spatial co-ordinate

$z$ z spatial co-ordinate

# Chapter 4

# Slow Flow Across Macroscopically Rectangular Fibre Lattices and an Open Region

Viscous flow of an incompressible Newtonian fluid across aligned and staggered rows of cylinders (fibre lattices) bounded by an open region from one side has been studied experimentally by Magnetic Resonance Imaging (MRI) velocimetry. The model systems are formed by circular cylindrical rods, macroscopically arranged in rectangular fashion and confined inside a Hele-Shaw cell. The thus formed fibre arrays are bounded by the wall of the cell from one side and the open region on the other side, thus forming a model system for a heterogeneous fibrous medium of dual porosity. The influence of structural parameters, specifically of the fibre lattice volume fraction and lattice unit-cell geometry on the local aspects of the flow in the interior of and exterior to the fibre arrays have all been investigated.

## *4.1 Materials and Methods*

The schematic diagram of the system used is depicted in Fig.(4.1). The experimental set up consists of the feed tank (1) containing one liter of glycerol whose viscosity was found to be 520 cP at 22°C, a multi-roller peristaltic pump (Watson-Marlow, UK) (2) easily adjustable to flowrates of the order of 1ml/min without significant pulsation and the MRI spectrometer (4) with the R.F. probe (3) in which the Hele-Shaw cell (5) is placed for imaging. All the connections were done in silicon tubing and the glycerol was recirculated through the flow loop during the experimental runs. The Hele-Shaw cell (enlarged in Fig.(4.1)) was made of Perspex and the bottom and the top plates were

sealed with a rubber gasket. The cell was designed in a way that the distance from the inlet to the first column of five cylinders is twice the width of the cell in order to minimise entry and exit effects. The dimensions of the cell are 220mm×29mm×3.3mm.

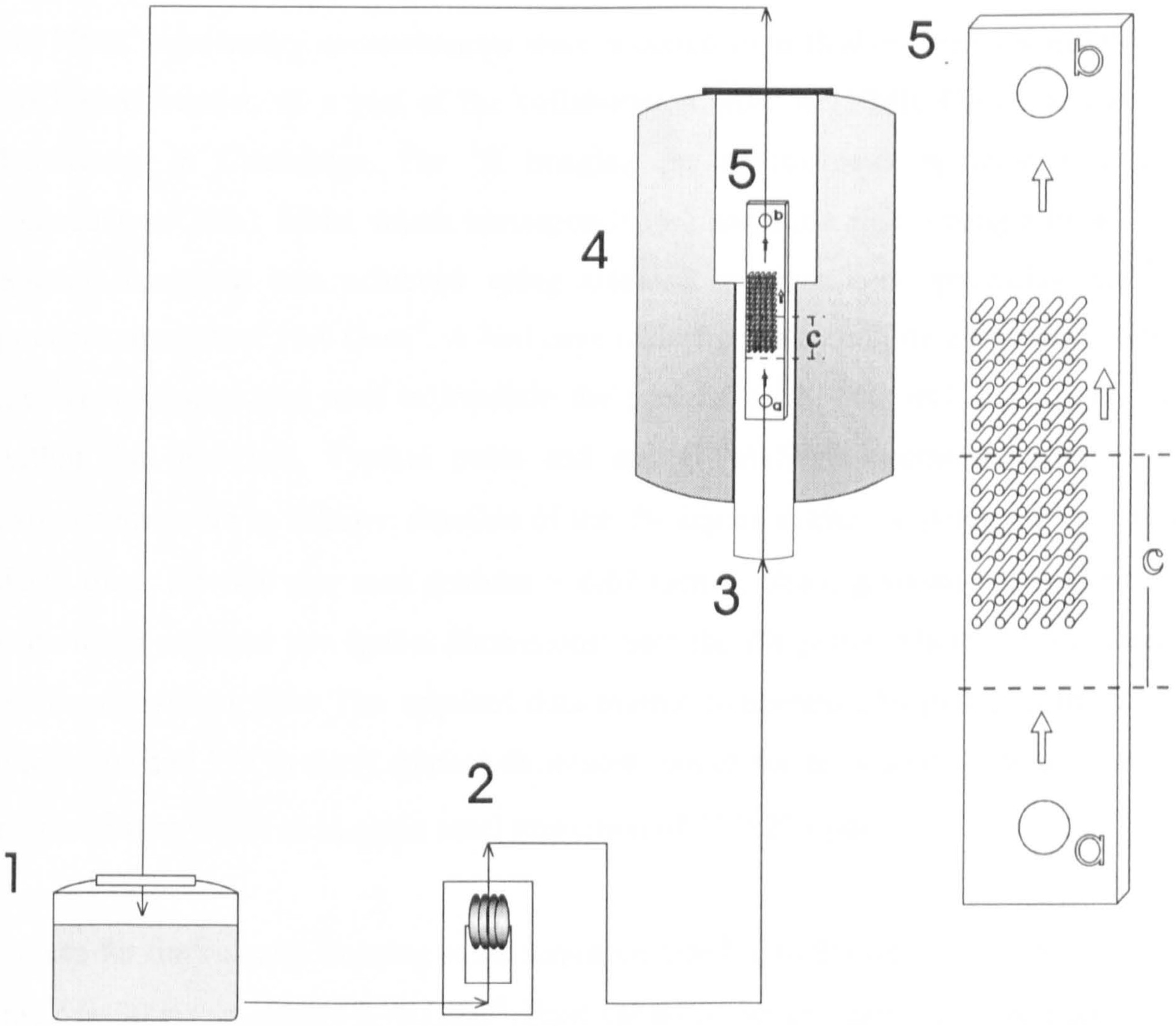


**Figure 4.1** Experimental setup used for MRI experiments: 1-fluid reservoir; 2-peristaltic pump; 3-probe 4-magnet 5-Hele-Shaw cell *a*-cell inlet, *b*-cell outlet *c*-experimental field of view.

Initially, glycerol solution was pumped into the unsaturated system at the minimum flowrate to avoid trapping of air bubbles. Following saturation of the flow cell (as determined by MRI images) the flowrate was set at the desired value (4.5ml/min) and the $V_z$ and $V_x$ velocity components averaged across the Y direction were obtained for flow across the square and hexagonally arranged arrays of circular cylinders.

## *4.2 MRI Measurements*

All NMR velocimetry measurements were acquired on a Bruker Spectrospin DMX 200 MRI spectrometer, as a part of the collaboration with the NMR Centre at Cavendish Laboratory in Cambridge. For $^{1}H$ imaging the spectrometer operates at a proton frequency of 200.1 MHz, which corresponds to a magnetic field strength of 4.7 Tesla. Spatial resolution was achieved using shielded gradient coils providing maximum gradient strength of 13.9 $Gcm^{-1}$. A bird cage radio frequency coil tuned to 200.1 MHz for the $^{1}H$ resonance was used to irradiate the protons in the glycerol solution contained within the flow cell. Typical pulse and spatial gradient parameters used in these experiments were as follows: duration of the 90 degree excitation pulse = 95 μs; recycle delay time, *TR*=400 ms; read gradient = 6.67 $Gcm^{-1}$; phase gradient = 2.6 $Gcm^{-1}$. The experiment required two spatial dimensions; here the ZX plane, where Z is the direction of the superficial flow. The acquired data matrix comprised 256 pixels in the Z (read) dimension and 128 in the X (phase) dimension, which for the studied field of view of 70 mm x 35 mm yields an in plane pixel resolution of 273×273 μm.

Values for the velocity imaging pulse sequence (see Fig.(4.2)) were: $\delta_x = 5$ ms, $\delta_z = 3.75$ ms; $\Delta_z = 30$ ms; $q_{inc}(zx) = 2.78$ $Gcm^{-1}$. Four values of the velocity encoding gradient were used. The velocity encoding gradient was increased in equal steps from zero to a maximum of 8.34 $Gcm^{-1}$. The acquired data were subsequently transferred to a Sun Sparc 20 workstation and the velocity maps were calculated as described in Chapter 3 using in house software.

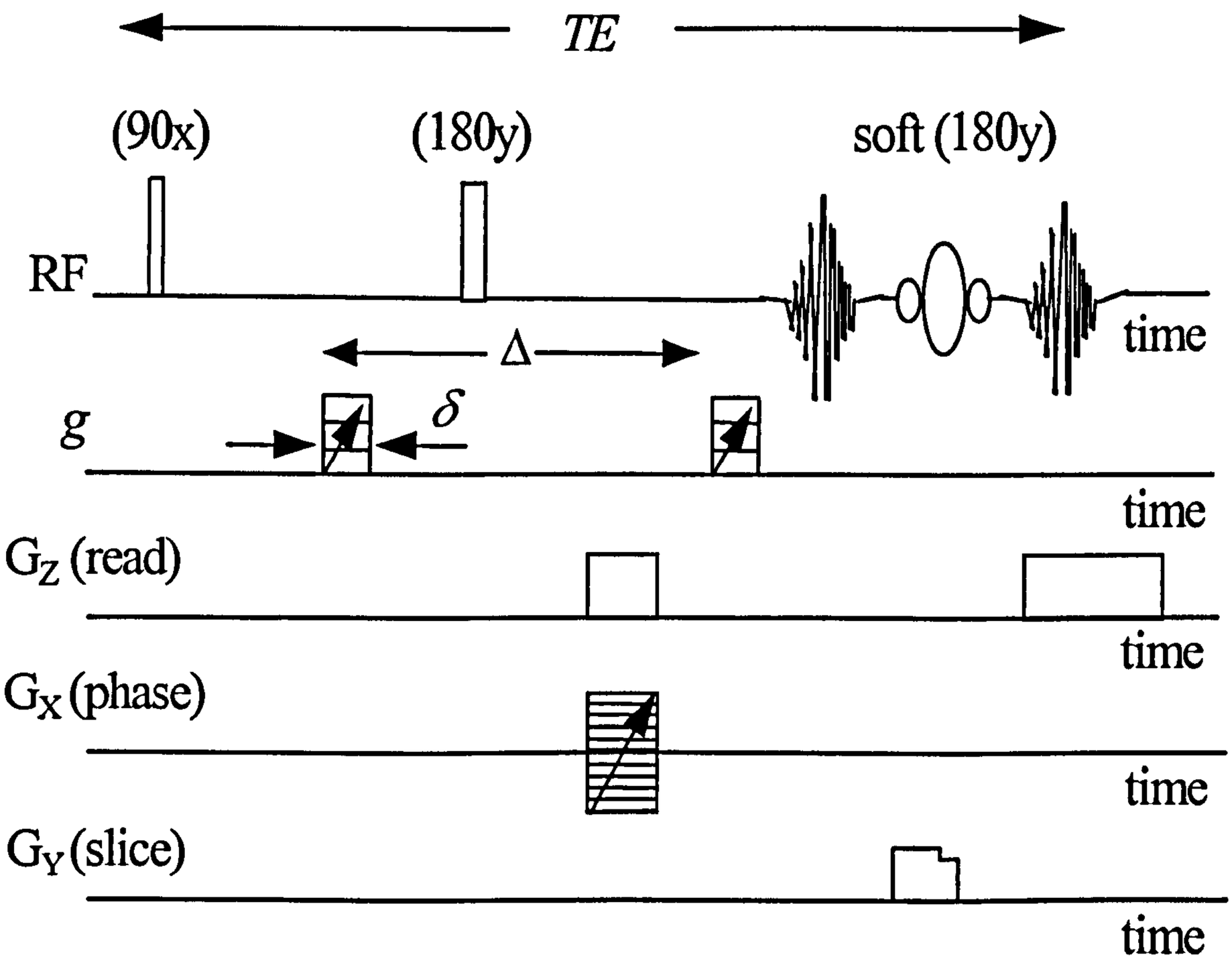


**Figure 4.2** Full pulse sequence used in the NMR velocimetry experiments: RF- radio-frequency signals, $g$ - velocity encoding gradient with the three equal increments applied, $G_X$, $G_Y$, $G_Z$ – spatial gradients, $\delta$- duration of applied velocity encoding gradient , $\Delta$ - observation time, $TE$ – spin echo time.

## *4.3 Results and Discussion*

In order to assess the influence of the fibre packing densities and lattice geometry on velocity distributions in the fibre arrays and the open channel placed in the Hele-Shaw cell the configurations depicted in Fig.(4.3) are examined. These are: (I), a square-unit cell lattice of cylinders with porosity $\varepsilon$ ($\varepsilon$=1-$\phi$, where $\phi$ is the fibre volume fraction in the arrays) of 50%, (II), a square-unit cell lattice of cylinders with porosity of 70%, and (III), a hexagonal-unit cell lattice of cylinders with porosity of 50%. All the lattices have a macroscopically rectangular shape. The characteristic parameters of each cell are the

diameters of the fibres (D), the distance between the fibres (g), the width of the open channel (W) and the small gap between the wall and the first row of the fibres (h).

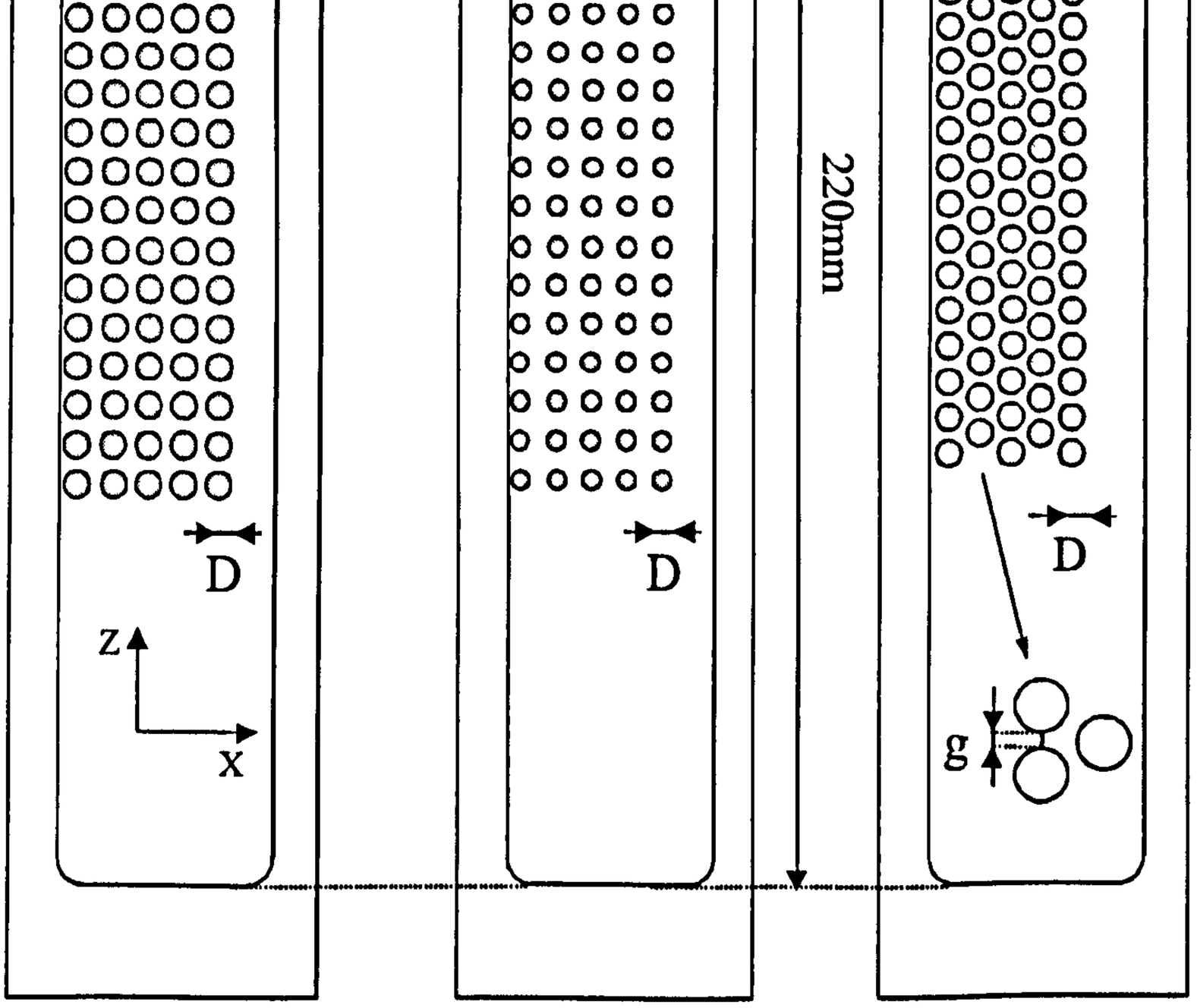


**Figure 4.3** The fibre array configurations used in the MRI experiments: cell I – macroscopically rectangular square unit cell lattice D=4mm, g=1mm, W=4.95mm, h=0.3mm, ε=0.5; cell II – macroscopically rectangular square unit cell lattice D=3mm, g=2mm, W=4.80mm, h=0.3mm, ε=0.7; cell III – macroscopically rectangular hexagonal unit cell lattice D=4mm, g=1.37mm, W=6.20mm, h=0.3mm, ε=0.5. Each lattice is consisted of five rows of cylinders aligned in the flow direction. The cylinders perpendicular to the flow direction make up the columns. Coordinate axis Y is perpendicular to the direction of flow (Z axis) and the in-plane of the cell (X axis).

The cross-wise and stream-wise pitch to diameter ratios are set to be equal i.e. the row separations are equal to the spacing of neighbouring fibres for all lattices. The interstitial porosities within the fibre lattices for the square-unit cell lattices ($\varepsilon_{sq}$) and the hexagonal-unit cell lattice ($\varepsilon_{he}$) are obtained from:

$$\varepsilon_{sq} = 1 - \frac{\pi D^2}{4(g+D)^2}, \quad \varepsilon_{he} = 1 - \frac{\pi D^2}{2\sqrt{3}(g+D)^2} \tag{4.1}$$

Spatially resolved images reveal the distribution of the steady-state fluid velocity components in the direction of superficial flow ($V_z$) and in the plane of the Hele-Shaw cell, perpendicular to the superficial flow ($V_x$). The component of the velocity vector in the direction perpendicular to the plane of the Hele-Shaw cell ($V_y$) was measured and observed to be at least one order of magnitude less than the other velocity components at all experimental points. The experimental field of view, as seen from 2D spin-density image of the cell I in Fig.(4.4), allows the measurement of $V_x$ and $V_z$ velocities in one half of each fibre array.

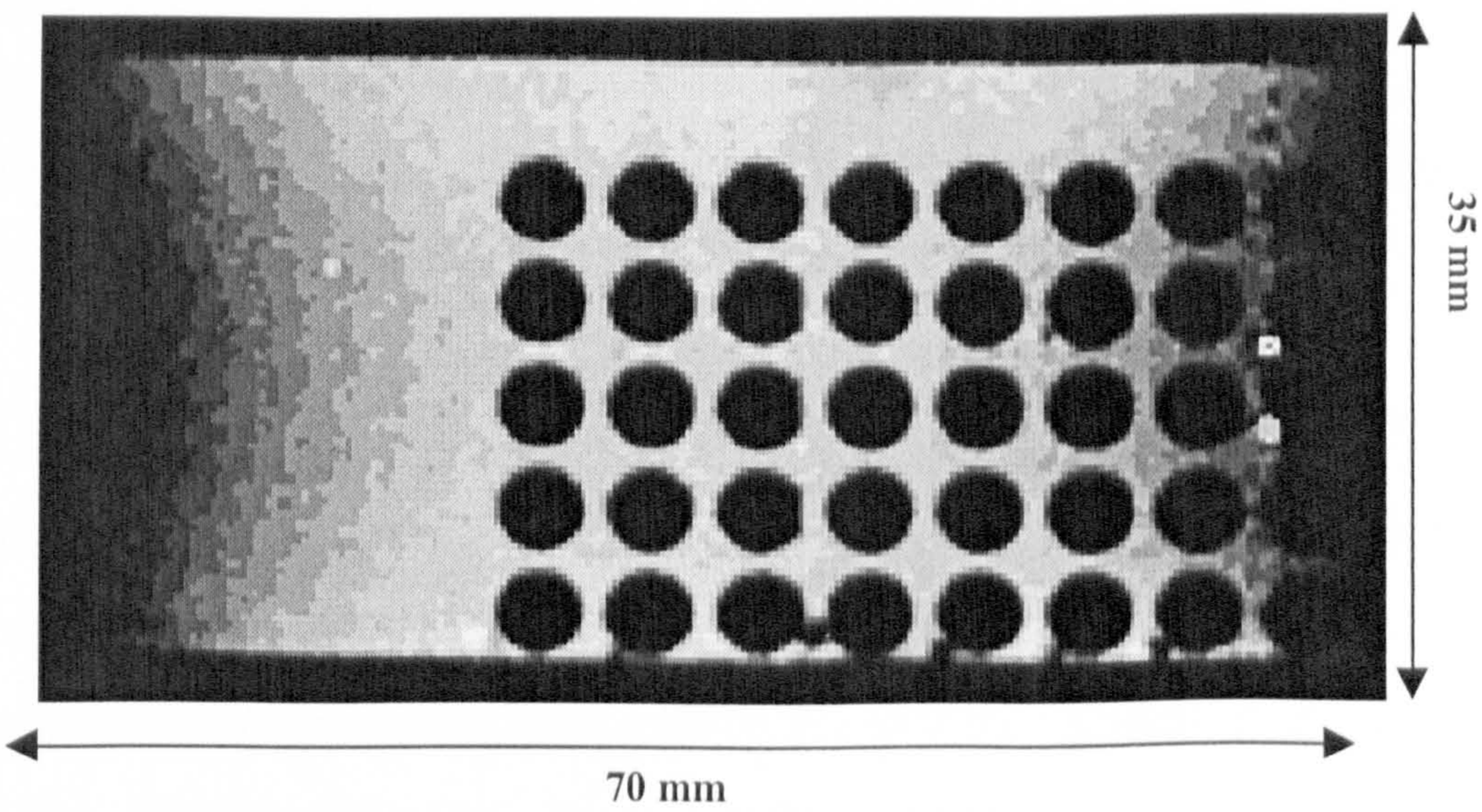


**Figure 4.4** 2D spin density image for the lower half of the fibre lattice in the cell I. The experimental field of view is 70 mm x 35 mm yields an in plane pixel resolution of 273×273 μm.

As all the fibre arrays are symmetrical and the experiments are carried out at practically zero Reynolds number, either the top or the bottom parts of the arrays are monitored and it is assumed that the velocity profiles are symmetrical in the rest of the cells.

All experimental values shown are for velocities averaged across the gap in the Y direction. Values for $V_z$ range from zero on the walls and the surface of cylinders ('no-slip') to a maximum value occurring in the open channel. The values for the $V_x$ velocity (the velocity transverse to the main direction of flow) range from negative to positive, depending on the flow direction along the X axis. The values for the fluid velocities at each pixel are obtained directly from the MRI data.

### *4.3.1 Local Aspects of Coupled Free Flow and Flow in a Fibrous Porous Medium*

The local features of coupled free flow and flow in a fibre lattice are presented on contour plots for velocity components in the Z (Fig.(4.5a)) and the X (Fig.(4.5b)) directions for the Hele-Shaw cell I. The cross section of the cylinders is shown in grey colour. The values on the contour lines are in mm/s. In Fig.(4.5b), contours corresponding to negative velocities are drawn as dotted lines for ease of recognition.

As seen in Fig.(4.5a), all the values for the $V_z$ velocities are positive indicating no backwards flow within the fibre array. The lines of the contour plots inside the lattice show the periodic flow patterns of both $V_z$ and $V_x$ velocities as flow passes through the series of contractions and expansions between the rows of cylinders. Preferred flow paths are in lanes between the rows, while the fluid between the cylinders (in the flow direction) is almost stagnant.

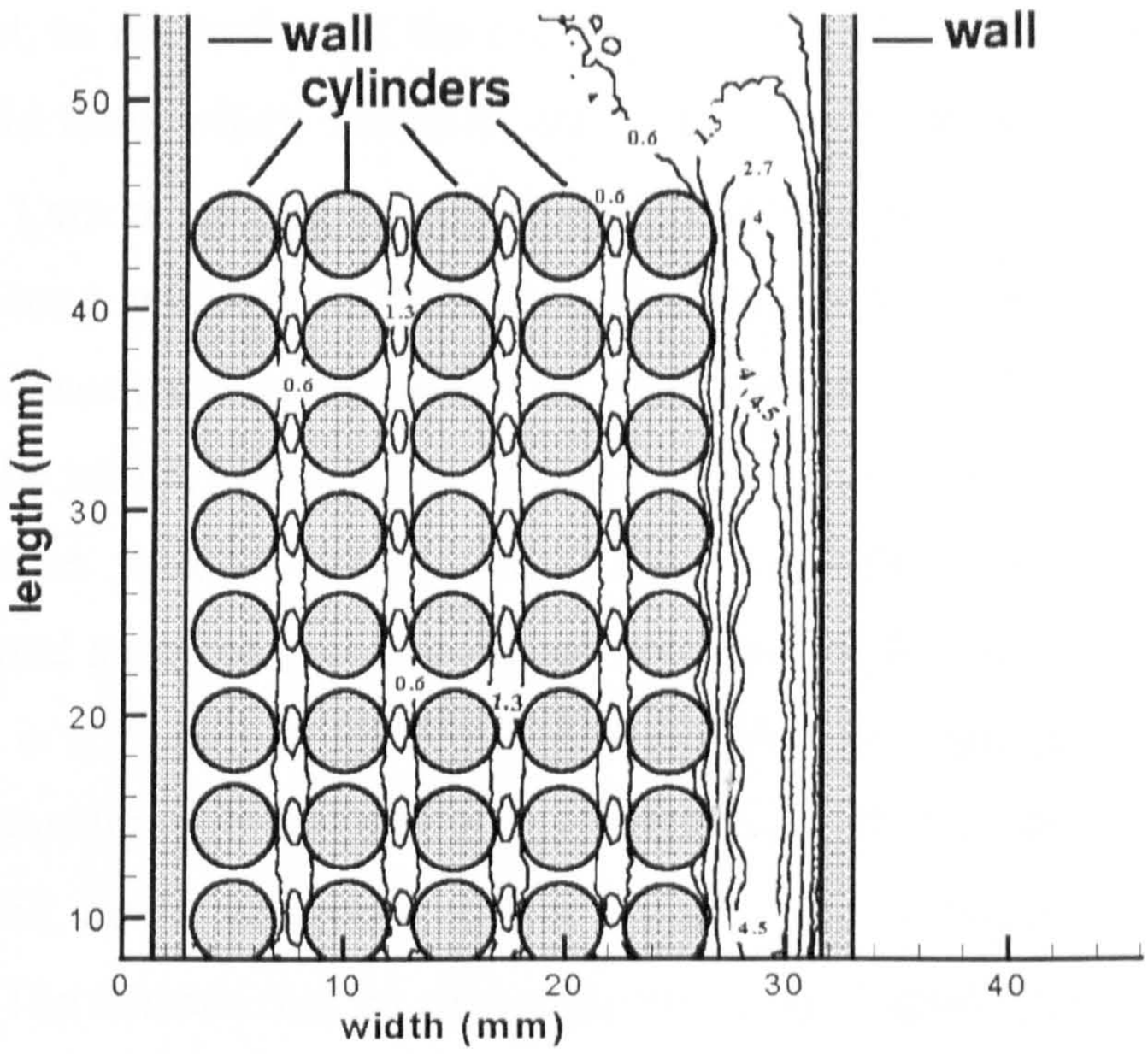


**Figure 4.5a** Contour velocity map for the velocity component in the flow direction ($V_z$) of the cell I.

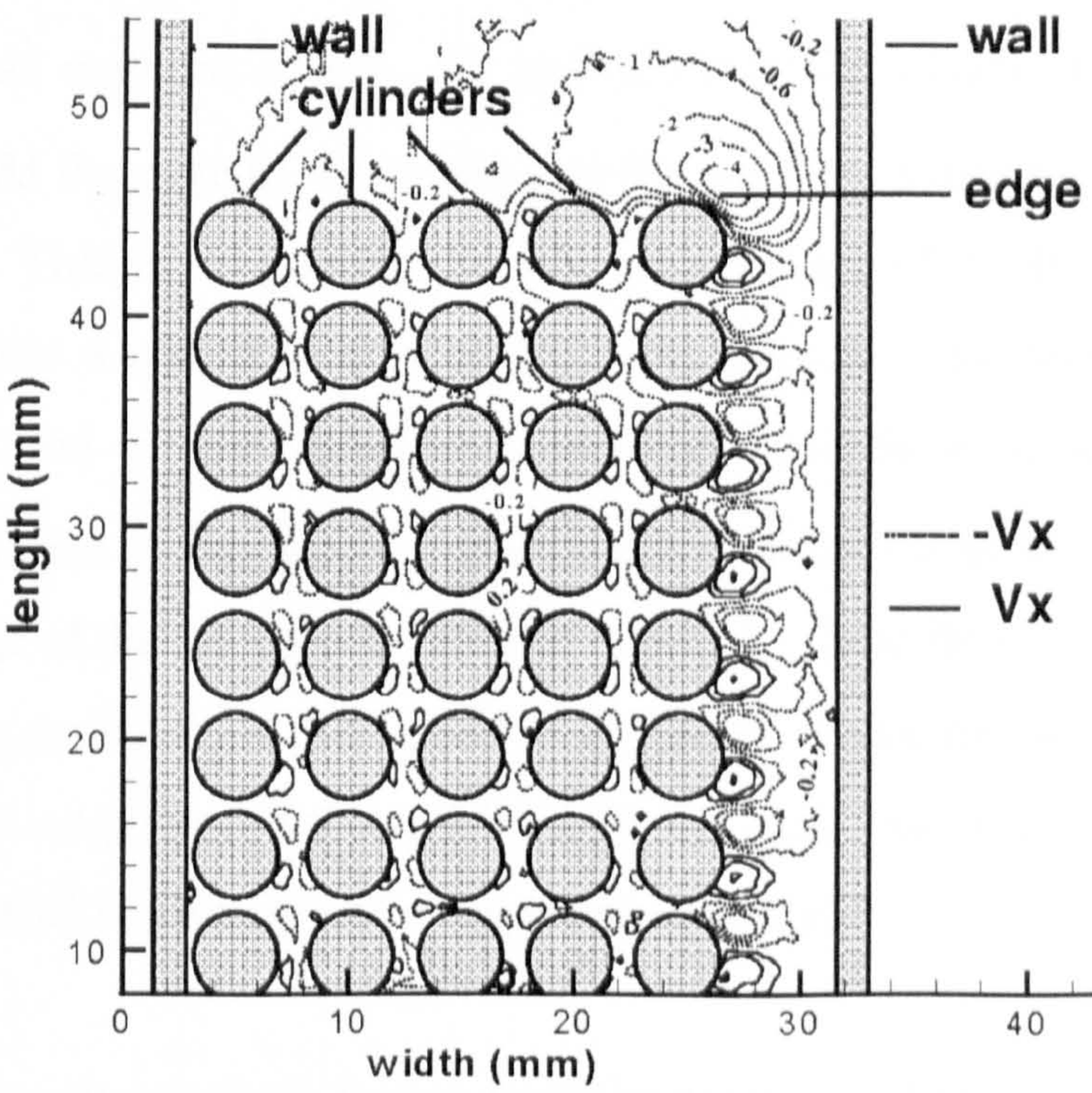


**Figure 4.5b** Contour velocity map for the velocity component perpendicular to the flow direction ($V_x$) of the cell I.

Extensive stagnant regions are undesirable in designing heat and mass transfer equipment, as the surface of the cylinders in the vicinity of these regions is not exposed to the fluid flow, which results in low heat or mass transfer coefficients. In a numerical study by Larson and Higdon (1987) [33] carried out for a pressure driven flow over infinitely long cylinders at moderate porosities, weak eddies were shown to occur in the regions between the cylinders (in the flow direction). However, as pointed out by the authors, the velocity magnitudes in these regions are extremely small. Moreover, in their studies of as little as a half of a degree inclined flow, the eddies vanished. This experimental study of pressure driven flow over cylinders of finite size shows that the velocities in regions between the cylinders in the flow direction are very low compared to the velocities through the passages between the rows of cylinders. Yet, at the lengthscale investigated, no recirculation regions between the cylinders in the flow direction were detected. The reasons may be those pointed out by Larson and Higdon earlier in the text; in real porous systems small deviations of the direction of the pressure gradient could be expected.

The values for $V_z$ velocities in the open channel increase only slightly with distance from the channel entrance or exit. $V_z$ shows a sharp maximum at the mid-point of the open channel. At the edge of the lattice (see Fig.((4.5b)), a rearrangement of fluid velocities is observed. This is the part of the free flow region where the fluid exits from the open channel into a region free of obstructions. This is manifested in substantial transverse velocities and in this region the maximum absolute local value for the $V_x$ velocities occurs, as seen in Fig.(4.5b). Consequently, the surface of the cylinders close to and right at the edge of the lattice will be most exposed to free flow. This finding has implications for all the applications mentioned in the introduction; the observed part of the free flow region (the edge) with substantially different local values for the velocity vector needs to be considered separately in the engineering design.

Noteworthy observations follow from the extent to which transverse velocities contribute to the velocity vector in the region near the lattice-channel interface. The velocity vector map of one such region taken from the mid-part of the cell I is shown in Fig.(4.5c). The

interface is marked as the dotted line connecting the tops of the interfacial cylinders. The imaginary doted circles with the same size as the cylinder diameter are drawn from the lattice-channel interface inside the free channel. The presence of transverse velocity in the open channel is evident from the alterations in the direction of the velocity vector; this is a measure of the flow disturbance in the open channel caused by the lattice.

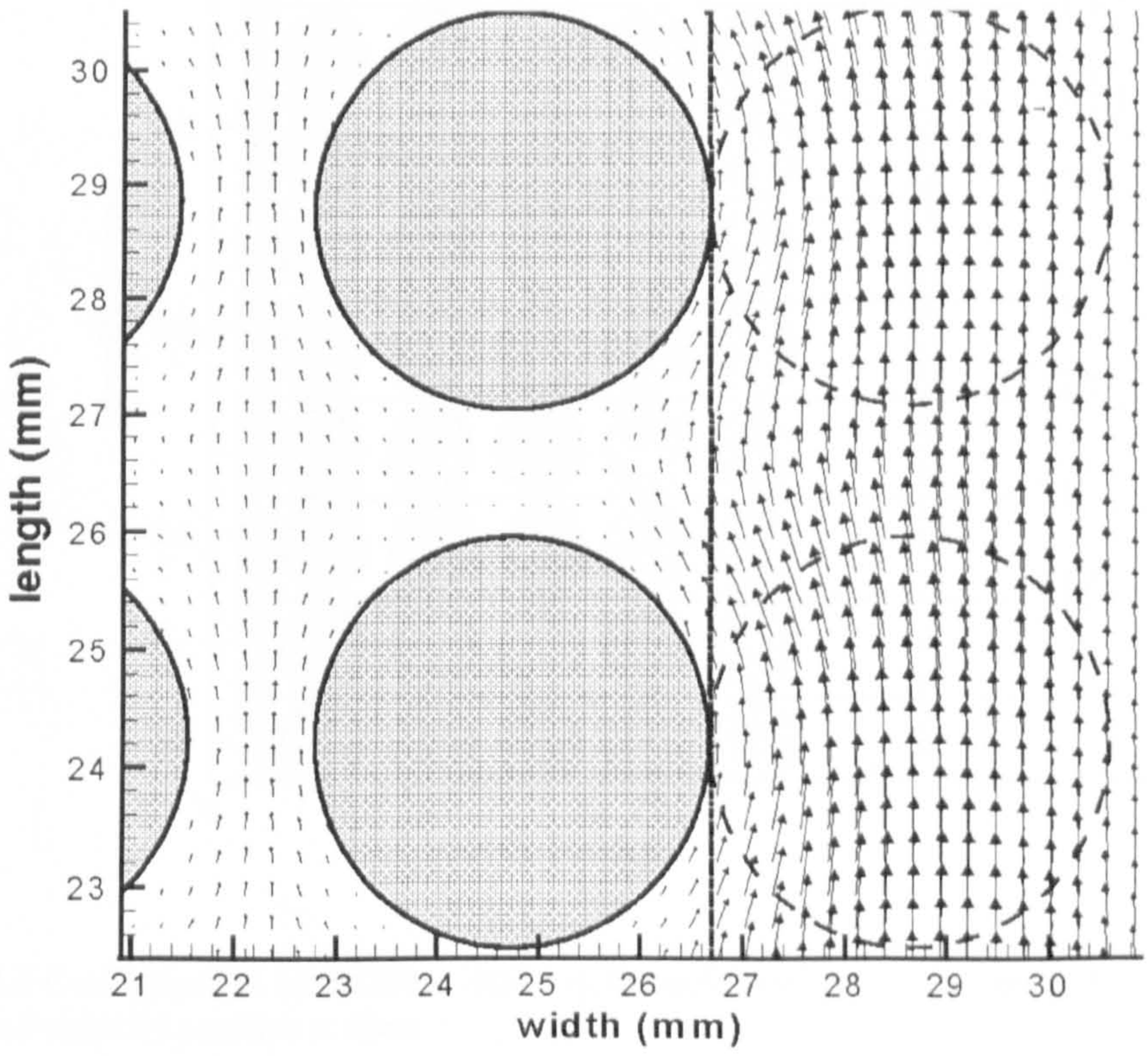


**Figure 4.5c** The vector velocity map taken in the region near the lattice-channel interface, which is marked as the dotted line connecting the tops of the interfacial cylinders. The doted circles in Fig.(4.5c) are drawn from the interface inside the free channel and have the same size as the cylinder diameter.

The flow disturbance in the open channel from the fibre lattice is assessed to be slightly less than the diameter of the cylinder. On the other side of the interface, the alterations in the direction of the velocity vector are completed within the half of the first row of fibres.

Analysis of $V_z$ and $V_x$ velocity profiles is performed along the lines of constant *z*-value both through the fibre lattice and outside the fibre lattice for cell I as indicated in Fig.(4.6). These lines pass through the half distance between the columns of fibres.

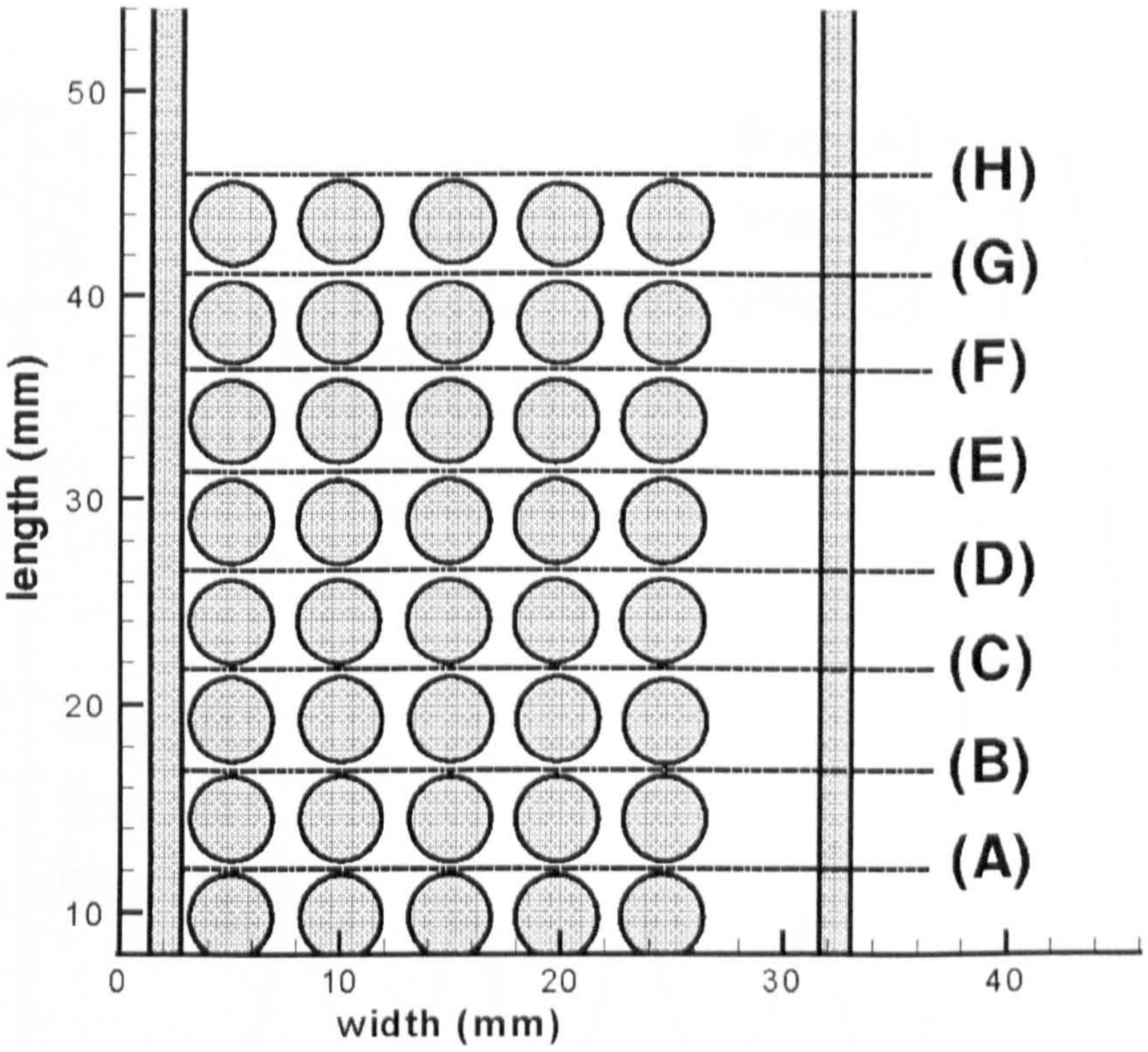


**Figure 4.6** Configuration of the fibre lattice in the cell I indicating the lines (A)-(H) along which the analysis of velocity profiles is done.

The experimental velocity profiles in the Z-direction along the lines (A), (B) and (C) are presented in Fig.(4.7a). The four peaks of lower magnitude represent maximum $V_z$ velocities within the fibre lattice. The peaks of higher magnitude represent maximum $V_z$ velocities in the open channel and are positioned on the far right in the figure. The extracted lines are very similar to one another implying no significant change in the $V_z$ velocity profiles as the fluid flows through the fibre lattice and the open channel. This is anticipated considering the very low Reynolds number used in the experiment. Velocity

rearrangement of $V_z$ velocities from open channel flow to flow within the fibre lattice is accomplished very fast and is complete within the first row of fibres. This is in agreement with predictions of some previous numerical [33] and experimental [41,42] investigations.

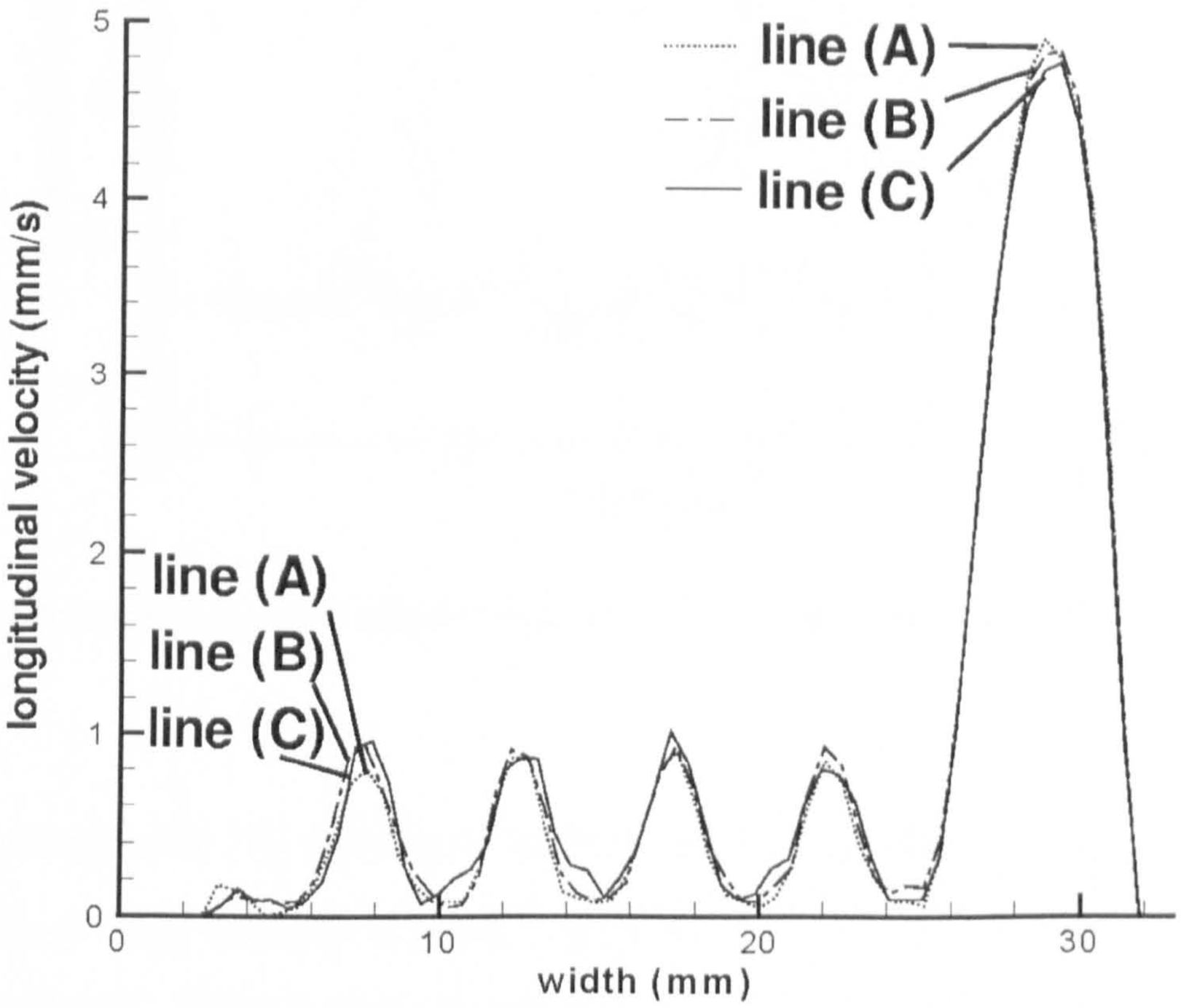


**Figure 4.7a** Comparison of the longitudinal velocity profiles in the cell I along the lines (A), (B) and (C).

The experimental velocity profiles in the X-direction along the lines (A), (B), (C), (G) and (H) are presented in Fig.(4.7b).

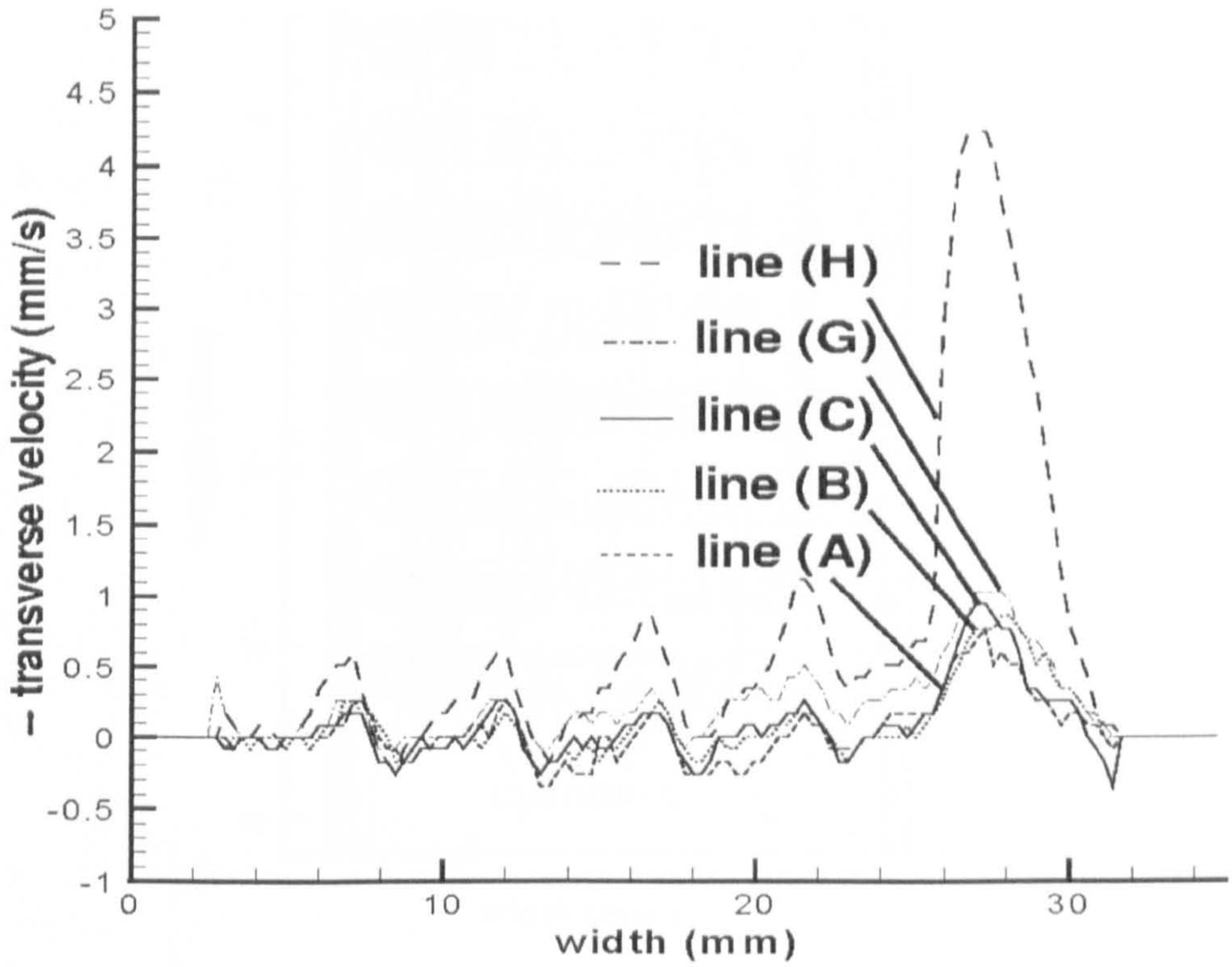


**Figure 4.7b** Comparison of the transverse velocity profiles along the lines (A), (B), (C), (G) and (H).

No decrease in the $V_x$ velocity throughout the lattice is observed along the lines (A), (B) and (C). A small decrease is present along the line (G), in the lattice region termed the 'lattice corner'. The velocity transitions are most prominent along the line (H), i.e. the line in the region where the fluid exits the open channel (the 'lattice edge'), as previously commented on the $V_x$ velocity contour plot maps.

### *4.3.2 Effect of the Fibre Volume Fraction (Porosity)*

The local features of the flow across the square lattice with a higher porosity of 70% (the cell II) follow very similar patterns to these of the cell I of 50% porosity, described above. The velocity contour maps for this cell are depicted in Figs.(4.8a,b).

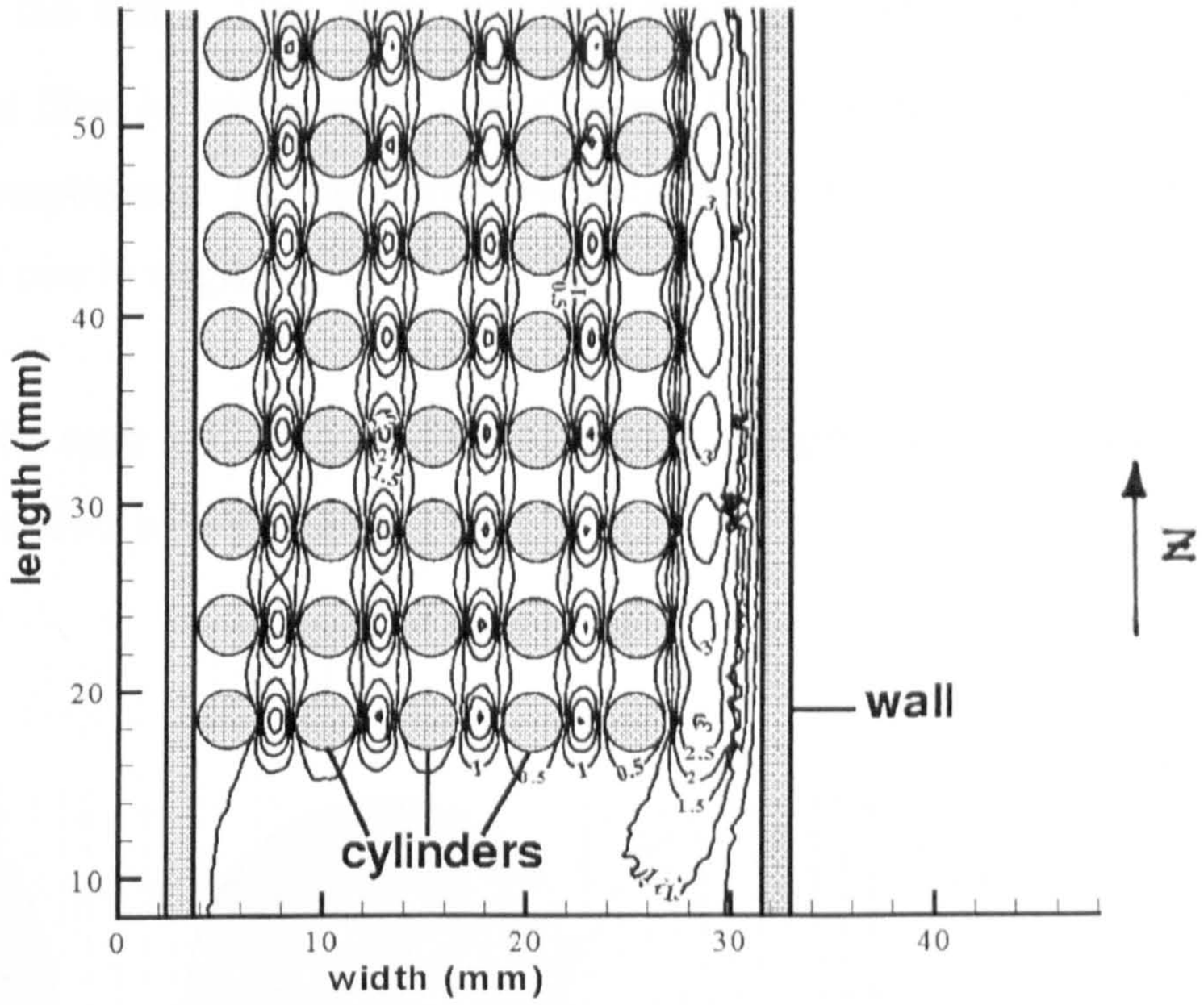


**Figure 4.8a** Contour velocity map for the velocity component in the flow direction ($V_z$) of the cell II.

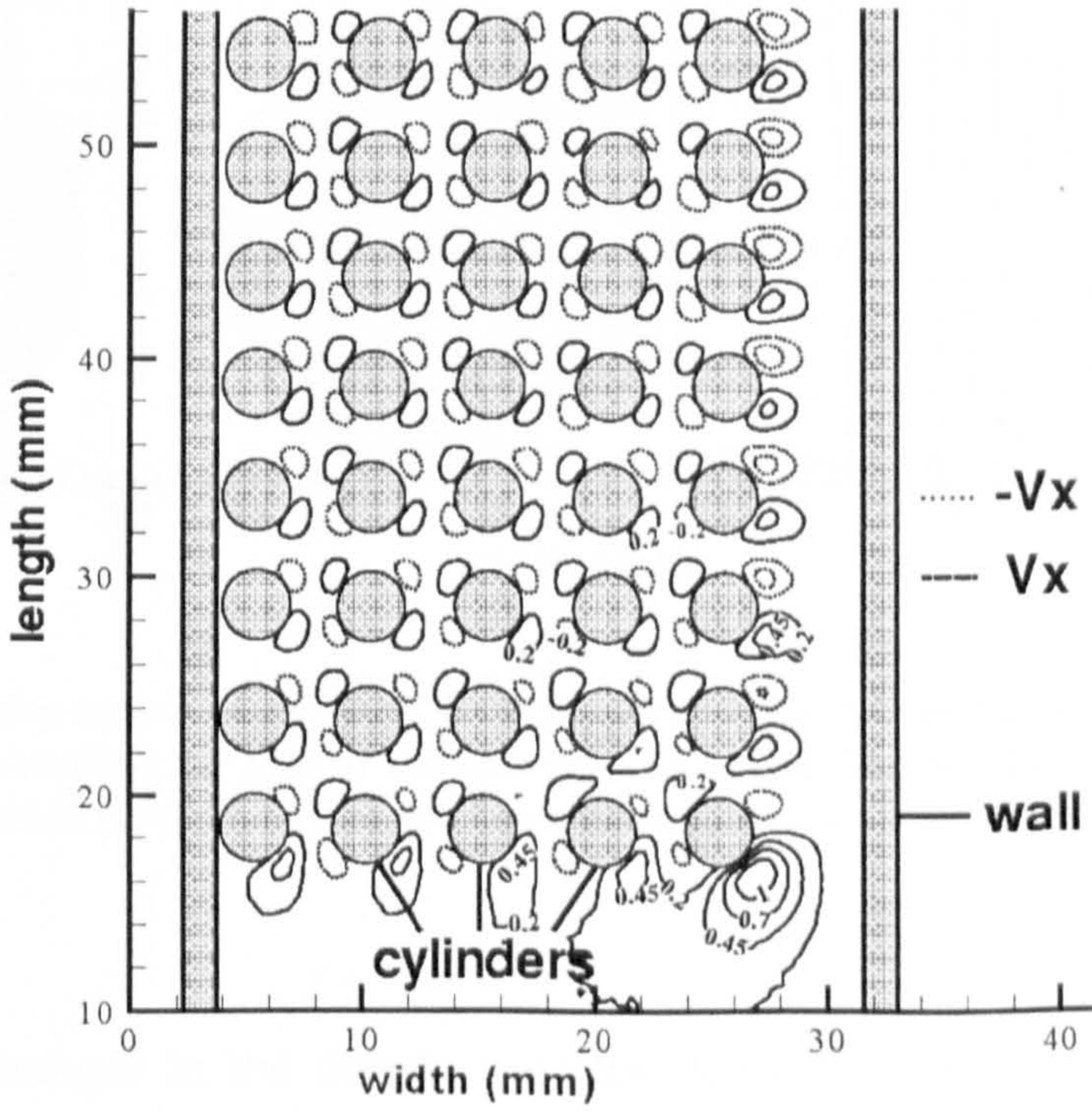


**Figure 4.8b** Contour velocity map for the transverse velocity component ($V_x$) of the cell II.

In the free flow region, a rearrangement of the fluid velocities are observed at the edge of the lattice, as in the cell I. The 'edge' effect is evident at the $V_x$ velocity map. Flow within the porous fibre lattice is again characterised by the regular velocity patterns for both velocity components. In the lattice regions between the cylinders in the flow direction, fluid is nearly stagnant.

The vector velocity map in the lattice-channel interface region is taken from the-mid part of the cell II and shown in Fig.(4.8c).

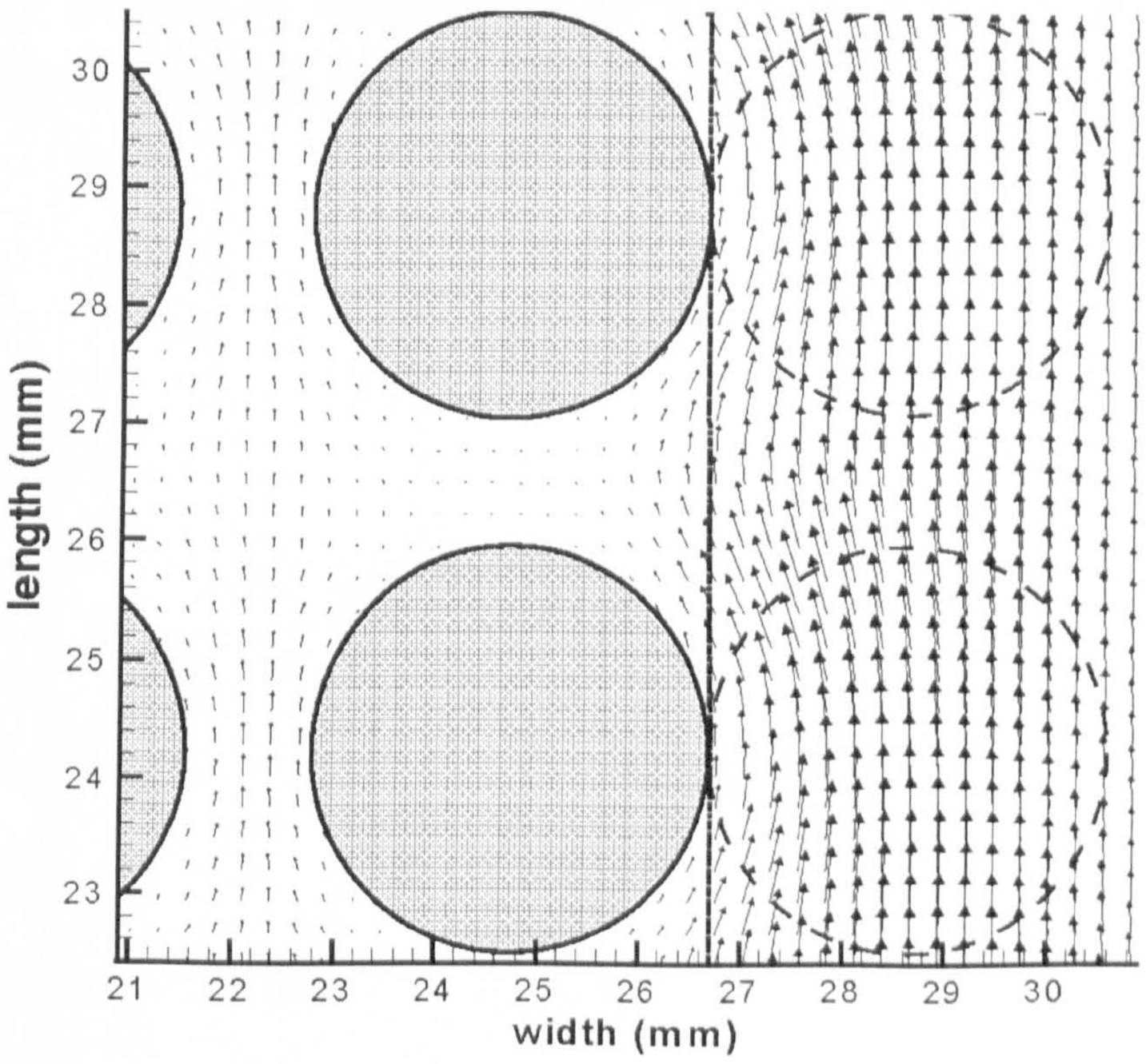


**Figure 4.8c** The vector velocity map taken in the region near the lattice-channel interface, which is marked as the dotted line connecting the tops of the interfacial cylinders. The doted circles in Fig.(4.8c) are drawn from the interface inside the free channel and have the same size as the cylinder diameter.

Observing the changes in the direction of the velocity vector, it is pointed out that the effect of the fibre lattice on the flow in the open channel is diminishing faster for the cell II than for the cell I. Recalling from Fig.(4.4) that the widths of the open channels in the

cells I and II are almost identical, this is ascribed to the smaller fibre diameter (D=3mm) and lower porosity of the cell II. On the other side of the interface in the cell II, the influence of the transverse velocity component on the velocity vector ceases within the half of the first row of fibres.

Shown in Fig.(4.9) are the comparisons of $V_z$ velocities along the lines of constant *z*-value (lines (B), as indicated in Fig.(4.6)) taken from the mid-part of fibre lattices in the cells I and II. As may be expected, the increased porosity of the lattice (the cell II) leads to an increase in the flow through the lattice yielding higher maximum $V_z$ velocities within the lattice than it is the case for the cell I of lower porosity. At the same time, a proportional decrease of the flow through the open channel in the cell II is detected leading to lower maximum $V_z$ velocities in the open channel for the cell II.

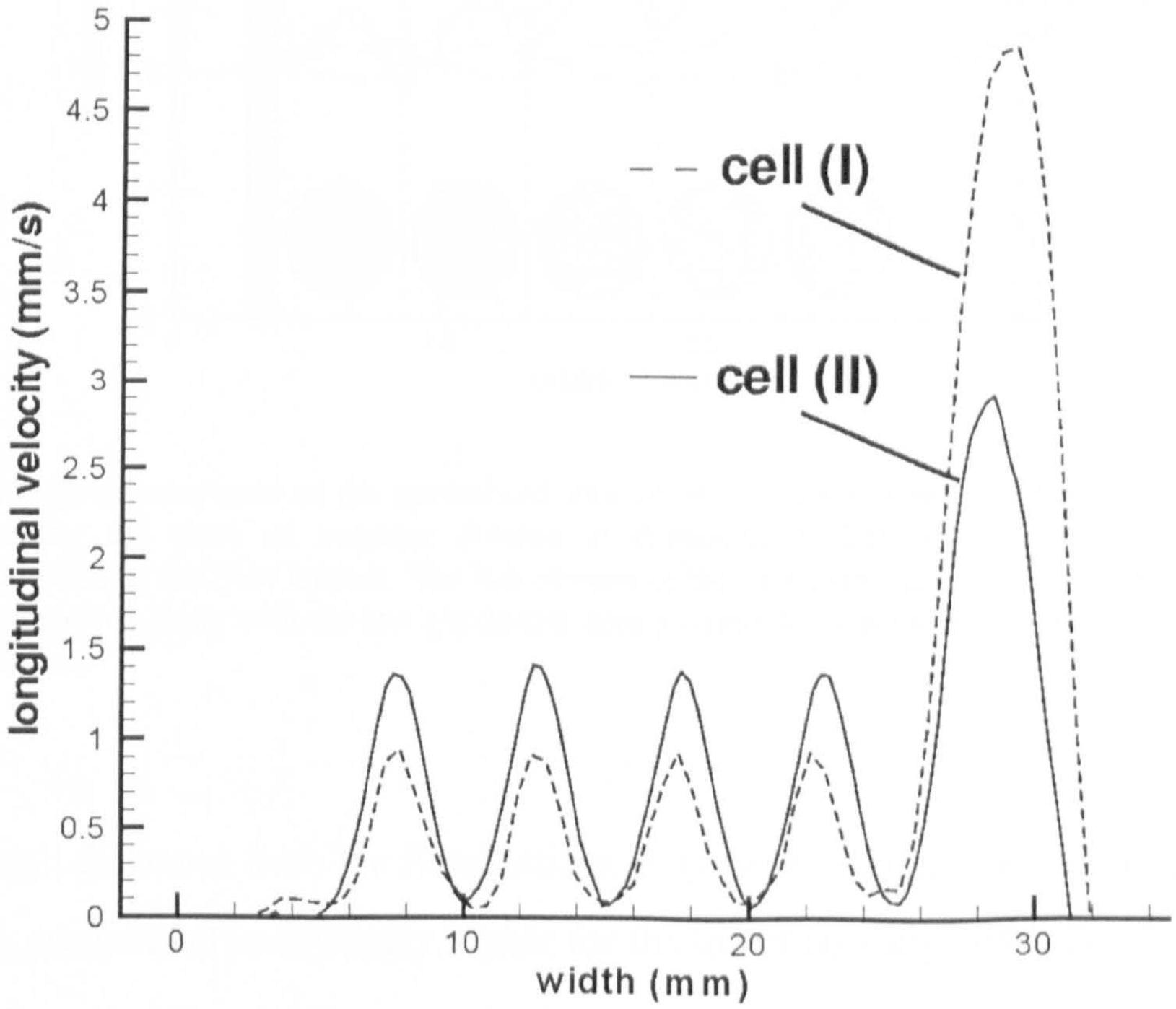


**Figure 4.9** Comparisons of the longitudinal velocity profiles for the cell I (ε=0.5) and II (ε=0.7) along the lines passing through the mid-points between the fibre columns in the middle of the fibre arrangements (lines (B) in Fig.(4.6)).

The higher flowrate in the higher porosity fibre lattice in the cell II leads to a reduced redistribution of velocity and therefore reduced $V_x$ at the edge and the exit/entrance of the fibre lattice. This can be seen in Fig.(4.10) from the profiles of $V_x$ taken along the lines of constant *z*-value at distances $d_1$=1.09mm and $d_2$=2.18mm behind or ahead (symmetry applies) of the fibre lattices I and II respectively.

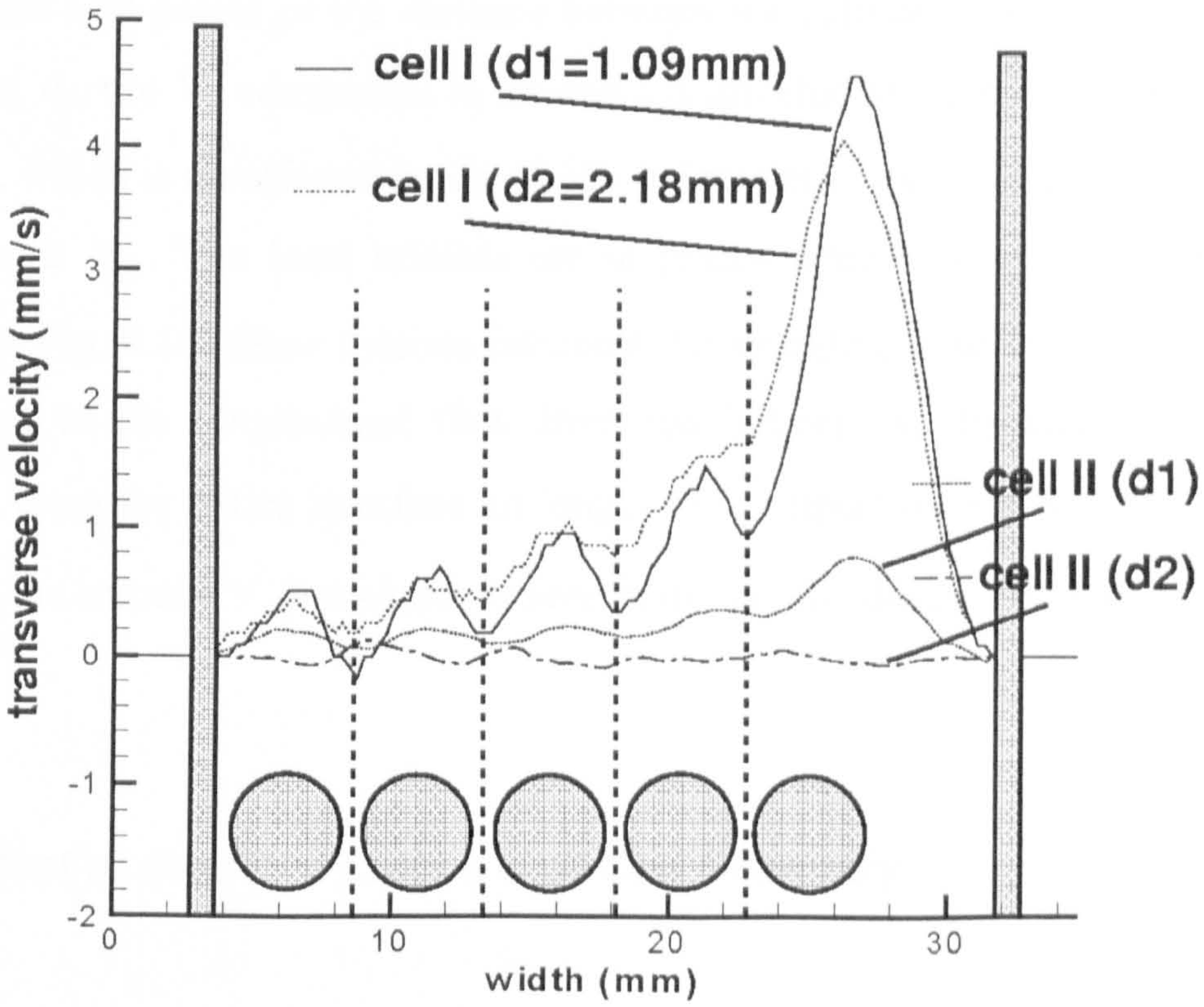


**Figure 4.10** Comparisons of the normalised transverse velocity components for the cell I and the cell II taken along the lines of constant *z*-value at distances $d_1$=1.09mm and $d_2$=2.18mm far from the beginning/end of the fibre lattices. The last column of the cylinders (the cylinders at the interface) from the cell I is depicted along with the straight dotted lines passing through the mid-points of the distance between the cylinders.

For small distances from the fibre lattices, $d_1$ (less than the cylinder radii in the two cells), the $V_x$ component is strikingly higher for the lower porosity cell I. Doubling the distance away from the fibre lattices to $d_2$ (still less than the cylinder diameter in the two cells), it is seen that the $V_x$ component in the cell II barely exists. At the same distance, $d_2$, the maximum value for the $V_x$ component in the cell I slightly decreases and is shifted

slightly to the left in the figure as the channel-lattice influence on the $V_x$ component gradually declines.

It is interesting to consider the shape of the decay curves of the $V_x$ component in the cell I. The last column of the cylinders (the cylinders at the interface) from the cell I is depicted in Fig.(4.10) for illustrative purposes i.e. the real distance from the interfacial column of cylinders is not scaled in the figure. The straight dotted vertical lines are drawn through the mid-points of the distance between the cylinders. At smaller distance from the lattice, $d_1$, the $V_x$ component in the cell I is affected by each cylinder from the lattice interface, which is manifested in Fig.(4.10) as local minima and maxima of the solid line decay curve $V_x$. The local minima are in places where the cylinder influence is the lowest (in Fig.(4.10) these minima intersect the straight dotted vertical lines, which are most open to the longitudinal flow from the lattice). At distance $d_2$, the individual cylinders from the lattice interface no longer have impact on the $V_x$ component, which results in the smooth $V_x$ transition, as seen in dotted line decay curve $V_x$.

### *4.3.3 Effect of the Fibre Lattice Unit-Cell Geometry*

Contour velocity maps for the hexagonal fibre lattice with porosity of 50% (the cell III) are shown in Figs.(4.11a,b). In Fig.(4.11b) contours corresponding to negative velocities are drawn as doted lines for ease of recognition.

Due to the hexagonal fibre lattice geometry, the flow lines through the array are more tortuous than the ones in the square lattices. This results in a greater portion of the cylinder surface area being exposed to the flow. Therefore, if the fluid contact with the cylinder surfaces is desired in the process design of fibrous porous media applications described in Chapter 2, hexagonal, rather than square unit cell fibre lattices, should be used.

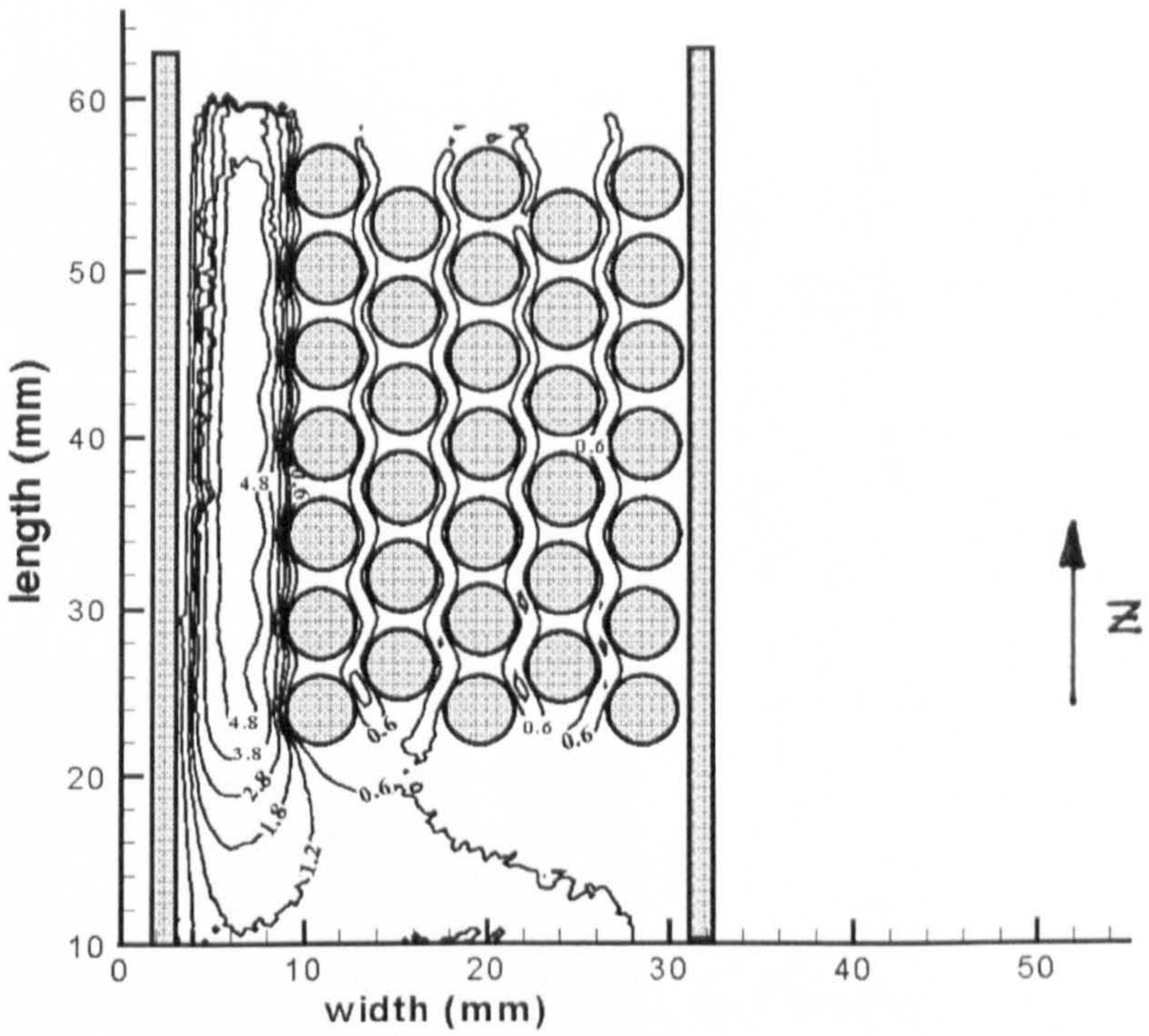


**Figure 4.11a** Contour velocity map for the velocity component in the flow direction ($V_z$) of the cell III.

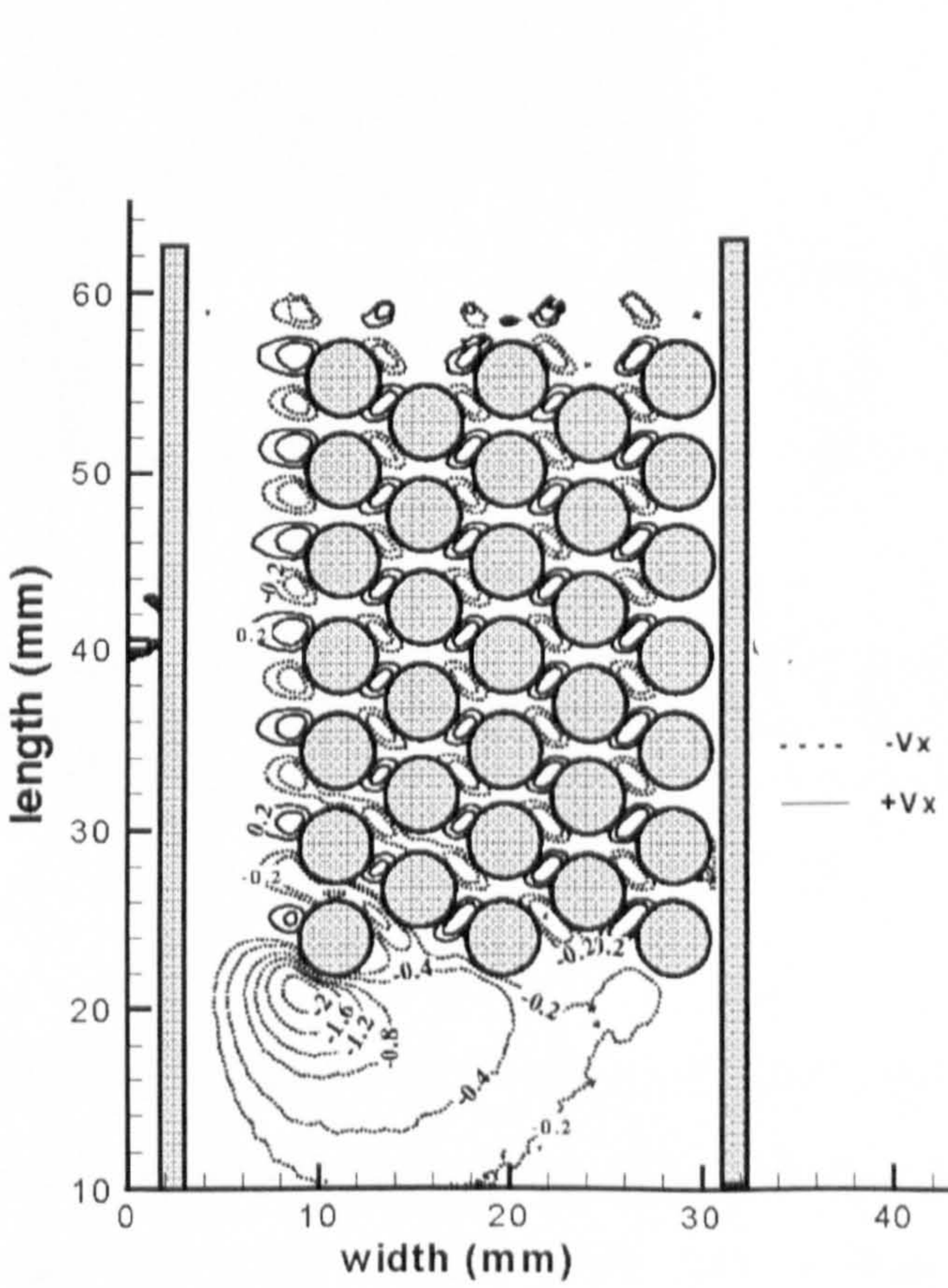


**Figure 4.11b** Contour velocity map for the transverse velocity component ($V_x$) of the cell III.

### *'Entrance' and 'exit' effects*

Fig.(4.12a) highlights parts of the hexagonal fibre lattice shown in Figs.(4.12b,c,d). The section where flow enters the lattice-channel arrangement is termed 'entrance', whereas the section taken from the middle part of the array includes a unit cell of the hexagonal array.

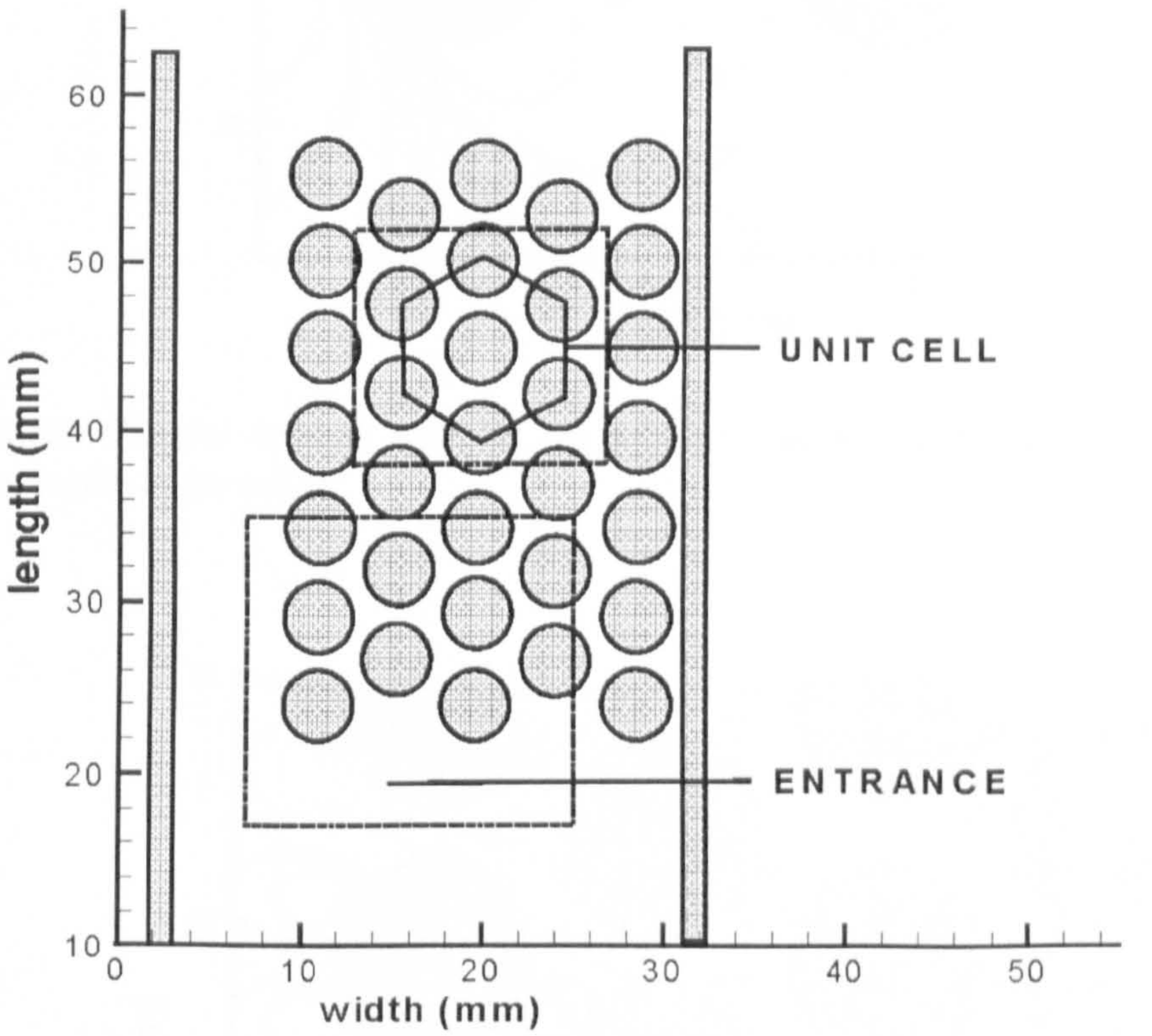


**Figure 4.12a** The inserts of the two-dimensional flow fields used in the analysis are taken: from the entrance region showing longitudinal and transverse velocity maps (4.12b,c) and within the fibre arrangement for a unit hexagonal cell showing the vector velocity map (4.12d).

From Figs.(12b,c) it is seen that magnitudes of both velocity components $V_z$ and $V_x$ are higher within the first three rows of cylinders, in the lattice region close to the open channel (termed the corner of the fibre lattice) than the average velocity values throughout the fibre arrays.

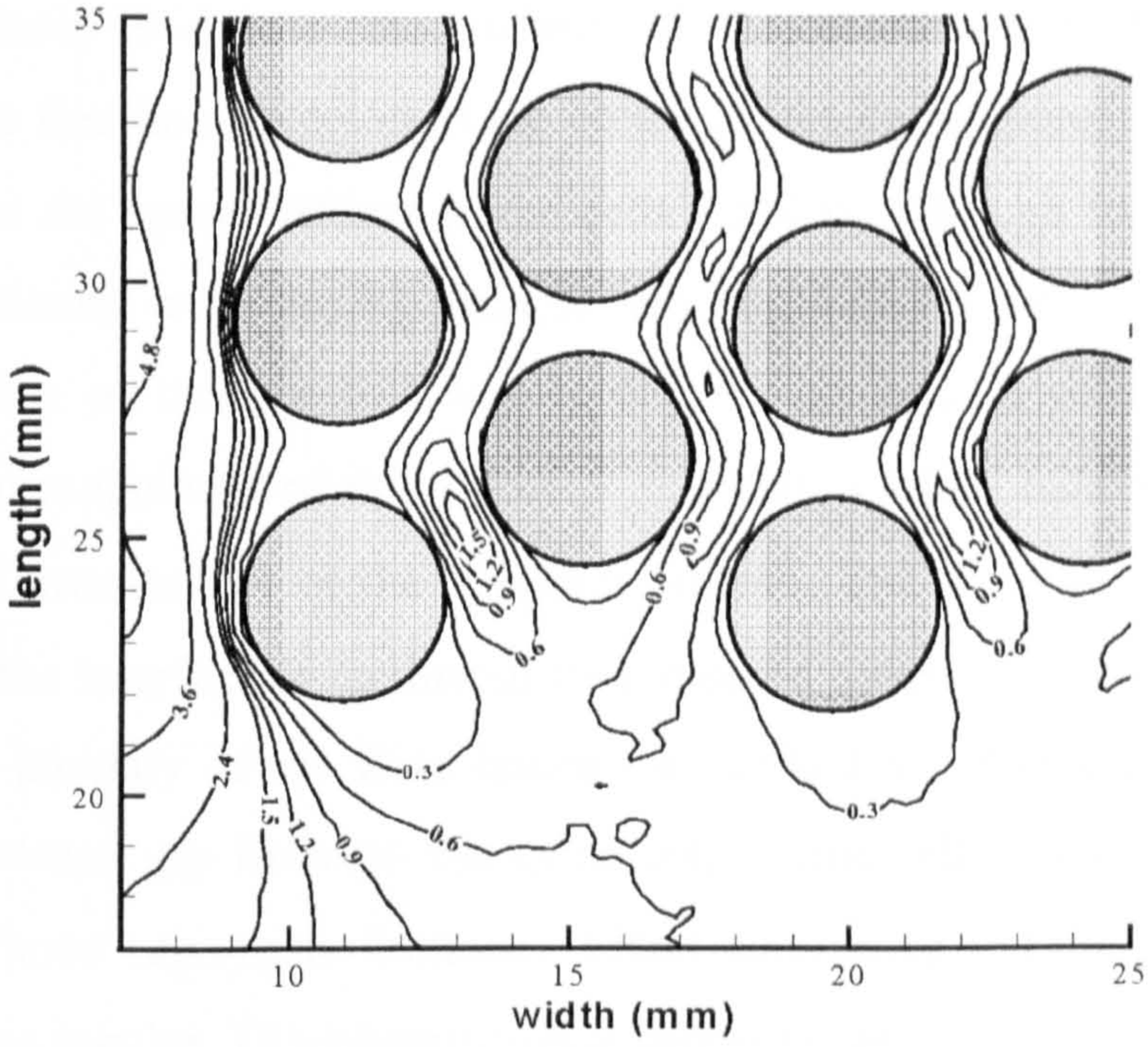


**Figure 4.12b** Contour velocity map for the velocity component in the flow direction ($V_z$) from the 'entrance' region in the cell III.

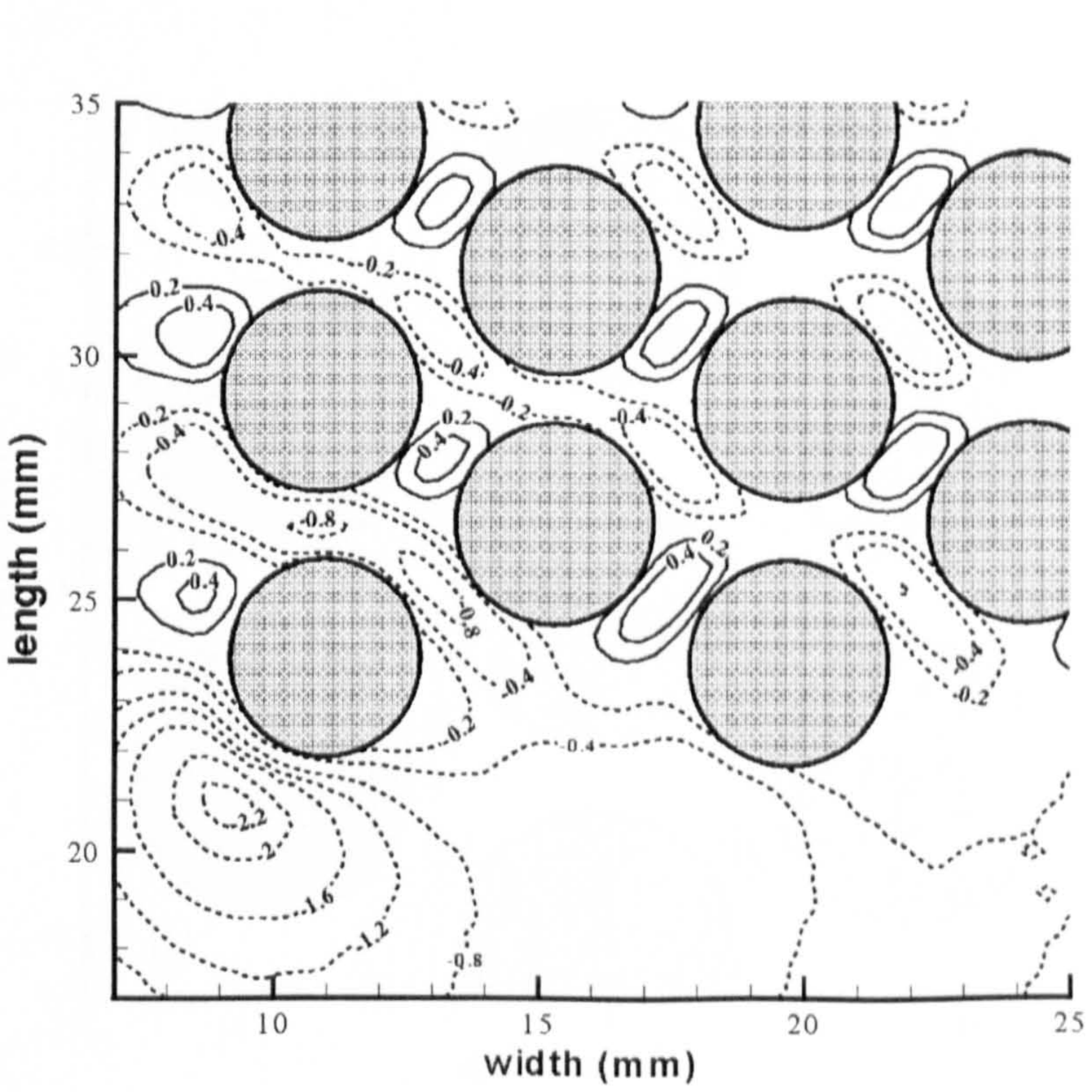


**Figure 4.12c** Contour velocity map for the velocity component perpendicular to the flow direction ($V_x$) from the 'entrance' region in the cell III.

Hence, this is the part of the lattice interior where the flow lines are preferential. This flow enhancement is due to the vicinity of the macroscopic flow rearrangements occurring as the free flow enters/exits the lattice-channel arrangement. The same effect is observed within the square lattices in the cells I and II, although its extent decreases in the order mentioned (refer to Fig.(4.5a,b) and Fig.(4.8a,b)). In order to explain these findings, the line of thought followed is that the magnitude of the 'entrance' effect depends on the magnitude of the velocity gradients, present near the interface of the lattice-channel arrangement in the 'entrance' region. The development of the velocity gradients near the interface is facilitated by increased open channel width (as in the cell III), decreased porosity of the fibre lattice (the cells I and III) and increased cylinder diameter / decreased gap between the cylinders, g, (the cells I and III). Once the fluid passes the 'entrance' region, the 'entrance' effect diminishes and the flow patterns within the array become regular. This observation is supported by the velocity vector plots of the hexagonal unit cell taken from the middle part of the array, as seen in Fig.(4.12d).

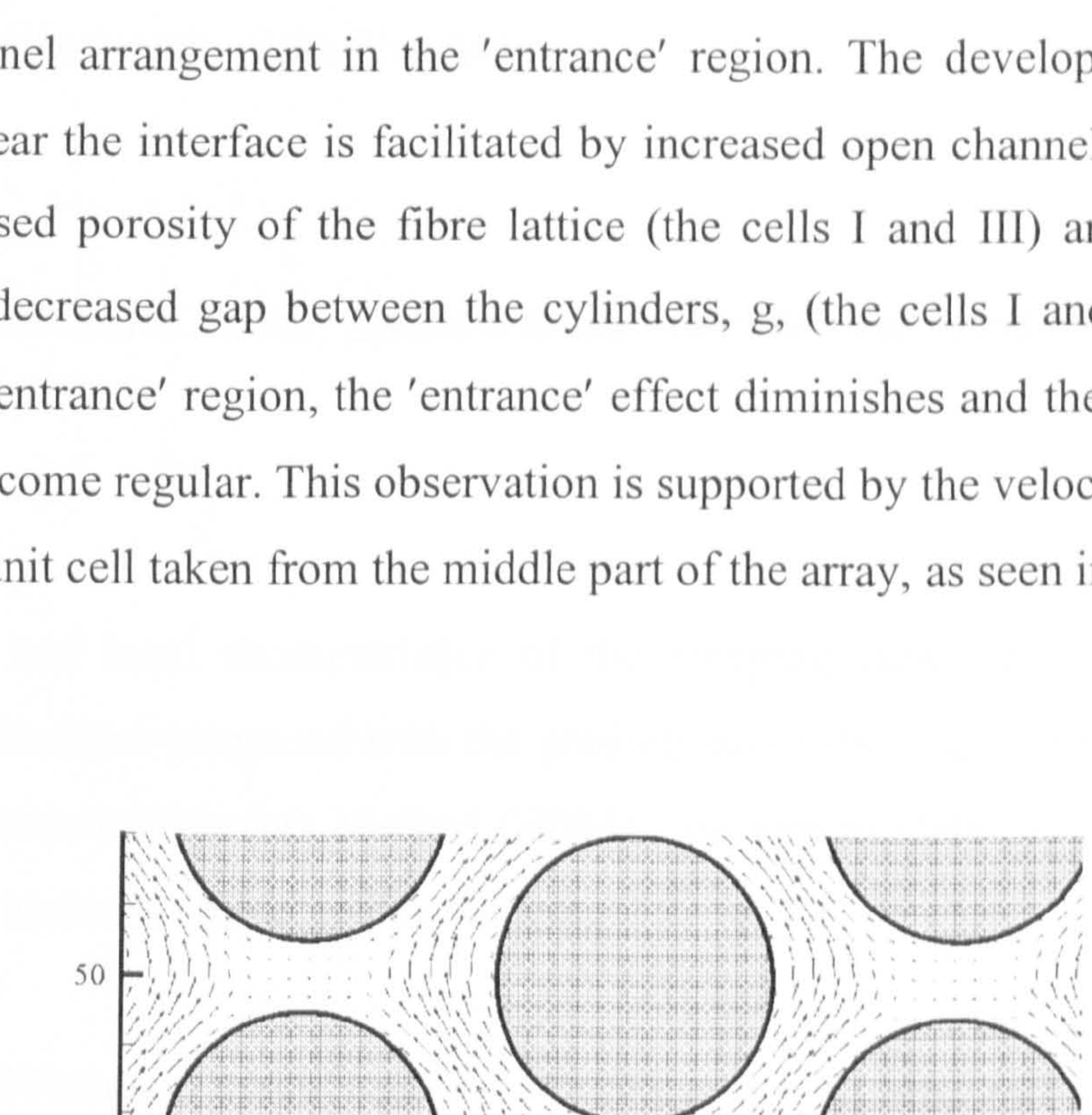


**Figure 4.12d** Velocity vector plots of the hexagonal unit cell taken from the middle part of the array in the cell III.

Similarly, in the 'exit' regions of the investigated symmetrical lattice-channel arrangements, the effect of flow enhancement within the corner of the array will again be observed.

These considerations imply that the entrance/exit effect could be of decisive importance for accurate flow description in heterogeneous fibrous media of dual porosity. The extent to which this local effect has an impact on the macroscopic flow field will also depend on the stream-wise length of the fibre lattices.

## *4.4 Comparisons with Lattice-Boltzman Model and Boundary Element Method*

The global and local characteristics of the creeping flow field in the lattice-channel porous medium are compared with the predictions of the lattice-Boltzman model (LBM) and the Boundary Elements Method (BEM). In both models the flow was modelled as Newtonian, incompressible and inertialess.

The lattice-Boltzmann model used for comparisons with MRI velocimetry was the model developed by Warren (1997) [59]. The simulations were performed within the NMR centre at Cavendish laboratories in Cambridge under the supervision of Prof. L. F. Gladden. The flow analysis using the lattice-Boltzmann model was done on a microscopic scale. On this scale, the particles in a fluid at equilibrium in the bulk phase were assumed to move in all directions with equal probability. In the numerical simulation of the same process, this motion is constrained on a coarse grid, or lattice. The fluid motion is simulated by following the time evolution of one-particle distribution functions $N_i$, which describe the number of particles at a lattice node $\boldsymbol{x}$ at time $t$ with velocity $\boldsymbol{c}_i$. In numerical simulations, only a finite set of $\boldsymbol{c}_i$ is possible; the magnitudes and directions of the $\boldsymbol{c}_i$ are such that particles remain on lattice nodes during the discrete time

evolution. The mass density $\rho$, momentum density $\rho u$, and stress $\sigma$, are given by distributions:

$$\rho = \sum_i N_i \ , \qquad \rho u = \sum_i N_i c_i \ , \qquad \sigma = \sum_i N_i c_i c_i \ . \tag{4.2}$$

The equation describing the dynamics of these distributions is:

$$N_i(x + c_i, t+1) = N_i(x,t) - \frac{1}{\tau}(N_i(x_i,t) - N_i^{(eq)}(x_i,t)) \quad , \tag{4.3}$$

where $N_i^{(eq)}$ is the pseudo-equilibrium distribution function and $\tau$ is the relaxation time for convergence, which is related to the fluid kinematic viscosity $\nu$.

In simulations, the lattice (coarse grid) is set such that the fluid-filled interparticle space is represented with the numerical values of one, whilst the intraparticle space is represented with the zero value. Fluid properties, i.e. viscosity, density and an arbitrary pressure drop (to produce a net flow in the direction of superficial flow) are supplied as the input parameters. The model by Warren [59] is based on a 3D cubic lattice. It takes into account the rest particle state, six links with the nearest neighbours and eight links with the next nearest neighbours. Periodic boundary conditions with bounce back on the solid nodes were used. Flow was achieved by imposing a pressure drop between the two extreme faces perpendicular to the direction of superficial flow (here the Z-direction), which are far from the fibre lattice-channel arrangement. The simulation was performed for Stokes flow, and the $N_i$ ($x$,t) were allowed to equilibriate for 25000 iterations, which ensured steady state conditions were reached. Full details regarding the simulation procedure are given in Manz *et al.* (1999b) [60]. For comparisons with the MRI experiments, the solutions for the velocities based on an arbitrary pressure drop were normalised in relation to the actual experimental flowrates used.

The experimental data are also compared with the numerical solutions for flow obtained by using a BEM, which belongs to the class of continuum models. In BEM models, only the fluid and the particle surfaces within the porous system are required to be discretised.

This renders boundary element methods advantageous when studying complex porous systems, in comparison to the methods in which the discretisation must be done on the entire fluid domain (i.e. as in the finite element method (FEM)).

In the flow analysis using the BEM, conservation equations for mass and momentum for the Stokes flow are recast in the form of a system of integral equations. For 2D flow problem studied here, the fundamental solutions to the Stokes equations for the velocities and tractions are given by Brebbia [61]. By using the BEM, the two dimensional geometry of the boundary of the flow domain and the boundary of each fibre is reduced to one. Hence, the boundary surface of the fibres is represented by a circle with a number of points (nodes).

To completely describe the problem, either the traction or the velocity boundary condition has to be prescribed at each of the node points. Thus, in order to determine the unique solution for the domain under consideration (the fibre lattice and the open channel arrangement), the no-slip velocity boundary conditions at the solid-fluid interface (the fibre surface and the walls of the Hele-Shaw cell) were specified. For the purposes of comparison in this study, an available BEM code existing in the literature [34] which considered the cross section of the cylinders of infinite length was used for the estimation of the average (with respect to the gap of the Hele-Shaw cell) local channel and fibre lattice velocities.

Once the fundamental solutions for the displacement and traction vectors at the boundaries are known, an equation, singular at the boundary points, named the Somigliana's identity (for more details refer to [61]) is used to obtain the displacements at any internal point in the fluid.

The actual physical geometry is then mapped onto a computational geometry that approximates the physical geometry using Lagrangian shape functions. The boundary integral element is evaluated at the collocation centre of each element and using the mapping to the computational element, a set of equations relating the unknown velocities

and tractions for each element is generated. An arbitrary (but constant) pressure drop across the lattice-channel arrangement in the flow direction was assumed, enabling the Stokes equations to be solved (see Fig.(4.13)) The velocities and tractions were then obtained at the boundary and the fluid domains. For comparisons with the MRI velocimetry data, the solutions for the velocities were normalised in relation to the actual flowrates used in the experiments.

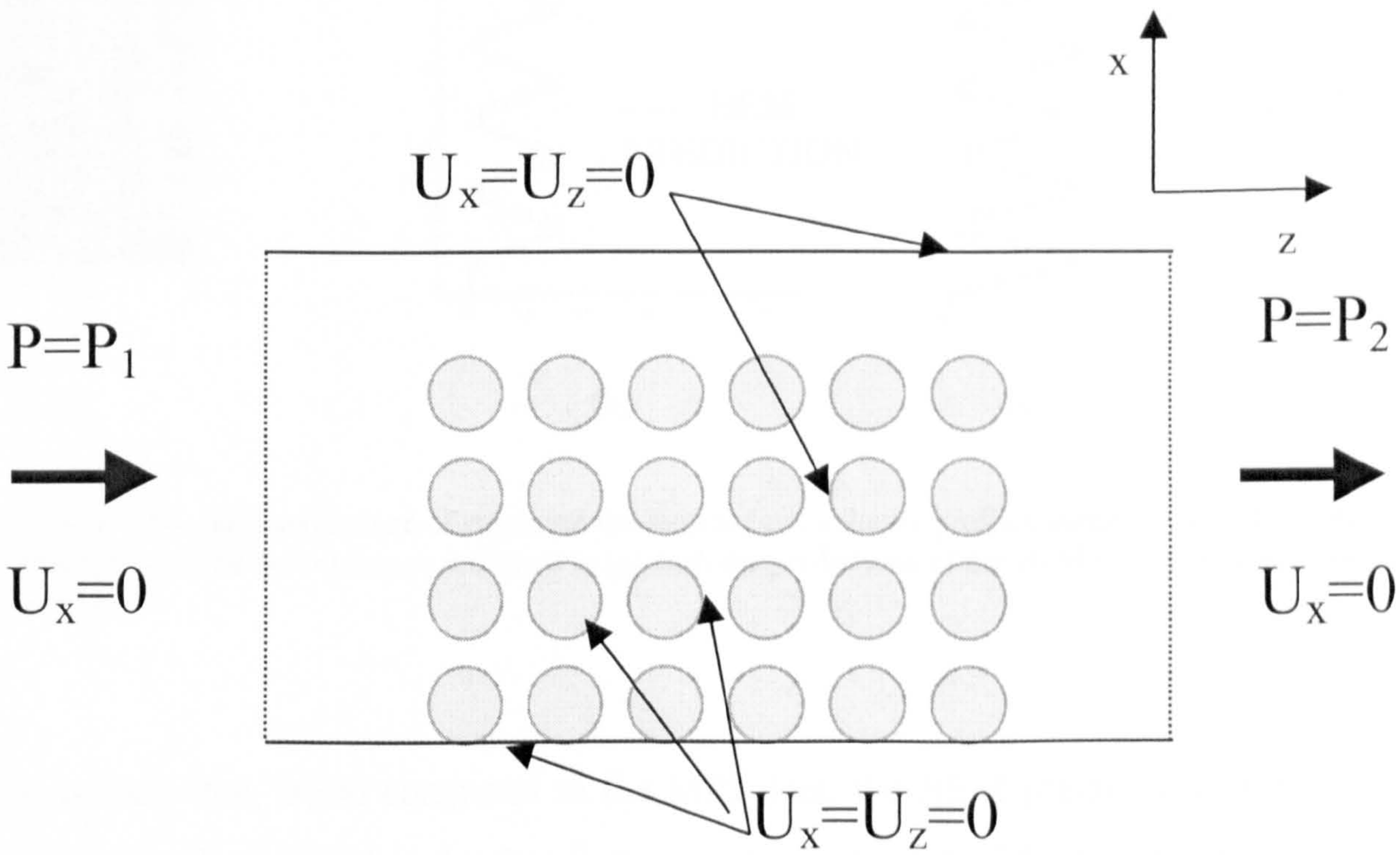


**Figure 4.13:** Numerical analysis using BEM in a cross section of the square fibre lattice. The no-slip velocity boundary conditions are imposed at the surface of the cylinders and the walls of the cell (marked as the solid lines). An arbitrary pressure drop is applied across the lattice-channel arrangement at lines marked as the dashed lines and the flow distribution at every point in the flow domain is calculated.

The comparison of the MRI data with the predictions of numerical models is commenced by analysing the local aspects of flow along the lines passing through the mid-points between the cylinder columns and the corresponding part of the free flow region. A typical example of such a comparative study is given in Fig.(4.14a,b,c). The figure presents the velocity profile along the dotted line through the lattice-channel arrangement

in the cell II, as marked in Fig.(4.14a). MRI data versus BEM and LBM predictions are shown in Fig.(4.14b) and Fig.(4.14c).

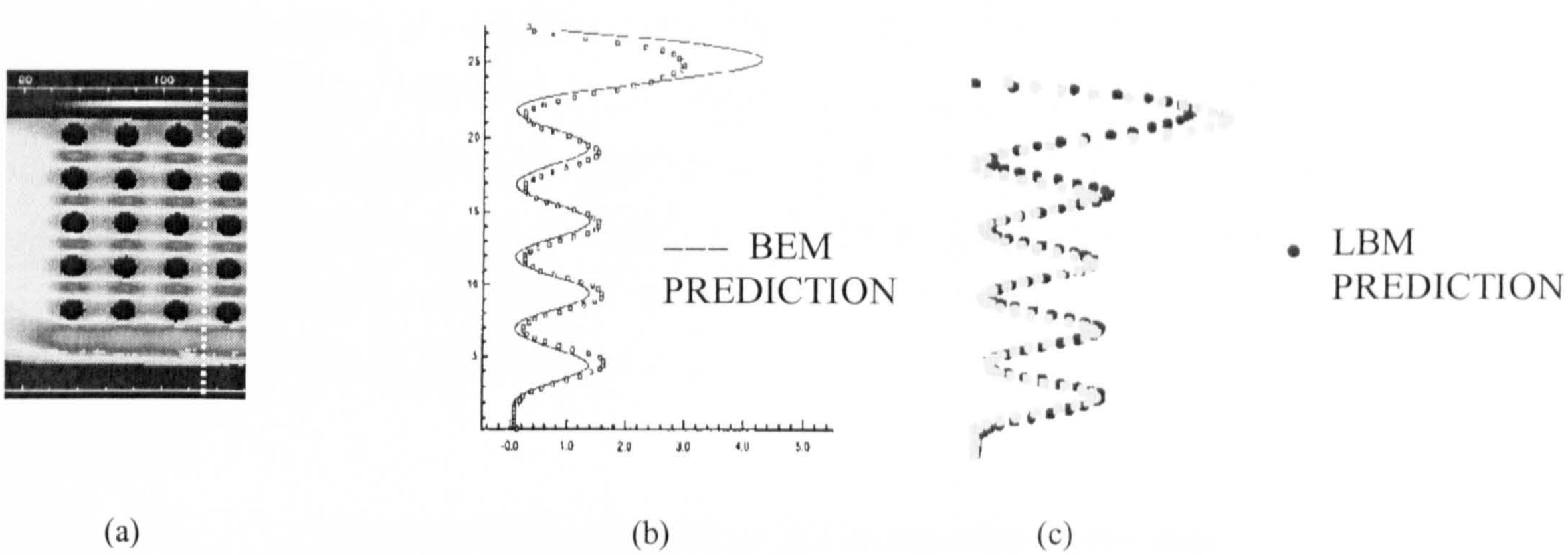


**Figure 4.14a,b,c** Comparison of experimental longitudinal velocity profiles along the line of constant *z*-values (the white dotted line as indicated in (a) with the predictions of the BEM (b) and LBM (c) along the same lines.

It is clear that, when compared to the MRI data, the BEM predictions overpredict the longitudinal velocities in the free flow region, on account of the lower velocity values in the lattice. As previously mentioned, the available BEM code was written to predict the average velocities across the cross section of the cylinders (perpendicular to the flow direction i.e. in the Y direction) of infinite length. In the real system studied the cylinders are of finite length, which, as the comparison confirms, makes the porous system essentially different. The decrease in the gap thickness in the Y direction of the lattice–channel arrangement leads to an increase in the flow through the lattice, in comparison to the flow in the free flow region. When the gap thickness has a finite value, an additional contribution to the total pressure drop across the lattice-channel arrangement arises from the velocity gradients along the Y direction. This contribution is, in relative terms, more pronounced in the lattice than in the free flow region, which results in the enhanced flow through the lattice, as evidenced in the experiment. On the other side, the agreement with

the lattice-Boltzmann model predictions, in which the gap thickness in the Y direction was set to the actual experimental value (3.3mm), is good, as confirmed in Fig.(4.14c). For this reason, for further comparisons with the MRI velocimetry data, only the lattice-Boltzmann model was used.

The characteristics of the global flow fields in the fibre lattice region and the free flow region are also analysed. As indicated in Fig.(4.15), the analysis is done by comparing the volumetric fraction of flow through the fibre lattice (F(latt)) to the overall flow through the lattice and the free region (F(tot) =F(latt)+F(free region)) in the experiment and the model. The interface between the two regions was the line connecting the tops of the cylinders comprising the interfacial row.

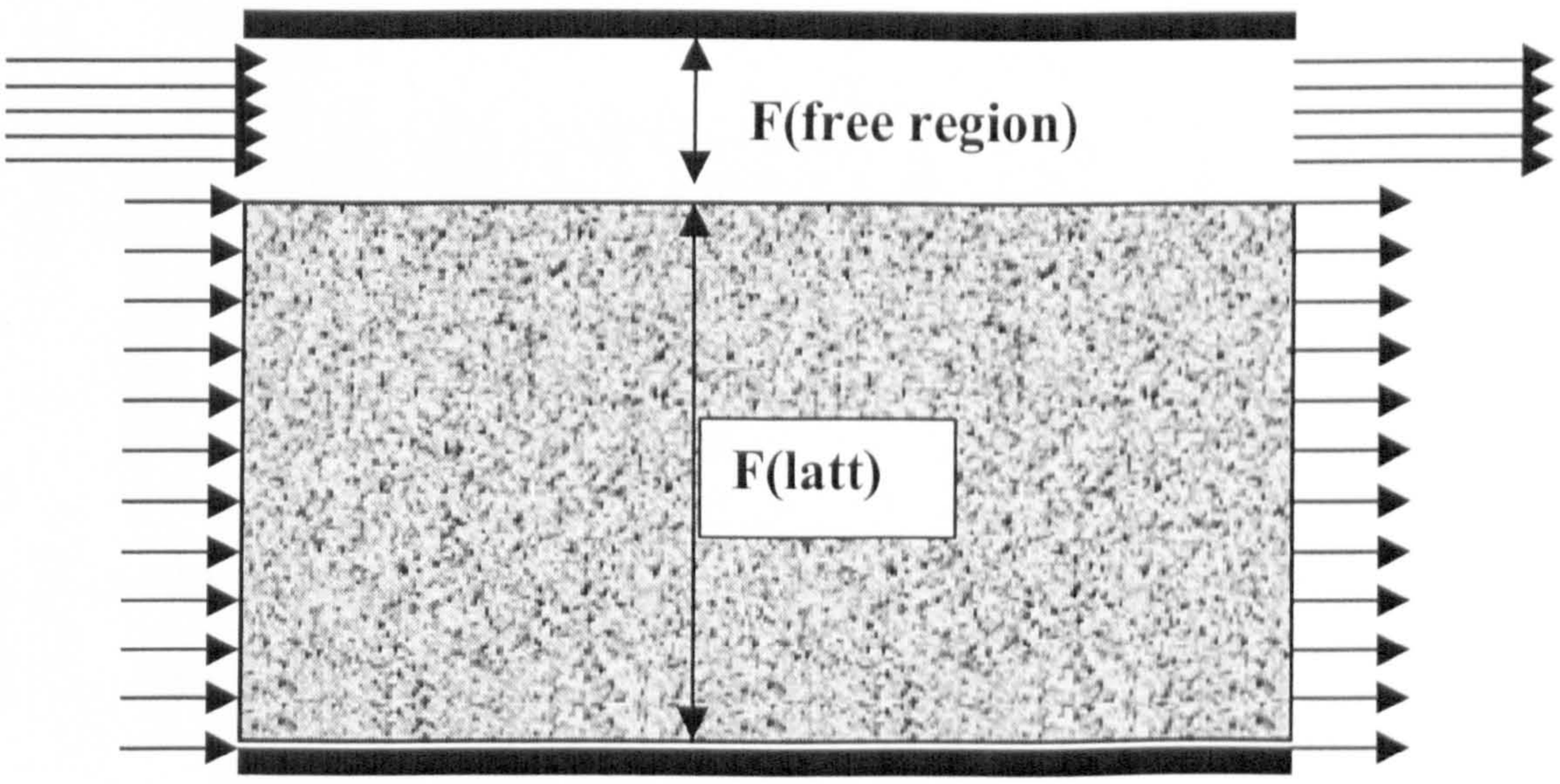


**Figure 4.15** Description of the analysis of the global flow fields in the fibre lattice region and the free flow region. Volumetric flowrates F(latt) and F(free region) are calculated in each region from the experiments and the LB model and subsequently compared.

One such flow comparison for a macroscopically rectangular fibre lattice with the square unit cell and the adjacent free flow region (the cell II) is presented in Fig.(4.16). The MRI data are represented by the dotted line, whereas the lattice-Boltzmann model predictions

are shown as the solid line. Note that the experimental curve collapses shortly after passing the symmetry axis in the cell II, which occurs at the boundary of the experimental field of view. It is reiterated here that the other part of the cell was not studied due to the anticipated flow symmetry in the creeping flow regime. The symmetry of the flow field in the examined cell is confirmed by the symmetrical solid line curve obtained in the lattice-Boltzmann model, but will also be experimentally proved in Chapter 5 with the studies of creeping flow across macroscopically semi-circular fibre lattices and variable width free flow region.

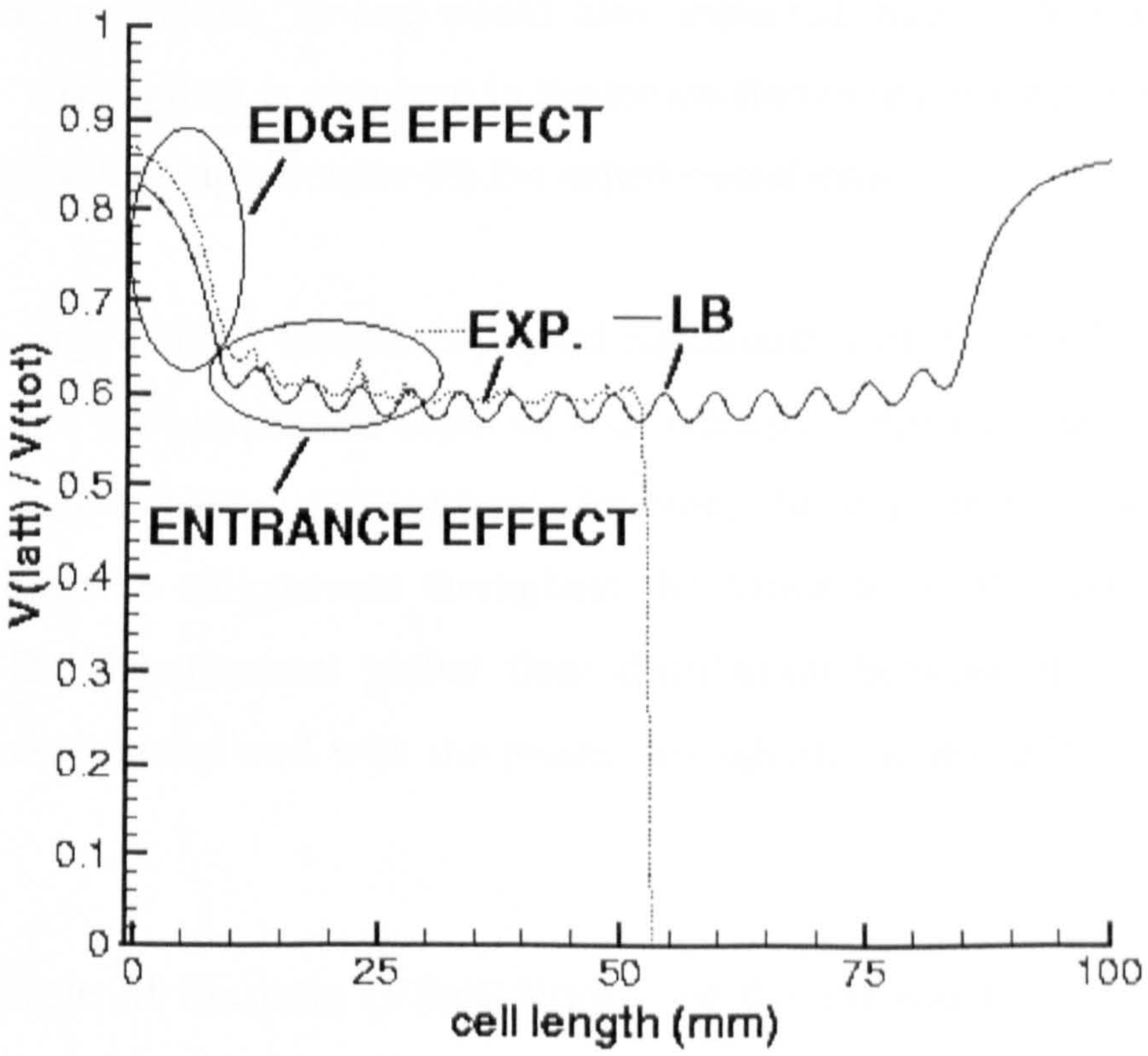


**Figure 4.16** Comparison between volumetric fractions of flow through the fibre lattice (V(latt)) to the overall flow through the lattice and the free region (V(tot) =V(latt)+V(free region)) in the cell II. The experimental data are presented as the dotted line, whereas the lattice-Boltzmann model predictions are shown as the solid line.

In Fig.(4.16) the parts of the free flow regions which are immediately ahead of, or immediately behind, the lattice-channel arrangement are positioned at the far left and the

far right in the abscissa respectively. It is emphasised that these parts are in the lattice exterior and include the regions in which fluid enters (or exits) the lattice-channel arrangement. As previously pointed out in Fig.((4.8b) for the cell II (or for the cells I and III in Fig.((4.5b) and Fig.((4.11b) respectively), at the edge of the fibre lattices a rearrangement of fluid velocities was observed, which was manifested in substantial transverse velocities.

The effect of transverse velocities at the edge of the lattice to the ratio of the volumetric flowrates through the fibre lattice and the free flow region (V(latt)/V(tot)) is marked in the far left part of Fig.(4.16). There is a gradual, rather than a sudden decline in values for the flow ratio examined, as one would have expected, had it not been for the 'edge' effect. The 'edge' effect is also seen in the lattice-Boltzmann predictions and its extent is in a reasonably good agreement with the experimental data.

As seen in Fig.(4.16), a remarkably good agreement with the model is found on the magnitude and the penetration depth of the 'entrance' effect in the region where flow enters the lattice-channel arrangement. In both, the experiment and the model, the 'entrance' effect is still present throughout the lattice up to the fourth column of the cylinders. The experimental global flow distribution between the two flow regions compare exceptionally well with the model throughout the rest of the examined part of the lattice.

The comparison of the ratio (V(latt)/V(tot)) for the macroscopically rectangular fibre lattice with a hexagonal unit cell arrangement is presented in Fig.(4.17). The extent of the 'edge' effect compares favourably with the model. Although the magnitudes of 'the entrance' effect throughout the cell differ, the penetration depths are, as in the cell II, present up to the fourth column of cylinders in both the experiment and the model. Therefore, the 'edge' effect and the 'entrance/exit' effect at the edge and the corner of the fibre lattices are intrinsic characteristics of the coupled flow in a fibrous porous medium and an adjacent free flow region.

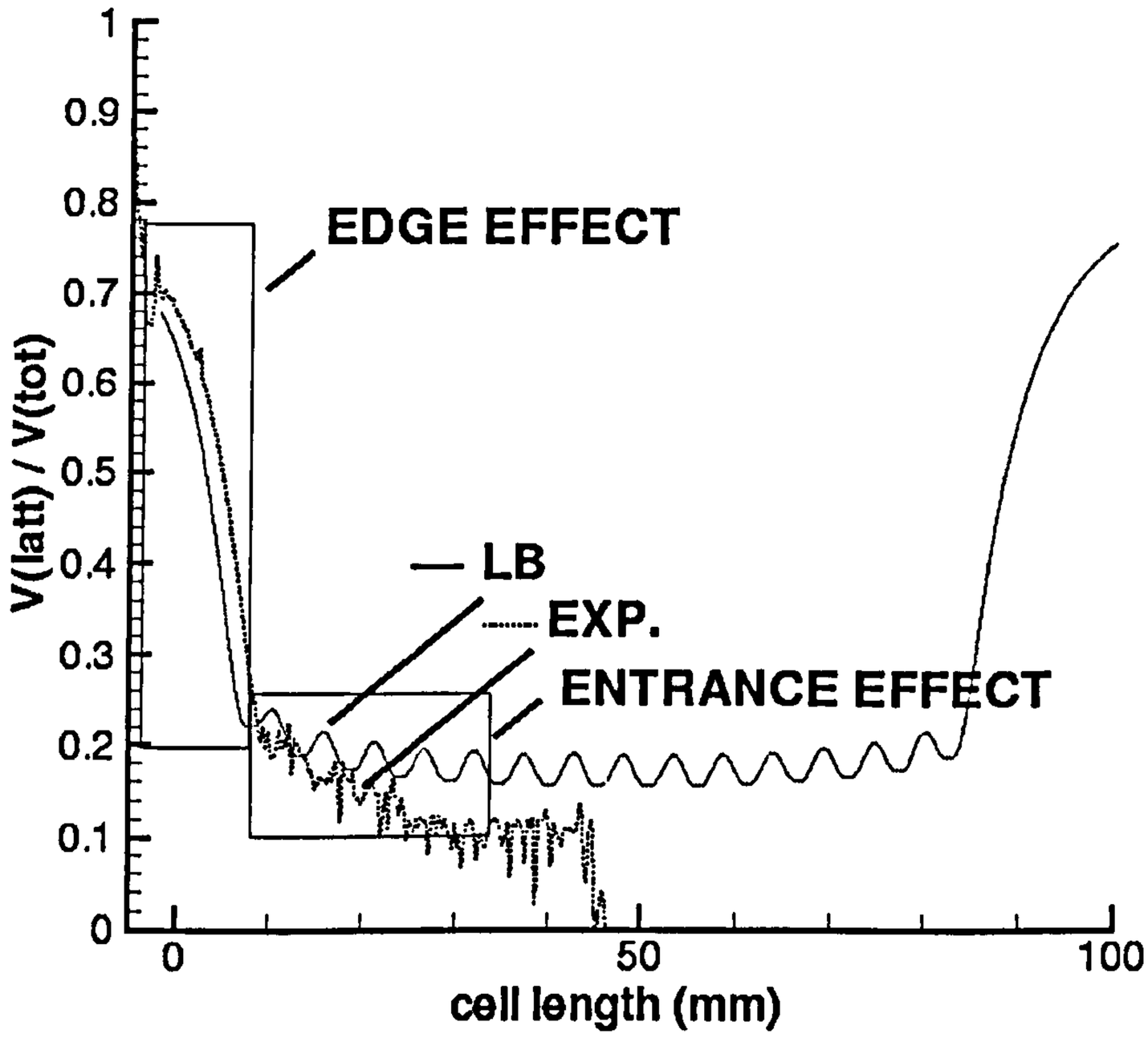


**Figure 4.17** Comparison between volumetric fractions of flow through the fibre lattice (V(latt)) to the overall flow through the lattice and the free region (V(tot) =V(latt)+V(free region)) in the cell III. The experimental data are presented as the dotted line whereas the lattice-Boltzmann model predictions are shown as the solid line.

## *4.5 Conclusions*

MRI velocimetry has been used to describe and assess the interrelation of macroscopic and local aspects of steady state slow flow fields across macroscopically rectangular fibrous porous media coupled with neighbouring free flow. This technique provides non-invasive, spatially resolved quantitative velocity measurements. From the distributions of the velocities observed it is seen that all longitudinal velocity component maps, i.e. the component in the direction of the superficial flow, have only positive values which yields

the conclusion that, for the low Reynolds number investigated, back-mixing is non-existent in the system. These results corroborated experimental findings from [39]. Within the fibre lattices no recirculation zones are present between the cylinders in the flow direction. The transverse velocity maps give a superior insight into the flow fields in the exterior and the interior of the fibre lattices. The ratio of maximum open channel velocity to maximum fibre lattice velocity decreases with increased porosity of the fibre lattices. It is observed that the disturbance to flow from the fibre lattice on the open channel flow extends to a length that is less than one cylinder diameter. The influence of the channel flow on the flow in the fibre lattice extends only to a distance of a half of one unit cell. These conclusions are consistent with references [33,41,42] since the size of cylinders is of the order of the gap thickness of the investigated Hele-Shaw cell. Regions with regular patterns of very low fluid velocities are identified throughout the fibre lattices.

In the parts of the free flow regions in which fluid enters (or exits) the lattice-channel arrangement a significant, but gradual rearrangement in fluid velocities is observed experimentally and confirmed by the lattice-Boltzmann model. This effect is termed 'edge' effect. Within the fibre lattices, local flow enhancements are observed at the corners of the lattices and termed 'entrance/exit' effects. They are a result of the additional velocity gradients, caused by the proximity of the macroscopic flow rearrangements in the entrance/exit region of the lattice-channel arrangements. The 'entrance/exit' effects are experimentally shown to depend on the channel width, the fibre lattice porosity and the fibre diameter. A good agreement with the lattice-Boltzmann model is found on the magnitude and the penetration depth of the 'entrance' effect.

Hence, the two effects, namely 'edge' effect and 'entrance/exit' effects have been established as the local phenomena of critical importance for an accurate description of creeping flow in fibrous media of dual porosity. The extent of both phenomena has been fully quantified experimentally, and independently confirmed by the predictions of the lattice-Boltzmann model. The available boundary element code, by providing a solution for the average velocities for the infinite-length lattice-channel arrangements in the gap

direction (unbounded flow), made it possible to clearly differentiate between these solutions and the experimental data and the solutions for flow across the finite-length lattice-channel arrangements in the gap direction (bounded flow).

# Chapter 5

# Slow Flow Across Macroscopically Semi-Circular Fibre Lattices and a Variable Width Free Flow Region

Viscous flow of an incompressible Newtonian fluid across aligned rows of cylinders (fibre lattices) bounded by a free flow region has been studied experimentally by Magnetic Resonance Imaging (MRI) velocimetry. The model systems for heterogeneous fibrous media of dual porosity were, as in the study of the macroscopically rectangular fibre lattices, formed by circular cylindrical rods and confined inside a Hele-Shaw cell. However, this part of the comparative flow study deals with the fibre lattices macroscopically arranged in a semi-circular fashion and adjacent to a variable width free flow region. As a result, they are likely to have different flow features. The experiments were focused on the local aspects of flow in the interior of and exterior to the fibre arrays for (i) three individual semi-circular fibre lattices, each bounded by an open channel and (ii) an assembly of five fibre lattices with the interstitial space between them forming a free flow region. All the lattices examined have a square unit cell. The parameters varied in the study of the first three individual fibre lattices were: a) the fibre lattice volume fraction and b) the size of the cylinders / the gap between the cylinders for the same fibre lattice volume fraction. The impact that the presence of neighbouring fibre lattices may have on local flow features of coupled free flow and porous medium flow has been studied on a model system consisting of the five fibre lattices and a variable but controlled width of the free flow region.

## *5.1 Materials and Methods*

The specifications of the experimental set up, the Hele-Shaw cell design and the MRI experimental runs are described in Sections (4.1) and (4.2).

## *5.2 Results and Discussion*

The general idea was to determine the flow distribution in a macroscopically semi-circular fibre lattice or a fibre lattice assembly and a free flow region of variable width, in order to assess possible interrelations between the flows in the two regions. Specifically, the influence of the macroscopic shape of fibre lattices, the fibre packing densities and the number of fibres for the same lattice porosity on the flow field in the lattice-channel arrangement placed in the Hele-Shaw cell has been studied. For this purpose, the configurations depicted in Fig.(5.1) were examined. These are: (IV), a semi-circular lattice of cylinders with porosity ε (ε=1-ϕ, where ϕ is the fibre volume fraction in the arrays) of 50% and the fibre diameter D=4mm, (V), a semi-circular lattice of cylinders with porosity of 70% and the fibre diameter D=3mm, and (VI), a semi-circular lattice of cylinders with the same porosity of 50% as the cell IV but with an increased number of cylinders of smaller diameter D=2mm. All the lattices have a square unit cell. The characteristic parameters of each cell are the diameters of the fibres (D), the distance between the fibres (g), the widths of the open channel (W1-W6) and the small gap between the wall and the first row of the fibres (h). The cross-wise and stream-wise pitch to diameter ratios are set to be equal i.e. the row separations are equal to the spacing of neighbouring fibres for all lattices.

The effect of neighbouring fibre lattices on local aspects of coupled free flow and flow in a fibrous porous medium is studied on the fibre lattice assembly (the cell VII).

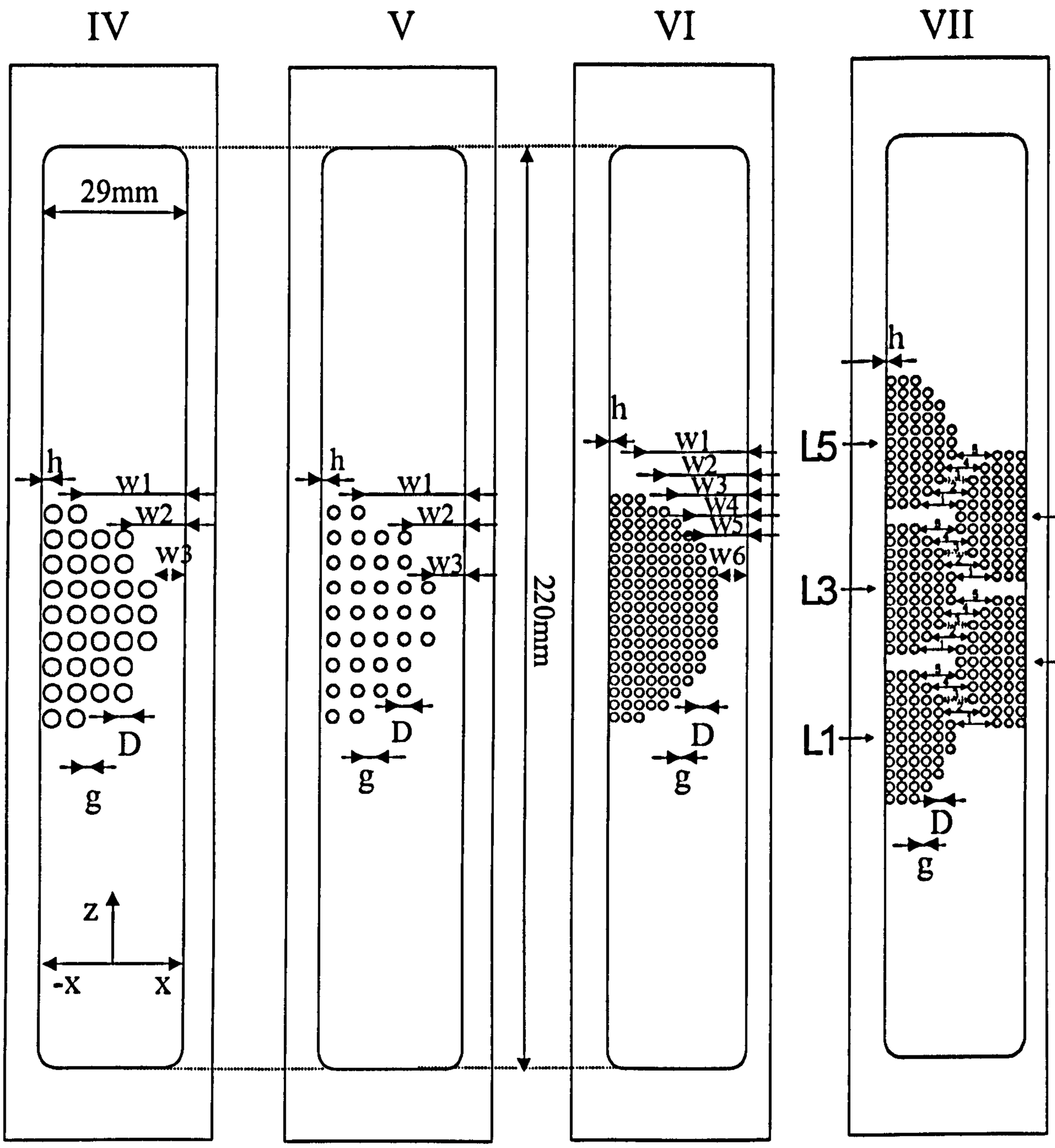


**Figure 5.1** The macroscopically semi-circular fibre array configurations used in the MRI experiments: cell IV –square unit cell lattice D=4mm, g=1mm, W1=20mm, W2=10mm, W3=5mm, h=0.3mm, ε=0.5; cell V - square unit cell lattice D=3mm, g=2mm, W1=21mm, W2=11mm, W3=6mm, h=0.3mm, ε=0.7; cell VI - square unit cell lattice D=2mm, g=0.5mm, W1=21.5mm, W2=16.5mm, W3=14mm, W4=11.5mm, W5=9 mm, W6=6.5mm, h=0.3mm, ε=0.5. Cell VII – the assembly of macroscopically semi-circular square unit cell lattices denoted as L1-L5 and arranged in hexagonal order, each with D=2mm, g=0.5mm, h=0.3mm, ε=0.5; the widths of the free flow region between the lattices marked with the solid lines and denoted as 1,2,4,and 5 are 6.7 mm whereas the widths of the free flow region between the lattices marked with the dashed lines and denoted as 3 are 4.2mm. Coordinate axis Y is perpendicular to the direction of flow (Z axis) and the in-plane of the cell (X axis).

In the cell (VII), the five fibre lattices are arranged in a hexagonal order. The porosity of each lattice was kept constant (ε=50%). The widths of the open channel between the lattices are designed to allow for the flow contraction in the free flow region at the places marked with the dashed lines and denoted as 3 in the cell which is the far right in Fig.(5.1). Hence, although the free flow region is of variable width as in the single-lattice-channel arrangements, its geometry is affected by the surface irregularities of the neighbouring lattices.

The unit cells in all fibre lattices have a square configuration with the interstitial porosity ($\varepsilon_{sq}$) obtained from:

$$\varepsilon_{sq} = 1 - \frac{\pi D^2}{4(g+D)^2}, \qquad (5.1)$$

The steady-state fluid velocity components were detected in the direction of superficial flow ($V_z$) and in the plane of the Hele-Shaw cell, perpendicular to the superficial flow ($V_x$). All experimental values shown are for velocities averaged across the gap in the Y direction, i.e. the thickness of the cell. The values for $V_z$ range from zero on the walls and the surface of cylinders ('no-slip') to a maximum value occurring in the open channel. The values for the $V_x$ velocity range from negative to positive, depending on the flow direction along the X axis. The values for the fluid velocities at each pixel are obtained from the MRI data.

### *5.2.1 Local Aspects of Coupled Free Flow and Flow in a Macroscopically Semi-Circular Fibrous Porous Medium*

The local features of coupled free flow and flow in a macroscopically semi-circular fibre lattice are presented as contour plots for the velocity components in the Z (Fig.(5.2a)) and the X (Fig.(5.2b)) directions for the Hele-Shaw cell IV.

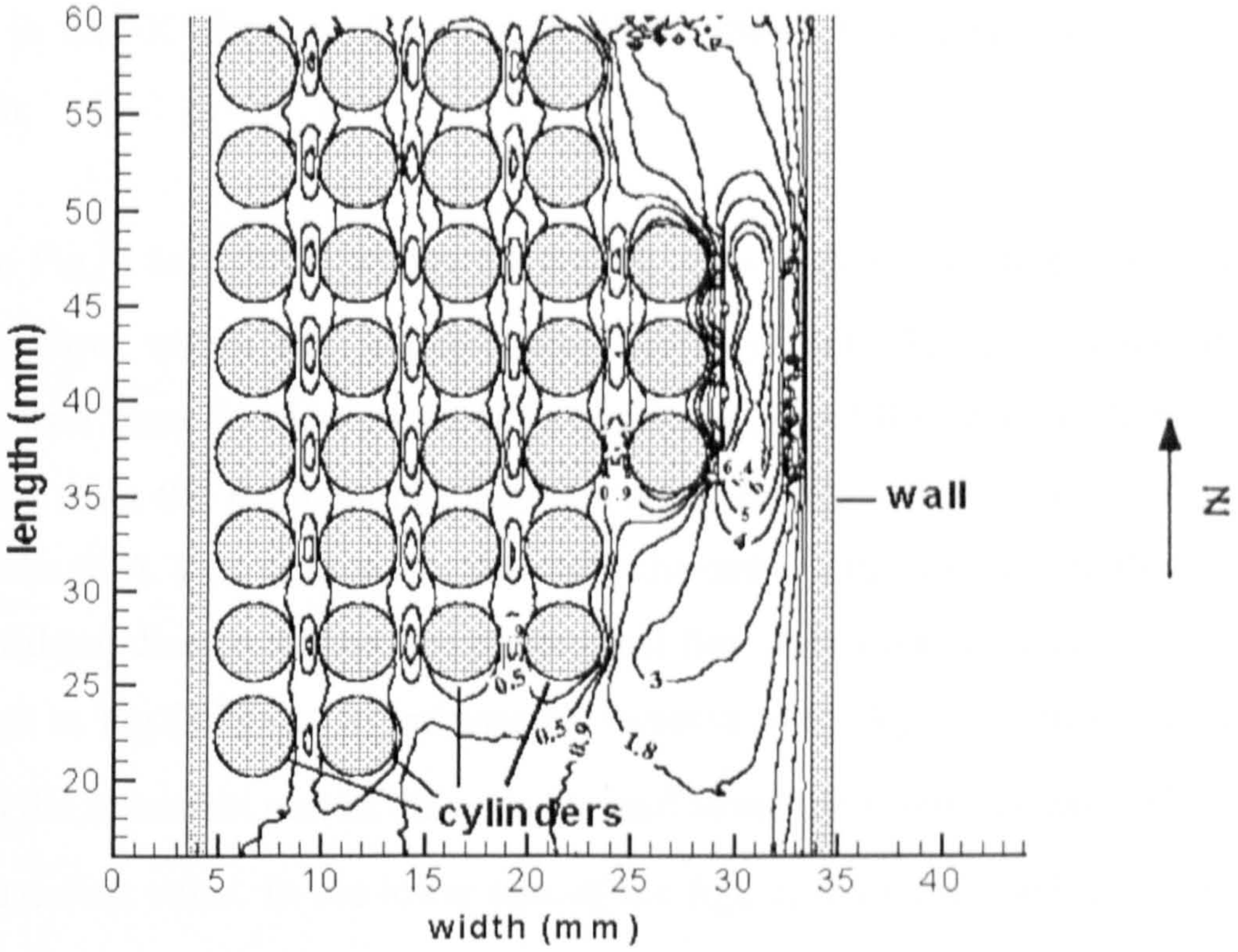


**Figure 5.2a** Contour velocity map for the velocity component in the flow direction ($V_z$) of the cell IV.

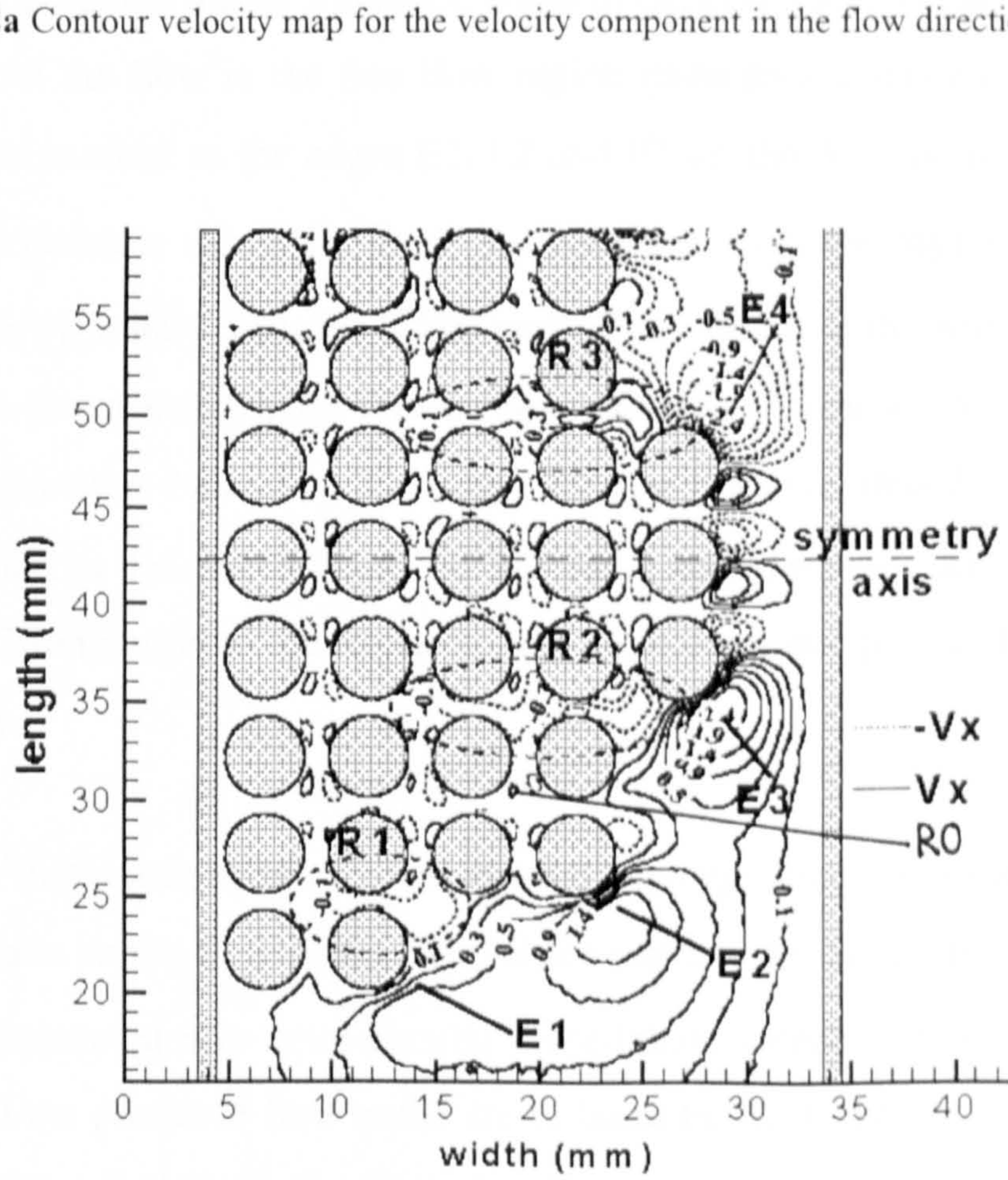


**Figure 5.2b** Contour velocity map for the velocity component perpendicular to the flow direction ($V_x$) in the cell IV.

The cross section of the cylinders is shown in grey colour. The values on the contour lines are in mm/s. In Fig.(5.2b), contours corresponding to negative velocities (the velocities in the -X direction from Fig.(5.1)) are drawn as dotted lines for ease of recognition.

As seen in Fig.(5.2a), all the values for the $V_z$ velocities are positive indicating no backwards flow within the lattice-channel arrangement. These findings are in agreement with those for flow in the Hele-Shaw cells I and II (recalling Figs.(4.5a,b) and (4.8a,b) from the previous chapter) and some previous flow studies in fibrous porous media [39]. The variation in the open channel width (which initially narrows and then widens) directly defines the preferential flow pathways in the lattice exterior. This is seen in Fig.(5.2a) as an increase or decrease of the $V_z$ velocities towards, or away from the narrowest part of the open channel along the symmetry axis, where $V_z$ takes a maximum value. In the lower part of the figure, the local maxima of the $V_x$ velocities are in the places where the width of the open channel narrows in a step-wise manner and the flow in the free flow region undergoes a sudden contraction. These regions are marked as the edges E1, E2 and E3 on the $V_x$ contour maps (Fig.5.2b). The same absolute values for local $V_x$ velocities as at the edge E3 are on the other side of the symmetry axis (the upper part of the figure) at the edge marked as E4. In this place the open channel widens in a step-wise manner and flow undergoes a sudden expansion. Note that $V_x$ values are now negative, thus describing flow in the –X direction as defined in Fig.(5.1). The same considerations are valid for the edges E1 and E2 in relation to the edges E5 and E6 in the upper part of the cell, not seen in Fig.(5.2b).

The issue that needs to be clarified is what bearing, if any, will these local free flow features have on the flow in the fibre lattice interior. Analysing the $V_z$ velocity maps in the macroscopically semi-circular fibre-lattice interior, it may at first look as though all the preferred flow paths are in lanes between the rows, whereby the fluid between the cylinders (in the flow direction) is almost stagnant. This is exactly the two-dimensional flow field feature found for flow within the fibre lattices of macroscopically rectangular shapes bounded by an open channel region of the

constant width. The only exceptions were in cases where the examined flow was close to the entrance/exit of the lattice-channel arrangement (Chapter 4).

Herein however, within the semi-circular fibre-lattice in the cell IV, the existence of considerable local velocity enhancements (LVE in the further text) is observed, as seen on the $V_x$ velocity maps in Fig.(5.2b). Notably, the enhancements occur in the encircled regions, which are denoted as R1 and R2 in the lower part of the figure, and R3 in the upper part of the figure. What is indicative is that these regions are adjacent to the parts of the open channel regions in the lattice exterior in which the local enhancements of the velocity vector are present, defined as the edges in Fig.(5.2b). In the lower part of the lattice, the local interior velocity enhancements are directed into the lattice (the regions R1 and R2) in the -X direction and hence are characterised by negative velocities, while in the upper part are directed out of the lattice (the region R3) in the X direction and described by positive velocities. It must be pointed out that the directions of $V_x$ velocities in the open channel are opposite to the direction of the local enhancements of $V_x$ velocities within the lattice. This is seen in Fig.(5.2b) (compare $V_x$ velocities at the edges E1, E2 and E3, with $V_x$ velocities in the regions R1 and R2, or $V_x$ velocities at the edge E4 with $V_x$ velocities in the region R3). These findings point to the conclusion that the velocity redistribution within both the fibre lattice and the open channel are subject to 'the least resistance to flow principle'. The additional flow into/out of the lattice originates from the local velocity variations in the free flow region, predominantly at the places where the width of the open channel suddenly varies (contracts or expands). Because of the variations of the open channel width, the fluid exerts an increased (or decreased) stress on the cylinders at the edges of the lattice. This, in turn, results in the formation of the additional local pressure gradients between the fluid in the lattice interior and the fluid at the edges. These additional local pressure gradients are the driving force for flow in the X direction and are countervailing in respect to the symmetry axis of the lattice. The magnitude of the LVE depends on the magnitude of the pressure gradients which are commensurate to the changes in the velocity vector in the free flow region. This reasoning explains lower values for $V_x$ velocities in the region R1 compared to the region R2, as well as the non-existence of the LVE in the X direction along the region

encircled with solid line and denoted R0. This region is adjacent to the part of the flow in the lattice exterior in which there is no change in the open channel width.

Moreover, the distribution of velocities in the flow direction in the semi-circular fibre-lattice interior is in accordance with 'the least resistance to flow' principle. The strong evidence adduced to support this argument is shown in Fig.(5.4). Presented are the $V_z$ velocity profiles along the lines of constant $x$-value in the passages P1-P4 between the cylinder rows in the fibre lattice in the cell IV as indicated in Fig.(5.3).

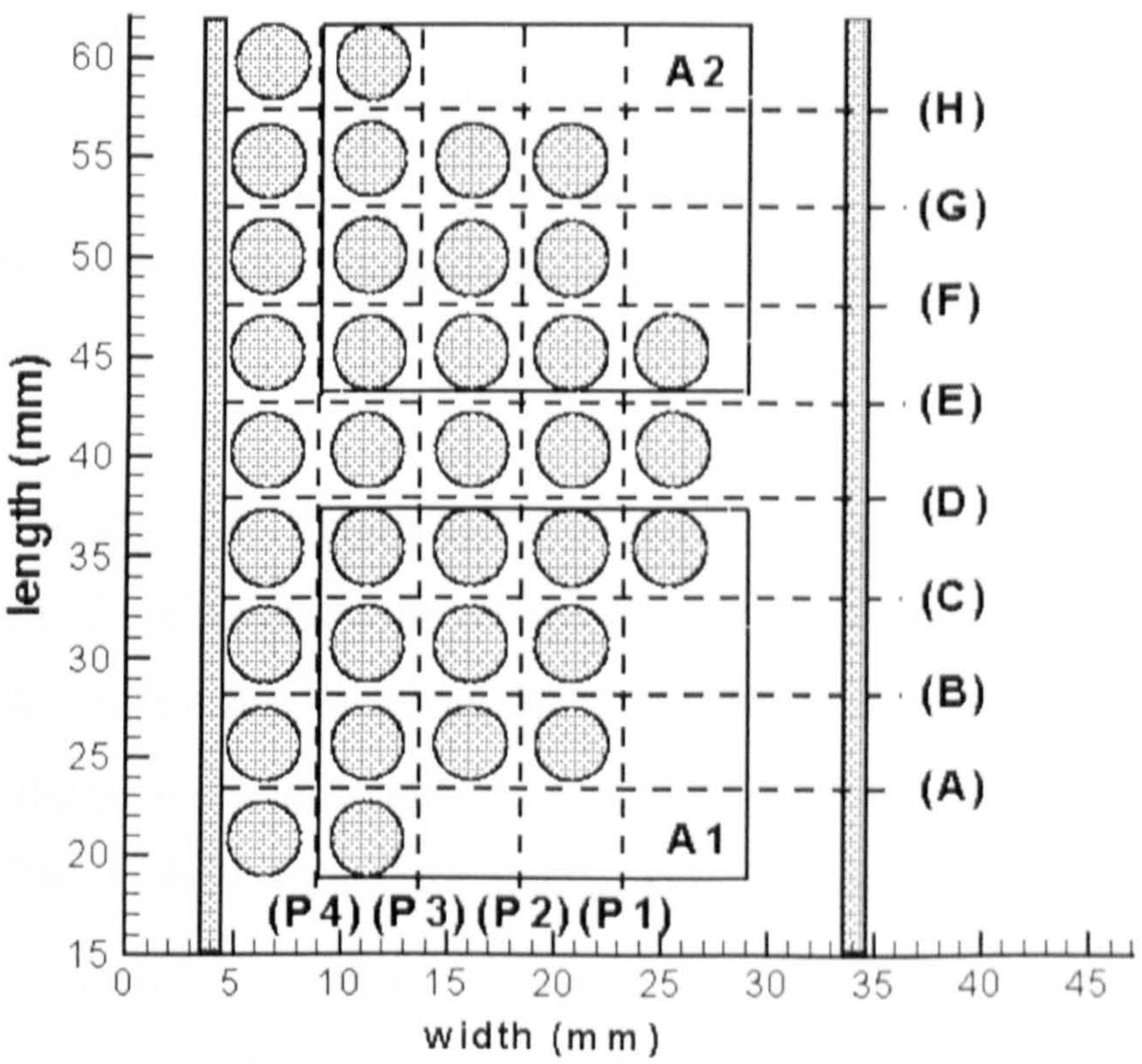


**Figure 5.3** Configuration of the fibre lattice in the cell I indicating the lines of constant $z$-values (A)-(H) and the lines of constant x-values (P1)-(P4) along which the analysis of velocity profiles is done. The symmetrical inserts A1 and A2 are used for the comparisons of the local velocity enhancements in the X direction (see Fig.5.11a,b).

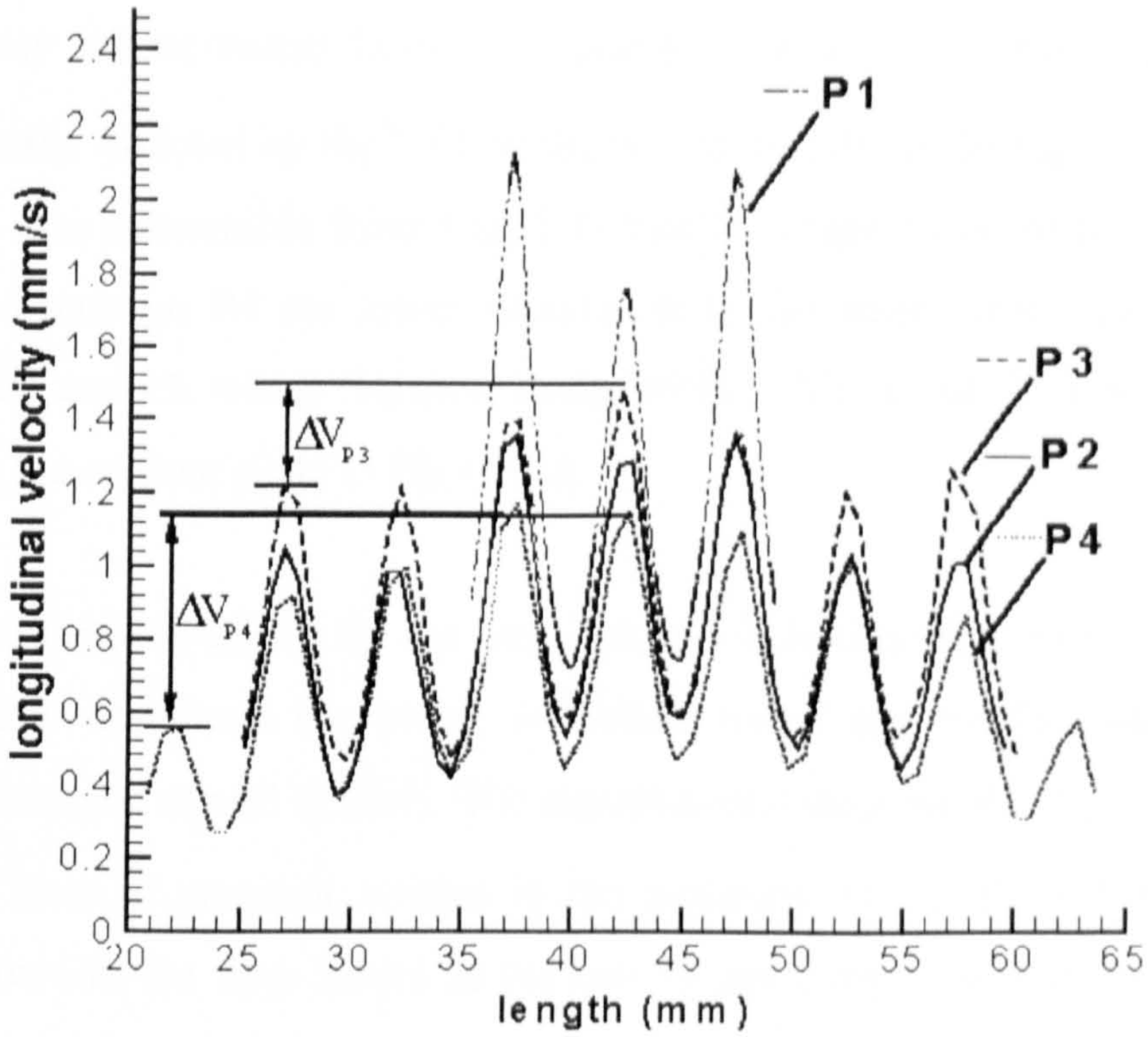


**Figure 5.4** Longitudinal velocity profiles along the lines of constant x-values (P1)-(P4) as indicated in Fig. (5.3).

Recalling Fig.(5.3) or Figs.(5.2a,b) it can be seen that fluid flow undergoes contraction in the places between the cylinders in the X-direction. Hence, these places are characterised by local maxima of $V_z$ velocities and are seen in Fig.(5.4) as a number of the peaks corresponding to each passage P1, P2, P3 and P4, as indicated in Fig.(5.3). The highest values for the $V_z$ velocities within the fibre lattice are in passage P1, which is exposed to the highest $V_z$ velocities from the free flow region. In Fig.(5.4), this is reflected in much higher magnitudes of the three isolated peaks than the peaks in the other three passages P2, P3 and P4. The lowest local maximum $V_z$ velocities in the fibre lattice are in the entering/exiting parts of the lattice (the peaks on the lines P2, P3 and P4 positioned far left and right in the figure). Towards the middle of the lattice, the magnitude of the peaks gradually increases and, towards the lattice exit, it decreases in the same manner. Remarkably, this $V_z$ velocity increase/decrease is dictated by, and is proportional to the magnitudes of the LVE in the X direction, which, from their side, have a cumulative effect. This fact is ascertained by comparing the velocity differences $\Delta V_{P3}$ and $\Delta V_{P4}$ from Fig.(5.4) to the

values $V_X$ of the LVE in the X-direction in the regions R1 and R2 on the contour plots in Fig.(5.2b). Note that the velocity difference $\Delta V_{P3}$ is affected only by the local $V_X$ velocity enhancements from the region R2, whereas the velocity difference $\Delta V_{P4}$ is additionally affected by the LVE in the X direction from the region R1. In the same way, it is also discernible from Fig.(5.4) that the magnitudes of the peaks from the line in the passage P4 are lower in relation to the peaks from the lines from the passages P2 and P3, where the magnitudes of the LVE in the X direction is higher as seen from the contour plots in Fig.(5.2b).

The experimental evidence for the local velocity enhancements within the fibre lattice in both flow directions examined, is further tested against the predictions of the lattice-Boltzmann model (LBM). The experimental data for the $V_z$ velocity profiles along the lines of constant *x*-value in the passages P1-P2, P3 and P4 between the cylinder rows in the fibre lattice in the cell IV are compared with the predictions of LBM along the same lines and shown in Fig.(5.5a), Fig.(5.5b) and Fig.(5.5c) respectively.

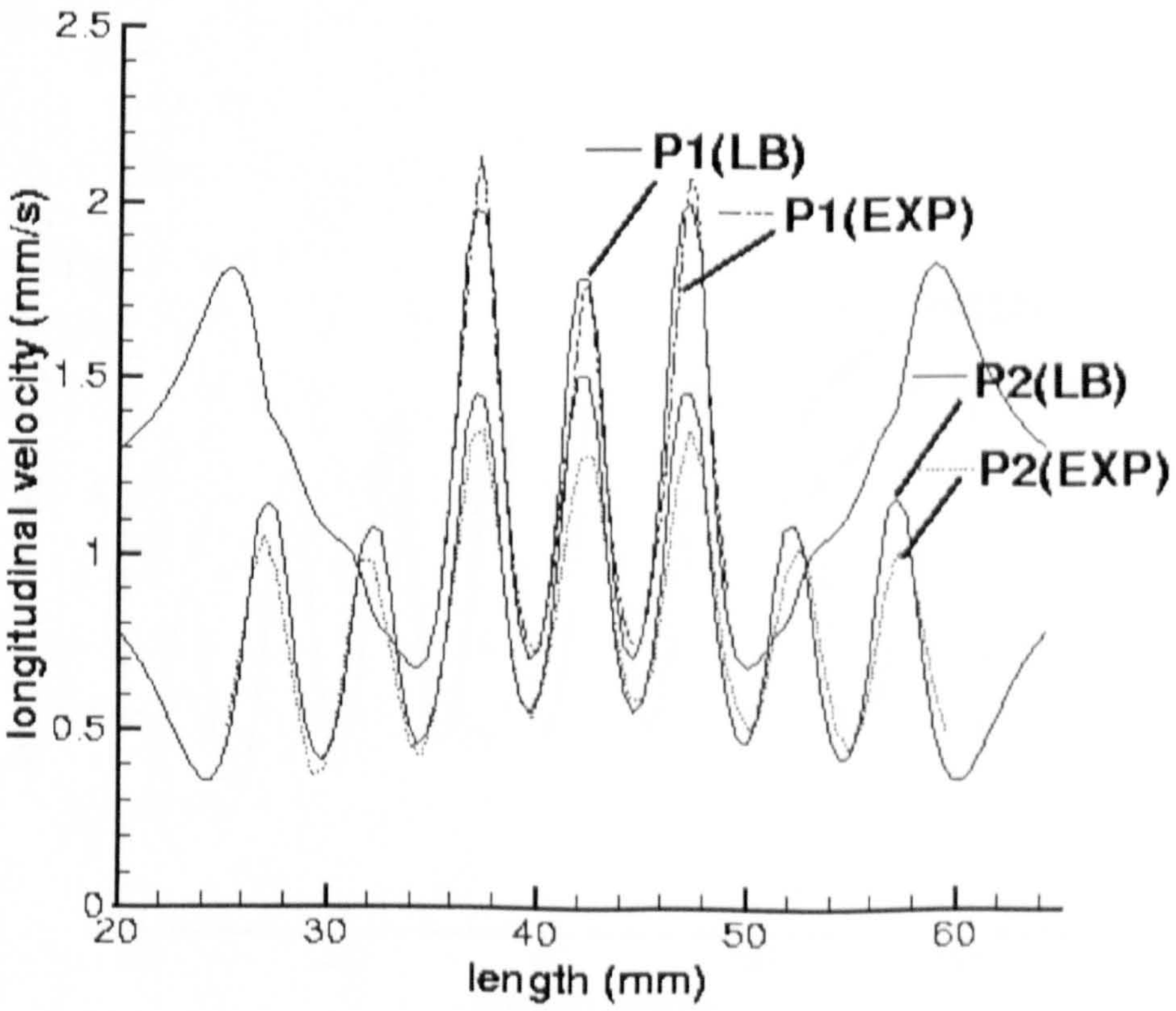


**Figure 5.5a** Comparison of experimental longitudinal velocity profiles along the lines of constant x-values (P1)-(P2) as indicated in Fig. (5.3) with the predictions of LBM along the same lines.

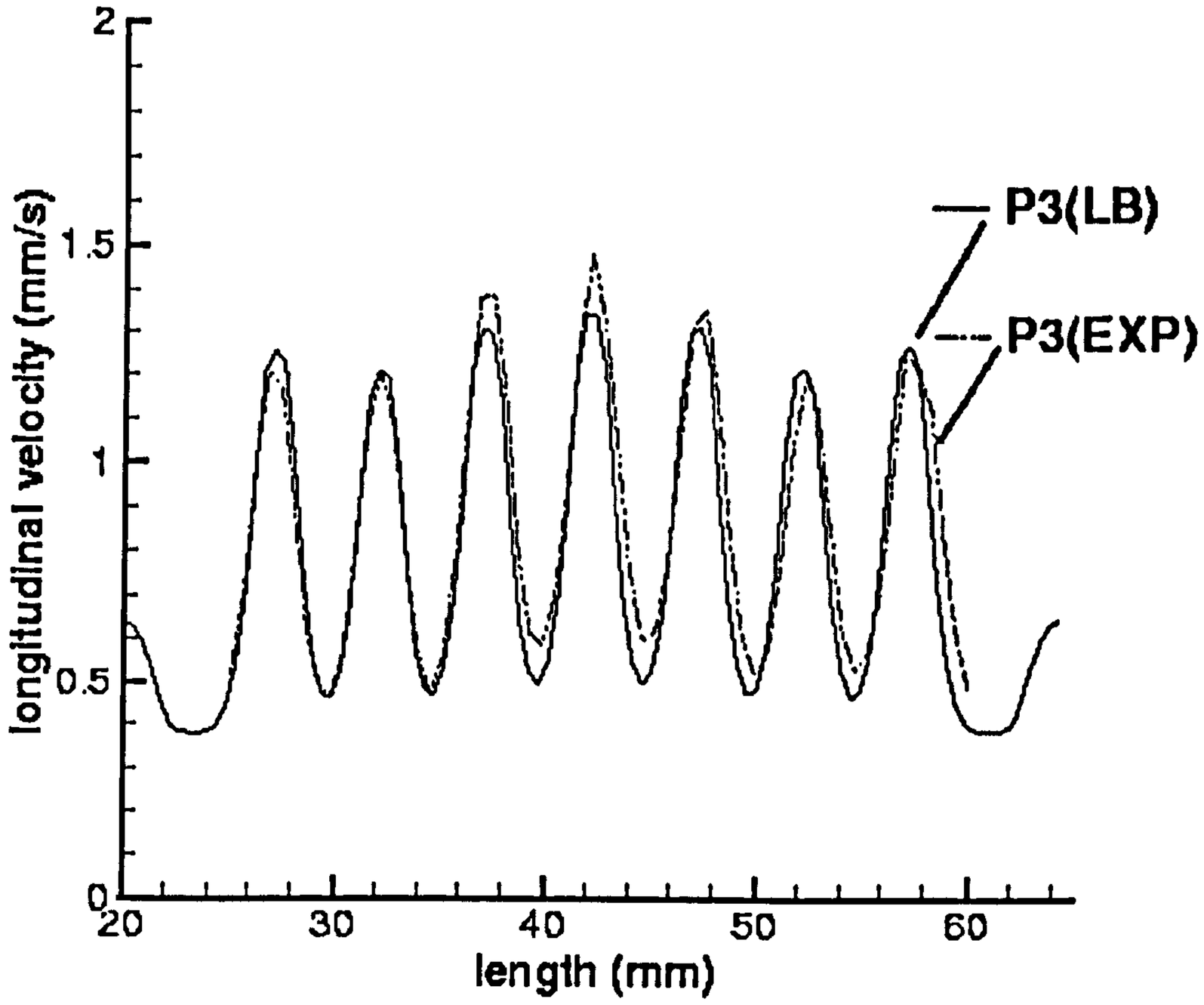


**Figure 5.5b** Comparison of experimental longitudinal velocity profiles along the line of constant x-values (P3) as indicated in Fig. (5.3) with the predictions of LBM along the same line.

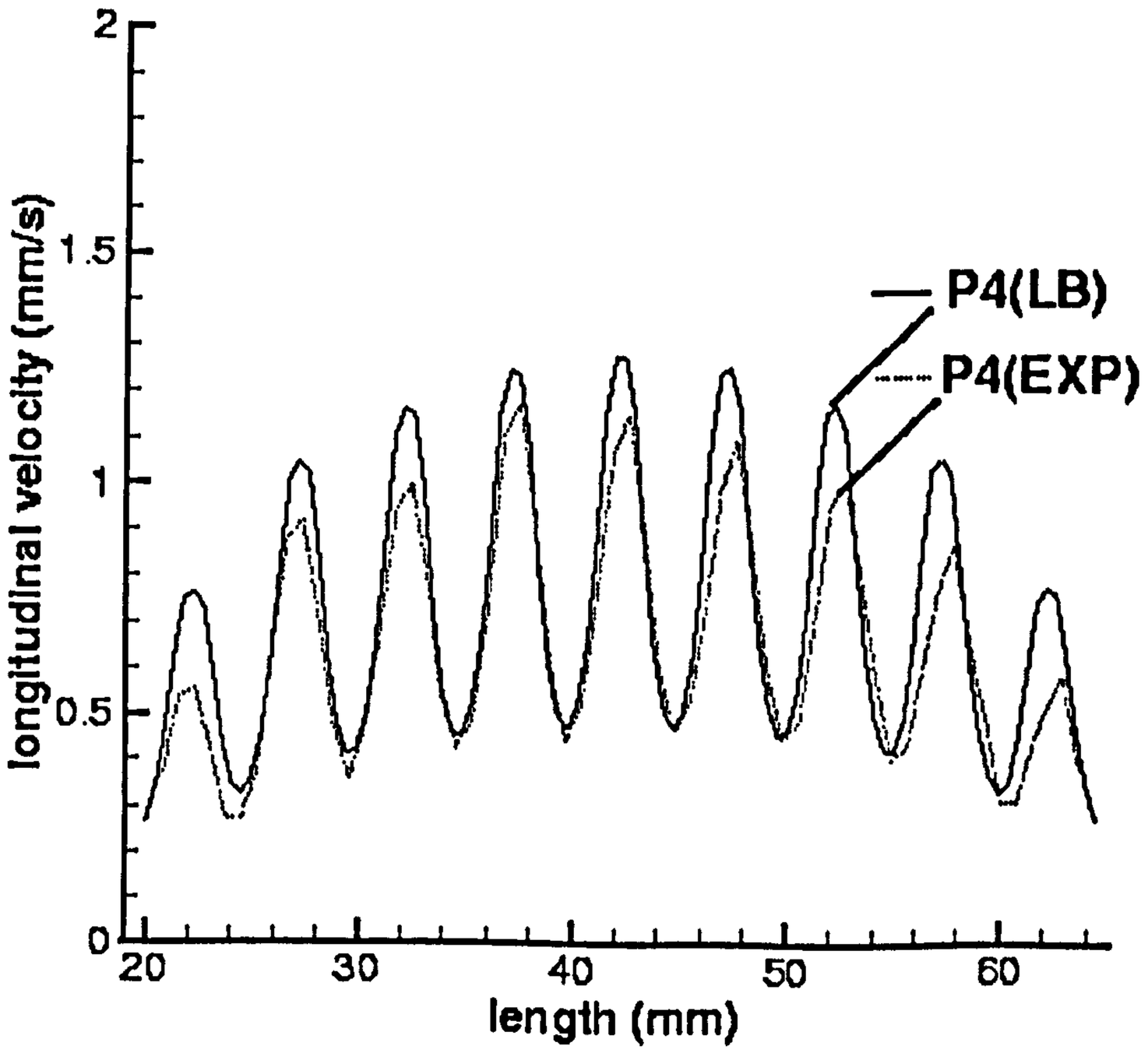


**Figure 5.5c** Comparison of experimental longitudinal velocity profiles along the line of constant x-values (P4) as indicated in Fig. (5.3) with the predictions of LBM along the same line.

It is immediately apparent from Fig.(5.5a) that the Lattice-Boltzmann model accurately predicts the highest values for the $V_z$ velocities within the fibre lattice in the passage P1, which is the nearest to the part of the free flow region with maximum $V_z$ velocities. Furthermore, a good agreement between the model and the experimental data is observed along the lines in the passages P2 in Fig.(5.5a) and P3 in Fig.(5.5b) and P4 in Fig.(5.5c). The sensitivity of the changes in the local flow features within the fibre lattice are best probed in the places between the cylinders in the X-direction where fluid undergoes contraction, which are seen as the peaks of various magnitudes. In this respect, the position and the magnitudes of the peaks obtained in the model simulations compares well with the experimental data for all the passages examined. The proportionality of the increase of the magnitudes of the peaks towards the centre of the fibre lattice to the magnitudes of the LVE in the X direction for the passages P3 and P4 is also clearly distinguished in the model predictions, hence reconfirming the experimental findings.

Having illuminated all the local flow features in the lattice-channel arrangement experimentally and theoretically, it is concluded that fluid redistribution from the free flow region does not occur only in the main flow direction (Z direction) but in all available directions, subject to the resistance offered by the local configuration of the arrangement. The existence and magnitudes of the LVE within the lattice depend on both alterations in the macroscopic shape of the lattice and the change in the width of the open channel that cause the local variations in the velocity vector near the lattice-channel interface. These findings are valuable, bearing in mind that an accurate description of local flow features in heterogeneous porous media is of paramount importance in all the relevant applications. In resin transfer moulding processes, for example, experiments by Sadiq *et al.* [10] indicated a notable difference in permeability between an ideal fibre bed made up of solid rods and a real fibre preform bed made up of fibre lattices, even though both beds had equal porosities. The difference in permeability was ascribed to the microstructural variations in the real fibre preform bed, which make such porous bed heterogeneous. The implications arising from the LVE in coupled flow in a free flow region and flow in a fibrous porous medium may be seen in a broader context of this type of heterogeneous porous media. For example, by reducing the examined lattice-channel arrangement size by a

few orders of magnitude, the change in the macroscopic shape of the fibre lattice will represent the surface roughness of the fibre lattice (or in 3D of a spherical particle). Some previous numerical studies pointed to the possibility of the existence of stagnant fluid regions between the cylinders (in the flow direction) in fibrous porous media (Larson and Hidgon, 1987) [33]. This work implies that, if not desired, the stagnant regions could be avoided by an appropriate design of the macroscopic shape of the fibre lattice and the free flow region.

The fact that, in this type of heterogeneous porous medium, the velocities in the flow direction are increasing towards the symmetry axis in the passages P2-P4 is important. Even the passage P4 that is furthest from the lattice-channel interface and practically passes through the middle of the lattice (if another symmetrical part of the semi-circular lattice is attached to the studied part) is affected by LVE. The conclusion follows that LVE in the system studied are not purely surface phenomena i.e. are not confined to the region immediately below the lattice interface, but are present deeper within the lattice, and may even be extended to the lattice centre.

Another noteworthy conclusion from the above considerations of the interrelation of the flows exterior to and in the interior of the fibre lattice is the clear evidence of the flow symmetry. This is shown by analysing the $V_z$ and $V_x$ velocity profiles along the lines of constant *z*-value ((A) to (H)) both through the fibre lattice and outside the fibre lattice for cell IV as indicated in Fig.(5.3).

The experimental velocity profiles in the Z direction along the pairs of lines equidistant from the symmetry axis of the lattice-channel arrangement are presented in Fig.(5.6). Shown are the pairs of lines (B) and (G), (C) and (F), as well as (D) and (E) as the two dashed, the two solid and the two dotted lines respectively. The three peaks of higher (but different for each pair) magnitude represent the maximum $V_z$ velocities for all lines in the open channel and are positioned on the far right in the figure. The three or four peaks of lower magnitude represent maximum $V_z$ velocities within the fibre lattice for lines (B) and (G) in the first case and (C) and (F), and (D) and (E) in the second case.

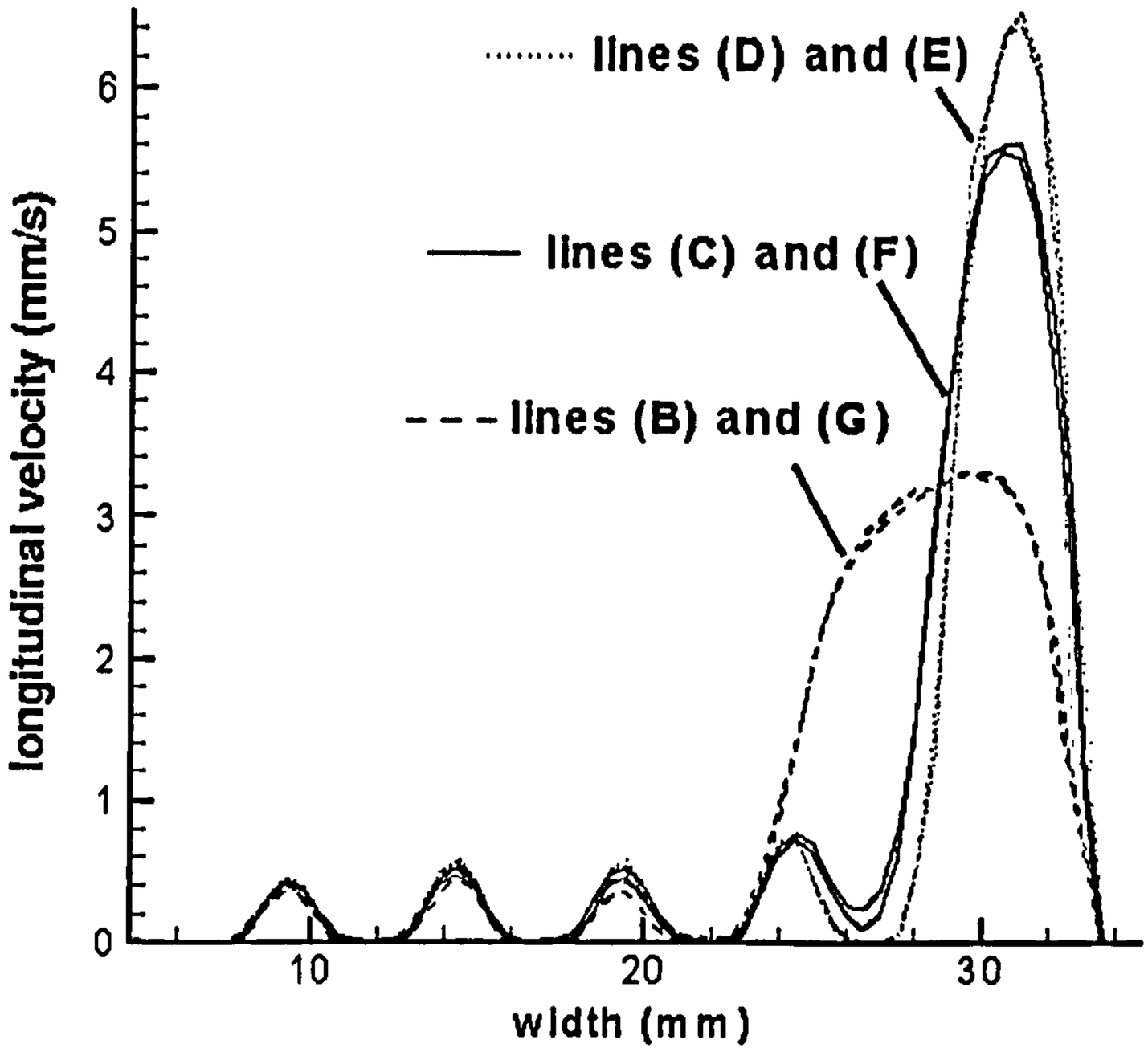


**Figure 5.6** Comparison of the longitudinal velocity profiles along the pairs of lines (B) and (G), (C) and (F), and (D) and (E), as indicated in Fig.(5.3). The lines in each pair are equidistant from the symmetry axis of the lattice-channel arrangement.

Each pair of extracted lines is almost identical implying that there is no change in the $V_z$ velocity profiles, irrespective of whether the fluid flows through the lower or upper part of the lattice-channel arrangement.

When compared to the LBM predictions, the experimental $V_z$ velocity profiles along the lines of constant *z*-value (the lines (A) and (H), (B) and (G) presented in Fig.(5.7a) and the lines (C) and (F), (D) and (E) presented in Fig.(5.7b)) are in a good agreement. The slight underprediction of the velocities in the open channel by the model is followed in a proportional overprediction of the flow throughout the fibre lattice. Nevertheless, the differences are minor and probably caused by the slight deviations in the cylinder diameters.

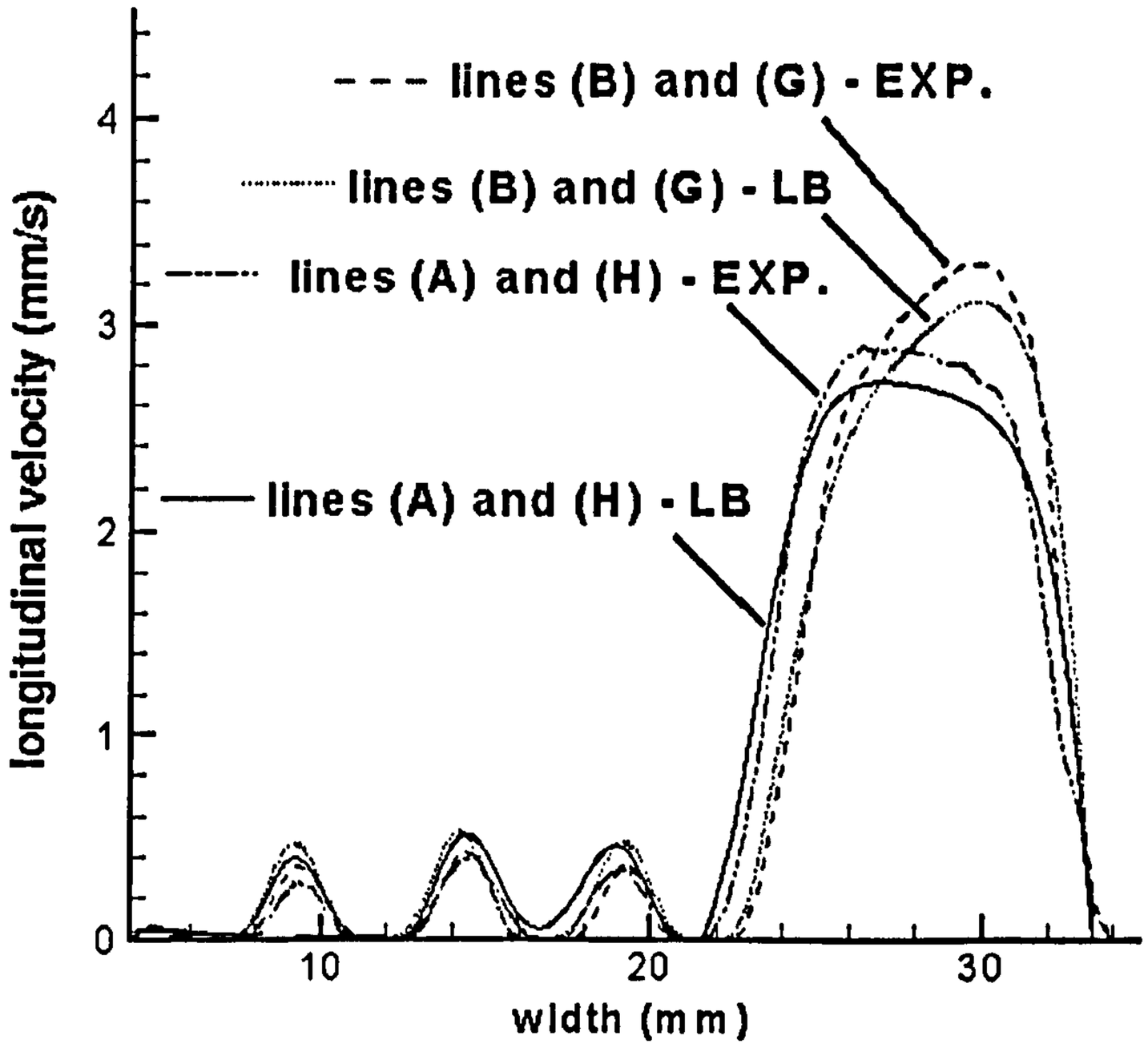


**Figure 5.7a** Comparison of experimental longitudinal velocity profiles along the lines (A),(B), (G) and (H) as indicated in Fig. (5.3), with the predictions of LBM along the same lines.

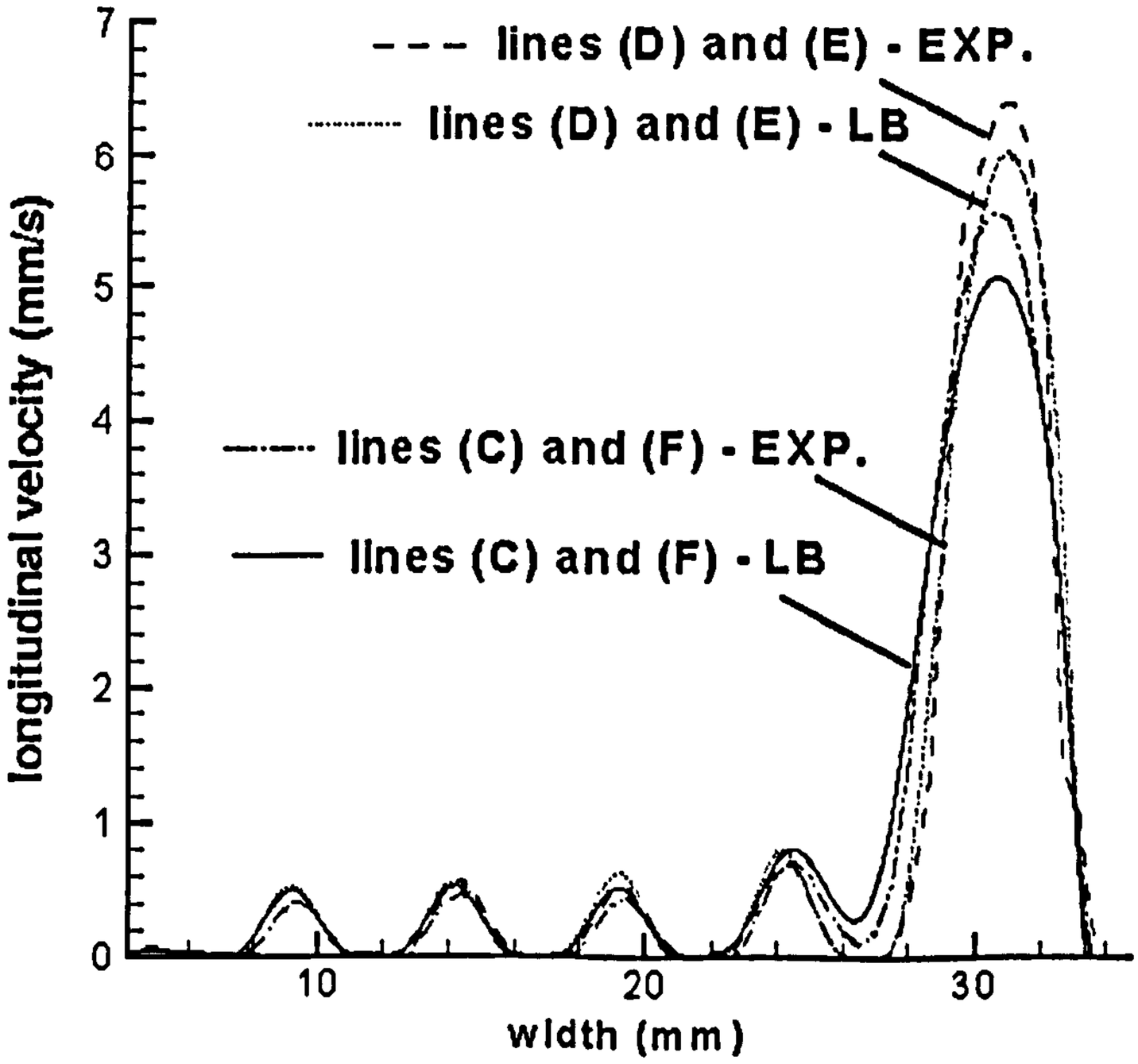


**Figure 5.7b** Comparison of experimental longitudinal velocity profiles along the lines (C), (F), (D) and (E) as indicated in Fig. (5.3), with the predictions of LBM along the same lines.

It is worth pointing out that, as expected, the lattice-Boltzmann model predictions show symmetrical $V_z$ velocity profiles along the each pair of the lines equidistant from the symmetry axes.

It is also of interest to verify if LVE in the X direction observed from the experiments are distributed within the lattice in a symmetrical fashion. For this purpose, the experimental $V_x$ velocity profiles along the corresponding pairs of lines (B) and (G), (C) and (F) as well as (D) and (E) are presented in Fig.(5.8).

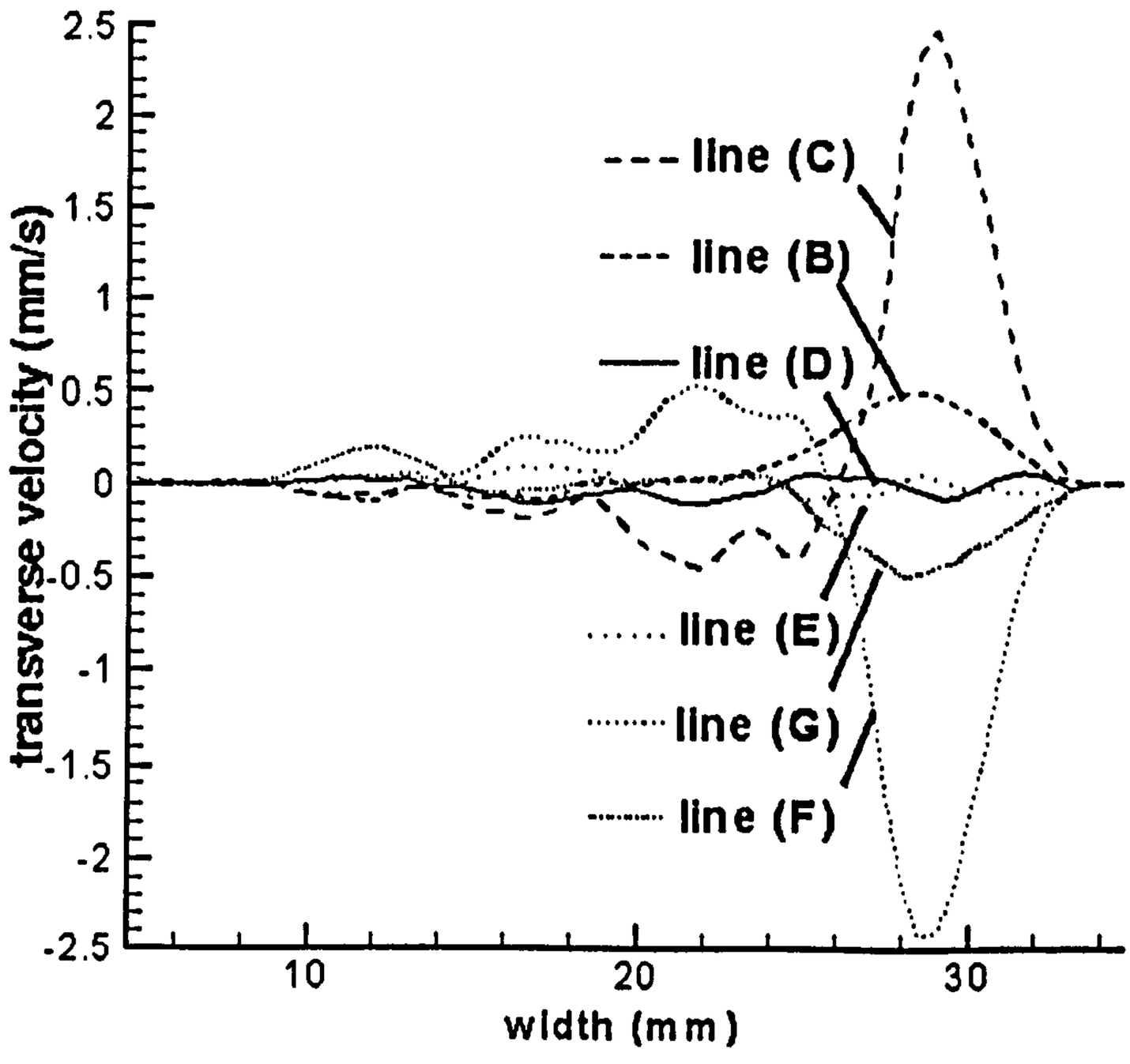


**Figure 5.8** Comparison of the transverse velocity profiles along the pairs of lines equidistant from the cell symmetry axis. Compared are the lines (B) and (G), (C) and (F) as well as (D) and (E) as indicated in Fig.(5.3).

The interrelation of the local flow enhancements in the open channel region and the local enhancements of flow in the fibre lattice is manifested in the changing sign of the $V_x$ velocities at the lattice interface. This is observed for the lines (C) and (F) with respect to both the free flow and lattice regions. Where LVE in the X direction within the lattice are not present, the $V_x$ velocities are seen only in the free flow region, as in the lines (B) and (G). In any case, the manner of the flow redirections is

nearly symmetrical in respect to the lower part (lines (C) and (B)) and the upper part (the lines (F) and (G)) of the lattice-channel arrangement. Insignificant $V_x$ velocities characterise flow in the middle part of the lattice-channel arrangement (lines (D) and (E)).

Even more interestingly, LVE in the X direction observed from the experiments should also exist in the lattice-Boltzmann model. Moreover, as previously pointed out for the $V_z$ velocities, the model should also be able to predict the flow symmetry along the pairs of lines equidistant from the symmetry axis of the lattice-channel arrangement. The evidence for both findings can be seen in Fig.(5.9a) in which the model predictions are plotted against the experimental data along the pairs of lines (B) and (G) and the lines (C) and (F).

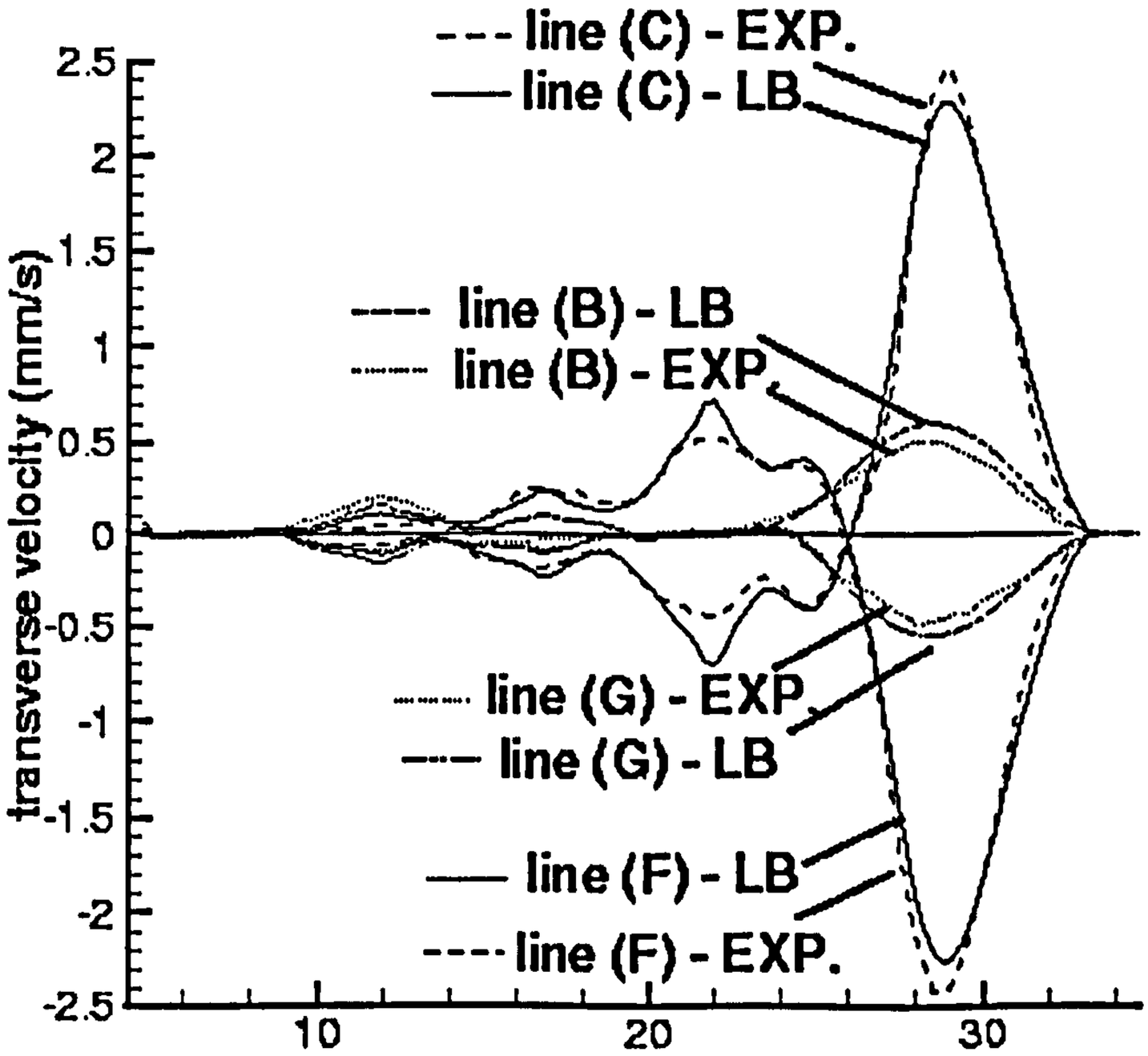


**Figure 5.9a** Comparison of the experimental transverse velocity profiles along the pairs of lines (B) and (G), and (C) and (F) with the predictions of lattice-Boltzmann model.

Remarkably, the local variations in the LVE in $V_x$ velocities within the fibre lattice in the places between the cylinders in the flow direction, are not only present in the model predictions but do follow the experimental $V_x$ velocity profiles. The model clearly distinguishes these LVE within the fibre lattice along the cell width and the cell length. The change in sign of $V_x$ velocities at the lattice–channel interface is;eee in excellent agreement with the observations from the experiment. The model predictions for $V_x$ velocities reach the maximum value in the channel and exactly follow the experimental values. The same evidence can be seen in Fig.(5.9b), in which the model predictions are plotted against the experimental data along the pairs of lines (A) and (H) and the lines (D) and (E).

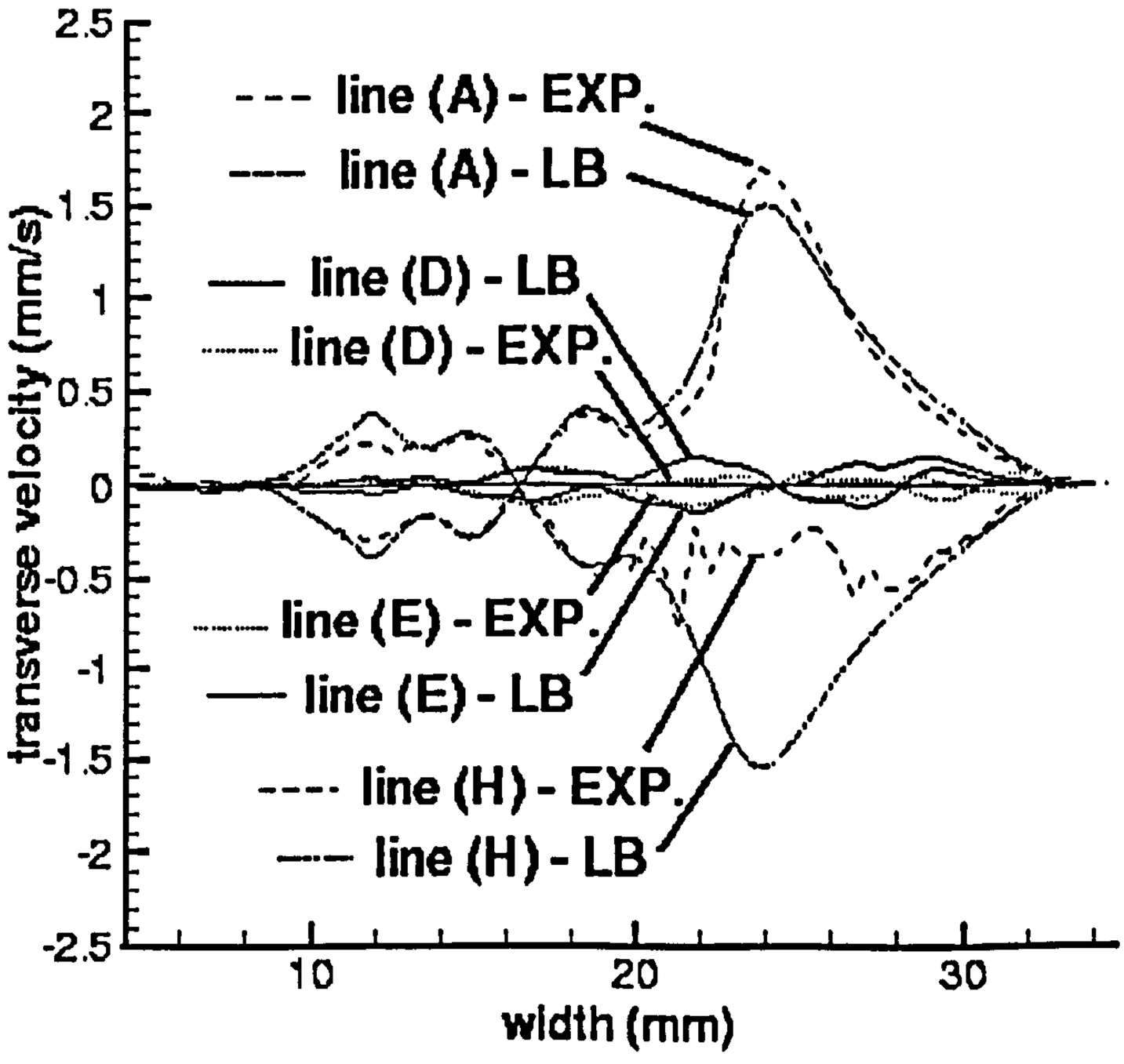


**Figure 5.9b** Comparison of the experimental transverse velocity profiles along the pairs of lines (A) and (H), and (D) and (E) with the predictions of lattice-Boltzmann model.

The only deviation is present along the line (H) in the free flow region; this is a consequence of the magnetic field heterogeneities present in the border region of the experimental field of view.

These findings give the firm evidence of the inherent symmetry of creeping flow in heterogeneous geometrically symmetrical porous media, provided an appropriate length-scale is examined. One could argue that, since the actual sum of the positive and negative values of the LVE in the X direction on a meso-scale (the scale associated with the size of the lattice-channel arrangement) is zero, the significance of the existence of the LVE is denied. However, in many real heterogeneous porous systems, the LVE within the fibre lattices may play a significant role in transport phenomena. Mass or heat transfer within a spherical porous particle adjacent to a variable width free flow region will be profoundly facilitated in the regions of LVE. Therefore, by an appropriate design, the presence of recirculation regions in heterogeneous porous particles in the creeping flow regime can be excluded.

Hence, studying heterogeneous fibrous porous media at local, rather than meso-scale, offers advantages in the flow description that can be practically applied.

### *5.2.2 Effect of the fibre volume fraction (porosity)*

The general features of the flow across the semi-circular lattice with a higher porosity of 70% (the cell V) follow very similar patterns to those in the cell IV with 50% porosity of the lattice, described above. From the contour maps of $V_z$ and $V_x$ velocities for this cell depicted in Figs.(5.10a,b), LVE are, analogously to the cell IV, observed at the edges of the lattice as well as within the fibre lattice. Flow symmetry in this type of geometry of heterogeneous porous media is, as seen in the figures, confirmed. A full description of the velocity profiles that would lead to this conclusion will not be repeated here.

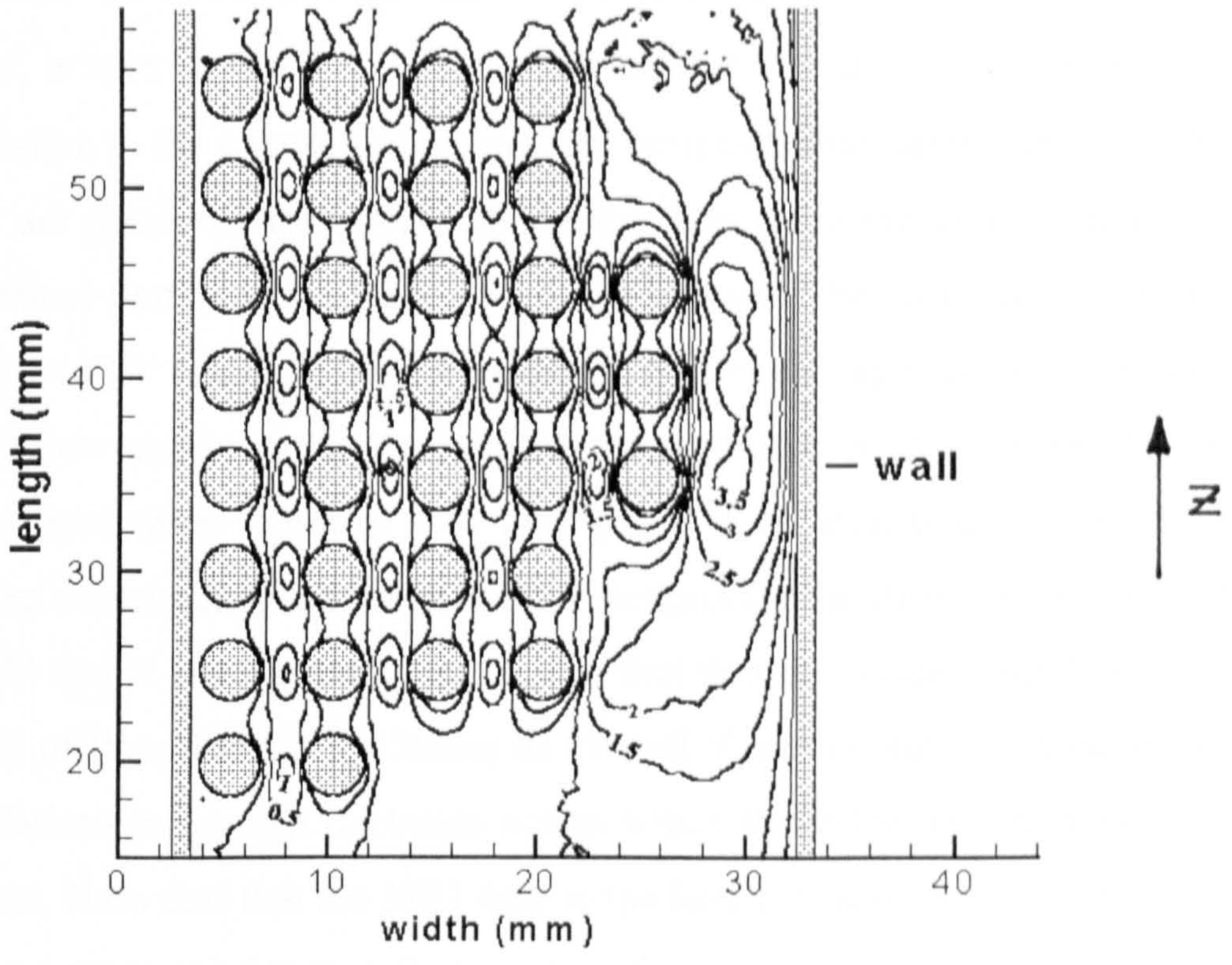


**Figure 5.10a** Contour velocity map for the velocity component in the flow direction ($V_z$) in the cell V.

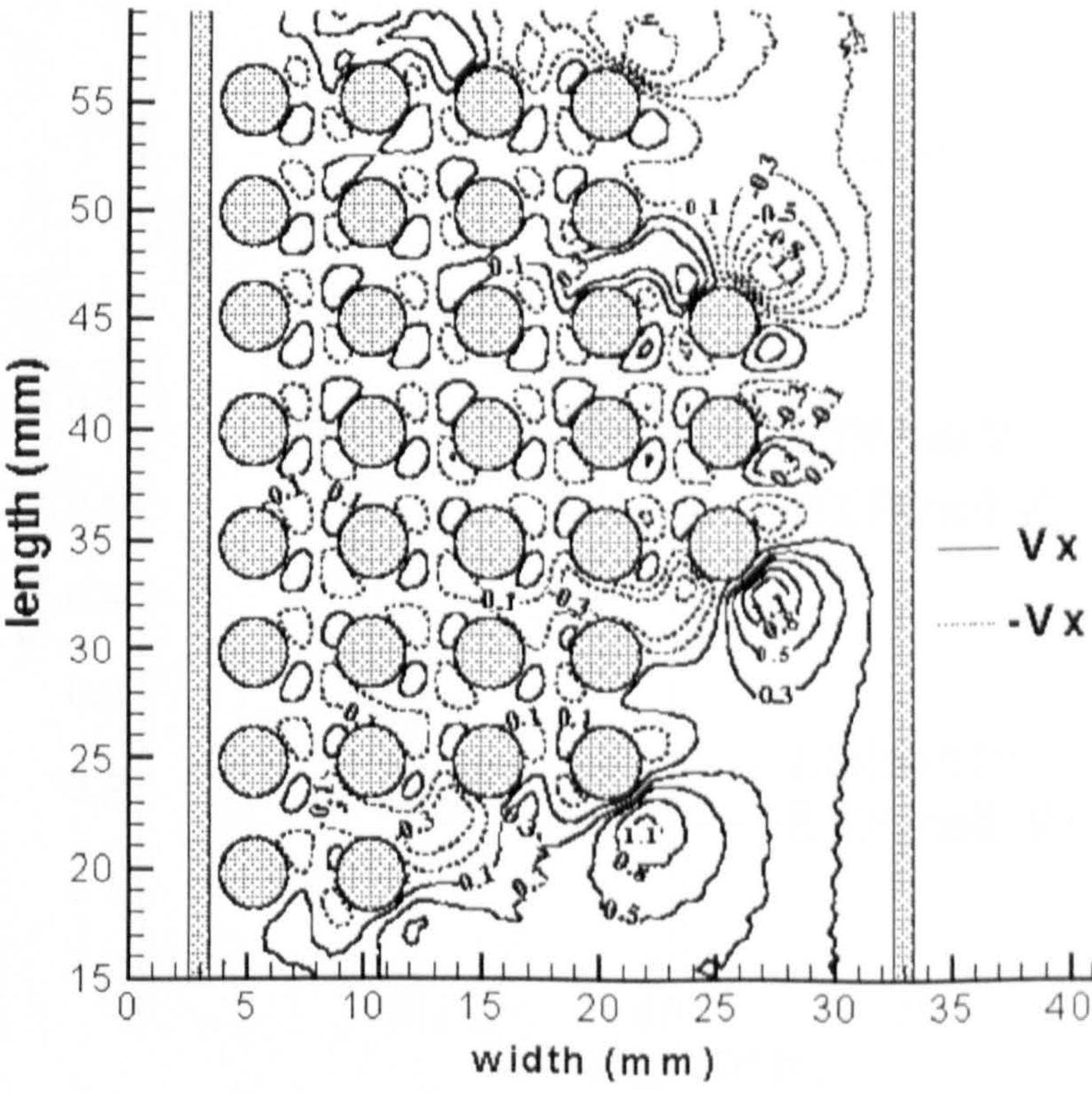


**Figure 5.10b** Contour velocity map for the velocity component perpendicular to the flow direction ($V_x$) in the cell V.

The effect of increased porosity of the semi-circular fibre lattice V on the global characteristics of flows through the lattice and the free flow region in the flow direction Z is seen in Fig.(5.11). The volumetric fractions of flow through the fibre lattices relative to the overall flow across the lattice-channel arrangements in the cells IV and V are presented for both experimental data (with the allowed field of view) and theoretical (lattice-Boltzmann model) predictions. The increased porosity of the lattice in the cell V results in a greater amount of flow through the lattice in relation to the overall flow across the lattice-channel arrangements. Both experimental data and theoretical predictions confirm this anticipated flow distribution. The agreement between the experiments and the model predictions for the flow through the lattice in the cells IV and V is remarkably good. The fact that the model slightly overpredicts the amount of flow through the lattice in the cell V is probably a consequence of the minor variations in the gap thickness across which the velocities are averaged in the experiments. Note also that the MRI data in the lattice-channel interface regions close to the symmetry axes of both cells do not perfectly capture the local variations in the volumetric flow distribution between the two regions, predicted by the model.

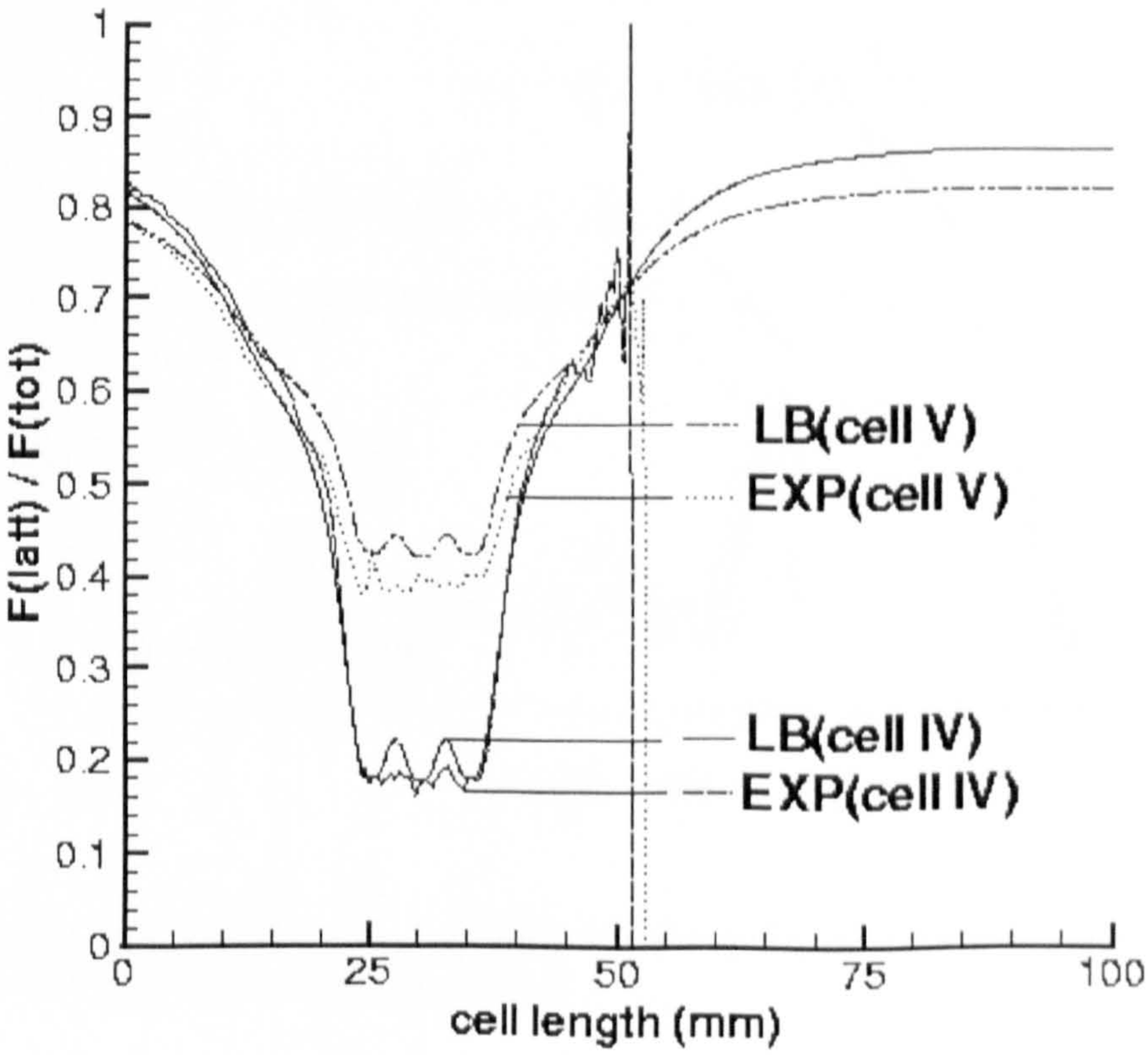


**Figure 5.11** Comparison between volumetric fractions of flow through the fibre lattices to the overall flow across the lattice-channel arrangements in the cells IV and V. The experimental data are presented as the dashed lines whereas the Lattice-Boltzmann model predictions are shown as the solid lines.

The effect of increased porosity of the semi-circular fibre lattice on the local characteristics of the coupled flow in the flow direction Z is shown in Fig.(5.12). Presented are the comparisons of $V_z$ velocities along the lines of constant *z*-value (lines (A) and (D), as indicated in Fig.(5.3)) for the cells IV and V. The three (lines (A)) or four (lines (D)) peaks of lower magnitude represent maximum $V_z$ velocities within the fibre lattice. The peaks of higher magnitude represent maximum $V_z$ velocities in the open channel and are positioned on the far right in the figure. The increased porosity of the lattice (cell V) leads to an increase in the flow through the lattice yielding higher maximum $V_z$ velocities within the lattice than it is the case for the cell IV of lower porosity. Alongside it, a proportional decrease of the flow through the open channel in the cell V is detected, leading to lower maximum $V_z$ velocities in the open channel for the cell V.

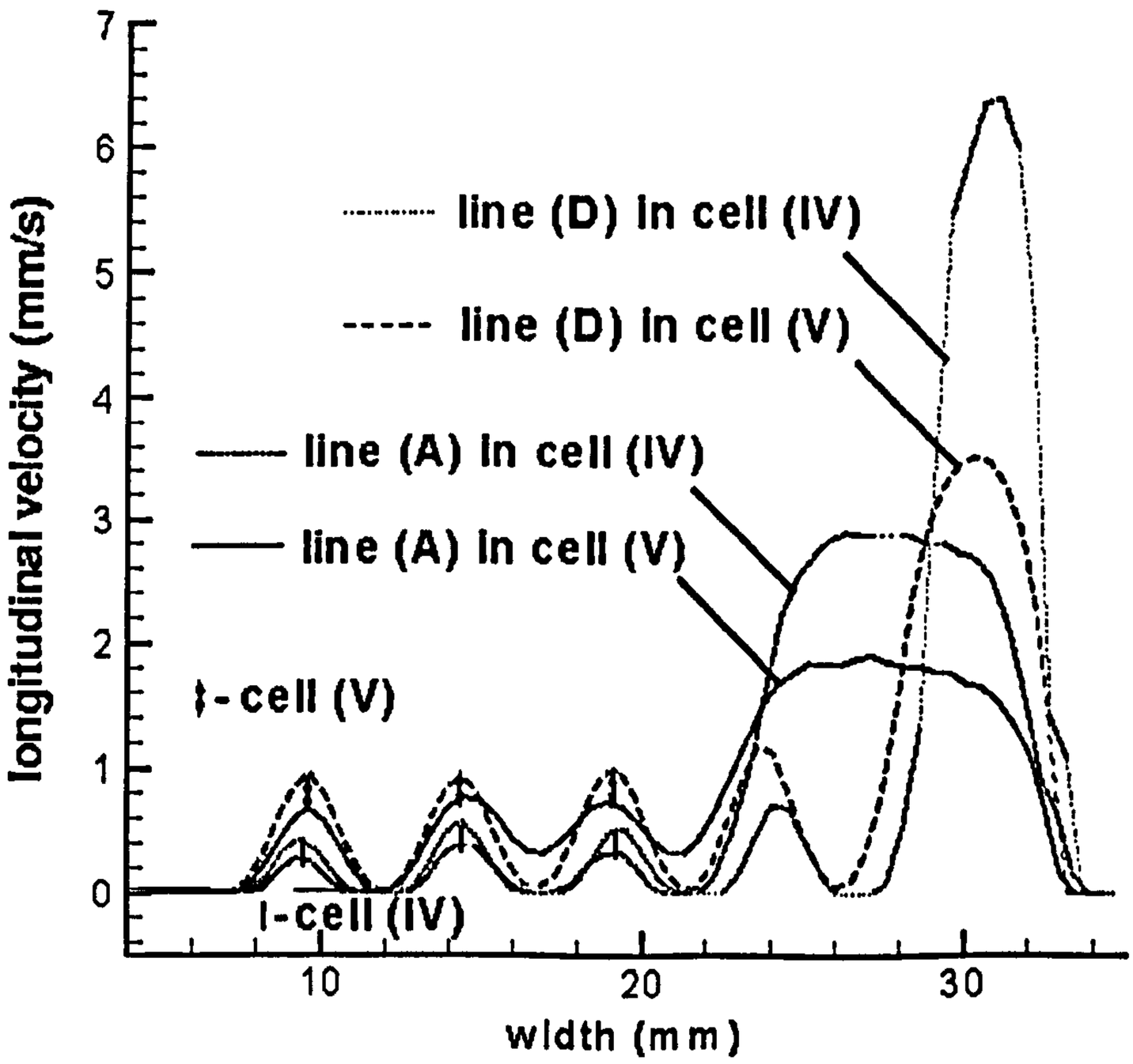


**Figure 5.12** Comparisons of the longitudinal velocity profiles for the cell IV (ε=0.5) and V (ε=0.7) along the lines (A) and (D) as indicated in Fig.(5.3)).

The effect of the LVE within the fibre lattice is reflected in a discernible increase of the magnitude of the peaks from the lines (A) and (D) within the fibre lattices of the same cells. In Fig.(5.12) this is highlighted by the lines with and without the arrows for cells V and IV respectively.

It is further instructive to compare the magnitude and shape of LVE in the X direction within the fibre lattices of different porosities and adjacent free flow regions. For this purpose, the insert of the $V_x$ contour plots from Hele-Shaw cell IV denoted as A1 in Fig.(5.3) along with the corresponding geometry in the cell V are presented in Figs.(5.13a,b). Not surprisingly, the values of $V_x$ velocity components at the edges of the lattice of lower porosity in the cell IV are greater than the corresponding velocities at the edges of the more porous lattice in the cell V. The same conclusion is valid for $V_z$ velocities (refer to Fig.(5.2a) and Fig.(5.10a)). The penetration depths of the local $V_x$ velocity enhancements within both fibre lattices are comparable and of the order of one (the region R1 as indicated in Fig.(5.2b) in the cell IV and the corresponding region in the cell V) and two (the region R2 as indicated in Fig.(5.2b) in the cell IV and the corresponding region in the cell V)) lattice unit cells. The greater gap size between the cylinders in more porous fibre lattice enables developments of broader regions of the enhanced $V_x$ velocities. On the other hand, within the less porous lattice, the $V_x$ velocity is more enhanced in the regions between the cylinders in the flow direction. This is a consequence of the more pronounced local flow contraction in the X direction.

Common to both cells is that the local flow enhancements within the fibre array configurations are redistributed according to the local configuration of the lattice that offers the least resistance to flow.

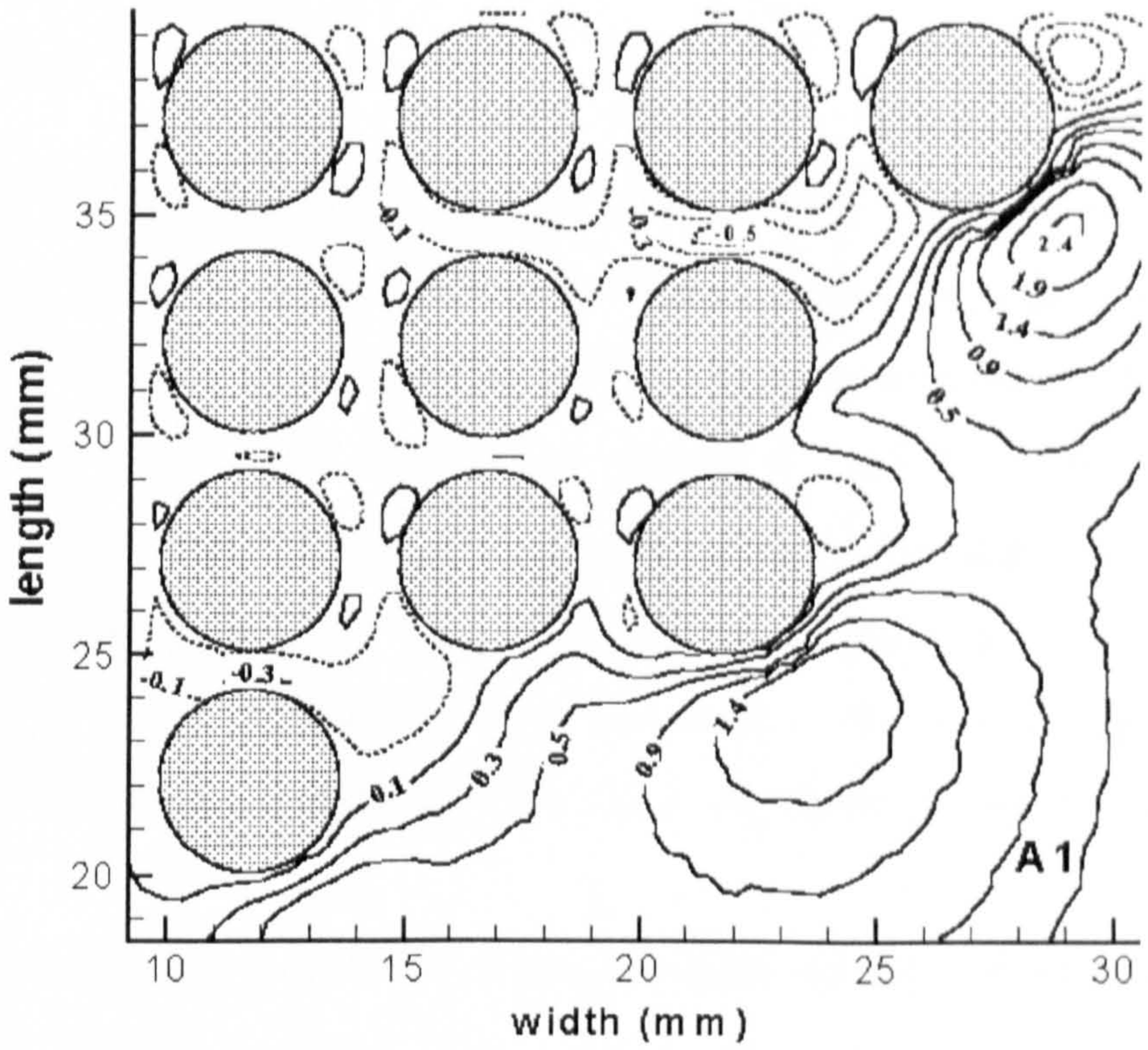


**Figure 5.13a** Contour velocity map for the velocity component transverse to the flow direction ($V_x$) taken from the insert A1 in the cell IV, as indicated in Fig.(5.3).

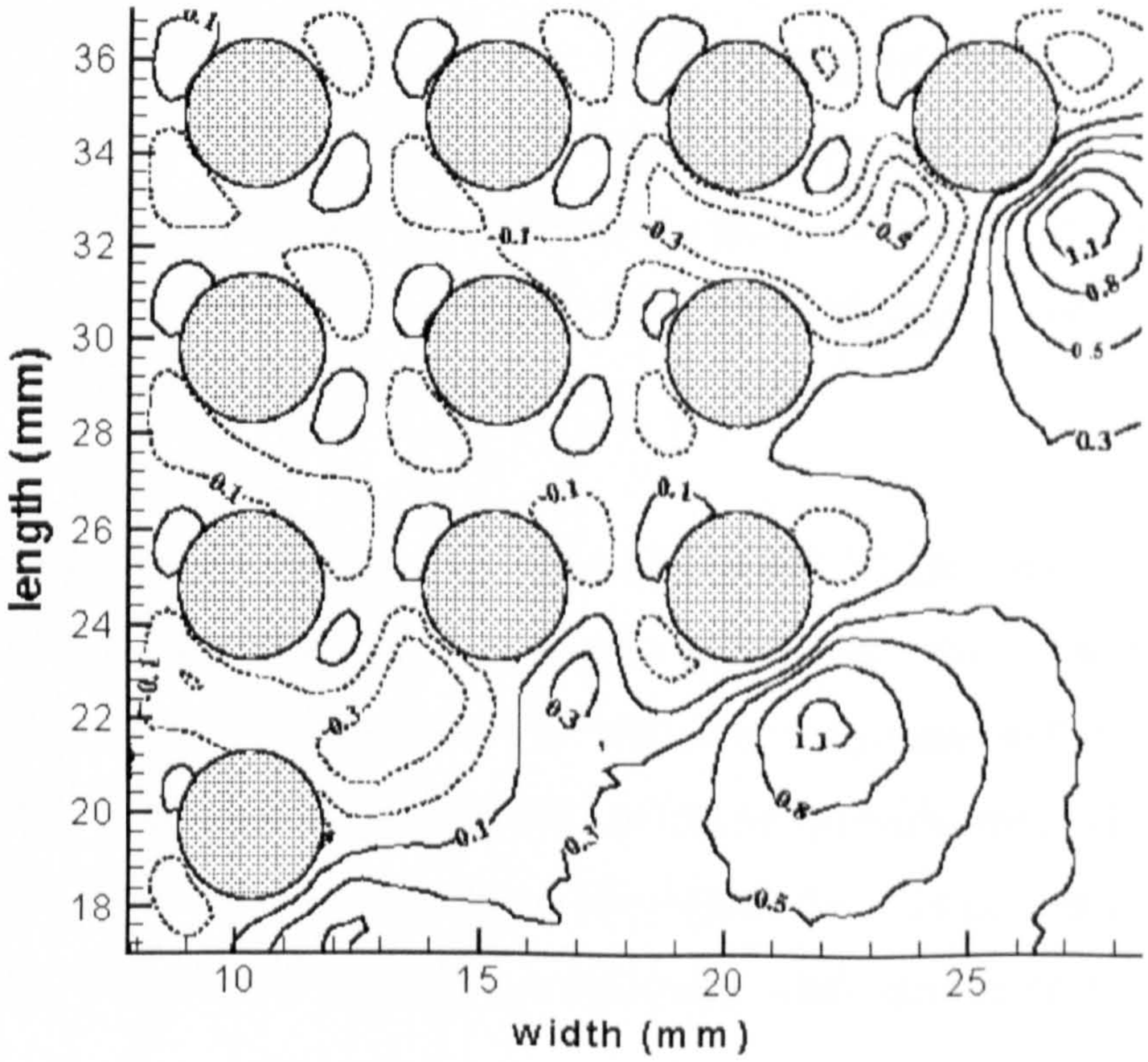


**Figure 5.13b** Contour velocity map for the velocity component transverse to the flow direction ($V_x$) taken from the insert A1 in the cell V, as indicated in Fig.(5.3).

### *5.2.3 Effect of Fibre Size/Gap Between the Fibres*

The effect of the reduced cylinder size for the same porosity (ε=50%) of the semi-circular lattice on the interrelation between the coupled flows in dual porosity fibrous media is investigated by monitoring the two-dimensional velocity field in the cell VI, as introduced in Fig.(5.1). The contour plots of $V_z$ and $V_x$ velocities in the cell VI are presented in Fig.(5.14a) and Fig.(5.14b) respectively. Note that, even though the lattice in the cell IV is of the same porosity as the lattice in the cell VI, the flow inside the latter is significantly reduced. This is a result of the smaller gap size between the cylinders and, hence, the greater surface area of cylinders causing fluid friction.

Once more, from the $V_x$ velocity maps, the local velocity enhancements in the lattice interior are identified at the lattice edges, where the width of the open channel suddenly narrows. The lattice regions exposed to the flow redistribution from the free flow region are encircled with the dashed lines in Fig.(5.14b). The determinants for the presence of LVE within the lattice are the local geometry of the lattice, i.e. local configuration of the fibres, and the variable channel width. To emphasize the combined impact of the aforementioned determinants, the lattice regions adjacent to the free flow regions where the channel width is constant are also highlighted in Fig.(5.14b) as solid rectangles. It is seen from the same figure that no discernible flow enhancements are present in these regions.

Despite the fact that the LVE in the lattice in the cell VI are considerably smaller than in the lattices in the cells IV and V (the maximum values for Vx velocities are 0.2mm/s in the former cell compared to 0.5mm/s in the latter cells), the very presence of the LVE is a noteworthy finding. It implies that consideration of the local velocity field preferences is essential in studies of coupled flows in dual porosity media, even when the gap between the cylinders is relatively small compared to the open channel width.

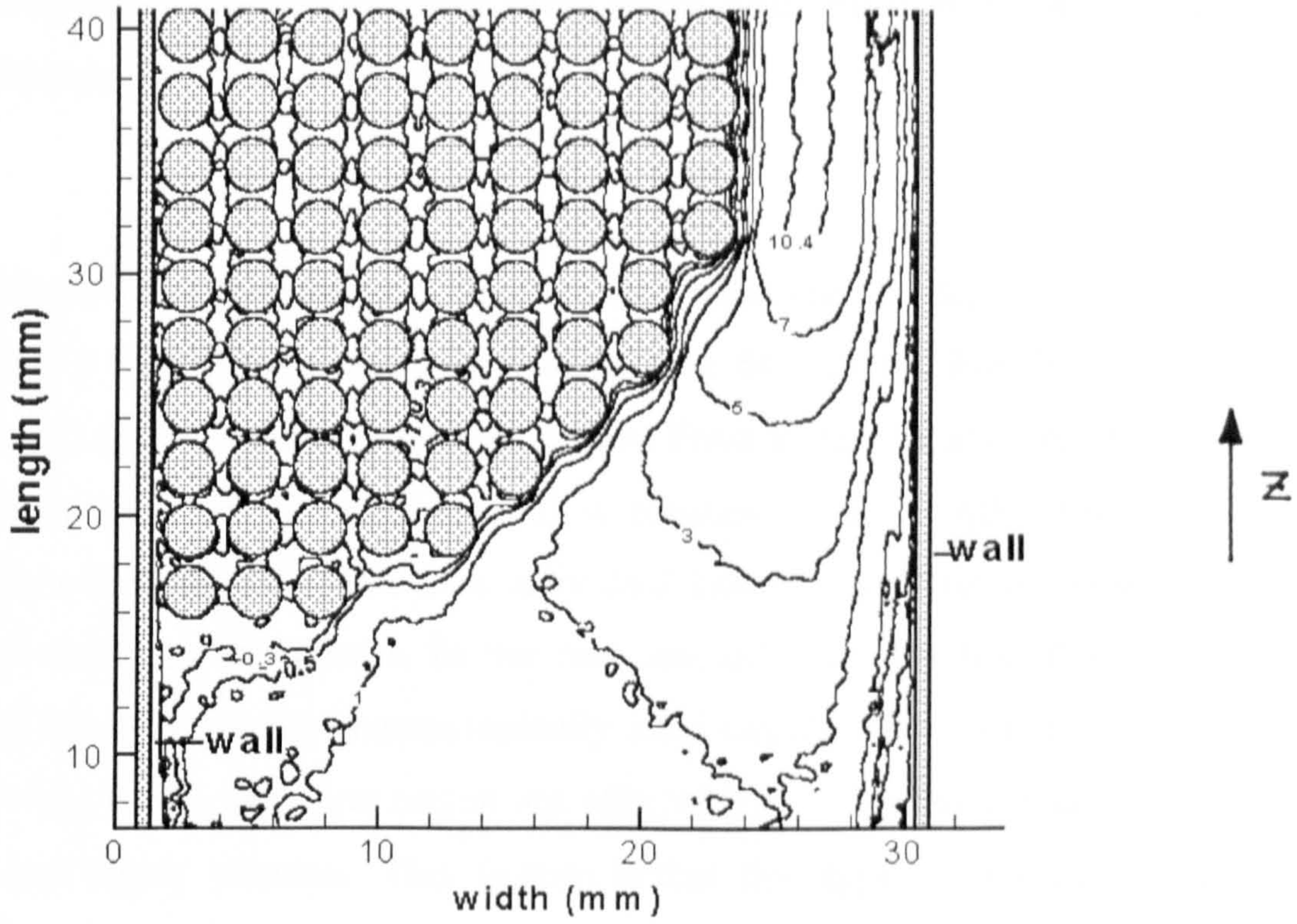


**Figure 5.14a** Contour velocity map for the longitudinal velocity component in the flow direction ($V_z$) in the cell VI.

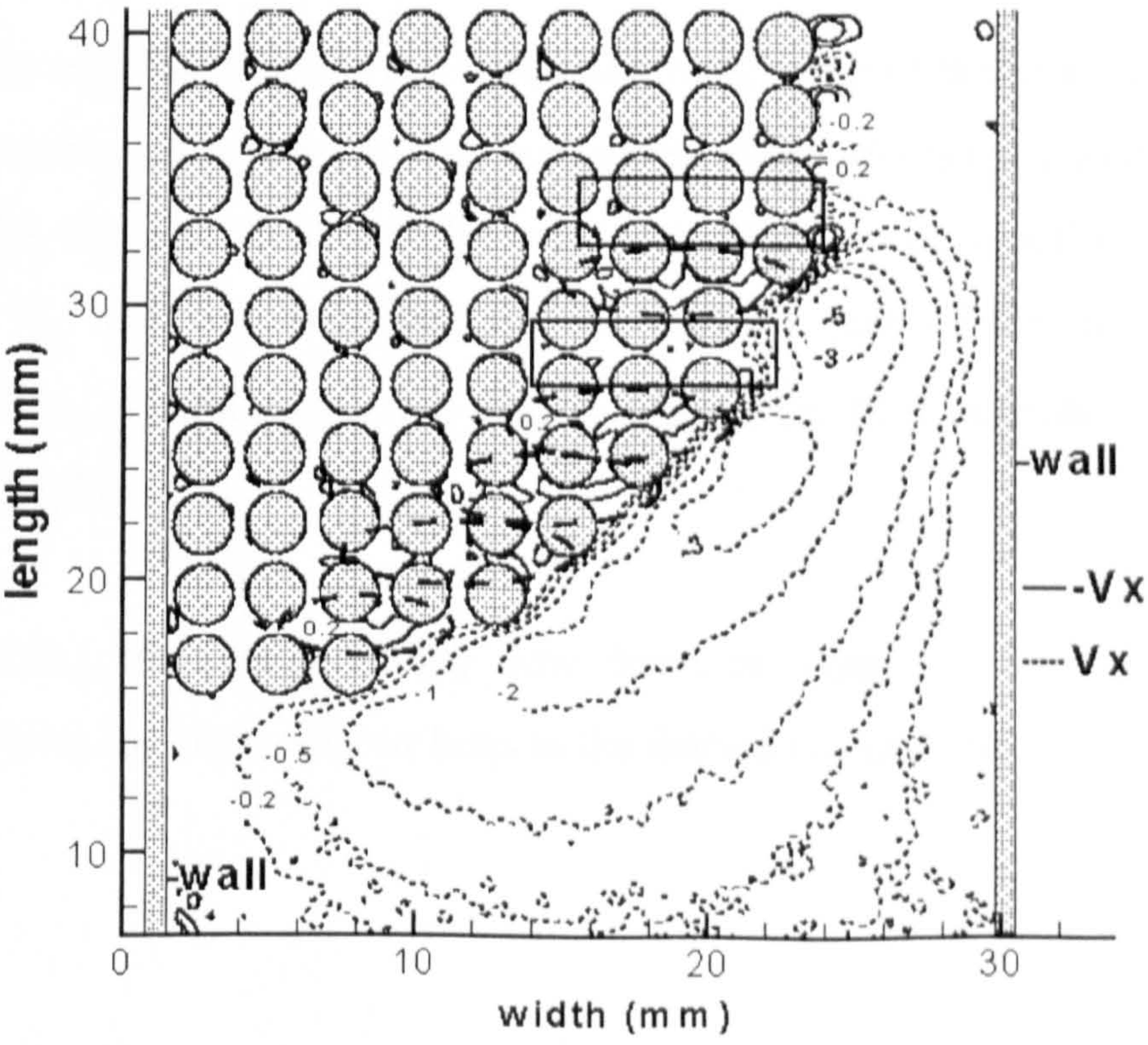


**Figure 5.14b** Contour velocity map for the velocity component perpendicular to the flow direction ($V_x$) in the cell VI. Note that, for the sake of clarity of the LVE within the lattice, only for this cell the negative $V_x$ contour plots velocities (which here stand for the flow into the lattice) are drawn as solid lines.

### *5.2.4 Local Aspects of Coupled Free Flow and Flow in an Assembly of Macroscopically Semi-Circular Fibre Lattices*

The most complex configuration of the fibre arrays has been modelled to combine the flow through a fibre lattices assembly with the flow through the free flow region (the open channel) adjacent to the individual lattices. From a theoretical point of view, it is an interesting issue to study the local flow features of the coupled flows in dual porosity fibrous media in which each individual lattice may affect the flow features within the neighbouring lattices. In the case studied here, the free flow region is surrounded on each side by macroscopically semi-circular fibre lattices. Hence, the flow pathways in the free flow region are affected by all the individual lattices and therefore are highly tortuous. This feature makes this type of the lattice-channel arrangement essentially different from the ones in earlier studies of the flow through the single fibre lattices of various geometries and porosities adjacent to the free flow regions, which were bounded by a lattice on one side and a wall on the other side.

The experimental field of view did not allow monitoring of the flow through the entire lattice assembly in one experiment. Instead, the flow field is examined in the entering part and the mid-part of the cell by two independent experimental runs. The contour maps of $V_z$ and $V_x$ velocities for the entering part of the cell are shown in Figs.(5.15a,b). It features the first three lattices of the fibre assembly, denoted as L1, L2 and L3 in Fig.(5.1).

In Fig.(5.15b), the change of the flow direction along the X axis is seen as the alteration from the solid contour lines to the dashed contour lines.

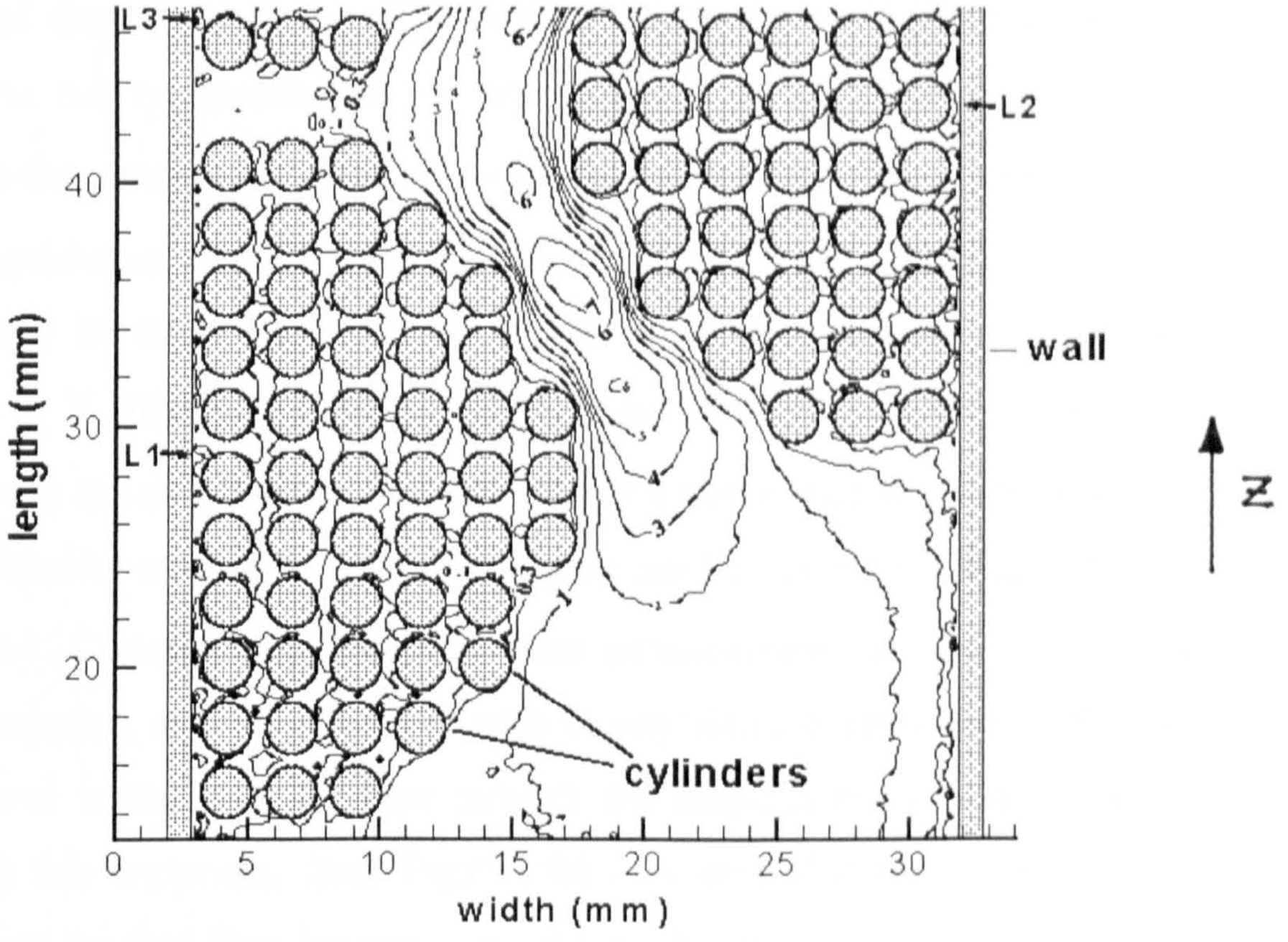


**Figure 5.15a** Contour velocity map for the velocity component in the flow direction ($V_z$) in the entering part of the fibre lattice assembly (lattices L1-L3) in the cell VII.

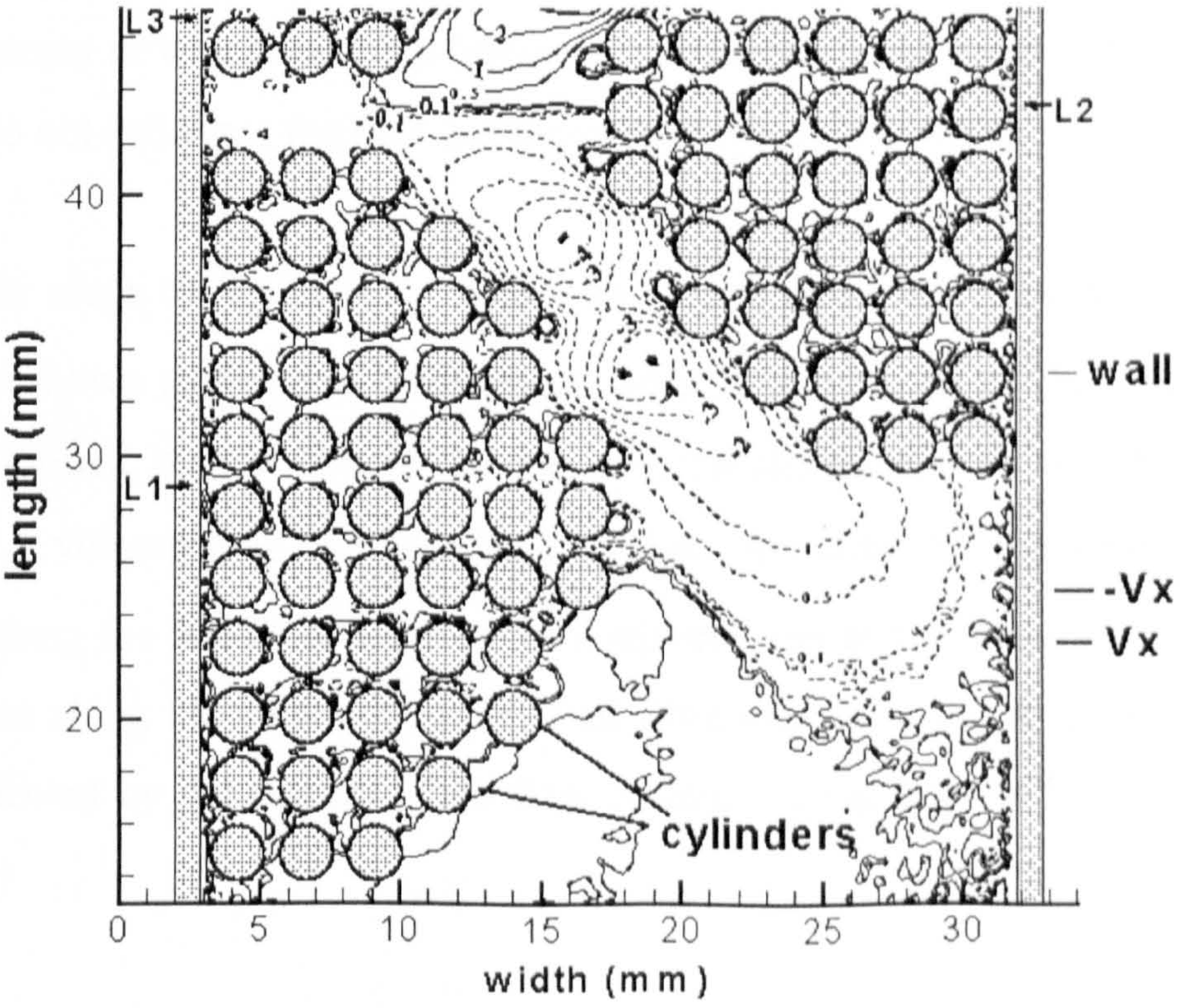


**Figure 5.15b** Contour velocity map for the velocity component perpendicular to the flow direction ($V_x$) in the entering part of the fibre lattice assembly (lattices L1-L3) in the cell VII.

As seen from Figs.(5.15a,b), flow in the free flow region is accelerated by the sudden contractions in the open channel width caused not only by the wall, but also by the presence of the neighbouring fibre lattices. Since the configuration of the lattice assembly is not symmetrical in the entering part of the lattice-channel assembly, neither are the measured $V_z$ and $V_x$ velocities in the free flow region. In fact, when the lines equidistant from the symmetry axis of the first lattice L1 (the symmetry axis as previously introduced in the study of the single fibre lattices) are compared, the difference in $V_z$ velocities in the free flow region can be, (as seen in Fig.(5.15a)), as high as seven times. Likewise, for the velocities perpendicular to the flow direction, $V_x$, this velocity ratio in the free flow region can be, (as seen in Fig.(5.15b)), of the order of 4:1. Consequently, the local flow enhancements within the fibre lattices, although existing, are not identified with clearly defined preferable pathways, as it was observed in the study of flow through the single lattice-channel arrangements. Supporting this argument, from Fig.(5.15b) it is seen that the local flow in the X direction into the first fibre lattice is now observed in the regions along and around the symmetry axis of the first lattice L1. Such flow details in more complex fibrous media of dual porosity clearly discriminate this type of flow from the flow where the adjacent free flow regions are bounded by walls or, from any other heterogeneous porous systems in which the fibre lattices are sufficiently far apart from one another that they do not influence the flow pathways in the free flow region.

The contour maps of $V_z$ and $V_x$ velocities for the mid-part of the cell (the lattices L1-L4) are shown in Figs.(5.16a,b) respectively. The mid-part of the lattice-channel assembly formed by the lattices L2-L4 is symmetrical, and so are the measured $V_z$ and $V_x$ velocities in the free flow region. Remarkably, the change of flow direction along the X axis in the free flow region (seen as the change of the velocity sign) occurs along the symmetry axis of all fibre lattices under consideration which are not affected by the entrance free flow region, i.e. the lattices L2-L4, as seen in Fig.(5.16b).

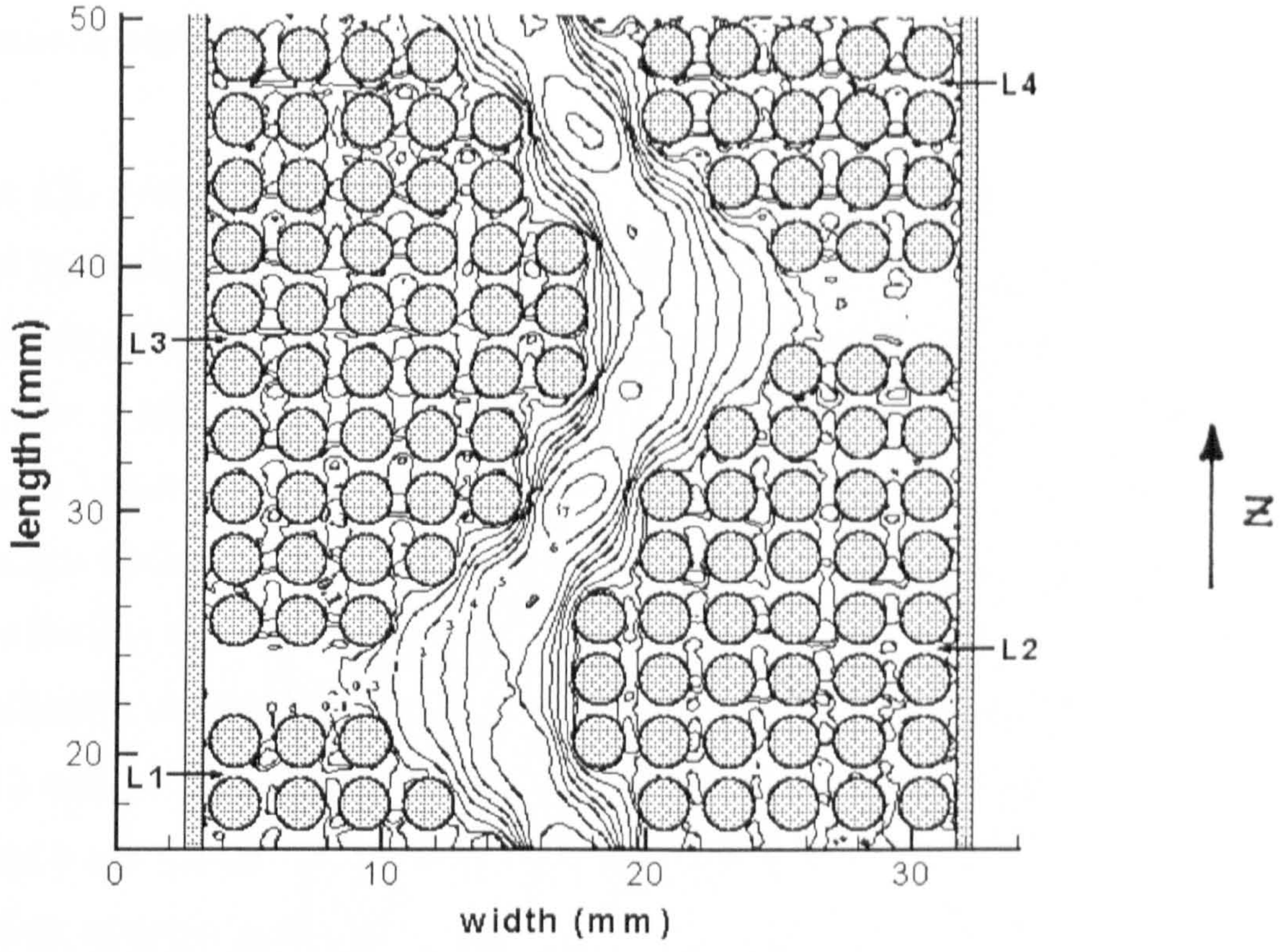


**Figure 5.16a** Contour velocity map for the velocity component in the flow direction ($V_z$) in the entering part of the fibre lattice assembly (lattices L1-L4) in the cell VII.

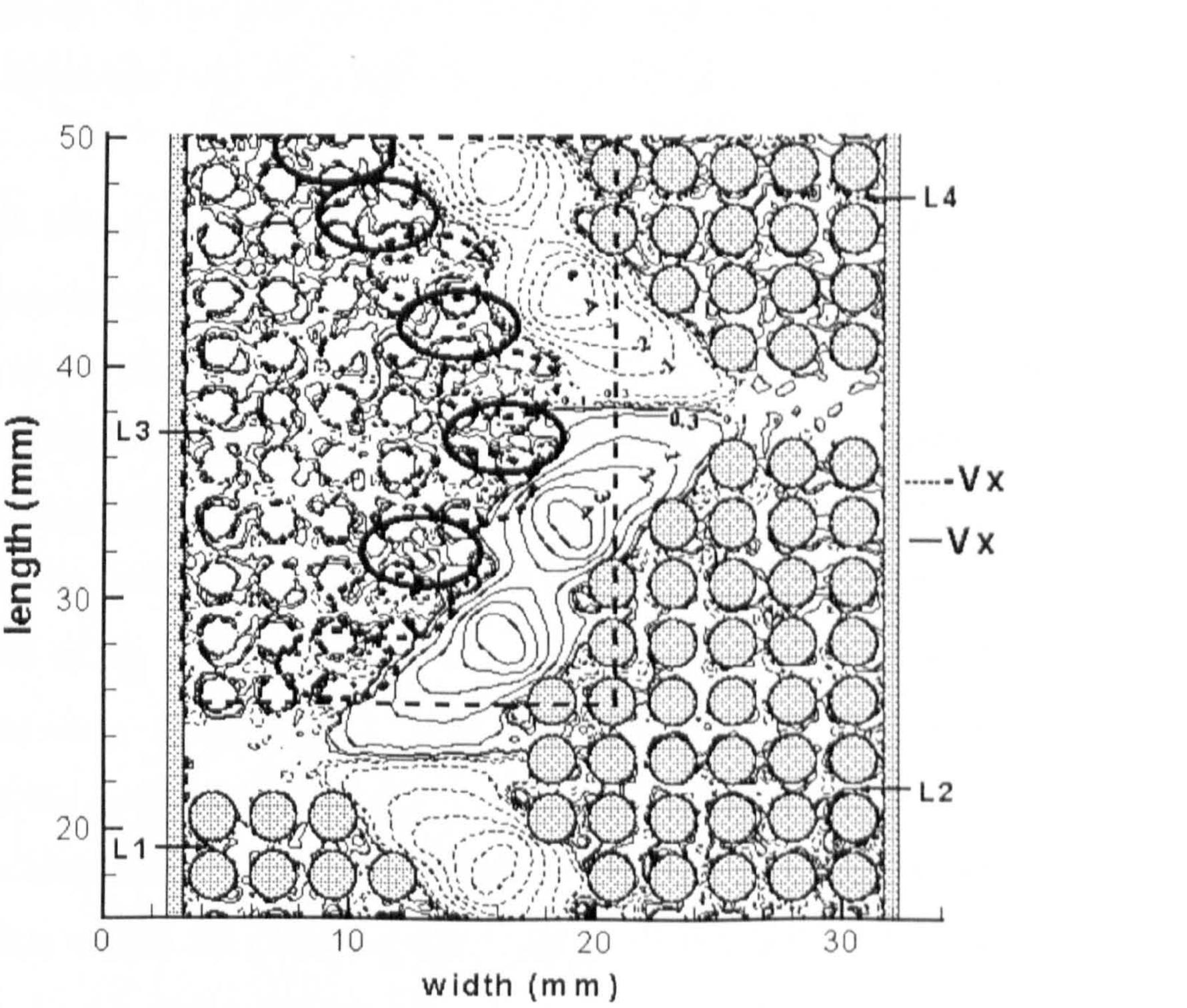


**Figure 5.16b** Contour velocity map for the transverse velocity component ($V_x$) in the mid-part of the fibre lattice assembly (lattices L1-L4) in the cell VII.

As seen in Fig.(5.16b), the $V_x$ velocity distributions within the lattice L2 are still under the influence of the non-symmetrical free flow region in the entering part of the lattice-channel assembly and therefore are not symmetrical.

The lattice L3, being in the middle part of the whole lattice-channel assembly, is surrounded by the symmetrical free flow region which is determined by the shape of the neighbouring lattices L2 and L4. This is the lattice to which exceptional attention is drawn, since it exemplifies a situation in which a lattice is completely surrounded by a complex lattice assembly. As a result of that, the width of the free flow region adjacent to this lattice varies in a different manner than was the case in studies of the single fibre lattices adjacent to the free flow regions which were bounded by the wall. More specifically, recalling from Fig.(5.1), the width of the open channel between the lattices L2 and L3 denoted as 3 was designed to be narrower than the preceding widths 2 and 1 and the subsequent widths 4 and 5. Therefore, flow in the open channel is expected to undergo contraction in the narrowest part of the free flow region and, after passing this line, expansion. It is challenging to observe the effect of these local flow changes in the free flow region on the velocities within the lattice L3, as well as a possible difference from the single fibre lattices-channel arrangements examined.

From Fig.(5.16b) it is seen that the variations in the directions of the $V_x$ velocities, although symmetrical in respect to the symmetry axis in the lattice L3, take a different form than in the single lattice-channel arrangements. This is clearly a result of the different configuration of the free flow region. In the places immediately below the lattice surface, which are adjacent to the parts of the free flow region that undergo contraction, the flow in transverse direction is observed into the fibre lattice (dashed contour lines of $V_x$ velocities within the encircled dashed regions in the lattice L3). In the same view, in the places immediately below the lattice surface which are adjacent to the parts of the free flow region that widen, the flow in the transverse direction is identified to be directed outside of the fibre lattice (solid contour lines of $V_x$ velocities within the encircled solid regions in the lattice L3). This evidence is better seen in Fig.(5.17), which shows the insert marked with dashed lines in Fig.(5.16b).

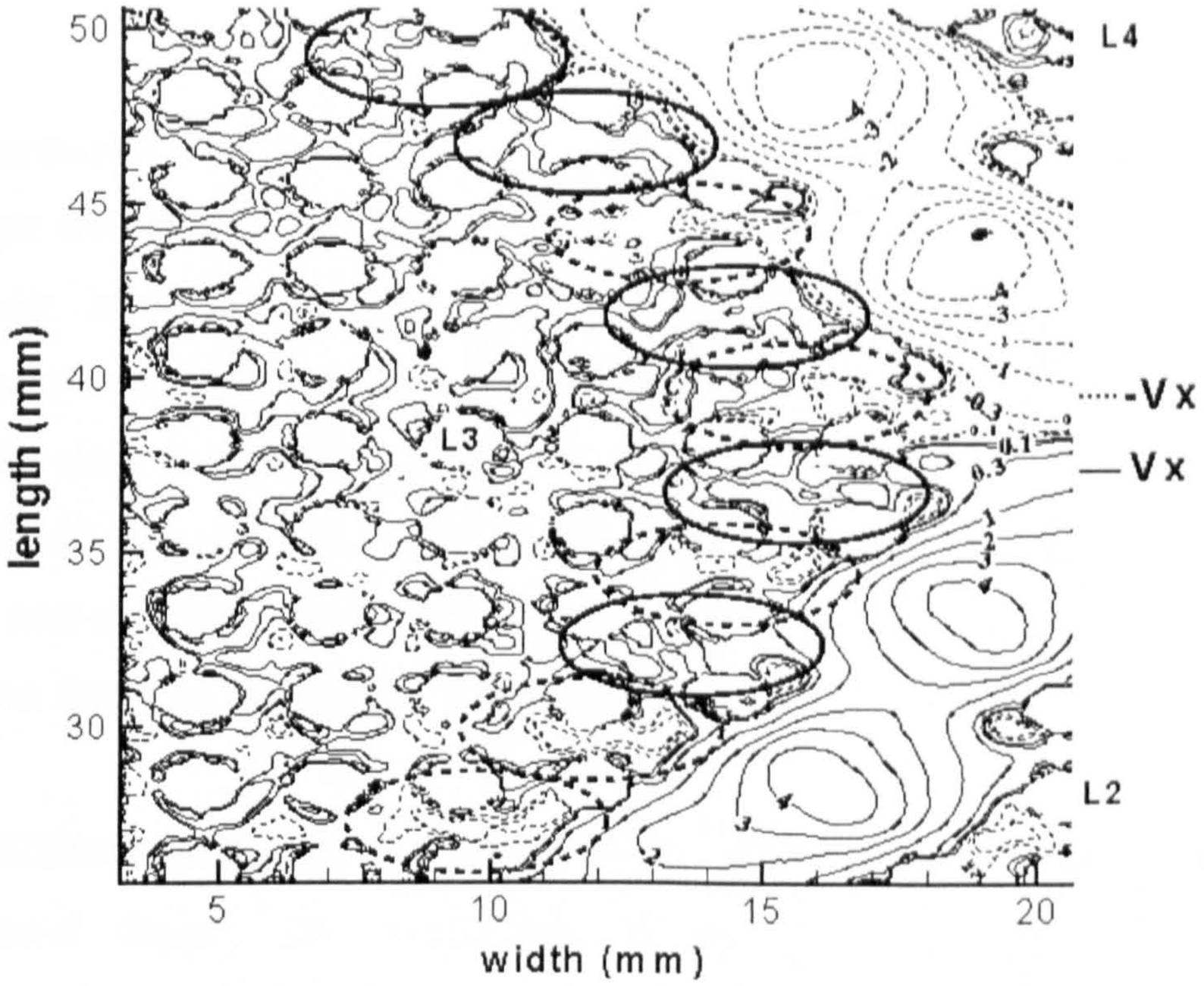


**Figure 5.17** The insert taken from Fig.(5.16) featuring contour velocity map of the transverse velocity component in the cell VII. Flow into (dashed encircled regions) or out of (solid encircled regions) the lattice L3 is dependent on the local configuration of the free flow region. The neighbouring fibre lattices L2 and L4 are at the bottom right and the top tight corner of the figure, respectively.

Hence, in the fibrous media of dual porosity in which the geometry of variable width free flow region is affected by the surface irregularities of the neighbouring lattices, the principle of 'the least resistance to flow' is once more obeyed.

These findings offer a more accurate description of local aspects of flow in more complex fibrous media of dual porosity. The implications of the findings are in the design of all relevant applications, which necessitate a better understanding of the interrelations between macroscopic and local aspects of the flows at meso and macro scales. With this contribution, the flow, heat and/or mass transfer characteristics of the porous systems can be better controlled and /or optimised.

## *5.3 Conclusions*

MRI velocimetry has been used to describe and assess the interrelation of macroscopic and local aspects of steady state slow flow fields across macroscopically semi-circular fibrous porous media coupled with neighbouring free flow. The model porous media were formed of single lattice-channel arrangements of various porosities and cylinder sizes. In addition, an assembly of lattices with a free flow region amongst the individual lattices is studied. The findings from the previous chapter that the back-mixing is non-existent in the system are confirmed. Within all the fibre lattices no recirculation zones occurred between the cylinders in the flow direction.

Due to a different macroscopic shape of the fibre lattice and the variable width of the open channel region, the distribution of both velocity components in the macroscopically semi-circular arrangement of fibres is fundamentally different from the velocity fields in the macroscopically rectangular fibre lattices adjacent to the channel of constant width. The experimental studies of flow over single lattice-channel arrangements have shown that, in many of the places between the cylinders in the flow direction, considerable local flow enhancements in the direction perpendicular to the main flow direction exist. These enhancements, in turn, produce the local velocity enhancements in the flow direction, which are present deeper within the lattice, and may even be extended to the lattice centre. The predictions of the lattice-Boltzmann model confirm, qualitatively and quantitatively, the existence and the concatenation of the local velocity enhancements in the two examined directions. The local flow enhancements are formed according to 'the least resistance to flow', i.e. are strongly dependent on the local macroscopic configuration of the fibre lattice. Hence, the flow within the fibre lattice must be treated in terms of its necessary connection with the flow in the free flow region. By controlling the macroscopic shape of the single fibre lattice and the width of the free flow region, the stagnant or recirculation regions within the fibre lattice could be either avoided (in heat and mass transfer applications) or facilitated (in filtration). It is shown that the local flow

enhancements within the fibre lattices are indispensable in the flow analysis in the fibrous media of dual porosity.

It has explicitly been demonstrated (by MRI experiments and the lattice-Boltzmann model) that slow flow over single symmetrical lattice-channel arrangements conforms to the laws of symmetry. The experimental and theoretical comparisons of the global characteristics of flows within the fibre lattices of different porosities and/or fibre diameters (gap sizes) and adjacent free flow regions have shown that the ratio of the maximum open channel velocities to the maximum fibre lattice velocities increase with decreased porosity of the fibre lattices and decreased size of the cylinders (gap between the cylinders). The agreement between the experimental findings and theoretical predictions is remarkably good, thus further establishing both MRI velocimetry and the lattice-Boltzmann model as powerful tools for the flow analysis in heterogeneous fibrous porous media.

The experimental evidence has shown that the penetration depths of the local transverse velocity enhancements are of comparable length within the fibre lattices in the cells IV (cylinder diameter D=4mm) and V (cylinder diameter D=3mm). The magnitudes of the local transverse velocity enhancements in these lattices are different, subject to the local internal configuration of the lattices. The local transverse velocity enhancements within the lattice in the cell VI (cylinder diameter D=2mm), although present, are considerably smaller in relation to the previous two fibre lattices due to increased surface area of the cylinders within the lattice offered for fluid friction.

The interrelation of macroscopic and local aspects of steady state slow flow fields across macroscopically semi-circular fibrous porous media coupled with neighbouring free flow is, in all fibrous porous media studied, based on the least resistance to flow principle offered by the local configuration of the lattices and the free flow regions. The local flow details in the vicinity of the lattice-channel interface of the more complex fibrous media of dual porosity (the lattice assembly) clearly discriminate this type of flow from the flows where the adjacent free flow regions are bounded by the walls or, from any other heterogeneous porous systems in which the fibre lattices are

sufficiently far apart from one another that they do not influence the flow pathways in the free flow region. Yet, the local features of flow in the interior of a lattice that constitutes the lattice assembly hinge on the local configuration of the adjacent free flow region, which is a fact common to all above mentioned types of flows. However difficult it seems to define the shape of fluid pathways in the free flow regions in complex porous media, it is advisable to assess the possibility of the presence or, in the more straightforward porous systems geometries, the number of the places in which fluid undergoes contraction or expansion in the free flow region. These places are a good indicator of the local velocity enhancements to occur within the adjacent fibrous (or any) medium of dual porosity. Hence, with knowledge of the geometry of the free flow and the porous region and an understanding of the interrelation between the two regions at the local and macroscopic levels presented here, the transport processes in porous systems of dual porosity are better understood.

*Bibliography*

[6] **Steenkamer D.A.; Mcknight S.H.; Wilkins D.J.; Karbhari V.M.:** Experimental Characterization of Permeability and Fibre Wetting for Liquid Moulding, *J. Mat. Sc.*, **30** (1995) 3207-3215.

[7] **Robertson F.C.:** Resin Transfer Moulding of Aerospace Resins- a Review, *Brit. Pol. J.*, **20** (1988) 417-429.

[8] **Luce L.T.; Advani G. S.; Howard J.G.; Parnas S.R.:** Permeability Characterisation. Part 2:Flow Behaviour in Multiple-layer Pperforms, *Pol. Comp.*, **16** (1995) 446-458.

[9] **Bruschke M.V.; Advani, S.G.; Parnas R.:** Resin Transfer Moulding. In: *Flow and Rheology in Polymer Composites Manufacturing*. pp. 465-516. Elsevier. Amsterdam, (1994).

[10] **Sadiq T.A.K.; Advani S.G.; Parnas R.S.:** Experimental Investigation of Transverse Flow Through Aligned Cylinders, *Int. J. Multiphase Flow*, **21** (1995) 755-774.

[11] **Phelan R.F.Jr; Wise G.:** Analysis of Transverse Flow in Aligned Fibrous Porous Media, *Comp. Part A*, **27A** (1996) 25-34.

[12] **Papathanasiou T.D.:** A Structure-oriented Micromechanical Model for Viscous Flow Through Square Arrays of Fibre Clusters, *Comp. Sc. Techn.*, **56** (1996) 1055-1069.

[13] **Bijeljic B.; Papathanasiou T.D.; Sederman A.J.; Mantle M.D.; Gladden L.F.:** Velocity Profiles Through and Over Arrays of Impermeable Cylinders, FED –vol.**243** / MD-Vol.**78**, *Rheology and Fluid Mechanics of Non-linear Materials*, *ASME* (1997).

[14] **Bergelin O.P.; Brown G.A.; Hull H.L.; Sullivan F.W.:** Heat Transfer and Fluid Friction During Viscous Flow Across Banks of Tubes-III: A Study of Spacing and Tube Size, *Trans. ASME*, August, (1950) 881-888.

[15] **Sangani A.S.; Acrivos A.:** Slow Flow Past Periodic Arrays of Cylinders With Application to Heat Transfer, *Int. J. Multiphase Flow*, **8**, 3 (1982) 193-206.

[16] **Geankoplis C.J.:** *Transport Processes and Unit Operations*. Boston (Mass.), London, Allyn and Bacon, 2nd edition, (1983).

[17] **Darcy H.:** Les Fontaines Publiques de la ville de Dijon. Paris:Dalmont. (1856).

[18] **Kozeny J.:** Uber Capillare Leitung des Wassers im Boden, *Sitz. Akad. Wissensch.*, **136** (1927) 271-306.

[19] **Carman P.C.:** Fluid Flow Through Granular Beads, *Trans. Am. Inst. Chem. Engrs.*, **15** (1937) 150-166.

[20] **Skartsis L.; Kardos J.L.; Khomami B.:** Resin Flow Through Fibre Beds During Composite Manufacturing Processes. Part I: Review of Newtonian Flow Through Fibre Beds, *Pol. Eng. Sc.*, **32**, 4 (1992) 221-230.

[21] **Chiemlewski C.; Petty C.A.; Jayaraman K.:** Cross Flow Permeation of Viscous and Viscoelastic Liquids in Cylinder Arrays. In: *Proceedings of the American Society for Composites*, Fifth Technical Conference, (1990) 557-565.

[22] **Pillai K.M.; Luce T.L.; Bruschke M.V.; Parnas R.S.; Advani S.G.:** Modeling the Heterogeneities Present in Preforms During Mould Filling in RTM, *25th International SAMPE Technical Conference*, **25** (1993) 279-288.

[23] **Beavers, G.S.; Joseph, D.D.:** Boundary Conditions at a Naturally Impermeable Wall, *J. Fluid Mech.*, **30** (1967) 197-207.

[24] **Bird R.B.; Stewart W.E.; Lightfoot E.N.:** *Transport Phenomena.* John Wiley&Sons Inc. 1960.

[25] **Brinkman H.C.:** A calculation of the Viscous Force Exerted by a Flowing Fluid on a Dense Swarm Systems of Particles, *Appl. Sci. Res.*, **1** (1947) 27-34.

[26] **Larson, R.E.; Higdon, J.J.L.:** Microscopic Flow Near the Surface of two-dimensional Porous Media. Part 1. Axial Flow, *J. Fluid Mech.*, **166** (1986) 449-472.

[27] **Durlofsky L.; Brady J.F:** Analysis of Brinkman equation as a Model for Flow in Porous Media, *Phys. Fluids*, **30** (1987) 3329-3341.

[28] **Nield, D.A.:** The Limitations of the Brinkman-Forcheimer equation in Modelling Flow in a Saturated Medium and at an Interface, *Int. J. Heat Fluid Flow*, **12** (1991) 269-272.

[29] **Martys, N.; Bentz, D. P.; Garboczi E.J.:** Computer Simulation Study of the Effective Viscosity in Brinkman's equation, *Phys. Fluids*, **6** (1994) 1434-1439.

[30] **Parnas, R.S.; Phelan,F. R.:** The Effect of Heterogeneous Porous Media on Mould Filling in Resin Transfer Moulding, *SAMPE Q.* , **22**, 2 (1991) 53-60.

[31] **Bruschke M.V.; Advani S.G.:** A Finite Element/control volume Approach to Mould Filling in Anisotropic Porous Media, *Pol. Comp.*, **11** (1990) 398-405.

[32] **Berdichevski A.L.; Cai Z.:** Preform Permeability Predictions by self-consistent Method and Finite Element Simulations, *Pol. Comp.*, **14**, 2 (1993) 132-143.

[33] **Larson, R.E.; Higdon, J.J.L.:** Microscopic Flow Near the Surface of two-dimensional Porous Media. Part 2. Transverse Flow, *J. Fluid Mech.*, **178** (1987) 119-136.

[34] **Papathanasiou T.D.:** On the Effective Permeability of Square Arrays of Permeable Fibre Tows. *Int. J. Multiphase Flow*, **23**, 1 (1997) 81-92.

[35] **Spaid M.A.A.; Phelan F.R.Jr.:** Lattice-Boltzmann Methods for Modeling Microscale Flow in Fibrous Porous Media, *Phys.* Fluids, **9**, 9 (1997) 2468-2474.

[36] **Chen S.; Doolen G.D.:** Lattice Boltzmann Method for Fluid Flows, *Annu. Rev. Fluid Mech.*, **30** (1998) 329-364.

[37] **Clague D.S.; Kandhai B.D.; Zhang R.; Sloot P.M.A.:** Hydraulic Permeability of (un)bounded Fibrous Media Using the Lattice Boltzmann Method, *Phys. Rev. E*, **61**, 1 (2000) 616-625.

[38] **Jackson G.W.; James D.F.:** The Permeability of Fibrous Porous Media, *Can. J. Chem. Eng.*, **64** (1986) 364-374.

[39] **Yarlagadda A.P., Yoganathan A.P.:** Experimental Studies of Model Porous Media Fluid Dynamics, *Exp. Fluids*, 8, (1989) 59-71.

[40] **Saleh, S.; Thovert, J.F.; Adler, P.M.:** Flow Along Porous Media by Particle Image Velocimetry, *AIChE J.*, 39 (1993) 1765-1776.

[41] **Gupte, S.K., Advani,S.G.:** Flow Near the Permeable Boundary of a Porous Medium: An Experimental Investigation Using Laser Doppler Anemometry, *Exp. Fluids*, **22** (1997) 408-422.

[42] **Gupte, S.K., Advani,S.G.:** Flow Near the Permeable Boundary of an Aligned Fibre Preform: An Experimental Investigation Using Laser Doppler Anemometry, *Pol. Comp.*, **18**, 1 (1997) 114-124.

[43] **Callaghan, P.T.; Xia, Y.:** Velocity and Diffusion Imaging in Dynamic NMR Microscopy, *J. Magn. Res.*, 91 (1991) 326-352.

[44] **Durst, F.; Melling, A.; Whitelaw, J.H.:** *Principles and Practise of Laser-Doppler Anemometry*, 2nd edition, Academic Press, London (1981).

[45] **Adrian, RJ.:** Particle-Imaging Techniques for Experimental Fluid Mechanics, *Ann. Rev. Fluid Mech.*, **23** (1991) 261-304.

[46] **Heath, C.A.; Belfort, G.; Hammer, B.E.; Mirer, S.D; Pimbley, J.M.:** Magnetic Resonance Imaging and Modeling of Flow in Hollow-Fibre Bioreactors, *AIChE J.*, **36**, 4 (1990) 547-558.

[47] **Givler, R.C.; Altobeli, S.A.:** A Determination of the Effective Viscosity for the Brinkman-Forcheimer Flow Model, *J. Fluid Mech.*, **258** (1994) 355-370.

[48] **Kutsovsky, Y.E.; Scriven, L.E.; Davis, H.T.; Hammer, B.E.:** NMR Imaging of Velocity Profiles and Velocity Distributions in Bead Packs, *Phys. Fluids*, 8, 4 (1996) 863-871.

[49] **Bloch, F.; Hansen, W.W.; and Packard, M.:** Nuclear Induction, *Phys. Rev.*, 69, (1946) 127.

[50] **Purcell, E.M.; Torrey, H.C.; Pound, R.:** Resonance Absorption by Nuclear Magnetic Moments in a Solid, *Phys. Rev.*, **69** (1946) 37.

[51] **Stejskal, E.O. ;Tanner, J.E.:** Spin Diffusion Measurements: Spin Echoes in the Presence of a Time-dependent Field Gradient, *J. Chem. Phys.*, **42** (1965) 288.

[52] **Lauterbur, P.C.:** Imaging Formation by Induced Local Interactions: Examples Employing Nuclear Magnetic Resonance, *Nature,* **242**, (1973) 190-191.

[53] **Mansfield, P.; Grannell, P.K.:** NMR 'Diffraction' in Solids, *J. Phys. C,* **6**, (1973) L422.

[54] **Mansfield, P.; Grannell, P.K.:** "Diffraction and Microscopy in Solids and Liquids by NMR," *Phys. Rev. B,* **12**, (1975) 3618.

[55] **Callaghan, P.T.:** *Principles of Magnetic Resonance Microscopy.* Oxford, Oxford University Press (1991).

[56] **Gladden, L.F.:** Nuclear-Magnetic-Resonance in Chemical-Engineering - Principles and Applications, *Chem. Eng. Sci.*, **49** (1994) 3339.

[57] **Fukushima, E.; Roeder, S.B.W.:** *Experimental Pulse NMR.* Reading, Massachusetts, Addison-Wesley (1981).

[58] **Edelstein, W. A.; Hutchinson J. M. S.; Johnson, G.; Redpath, T.:** Spin Warp Imaging and Application to Human Whole-Body Imaging, *Phys. Med. Biol.*, **25** (1980) 751-756.

[59] **Warren, P.B.:** Electroviscous Transport Problems via lattice-Boltzmann, *Int. J. Mod. Phys. C*, **8** (1997) 889-898.

[60] **Manz, B.; Warren, P.B.; Gladden, L. F.:** Flow and Dispersion in Porous Media: lattice-Boltzmann and NMR Studies, *AIChE. J.*, **45** (1999b) 1845-1854.

[61] **Brebbia, C.A.; Dominguez, J.:** *Boundary Elements: an Introductory Course,* 2nd edition, Computational Mechanics Publications, Southampton (1992).

# PART II

## *Flow and Mass Transfer in a Granular Porous Medium of Dual Porosity*

# Chapter 6

# Mass Transfer in Fixed Beds of Porous Particles

The porous medium used in this part of the study was comprised of a fixed bed column packed with porous spherical calcium-alginate particles. It is a system in which mass transfer phenomena may occur in the interparticle and intraparticle spaces, i.e. two porous media with different structures and scales. In the following, the reasons for making the selection of this particular system are explained; the relevant background in this research field is given together with the way in which it led to gaining the motivation for this investigation.

## *6.1 Packed Bed Column as a Choice for Heterogeneous Catalytic Bioreactor*

Mass transfer in systems consisting of beds of porous particles and a flowing liquid arises as an essential issue in the design of many industrial devices used for adsorption, chromatography, ion exchange, leaching and, particularly important, heterogeneous catalysis. In heterogeneous catalytic reactors, catalyst particles can be fixed (fixed beds, trickle beds) or suspended in fluid and constantly moving (fluidised beds, slurry reactors). In fixed bed reactors, the motion of catalyst particles relative to one another is insignificant. Fixed bed reactors are often referred as packed beds; the latter is the nomenclature that will be used in the subsequent parts of this thesis.

Classic two-phase packed bed reactor is selected as it is commonly used in the deployment of fixed immobilised catalysts [62]. The merits of packed beds predominantly lie in their simplicity and flexibility. The construction, operation and maintenance costs are relatively small which makes them suitable for the use as small commercial units. Further, the operating conditions can be varied broadly rendering

them as the first choice where the wide variations in the quality and quantity of the feedstock occur. In addition, there are no requirements for the catalyst separation from the effluent stream, although care must be taken in designing when the catalyst deactivation is rapid and the catalyst needs to be regenerated.

Calcium-alginate particles were selected in this study as they have been increasingly used as the biocatalyst porous matrices for the immobilisation of enzymes or cells in fermentation processes. Their applications range from the production of foods to pharmaceuticals, from liquid fuels to organic chemical feedstocks [63]. Some particular examples of bio-processes utilising immobilised cells or enzymes are the continuous production of fructose syrup from corn starch [64], production of penicillin from penycilin acylase [65], production of ethanol from sugars [66,67] and the use of immobilised urease for the removal of urea from blood plasma in an artificial kidney device [68]. When biocatalysts are retained in the immobilised state inside highly porous, insoluble support matrices they have a good resistance to accidental changes in operational conditions, allowing the use of higher flowrates during wash-out and yielding more uniform and less contaminated products [64,69].

## *6.2 The Performance of Heterogeneous Packed Bed Reactors*

The overall performance of heterogeneous packed bed reactors can be affected by various mechanisms. Generally, the global reaction rate in the reactor depends on the following rates:

- the rate of mass transfer of the reactants from the bulk liquid to the external surface of the particles;
- the rates of diffusion of reactants from the particle exterior surface to the particle interior;
- the rates of adsorption of reactants;
- the rate of chemical reaction;
- the rates of desorption of products;

- the rates of diffusion of products from the particle interior to the particle external surface;
- the rates of mass transfer of the products from the external surface to the bulk liquid.

Determination of the global reaction rate of the reactor necessitates a comprehensive study of the intrinsic rate expressions, the flow conditions (velocity), properties of the fluid (concentration, diffusion coefficient), properties of the catalyst (porosity, diffusion coefficient) as well as the bed properties (bed voidage, reactor diameter, the size and the shape of the catalyst).

The prediction of these properties, being based on theoretical and empirical laws, is subject to large uncertainties and therefore experimental techniques are often employed for the 'on-line' determination of the parameters of interest. For this purpose steady state or dynamic experiments are commonly used. Steady state experiments are utilised in a variety of processes such as dissolution, evaporation, sublimation and vaporisation. At steady state, the individual rates of the various mass transfer and consumption mechanisms are identical and, thus, steady state experiments can yield only the global rate or the rate of the controlling step. However, in a heterogeneous catalytic reactor operational parameters are never free from disturbances. Thus, a good description of the rector dynamics is often required. During a transient experiment, the individual steps, characterised by the individual rate constants, proceed with unequal rates. This fact allows for the simultaneous determination of several rate constants from one experiment. In addition, transient experiments are carried out to characterise start-up and shutdown reactor performances, transitions between multiple steady states and the analysis of the regulation or control by injecting inhibitors, activators and cosubstrates.

### *6.2.1 Objectives in Studying Hydrodynamic Dispersion and Mass Transfer in Packed Beds*

As outlined in the previous paragraph, besides knowledge of adsorption, desorption and reaction kinetic properties, prediction and optimisation of the performance of packed bed reactors requires quantitative knowledge of hydrodynamic dispersion and mass transfer rate characteristics. Hydrodynamic dispersion and mass transfer in packed beds occur and therefore need to be scrutinised at different length-scales.

The length-scales of molecular mean free path characterised by transport of species by diffusion and the scale of the leading dimension of the reactor characterised by transport of species by convection are immediately recognisable as relevant. In addition, in packed beds there is the movement of molecules and aggregates under the influence of concentration gradient at an intermediate length-scale that is characterised by the dispersion phenomena.

Fluid molecules, or aggregates, are moving through the gaps between porous particles in a packed bed under the influence of concentration gradient in a random fashion. In the intraparticle space, fluid elements are deflected sideways and mixing occurs. The mixing takes place frequently and can be considered statistical. As a result, there will be concentration fluctuations arising in the direction of flow due to slippage (molecular diffusion) and due to formation of eddies (convective back-mixing or turbulent diffusion). Moreover, the velocity distribution over a cross section is non-uniform and the residence time of the fluid elements travelling along the different streamlines is different. This is valid only if the flow direction is opposite at different positions in the cross sections of the reactor. All these effects give rise to dispersion phenomena.

Dispersion in tubes (Taylor, 1953,1954; Aris 1956) [70-72] and packed beds (Bischof, 1961; Levenspiel, 1999, Chang and Wen, 1968) [73-75] have been well documented in the literature. Due to specific complicated geometry in packed beds, it is advisable

to determine dispersion characteristics of the studied column experimentally. Hydrodynamic dispersion is typically characterised by analysing the dynamic response of a column to a step or pulse change in the inlet tracer concentration according to either the tanks-in-series or the dispersion models [74].

It is of practical interest to see if the change in the packing of the column from non-porous to porous particles would alter the hydrodynamic dispersion in the column. Moulijn [76] studied axial mixing in the column of porous particles concluding that the degree of overall axial mixing in the column is higher compared to the column packed with non-porous particles. As suggested by Westerterp *et al.* [77] the interparticle and intraparticle space regions should be distinguished; this idea has been pursued in this study. Leitao *et al.* (1994) [78] experimentally studied liquid phase axial dispersion in the intraparticle space of the columns filled with porous and non-porous packing at Reynolds numbers ranging from 1 to 50 and various bed to particle diameters. They inferred that, within the range of the experimental error, the effects of axial dispersion were equal in both cases.

However, the dynamic response of a packed bed column made up of porous particles is known to be also affected by fluid-to-particle mass transfer [79, amongst many others]. The complexity of geometry of porous spherical (or any other geometry) particle assembly in packed beds makes investigation and prediction of overall mass transfer effects difficult. A logical attempt in looking into fundamental mechanisms of mass transfer in packed beds is to define an element large enough to be representative of the bed and, at the same time, small enough to allow complete understanding of what is happening within. By defining such an element, i.e. unit cell of the bed, the overall behaviour of the heterogeneous system, with complex geometry, is represented by the behaviour of its strictly defined elements (unit cells) that make up a quasi-homogeneous system. These type of models are termed cell models.

In cell models, a sphere of radius $R$ is assumed to be surrounded by a spherical shell of fluid (continuous medium), sometimes also called fluid envelope, of radius $a$. The relative volume of the fluid envelope to the particle volume in the unit cell is the same as the ratio of the intraparticle space (bed voidage) to the volume fraction of the

spheres in the bed. An illustration of the cell model, in which the concentration gradients in the fluid envelope are shown, is presented in Fig.(6.1).

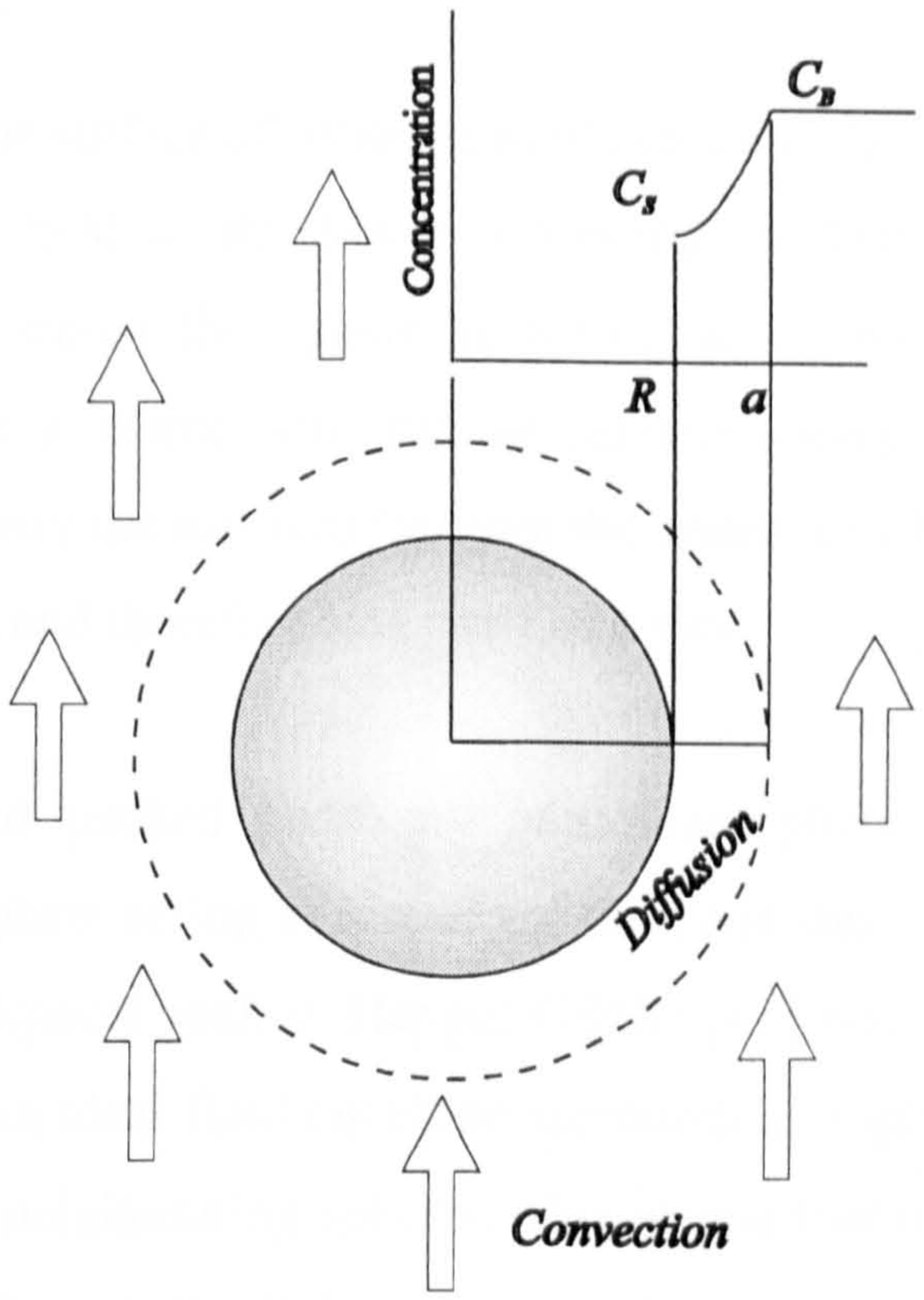


**Figure 6.1** Unit cell consisting of a spherical particle. The particle radius is $R$ and the fluid envelope radius is $a$. The gradient between the fluid concentrations in the bulk ($C_B$) and the concentration at the particle surface ($C_s$) is illustrated. Mass transfer occurs by convection in the bulk liquid and diffusion near the particle surface.

The first theoretical analysis of heat and mass transfer from a single sphere into an infinite medium was done by Froessling (1938) [80] and in the engineering practice was introduced by Ranz and Marshall (1952) [81]. Mass transfer from a single sphere is given by the equation:

$$Sh_p = 2 + 0.6 Re_p^{1/2} Sc^{1/3}, \tag{6.1}$$

where $Sh_p$ is dimensionless numbers which represents the ratio of total mass transfer (including advection and diffusion) to molecular mass transfer from the particle, through the dependence on the particle Reynolds number, $Re_p$, and the Schmidt

number, *Sc*. Definition and physical meanings of these numbers are given in Appendix 2. It is important to note that for steady-state conditions the value for mass transfer for mass transfer from a single sphere has the finite value 2. This is the result of the following considerations [82]:

The concentration at the surface of sphere is held constant (the sphere acts as a source) while the medium is held at the lower concentration. One can also assume the opposite situation in which the sphere is acting as a sink and the surrounding continuous medium is a source with similar considerations. When the radius $a$ is increased towards infinity the medium far from the sphere can be considered to have a constant concentration and therefore acts itself as a sink.

However, in undiluted packed beds any particular sphere is a member of the assembly, with each sphere acting as a source / sink, and this boundary condition can no longer represent physical reality. Happel (1958) [83] postulated a 'free surface' model, assuming that an ideal fluid envelope surrounding a sphere that is undistorted by the presence of the neighbouring spheres. This means that the surface boundary of the fluid envelope ('free surface') is not in contact with solid boundaries of the neighbouring particles. The solution for heat and mass transfer is also a function of the distance between the spheres (or bed voidage) and is given by Pfeffer in [84]:

$$Sh_p = 1.26\left(\frac{1-x^5}{2-3x+3x^5-2x^6}\right)^{1/3}(Re_p Sc_p)^{1/3}, \qquad (6.2)$$

where $x$ is proportional to the bed voidage $x=(1-\varepsilon)^{1/3}$.

Nelson and Galloway (1975) [85] have used a similar fluid envelope concept with the finite radius $a$ boundary condition. That is, the radial gradient of concentration at the surface of the fluid envelope is zero in respect with space and time. The fluid concentration at the surface of the sphere is spatially uniform but time dependent, being renewed according to the Danckwerts penetration theory [86] with a renewal frequency, $s$. The particle Sherwood number, $Sh_p$, is defined as the ratio between time averaged mass transfer rate per unit area of the particle surface, $N_{av}$, to the mass

transfer rate in the external fluid envelope per the same unit area, $N_{ext}$. The solution of Nelson and Galloway in the final form is:

$$Sh_p = \frac{2z + \{\frac{2z^2(1-\varepsilon)^{1/3}}{[1-(1-\varepsilon)^{1/3}]^2} - 2\}\tanh z}{\frac{z}{1-(1-\varepsilon)^{1/3}} - \tanh z}, \qquad (6.3)$$

where

$$z = [\frac{1}{(1-\varepsilon)^{1/3}} - 1]\frac{\alpha}{2} Re^{1/2} Sc^{1/3}. \qquad (6.3a)$$

The model has an adjustable parameter, α, and for infinite dilution ($\varepsilon$=1) matches Froessling solution for the single sphere. The authors suggest its use in the range of $0.08<Re_p<100$. The model predicts an increase in mass transfer coefficient with the increase in the bed voidage, which is not logical since the interstitial velocity increases with decreasing bed voidage (Rowe) [87]. Besides, the definition of $Sh_p$ in the model is based on the initial time concentration difference between the surfaces of the fluid envelope and the sphere, instead of the time averaged concentration difference, since the concentration of the fluid envelope may vary with time.

As could be seen from the above discussion, the analytical solutions obtained from Navier-Stokes equations have their merits and disadvantages. Yet what is common to all of them is the functional dependence of the particle Sherwood number on the particle Reynolds number, the Schmidt number and bed voidage (which is affected by geometry). Another way of solving this functional dependence is by dimensional analysis. Dimensional analysis is used for problems in which the available knowledge is not sufficient and whose physical laws are therefore only accessible by experiments. The relevant physical variables in packed beds are known and by setting up the list of relevant parameters and using the Buckingham pi-theorem [16], the following equation can be obtained:

$$Sh_p = ARe^b Sc^c. \qquad (6.4)$$

An enormous number of data for gas and liquid to particle mass transfer exists in the literature. The often cited reviews are these by Thoenes and Kramers [88], Kunii and Suzuki [89], Wakao and Funazkri [90] as well as by Dwivedi and Upadhyay [91]. All of them give various correlations of the form of equation (6.4) and will be used for comparison in this study.

On the other hand, experimental data for mass transfer in packed beds are interpreted in the literature in different ways, leading to a different definition of the Sherwood number. Many authors in the past [92] have used a simple plug flow model assuming no axial dispersion in the bed. They related the Sherwood number to a bed averaged inlet and outlet concentration driving force across the bed, thus obtaining so called 'overall', or 'effective' Sherwood number of the bed. Alternatively, the particle Sherwood number of the unit cell described previously in the text can be calculated by parameter fitting the experimental data to the solution of the governing differential equations given by the tanks-in-series or dispersed plug flow models. The advantage of the latter interpretation lies in the fact that the axial dispersion is accounted for as an individual effect in the analysis.

Many authors have pointed out on the influence of axial dispersion in the low Reynolds-low Peclet number regime (Gunn [93], Fedkiew and Newman [94], Wakao and Funazkri [90], Glicksman and Joos [95]) and, more recently, (Tsotsas [96], Rexwinkel *et.al.* [97]) in order to justify the surprising drop in Sherwood number at low Peclet numbers. Other authors (Schlunder [98], Westerterp *et al.* [99]) did not ascribe this peculiarity to molecular kinetics but to the non-uniform pore size distribution of the system. It is very important to distinguish the convection-diffusion regime at low Reynolds-low Peclet number regime from the one studied here; in liquids, the Peclet number is usually three orders of magnitude higher than in gases so the regime can be termed the low Reynolds-high Peclet number regime which has intrinsically different physical mechanisms governing mass transfer.

To summarise, many attempts to measure, model and correlate steady-state mass transfer data in traditional packed-bed reactors have been made but the effect of fluid-

to-particle mass transfer on the dynamic characteristics of reactors still needs to be investigated in detail. In transient experiments the concentration of the fluid at the particle surface and the surface of the fluid envelope may be postulated to be uniformly accessible (constant in respect with space); however both concentrations vary with time which makes the problem more complex. A dynamic model based on the unit cell approach with time dependent surface concentrations is used for the analysis of flow and mass transfer in a packed bed in this study. Its features are outlined in the Chapter 7.

The mechanisms of mass transfer in bioreactors were studied by Gilson and Thomas [66], who considered the steady state intraparticle diffusion and consumption of substrate in a fluidised bed made up of alginate beads in the 1-5mm size range. Although they attributed the observed lower yield in the immobilised cell reactor as compared to a free-cell reactor to the lower substrate concentration occurring towards the centre of the bead they did not consider the dynamics of intraparticle transport or its coupling with substrate transport in the bulk liquid. De Backer and Baron [100] measured the dynamic response of packed beds of porous and non-porous glass particles of 3 mm in diameter, in the presence or absence of immobilised yeast cells, using methyl orange as a tracer. They observed that the response of a bed loaded with porous particles exhibits a longer tail, compared to the response of a bed filled with impermeable particles. The experimental data were fitted successfully to the dispersion model coupled with the equation for mass transfer in the intraparticle space. An increase in the apparent intraparticle diffusivity with Reynolds number (for the narrow range $Re_p$<10 examined) led the authors to comment that intraparticle convection might become important at $Re_p$>1.

Provided that the pressure drop is not sufficient to force a perceptible amount of fluid through very small pores of catalyst particles, the intraparticle mass transfer will be driven by diffusion. If the particle size is smaller than 0.16mm, the pressure drop is deemed excessive and affects the mechanical strength of the particles. In liquids, the mean free path of their molecules is small compared with the diameter of the pore. Under these conditions, the collisions with other liquid phase molecules will be much more frequent than the collisions with the pore walls. Thus, the effective diffusion

coefficient in the porous catalyst is not a function of the pore diameter and the diffusion coefficient from the first Fick's law can be used in evaluating the rate of mass transfer. Bearing in mind that the size of the immobilisation beads is frequently of the order of a few millimetres and that Fickian diffusion in the intraparticle space is an intrinsically slow process compared to convection in the bulk liquid phase, it is of substantial interest to specifically quantify the effect of the former on the dynamic characteristics of an heterogeneous catalytic packed bed reactor.

The objective of this investigation is to carry out detailed dynamic tracer experiments, using typical biological support matrix material namely Ca-alginate beads of various sizes, in order to determine the extent to which intraparticle diffusion affects the observed (apparent) transient response of a packed bed column. It seeks to determine the flow conditions that give a physical limitation on the rate at which the fluid reactant is transported from the bulk liquid onto the particle exterior surface. Under these flow conditions, the maximum rate of fluid to particle mass transfer will be quantified. An increase of turbulence in the bulk liquid would have no significant influence on the rate of mass transfer.

### *6.2.2 Objectives in Studying The Influence of The External Mass Transfer Resistance on The Reactor Performance*

Various flow conditions with lower tracer velocities in the column will influence the average rate at which the fluid is supplied from the bulk liquid. Velocity patterns in the interstitial space of the column will be changed and interaction of fluid elements flowing over particles will be affected. The fluid to particle mass transfer will be, in general, impeded in the external film of liquid surrounding the particles as well as in the particles interior. In particular, if in a heterogeneous catalytic reactor the catalyst is highly active (fast chemical reaction), the reactants are converted to the products at the surface or within the shallow part of the periphery of the pellet. As a result, the internal surface area of the pellet closer to the centre is not used which leads to low effectiveness and conversion. At the same time, the concentration gradient between

the pellet surface and the fluid is large and the external resistance to mass transfer is likely to be the controlling step in the global reaction rate. In order to predict and optimise the operating conditions in such a heterogeneous catalytic reactor it is necessary to determine the extent to which both the internal and the external mass transfer rates are affected by various flow conditions.

The time scale of mass transfer rates occurring in the external liquid film and the particle interior is described by the dimensionless Biot number (see Appendix 2).

The effect of diffusional resistance on the action pattern of α-amylase immobilised on corn-grits and porous silica as water-insoluble supports was investigated by Siso *et.al.* (1990) [101]. The external mass transfer resistance for the transfer of the products of reaction were found to be considerable, being most pronounced when the surface contact area between the liquid and the catalyst was the smallest.

The influence of the external and internal mass transfer resistance on the production of ethanol from deprotenised whey in a reactor packed with calcium alginate beads was modelled by Axelsson and Zacchi (1991) [102]. Assuming steady state conditions they present the concentration profiles versus reactor length curves from which they ascertain the external mass transfer to be of minor importance for Biot numbers 10-100 whereas the curve with Biot number 1 is appreciably different. Similar conclusion that the external resistance become negligible above a certain value of the external mass transfer coefficient and Biot number was drawn by Hassan *et al.* (1995) [103] in their analysis of non-isotermal reactors. Nath and Chand (1996) [104] considered the quantitative treatment of steady state mass transfer combined with biochemical reaction in heterogeneous catalytic reactors. They found out that the effect of the external film diffusion on reaction rate is significant and should not be ignored in engineering analysis. They suggest the use of a mass transfer correlation for the continuous conversion of sugars to ethanol in heterogeneous catalytic reactors, estimating the effect of external mass transfer on the observed reaction rates.

From the above considerations arises the motivation for this part of the study. Herein, the objective of the investigation is to determine the flow conditions under which the

fluid to particle mass transfer resistance in the external film of liquid surrounding the packing is sufficiently large that it alters the observed (apparent) transient response of a packed bed column packed with porous Ca-alginate beads. This information can be very valuable for operating a heterogeneous catalytic reactor in practice. For instance, if the fluid to particle mass transfer is mainly limited in the external film, increasing the turbulence in the bulk liquid could be the best way to enhance the overall mass transfer rate. On the other hand, if the mass transfer is profoundly hindered in the particles interior, the effort should be spent on decreasing the particle size or increasing the porosity of the pellets.

In order to examine how the effective fluid-to-particle mass transfer varies by altering the velocity patterns in the bulk liquid the experiments were carried out in the moderate and low Reynolds number regime with Reynolds numbers decreasing from 50 down to 0.3. At the same time particle Peclet numbers in this investigation were high or moderate, ranging from 40000 down to 250. The experimental observations are compared with the predictions of a model for the dynamic response of a heterogeneous catalytic reactor developed by Papathanasiou *et al.* [105].

# Chapter 7

# Mass Transfer Theory Pertinent to Granular Porous Media in Packed Beds

This chapter commences with the fundamental theory of mass transfer in a diluted binary mixture. Further, adequate mathematical models for fluid flow and mass transfer in fixed beds of porous particles are delineated to the extent necessary for understanding and analysing the issues relevant to this study. Besides, it is shown how to implement the models in a way that does not affect the quantitative accuracy in the interpretation of the experimental data. Finally, the empirical correlations as the most common way of presenting the results for mass transfer in packed beds in the literature are briefly explained.

## *7.1 Fundamentals of Mass Transfer*

Mass transfer is a physical phenomenon in which species are transported due to a concentration difference existing in a medium. At the molecular level, the movement of species can occur by two different mechanisms: diffusion and convection.

### *7.1.1 Diffusion*

Diffusion occurs as a consequence of the random molecular motion. Diffusion of one component in a diluted binary mixture is illustrated in Fig.(7.1). Different concentrations of a fluid *a* in a solvent fluid *b* are placed in two regions (1 and 2) of a closed vessel. The difference in concentration is represented by the numbers of fluid molecules *a* (exaggerated spheres in Fig.(7.1)) in both regions. The regions are

separated by a completely permeable membrane that offers no resistance to the fluid motion. The fluid molecules are in constant motion and their interactions with one another, molecules of the solvent and the wall frequently take place. The molecules have equal probability of moving in any direction.

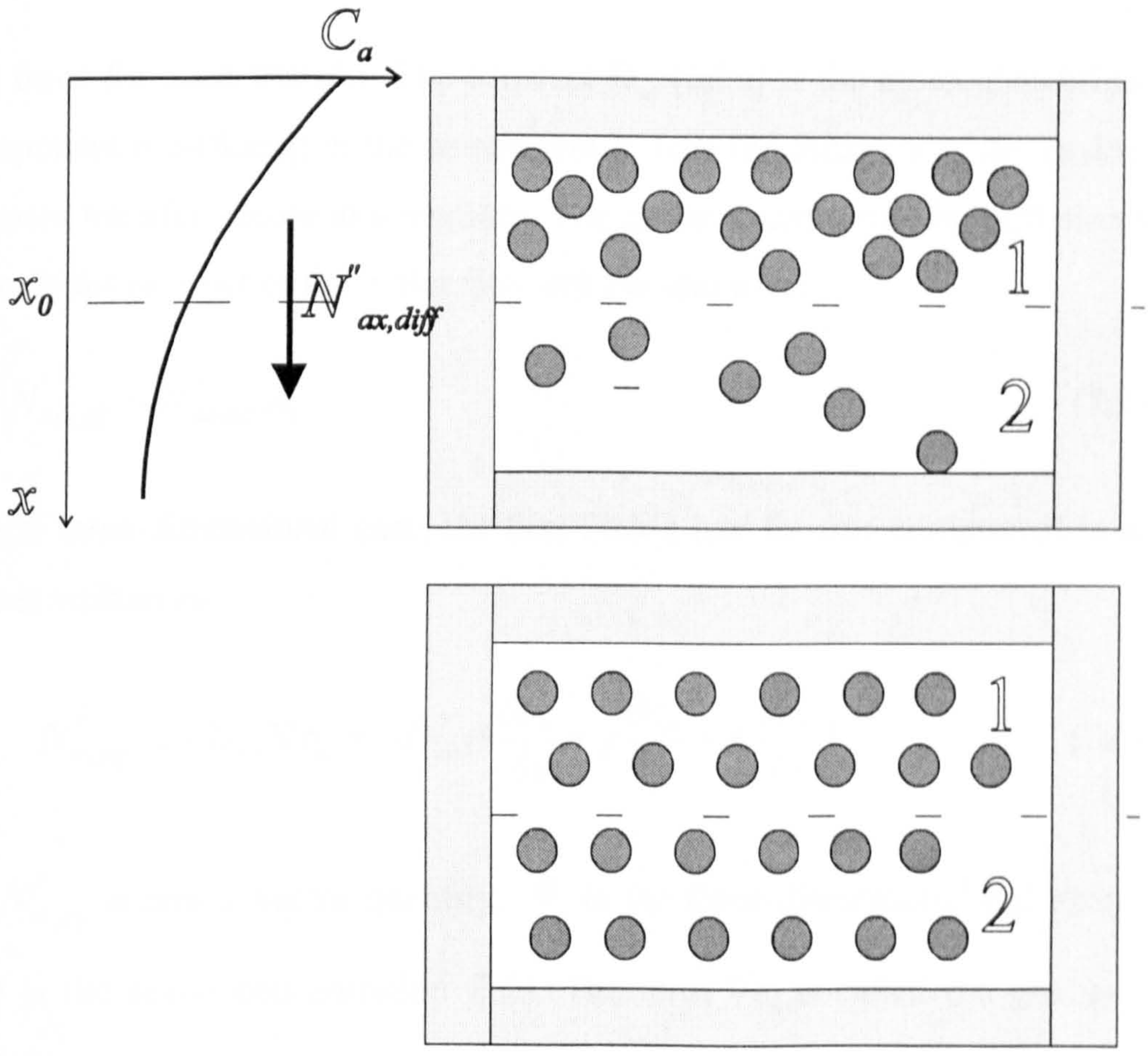


**Figure 7.1** Diffusion of one component in a diluted binary mixture of *a* and *b*. The direction of mass flux is always from the region with higher concentration to the region with lower concentration. A) initial state with different fluid concentrations B) the equilibrium state.

After a period of time, more molecules from the region 1 associated with the higher fluid concentration will cross into the part 2 with the lower fluid concentration then in the vice versa transport process. As a result, there will be transfer of species in the $x$ direction that can be described by the equation:

$$N''_{ax,dif} = -D_{ab}\frac{\partial c_a}{\partial x}. \tag{7.1}$$

This equation is known as the first Fick's law of diffusion. The molar flux $N''_{ax,dif}$ [mol/m$^2$s] is the molar transfer rate in the $x$-direction per unit area, $A_n$, perpendicular to the direction of mass transfer. The existence of the concentration gradient $\frac{\partial c_a}{\partial x}$ is the driving force for mass transfer. The constant $D_{ab}$ [m$^2$/s] is the molecular diffusivity of the component $a$ diffusing in the component $b$. It is the measure of the easiness with which mass transfer occurs in a medium. The molar transfer rate by diffusion in the $x$ direction is the product of the molar flux and the unit area:

$$N_{ax,dif} = N''_{ax,dif} A_s. \tag{7.2}$$

In general three-dimensional case, the first Fick's law for one component in a binary mixture is written as:

$$N''_{a,dif} = -D_{ab}\nabla c_a = -D_{ab}(i\frac{\partial c_a}{\partial x} + j\frac{\partial c_a}{\partial y} + k\frac{\partial c_a}{\partial z}), \tag{7.3}$$

where $N''_{a,dif}$ is now a vector quantity, $\nabla$ is the three-dimensional del operator and $c_a(x,y,z)$ is the scalar concentration field. The term $\nabla c_a$ is called the gradient of the scalar field $c_a$.

### 7.1.2 Convection

When a fluid flows large number of molecules are moving collectively and can be viewed as aggregates. Mass is transferred by bulk, macroscopic motion of such molecular aggregates due to concentration differences amongst them. This mechanism of mass transfer is called advection. The total mass transfer which includes the random molecular motion (diffusion) and the bulk macroscopic motion of fluid (advection) is referred to as convection mass transfer.

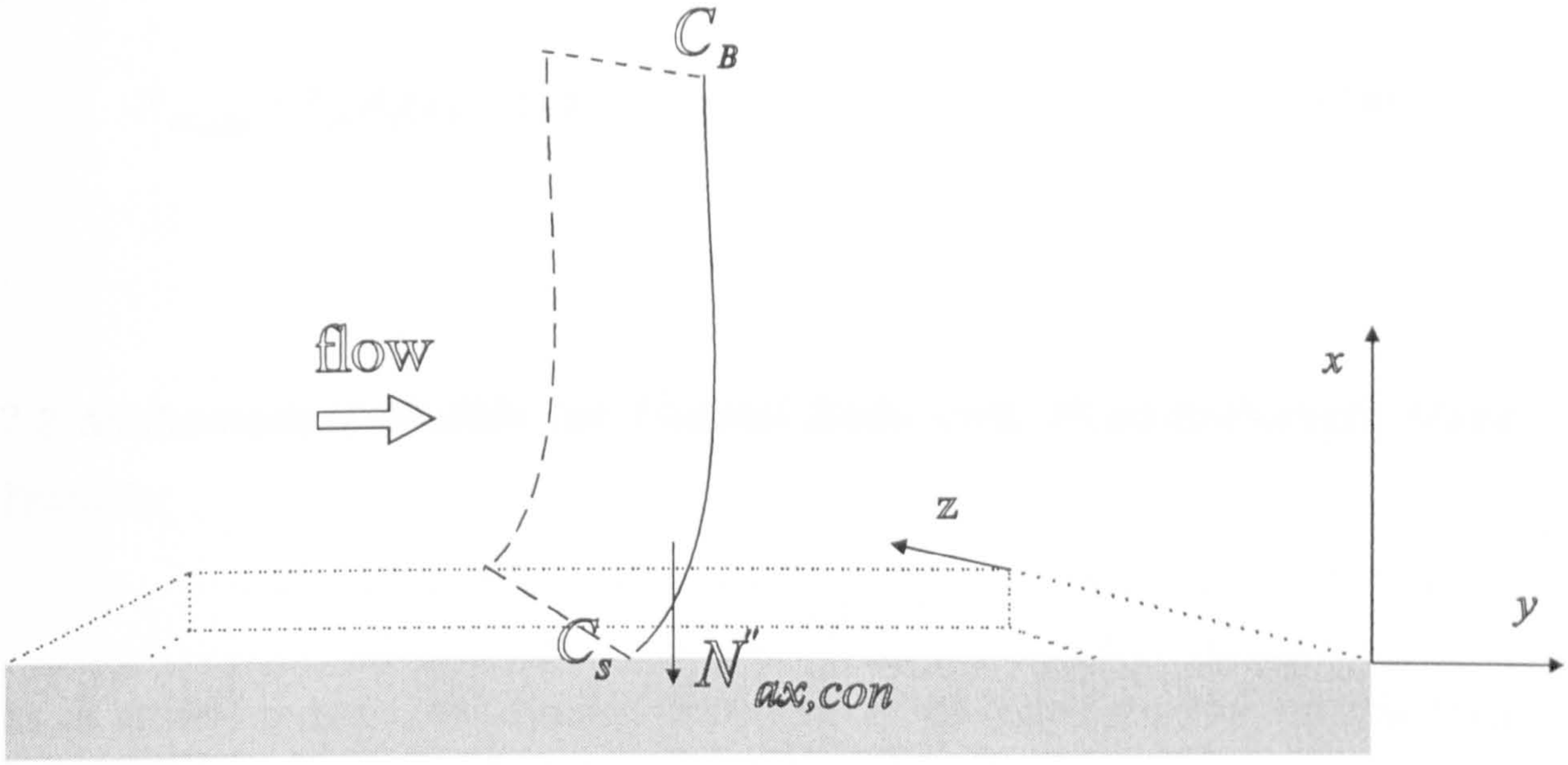


**Figure 7.2** Convection as a mechanism of mass transfer. Concentration boundary layer of fluid is developed in the vicinity of the solid porous surface. $C_S$ and $C_B$ are fluid molar concentrations of the fluid at the surface and in the bulk respectively.

Fig.(7.2) shows one-dimensional flow of a fluid *a* over an infinite flat porous surface. If $c_S$ and $c_B$ are molar concentrations of the fluid at the surface and in the bulk respectively, then the species transfer in the *x*-direction expressed as a convective molar flux $N''_{a,con}$ is:

$$N''_{ax,con} = k(c_B - c_S), \tag{7.4}$$

where *k* is the molar mass transfer coefficient given in [m/s]. The coefficient *k* is influenced by surface geometry, nature of the fluid motion and fluid properties. It is therefore suitable to deal with the surface averaged mass transfer coefficient, $k_{av}$, which can be written as:

$$k_{av} = \frac{1}{A_s}\int_{A_S} k\, dA_s \ . \tag{7.5}$$

The total molar transfer rate $N_{ax,con}$ for the component ***a*** across the entire surface perpendicular to the $x$ direction, $A_s$ is then:

$$N_{ax,con} = k_{av} A_s (c_B - c_S). \tag{7.6}$$

## *7.2 Mathematical Models for Packed Beds with Fluid-to-Particle Mass Transfer*

As in all real reactors, the dynamic behaviour of fixed bed reactors deviates from standard ideal behaviours of the ideally mixed or the plug flow vessels. It is the degree of dispersion in fixed beds that determines how nearly will the real fixed bed reactor approach either of the two cases with the ideal flow patterns.

To dispose of the dispersion problem two modelling concepts are conventionally used: tanks-in-series and dispersion model. In the former concept, the back-mixing characteristics of the fixed bed column are accounted for by resembling the column with multiple continuously stirred tank reactors (CSTRs) in series. The latter concept represents the behaviour of a fixed bed reactor as to that of an ideal plug flow tubular reactor with the addition of a dispersion flow term based on Fick's diffusion with an empirical diffusivity coefficient. Both models have gained acceptance over the last four decades, acquiring the reputation of being reasonably accurate for the flow analysis in packed beds (Levenspiel, 1999 [106]).

Mixing is presumed to be sufficiently intense and uniform such that reaction conditions and catalyst levels are effectively homogeneous. This is valid only when the gradients really existing are small. Alternatively, if the reactants circulate very rapidly throughout the reactor.

In order to analyse the dynamics of the fluid to particle mass transfer in the columns packed with spherical non-porous and porous beads a transient tanks-in-series model

developed by Papathanasiou *et al.* (1988) [105] is implemented using ICML libraries and used for comparisons with the experiments.

### *7.2.1 The Tanks-In-Series Model for Fluid-to-particle Mass Transfer in Columns Packed with Spherical Particles*

According to the tanks-in-series model, to account for fluid back mixing in the flow through a column with fixed-bed of spherical particles, the column is thought over as a cascade of a number ($N$) of continuously stirred tank reactors (CSTRs) of equal volume ($V$), as depicted in (Fig.(7.3)).

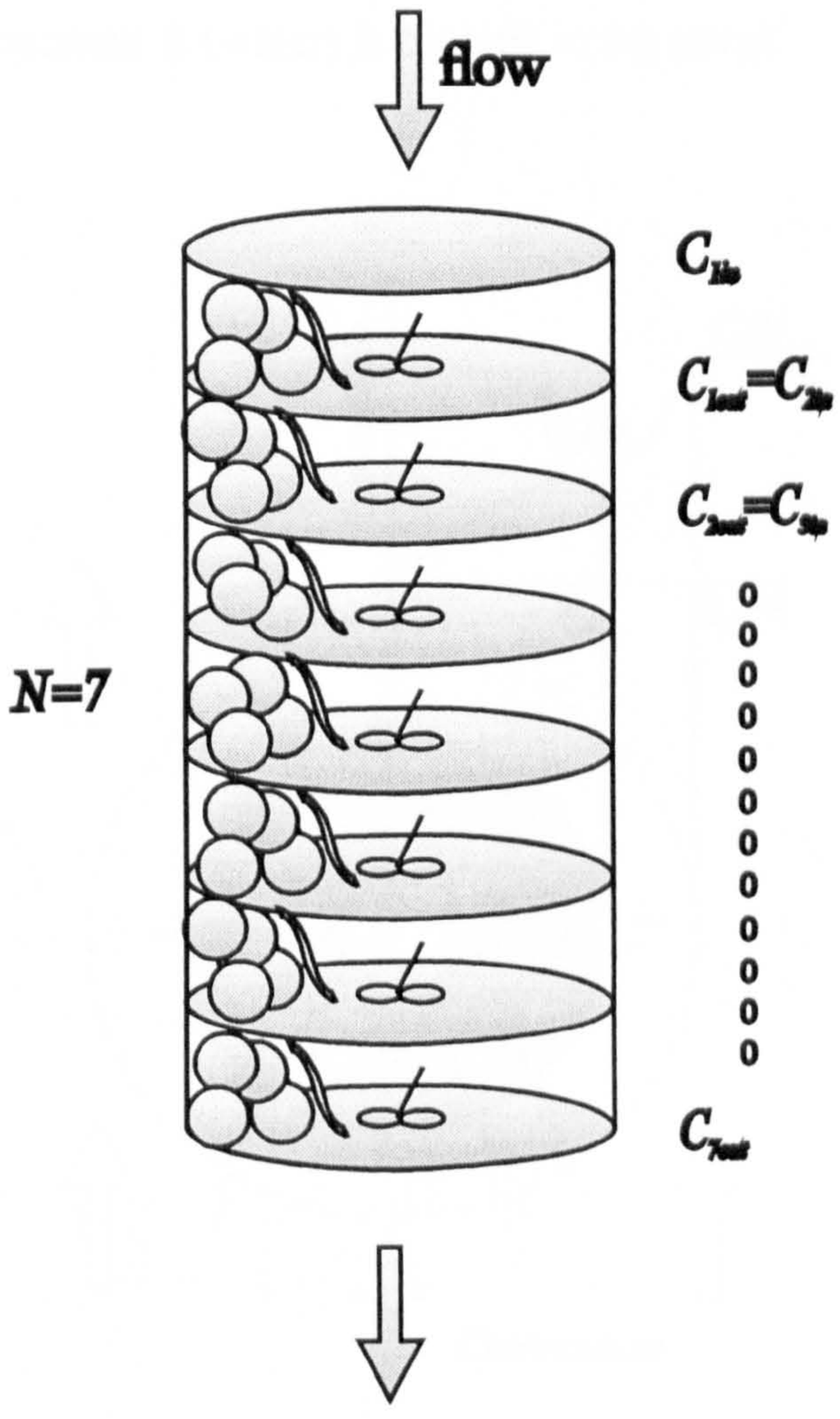


**Figure 7.3** Tanks-in-series model: column is idealised as a number ($N$=7) of CSTRs in series.

The exit concentrations ($c_{out}$) in each CSTR is equal to the input concentration ($c_{in}$) of the subsequent CSTR. The limiting values of $N$=1 and $N \rightarrow \infty$ yield the perfectly-mixed and plug flow columns respectively. Increasing values of $N$ indicate response closer to that of a plug-flow reactor.

#### *7.2.1.1 Particle Surface Boundary Condition in Fixed Beds Made of Porous Particles*

The model further assumes that in each of these CSTRs containing porous spherical particles mass transfer occurs in the interparticle space by virtue of fast bulk convection and in the intraparticle space by virtue of slow radial diffusion. Depicted in Fig.(7.4) is a spherical particle, initially free of component A (tracer). Within the particles only the component B (water) is present in the pores.

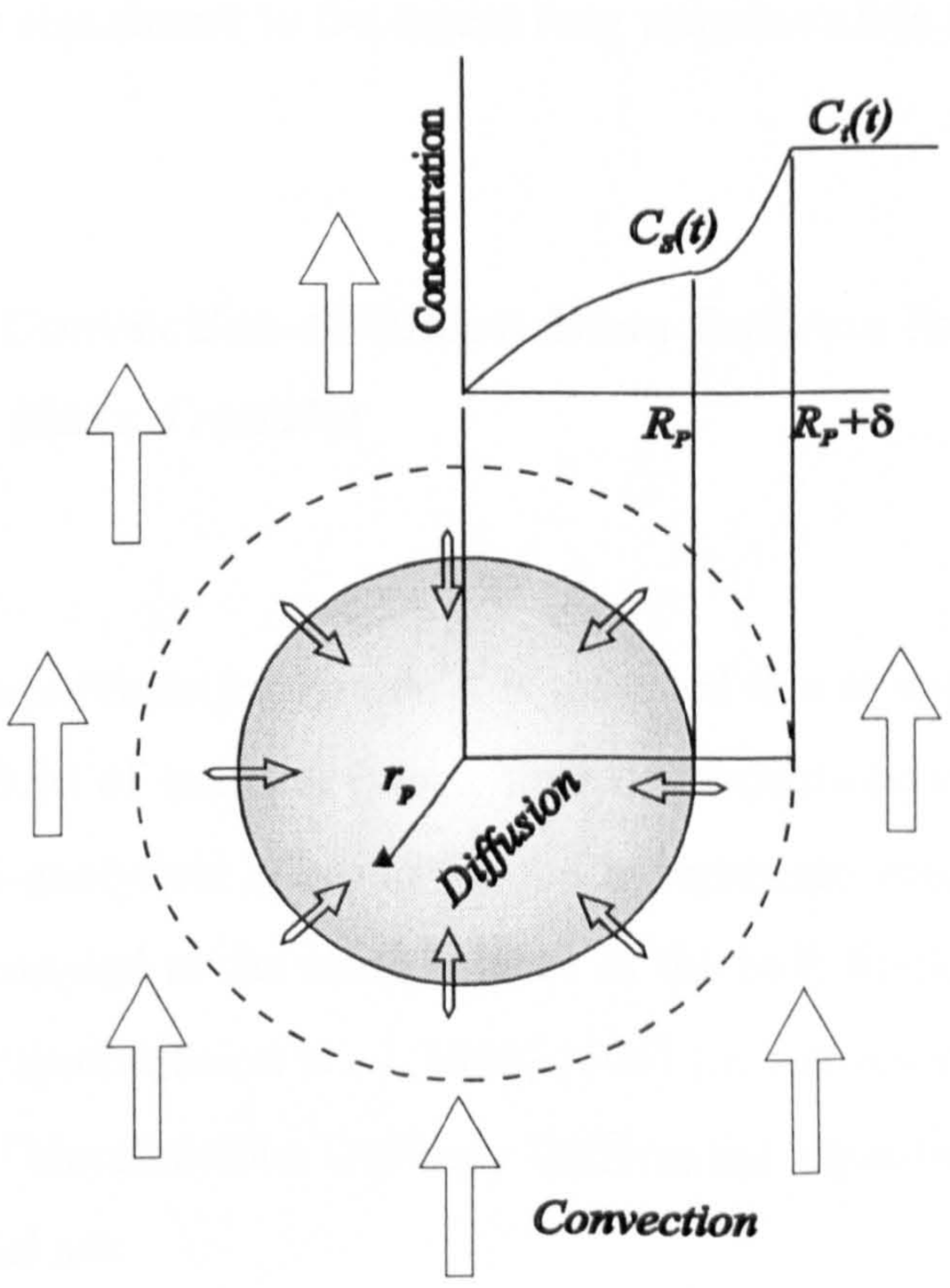


**Figure 7.4** Bulk convection and intraparticle diffusion as competing mechanisms of mass transfer to a single porous particle (initially free of tracer) of radius $R_p$ in packed beds. The concentration gradients developing in the liquid film with thickness $\delta$ surrounding the particle surface and within the spherical particle.

The component A is allowed to diffuse into the spherical beads radially, in one direction, *r*. It is assumed that the particle surface is uniformly accessible to the acetone molecules from the bulk liquid. Therefore the concentration of acetone at the surface is constant in regard with the spatial coordinate but still time dependent as in any transient experiment, i.e. $c_b(r_p = R_p, t) = c_s(t)$. Further, at any point $r_p > R_p$ the species transfer is due to both advection and diffusion. However, at $r_p = R_p$ there is no bulk fluid motion and species transfer is by diffusion only. The Fick's law at this point can be equated to the molar convection flux yielding the following equation:

$$-D_{ab}\varepsilon_p\left(\frac{\partial c_b}{\partial r_p}\right)_{r_p=R_p} = k_e(c_s - c_l), \tag{7.7}$$

where constant $k_e$ is the average external mass transfer coefficient, concentration $c_b$ indicates the concentration of tracer in the intraparticle space, $c_l$ indicates the concentration of tracer in the bulk liquid and $\varepsilon_p$ is the intraparticle porosity. The intraparticle porosity was taken as 0.99 in this work, since Ca-alginate beads are practically water; this was confirmed by allowing Ca-alginate beads to dry and observing that their size shrank to the extent they were invisible to the naked eye.

#### *7.2.1.2 Coupled Convection-Diffusion Mass Balance for Packed Bed with Fluid-to-Particle Mass Transfer*

As explained in the previous paragraph, it is assumed that at any instant each particle is surrounded by fluid of uniform (albeit time-dependent) concentration. Under this assumption, a semi-analytical solution for the intraparticle concentration profile can be developed and coupled to the mass balance in the bulk liquid, resulting in a semi-analytical model (Papathanasiou *et.al.*,1988) [105] for the response of the column in the form of a set of simultaneous Ordinary Differential Equations (ODEs). The main features of the model are:

*Mass Balance in the Bulk Liquid*

Provided that the fluid density is constant throughout the reactor the mass balance equation is:

$$\frac{dc_i(t)}{dt} = \frac{F}{\varepsilon V}(c_{i-1}(t) - c_i(t)) - Q^{(i)}(t), \qquad (7.8)$$

subject to initial conditions: $c_i(t)=0$ for $t=0$ and $c_0(t)=c_{in}(t)$ at $t>0$. $c_i(t)$ and $C_{i+1}(t)$ are the bulk tracer concentrations in the $i^{th}$ and $(i+1)^{th}$ CSTR in the cascade respectively, $F$ is the volumetric flowrate, $V$ is the bed volume and $\varepsilon$ is the voidage of the column. The value for inter-particle porosity $(\varepsilon)$ in this study was taken as 0.4. The term $Q^{(i)}(t)$ from equation (7.8) stands for the molar mass transfer flux from the bulk liquid to the beads, expressed according to the ratio of the external surface area of the catalyst ($A_{ext}$) per bed volume, i.e. $Q^{(i)}(t) = \frac{Q''^{(i)}(t)A_{ext}}{V}$ and its units are [mol/m$^3$s]. For spherical geometry dynamics of this term is given by equation:

$$Q^{(i)}(t) = 3(1-\varepsilon)(\frac{D_{eff}}{R_p})(\frac{\partial c_b}{\partial r_p})^{(i)}_{r_p=R_p}, \qquad (7.9)$$

where the superscript *(i)* indicates the $i^{th}$ CSTR in the cascade, $R_p$ is the particle radius $r_p$ is the radial coordinate of tracer within the particle and $D_{eff}=D_{ab}\varepsilon_p$ is the effective diffusivity in the intraparticle space.

*Intraparticle Diffusion*

Diffusion in the intraparticle space is assumed to be one-dimensional and governed by Fick's law. This is illustrated in Fig.(7.5) in which an element of volume in the intraparticle space is depicted in the spherical coordinates. Mass transfer is deemed not to take place through the shaded surfaces in Fig.(7.5).

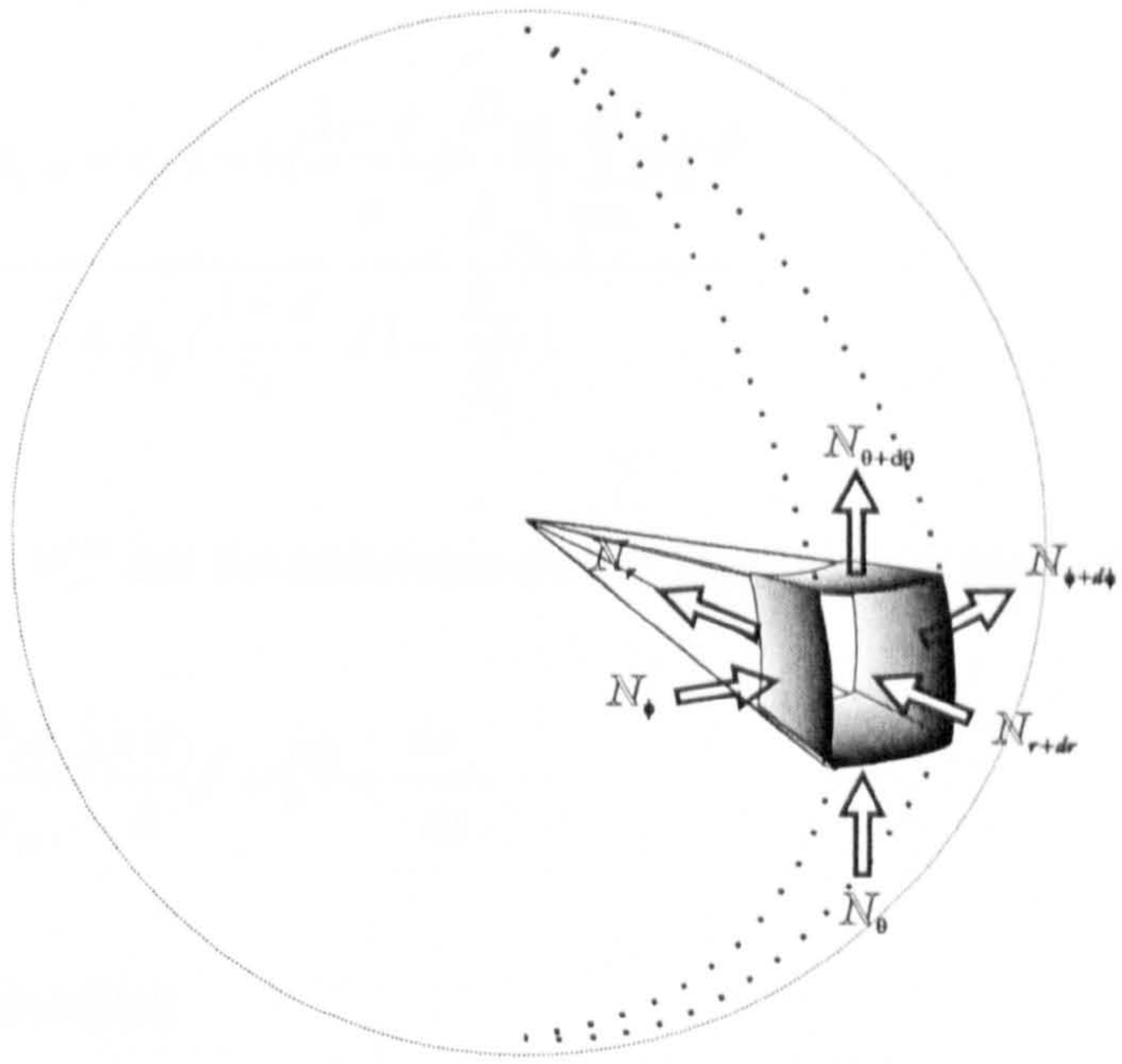


**Figure 7.5** Element of volume within the spherical particle given in spherical coordinates.

The equation governing one-dimensional transient intraparticle diffusion in the absence of chemical reaction is:

$$D_{eff}\left[\frac{\partial^2 c_b}{\partial r_p^2}+\left(\frac{2}{r_p}\right)\frac{\partial c_b}{\partial r_p}\right]=\varepsilon_p\frac{\partial c_b}{\partial t} \qquad \textbf{(7.10)}$$

subject to the conditions of zero flux (symmetry) at the centre ($\left(\frac{\partial c_b}{\partial r_p}\right)_{r_p=0}=0$) and of a prescribed, time-dependent concentration at the surface given by equation (7.7)

An analytical solution to equation (7.10) can be obtained by applying Duhamel's theorem (Carslaw and Jaeger, 1958; Crank (1983)) [107,108]. From this, the derivative $\left(\frac{\partial c_b}{\partial r_p}\right)_{r_p=R_p}$ that needs to be known in equations (7.7), (7.8) and (7.9) can

be evaluated. Equations (7.8) and (7.9) can thus be coupled, resulting in the following set of ODEs for the response of the column:

$$\frac{dc_i}{dt} = \frac{\frac{F}{\varepsilon V_i}(c_{i-1} - c_i) - 6(\frac{1-\varepsilon}{\varepsilon})\frac{D_{eff}}{R_p{}^2}\sum_{n=1}^{n_0}\psi_n^{(i)}}{1+\varepsilon_p(\frac{1-\varepsilon}{\varepsilon})(1-\frac{S_n}{S_l})} \qquad (7.11)$$

where the functions $\Psi_n^{(i)}$ are the solutions of the following differential equations:

$$\frac{d\psi_n^{(i)}}{dt} = -\frac{D_{eff}}{\varepsilon_p}(\frac{n\pi}{R})^2\psi_n^{(i)} + \frac{dc_s}{dt} \qquad (7.12)$$

and $S_n$, and $S_l$ are defined as:

$$S_n = \sum_1^{n_0}(\frac{1}{n})^2 \quad , \qquad S_l = \sum_1^{\infty}(\frac{1}{n})^2 \qquad (7.13)$$

*Biot number as a measure of the extent of mass transfer resistances*

The substitution for the value of $\left(\frac{\partial c_b}{\partial r_p}\right)_{r_p=R_p}$ in equation (7.7) yields to:

$$c_i(t) - c_S(t) = \frac{2\varepsilon_p}{\frac{k_e R_p}{D_{eff}}}(\sum_1^{n_0}\psi_n(t) + \frac{S_l R_p{}^2}{D_{eff}}(\frac{dc_S}{dt}). \qquad (7.14)$$

where $S_l = \sum_{n_0+1}^{\infty}\frac{1}{(n\pi)^2}$ and the expression $\frac{k_e R_p}{D_{eff}}$ is termed the mass Biot number, *Bi*.

It is defined as the ratio of the internal to the external mass transfer resistances in the system (Appendix 2). In this way, the Biot number determines the time scale of fluid to particle mass transfer in fixed beds of porous particles by considering two competing mechanisms of mass transfer in the bulk liquid (convection) and mass transfer in the intraparticle space (diffusion).

For sufficiently high superficial velocities in the column, the bulk convection occurs much faster than the intraparticle diffusion, which results in a very small concentration difference on the left-hand side of equation (7.14) ($c_i(t)$-$c_s(t)\rightarrow 0$) and values for $k_e$ are very high (thus $Bi\rightarrow\infty$). This in turn means that the effect of the mass transfer resistance in the external film of the fluid can be neglected and the major resistance to mass transfer takes place in the intraparticle space. When the fluid velocity decreases this assumption is no longer justifiable, as the difference between concentrations $c_s(t)$ and $c_i(t)$ increases, values for $k_e$ and $Bi$ decrease, and mass transfer is controlled by the resistance in the external film of liquid in the vicinity of the beads.

### *7.2.1.3 The Model Implementation*

Only a small number ($n_O$) of the ODEs of equation (7.11) need to be solved numerically. For $n>n_O$ the $\Psi_n^{(i)}$ 's in equations (7.12) are evaluated using the quasi-steady-state approximation:

$$\Psi_n^{(i)} = \frac{\varepsilon_p}{D_{eff}}\left(\frac{n\pi}{R_p}\right)^{-2}\frac{dC_s}{dt} \quad . \tag{7.15}$$

This approximation enhances drastically the computational efficiency of the method and, if implemented properly, has no discernible effect on quantitative accuracy [109].

The effect of the number of equations (7.12) solved ($n_O$) on the predicted response of cascades of 15 CSTRs is shown in Figs. (7.6a.b) for two extreme values of the Biot number $Bi$=0.1 and $Bi$=50. The percent difference between the responses obtained for $n_O$=55 ($c_{out}^{55}$) and those obtained for $n_O$=45,35,25,15 ($c_{out}^{45}$, $c_{out}^{35}$, $c_{out}^{25}$, $c_{out}^{15}$) are plotted for a volumetric flowrate of 1.4 l/min.

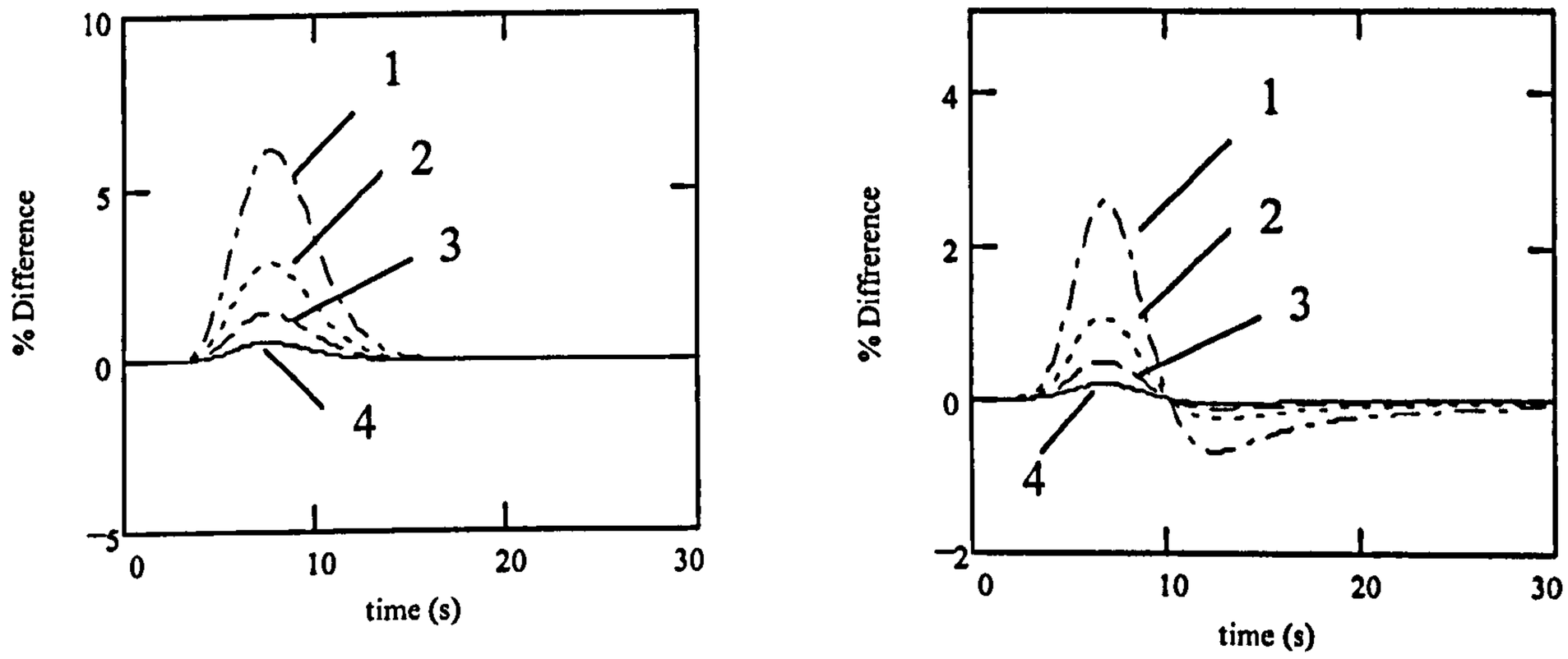


**Figure 7.6 a,b** The effect of the number ($n_0$) of $\Psi_s$ calculated through numerical solutions of equations (7.12) on the predicted response. Plotted are percent differences, defined as $100\bullet(C_{out}^{55} - C_{out}^{m})$ where m=15 (curve 1), m=25 (curve 2), m=35 (curve 3) and m=45 (curve 4). Presented are the comparisons for two extreme values for the Biot number *(a)* $Bi$=0.1, and (*b*) $Bi$=50. Particle radius was $R_p$=2mm, the number of CSTRS was $N$=15 and flowrate $F$=1.4l/min.

It is evident that by increasing $n_0$, the predicted response curves become progressively indistinguishable - as indicated by diminishing values of the relative differences. The satisfactory $n_O$ in all cases was found to be 45 and further increase of $n_O$ did not affect accuracy in solving the system of ODEs. Overall, the mathematical model for a cascade of ($N$) CSTRs comprises $N(n_0+2)$ ordinary differential equations in time. These are solved using Gears method for stiff systems [110] implemented on a personal computer.

### 7.2.2 The Dispersion Model

As a good alternative to the tanks-in-series model the dispersion model can be used for describing the dispersion characteristics of a fixed bed column.

#### 7.2.2.1 Shell Mass Balance for Forced Fluid Flow in Packed Beds

Hereby, the control volume approach is used for the analysis of the forced fluid flow in packed beds. Depicted in Fig.(7.7) is a packed bed made of non-porous glass beads. A cylindrical coordinate system with parameters $r$, $z$ and $\varphi$ is chosen for the analysis. In such a system, the fluid concentration will not be a function of angle $\varphi$ because of cylindrical symmetry. An annular ring (a shell) of finite width $\Delta R$ and finite thickness $\Delta z$ is selected for representing a control volume through which the fluid flows.

The column is initially filled with the fluid B (water) and at time $t=0$ the fluid A with concentration $c_A$ begins to flow from the top of the column downwards. As a result of fluid motion, the species concentration gradients will be developed leading to a relative transport of species.

The shell mass balance for fluid A is in general obtained by counterbalancing the amounts of fluid A in the control volume due to fluid inflow and outflow through the control surfaces perpendicular to flow direction, with the amounts of the fluid generation and accumulation in the control volume.

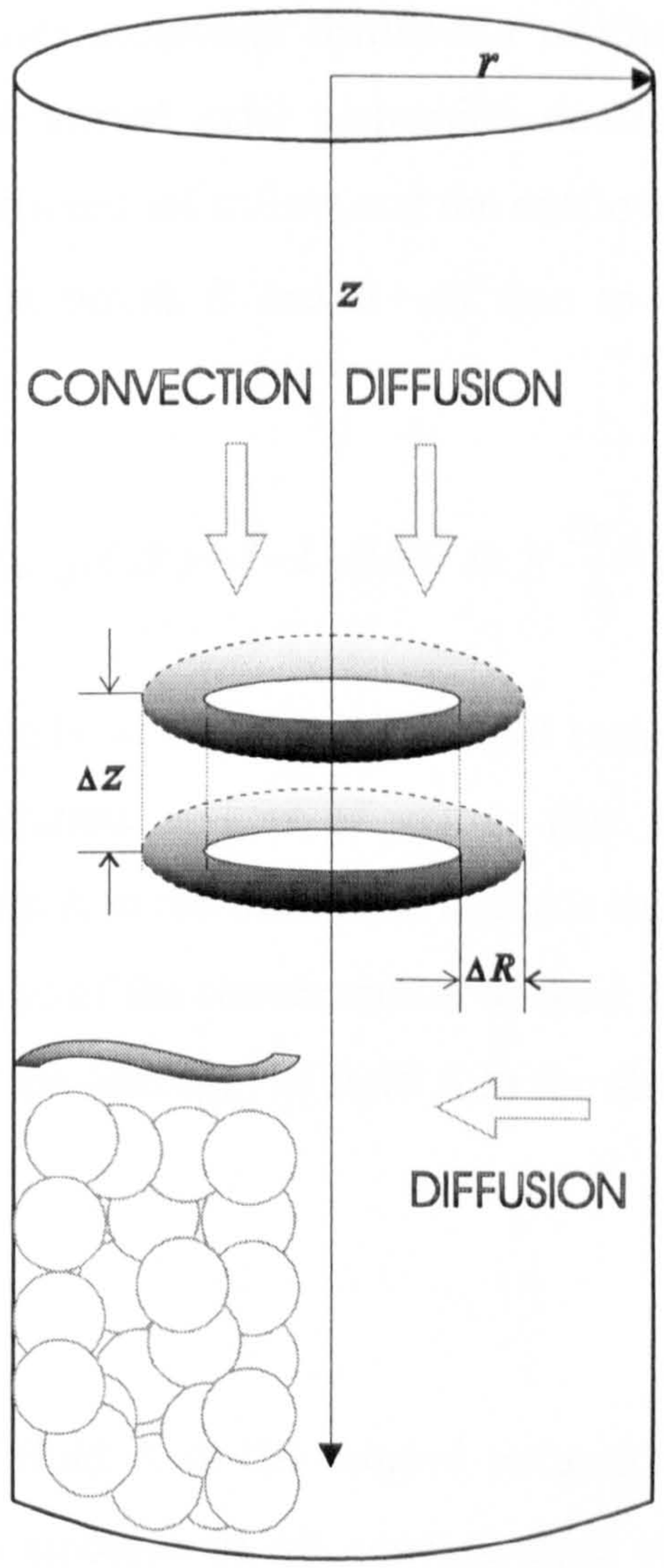


**Figure 7.7** Finite control volume analysis in the cylindrical coordinates for a packed bed column.

The difference between the amounts of fluid A that enter and exit the shell through the control surface $2\pi R\Delta R$ at points $z$ and $z+\Delta z$ due to longitudinal bulk flow with velocity $u_z$ over a time interval $\Delta t$ is: .

$$[c_A u_z 2\pi R(\Delta R)]_{z+\Delta z}\Delta t - [c_A u_z 2\pi R(\Delta R)]_z \Delta t . \quad \textbf{(7.16)}$$

Over the same time, the difference between the amounts of the inflow and the outflow of fluid A through the shell control surface $2\pi R\Delta R$ at points $z$ and $z+\Delta z$ due to diffusion in the axial direction is given by:

$$[-D_{ax} 2\pi R(\Delta R)(\frac{\partial c_A}{\partial z})]_{z+\Delta z}(\Delta t) - [-D_{ax} 2\pi R(\Delta R)(\frac{\partial c_A}{\partial z})]_z(\Delta t) . \quad \textbf{(7.17)}$$

The parameter $D_{ax}$ encompasses molecular diffusivity of fluid A as well as eddy (turbulent) diffusivity and is termed axial dispersion coefficient in packed beds. Analogously, the difference between the inflow and the outflow of fluid A through the shell control surface $2\pi R\Delta z$ at points $R$ and $R+\Delta R$ due to diffusion in the radial direction can be written as:

$$[-D_r 2\pi R(\Delta z)(\frac{\partial c_A}{\partial r})]_{R+\Delta R}(\Delta t) - [-D_r 2\pi R(\Delta z)(\frac{\partial c_A}{\partial r})]_R(\Delta t). \quad (7.18)$$

Further, it is assumed that there is no any change of fluid concentration in the control volume associated with generation or loss of matter (i.e. by chemical reaction). Finally, since the inflow of fluid A in the fluid shell exceeds the fluid outflow over the time $\Delta t$, there will be an increase of the concentration of fluid A in the control volume over that time. This accumulation (storage) of fluid A in the shell volume is expressed as:

$$\Delta c_A 2\pi R(\Delta R)\Delta z \ . \quad (7.19)$$

The conservation of mass of fluid A in the control volume must be satisfied. The balance existing between the amounts of all concentration changes is obtained by adding up all the contributions from equations (7.16-7.19). Dividing all the terms from equations (7.16-7.19) by $2\pi(\Delta R)(\Delta z)(\Delta t)$ and subsequently taking the limits as $\Delta R$, $\Delta z$ and $\Delta t$ go to zero, we obtain:

$$D_{ax}R\frac{\partial^2 c_A}{\partial z^2} + D_r\frac{\partial}{\partial r}(R\frac{\partial c_A}{\partial r}) - R\frac{\partial(c_A u_z)}{\partial z} = R(\frac{\partial c_A}{\partial t}). \quad (7.20)$$

Here it should be pointed out that, by taking the limits over the entire column cross section including the particles and the void space, the particulate system is treated as continuum. Consequently, the values for concentration, velocity and the axial dispersion coefficient take average values over the cross section rather than the point values.

When radial diffusion is neglected and the fluid density is not changing, equation (7.20) reduces to:

$$D_{ax}\frac{\partial^2 c_A}{\partial z^2}-u_z\frac{\partial c_A}{\partial z}=\frac{\partial c_A}{\partial t}. \qquad (7.21)$$

The mass balance from equation (7.21) can be directly applied in the analysis of the columns packed with impermeable beads. When the particles are porous there will be a mass transfer occurring from the interstitial column space (bed voidage) into the permeable particles. Therefore, as in the tanks-in-series model, the mass balance will have an additional term $Q_1$ (mass flux based on the ratio $\frac{A_{ext}}{V}$), accounting for mass transfer into the permeable beads.

In this case mass balance in the column, given in the non-dimensional form (by introducing dimensionless parameters $t^*=\frac{tu_z}{L}$ and $z^*=\frac{z}{L}$, where $L$ is the column length), reads:

$$\frac{\partial c_A^*}{\partial t^*}=(\frac{D_{ax}}{u_z L})(\frac{\partial^2 c_A^*}{\partial z^{*2}})-\frac{\partial c_A^*}{\partial z^*}-Q_1^*, \qquad (7.22)$$

where the asterisks denote dimensionless variables. The first term on the left-hand side of equation (7.22) includes a dimensionless number, *Pe*, describing the degree of axial dispersion in the column, defined by:

$$Pe=\frac{u_z L}{D_{ax}}, \qquad (7.23)$$

where $u_z=u_i$ is the interstitial velocity of the fluid in the flow direction. *Pe* is often referred to as the column Peclet number (see Appendix 2).

The initial and boundary conditions for equation (7.22) were:

$$c_A^*(0,z^*)=0.0, \qquad (7.24)$$

$$(\frac{\partial c_A^*}{\partial z^*})_{z^*=0}=-Pe(c_{A,in}^*-c_A^*), \qquad (7.25)$$

$$\left(\frac{\partial c_A^*}{\partial z^*}\right)_{z^*=1} = 0 . \qquad (7.26)$$

The particle Peclet numbers ($Pe_p$) can be calculated by simply multiplying the column Peclet numbers with the dimensionless term $d_p/L$ where $d_p$ is particle diameter. The Reynolds number is related to the particle diameter:

$$Re_p = \frac{u_s d_p \rho}{\mu} , \qquad (7.27)$$

where $u_s = u_i \varepsilon$ is superficial velocity in the flow direction, $\rho$ is density and $\mu$ is dynamic viscosity of the fluid.

Chung and Wen [75] gave the correlation describing the axial dispersion of liquid flowing through fixed and fluidised beds:

$$Pe_p = \frac{0.20 + 0.011 Re_p^{0.48}}{\varepsilon} . \qquad (7.28)$$

This correlation was used for the comparisons with the experimentally determined column Peclet numbers in Chapter 8.

## *7.3 Comparison Between the Tanks-In-Series and the Dispersion Model*

Values of the column Peclet number (from the dispersion model) can be compared with the corresponding number of CSTRs (from the tanks-in-series model) using the following equation given by Cramers and Alberd [111]:

$$\frac{1}{N-1} = 2\left(\frac{D_{ax}}{u_i L}\right), N \geq 10 . \qquad (7.29)$$

This equation can be used for relatively low dispersion in the column.

For the analysis of experimental dynamic responses of a packed bed column, the tanks-in-series model was primarily used. The dispersion model was only used to confirm the results from the tanks-in-series model for hydrodynamic dispersion, using equation (7.29).

## *7.4 Notation*

A tracer

$A_{ext}$ external surface area of the catalyst particle, [$m^2$]

$A_s$ unit area perpendicular to the direction of mass transfer, [$m^2$]

B particles

$C(t)$ tracer concentration in the bulk liquid, [$m^3/s$]

$C_b$ tracer concentration in the intraparticle space, [$m^3/s$]

$C_B$ tracer concentration in the bulk liquid, [$m^3/s$]

$C_i(t)$ tracer concentration in the bulk liquid in the *i-th* CSTR, [$m^3/s$]

$C_{in}$ initial concentration of the tracer in the particles, [$m^3/s$]

$C_s(t)$ tracer concentration at the particle surface, [$mol/m^3$]

$D$ diffusivity of the tracer A in water, [$m^2/s$]

$D_{ax}$ axial dispersion coefficient, [$m^2/s$]

$D_{ab}$ molecular diffusivity of the component ***a*** diffusing in the component ***b***, [$m^2/s$]

$D_{eff} = \varepsilon_p D_{AB}$ effective diffusivity of the tracer A into the particles B, [$m^2/s$]

$d_p$ bead diameter, [m]

$F$ volumetric flowrate, [$m^3/s$]

$k_{av}$ surface averaged mass transfer coefficient, [m/s]

$k_e$ external mass transfer coefficient, [m/s]

$L$ column length, [m]

$M$ number of the beads

$N$ number of continuously stirred tank reactors (CSTR) modelling back mixing in the column

$N''_{ax,dif}$ diffusive molar flux of the component *a* in the *x* direction, [$mol/m^2s$]

$N_{ax,dif}$ diffusive molar transfer rate of the component *a* in the *x* direction, [mol/s]

$N''_{ax,con}$ convective molar flux of the component *a* in the *x* direction, [$mol/m^2s$]

$N_{ax,con}$ convective molar transfer rate of the component $a$ in the $x$ direction, [mol/s]

$Q^{''(i)}(t)$ molar mass transfer flux from the bulk liquid to the particles, [mol/m²s]

$Q^{(i)}(t)$ molar mass transfer flux from the bulk liquid to the particles expressed according to the ratio of the external surface area of the catalyst per bed volume, [mol/m³s]

$q_n$ non-zero positive roots of equation: $\tan(q_n) = \frac{3q_n}{3+\alpha(q_n)^2}$

$R_p$ bead radius, [m]

$r_p$ radial coordinate of tracer within the particle

$r$ radial coordinate in the packed bed in the cylindrical coordinate system

$t$ time, [s]

$t^* = t\frac{u_z}{L}$ dimensionless time

$u_i$ bulk fluid interstitial velocity in the flow direction, [m/s]

$u_s$ fluid superficial velocity in the flow direction, [m/s]

$V$ bed volume, [m³]

$z$ longitudinal coordinate of the packed bed in the cylindrical coordinate system

$z^*$ dimensionless longitudinal coordinate of the packed bed in the cylindrical coordinate system

*Greek Letters*

$\alpha$ the ratio of the bulk liquid volume over the volume occupied by the beads

$\varepsilon$ interparticle porosity (bed voidage)

$\varepsilon_p$ intraparticle porosity

$\mu$ fluid dynamic viscosity, [Pas]

$\rho$ fluid density, [kg/m³]

$\Psi_n^{(i)}$ solutions of the differential equations given by (7.12), [mol/m³]

*Dimensionless Numbers*

$Bi = \frac{k_e R}{D_{eff}}$ mass Biot number

$Pe = \frac{u_i L}{D_{ax}}$ column Peclet number

$Pe_p = Pe\,(d_p/L)$ particle Peclet number

$Re_p = \frac{u_s d_p \rho}{\mu}$ particle Reynolds number

$Sc = \frac{\mu}{\rho D}$ Schmidt number

$Sh_p = k_e \frac{d_p}{D}$ particle Sherwood number

# Chapter 8

# Dynamic Experiments in Fixed Bed Columns

## *8.1 Introduction*

The effects of intra and inter- particle flow and mass transfer of a non-reactive liquid substance (tracer) on the transient response of fixed-bed columns containing impermeable glass and porous Ca-alginate beads are investigated experimentally. Section (8.1) is an outline of the materials, the experimental apparatus and of the procedure used for (i) independent experimental determination of the pertinent physical parameters and (ii) conducting dynamic response experiments.

The principal aim of the experimental program in Section (8.2) was to observe how the change from the non-porous (one porous medium) to the porous (dual porous media) column packing affects dynamic responses of such columns. The experiments with porous packing were designed to determine flow conditions giving the absence of the mass transfer resistance in the inter-particle space (the external mass transfer resistance). On the assumption that the porous nature of the Ca-alginate beads does not alter the hydrodynamic dispersion in the column, the predictions of the model based on the tanks-in-series concept in dual porous media, described in Chapter 7, are compared to the experimental data for fixed beds made up of two particle sizes. The mechanism responsible for tracer transport into the spherical beads is discussed.

Further, in Section (8.3) the influence of various flow conditions on the external mass transfer hindrance was investigated for a range of the particle Reynolds numbers in the high particle Peclet numbers regime. The experimental results are compared to the predictions of the model based on the tanks-in-series concept in dual porous media that, in addition, accounts for mass transfer resistance in the inter-particle space. The

obtained results are compared to the analytical models and correlations from the literature and, finally, conclusions are drawn.

### *8.1.1 Materials and Methods*

Spherical gel beads were prepared by dropping a sodium alginate solution (BDH Merck, UK) into a well-stirred solution of calcium chloride (BDH Merck, UK), as in [112]. The droplets gelled upon contact with the $CaCl_2$ solution, producing almost perfectly spherical beads. These were left to cure in the same solution under gentle agitation for 2 hours to allow the gel to harden and then washed with deionised water. Beads were produced in two sizes (radii 1 and 2 mm) by modifying the diameter of the orifice used to form the drops as well as by modifying the surface tension of the Ca-alginate solution by adding small amounts of surfactant. As was the case in previous studies where gel beads were formed in a similar way [113], the particle size distribution in each batch was very narrow; typical 95% confidence intervals for the beads of 2mm radius was ±0.045 mm. Acetone was used as tracer (Fisher Scientific, UK), in aqueous solutions whose concentration was measured using UV-sensor AF42 at 280nm wavelength and UV-analyser model 660-(Wedgewood Technology, USA).

### *8.1.2 Determination of the Intraparticle Diffusivity*

A standard method for the determination of the diffusivity of a substance into spherical porous particles is described by Crank [108]. In this, spherical porous particles containing the diffusing substance (tracer) at a uniform initial concentration are placed within a fixed volume of tracer-free solvent. The mixture is vigorously stirred so that the bulk liquid is well mixed and the liquid-to-particle mass transfer resistance may be neglected. Under these conditions, tracer diffuses from the beads to the bulk liquid and the rise of tracer concentration in it is recorded. Assuming Fickian

diffusion within the particles is the only mechanism of tracer transport, the concentration rise in the bulk liquid is described by the following equation:

$$C(t) = \frac{C_{in}}{1+\alpha}\left[1 - \sum_{n=1}^{\infty} \frac{6\alpha(1+\alpha)e^{-\frac{D_{AB}q_n^2 t}{\alpha^2}}}{9+9\alpha+q_n^2\alpha^2}\right], \qquad (8.1)$$

where $D_{AB}$ is the diffusivity of the tracer A into the particles B, $C_{in}$ is the initial concentration of the tracer in the particles and the parameter $\alpha$ is defined as the ratio of the bulk liquid volume ($V_{blk}$) over the volume occupied by the beads:

$$\alpha = \frac{3V_{blk}}{4\pi R^3 M}. \qquad (8.2)$$

In equation (8.2) $M$ is the number of the beads and $R$ is the bead radius. The parameters $q_n$ ($n$=1,2,..) in equation (8.1) are the non-zero positive roots of equation:

$$\tan(q_n) = \frac{3q_n}{3+\alpha(q_n)^2}. \qquad (8.3)$$

To determine $D_{AB}$, a fixed volume (90 ml) of Ca-alginate beads was placed in 300ml of 2% or 4% acetone solution and left for up to 4 hours to ensure they were fully impregnated by acetone. Following saturation, the beads were transferred to a stirred vessel (working volume of 1500 ml) placed in a recirculation loop, as schematically shown in Fig.(8.1).

A peristaltic pump (model 302 RS, Watson-Marlow Ltd., UK) was used to recirculate the bulk liquid and a UV analyser, located in the recycle stream, was used to record, on-line, the variation of concentration in the bulk liquid with time.

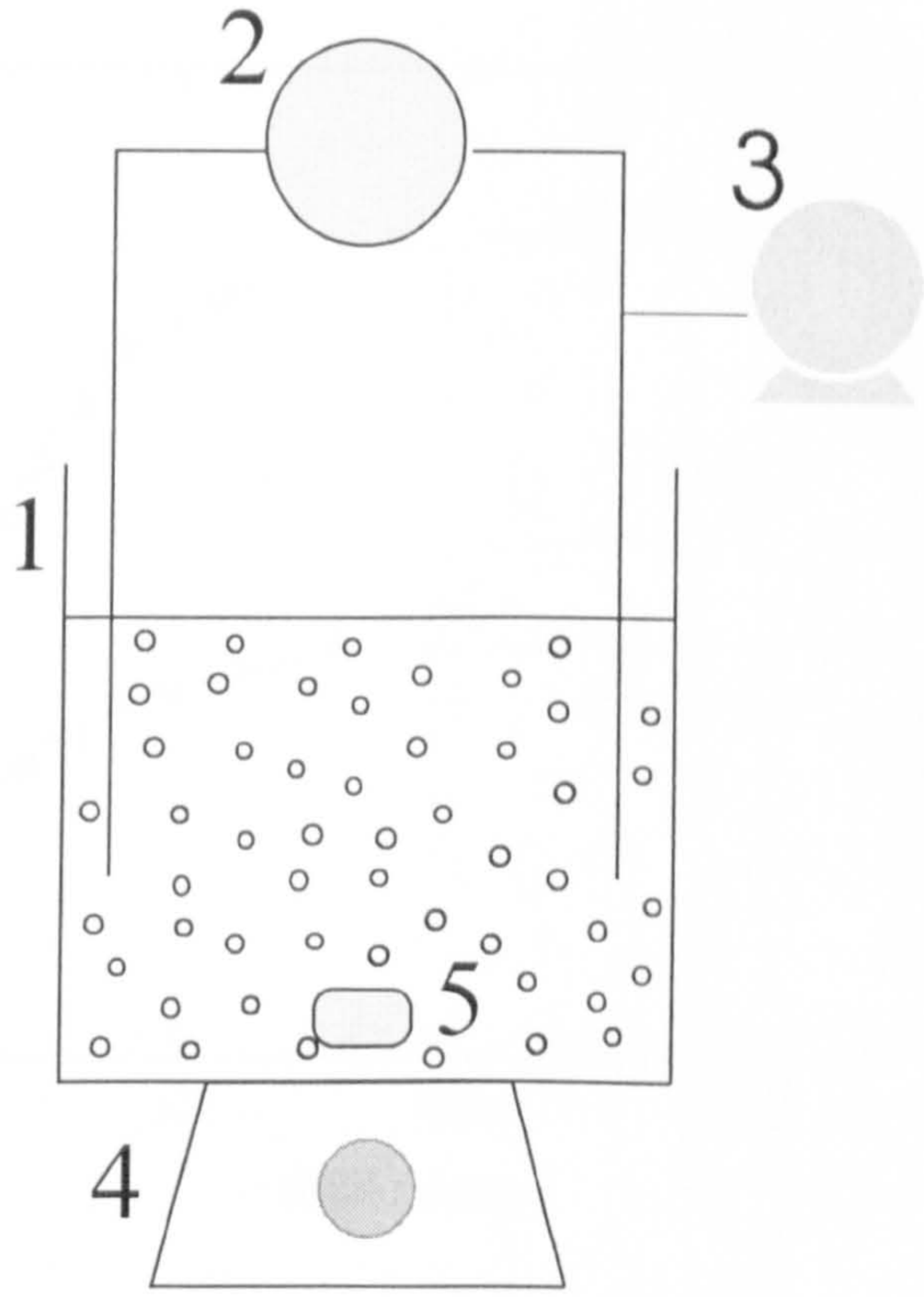


**Figure 8.1** Schematic of the test rig used for the determination of the intraparicle diffusivity of acetone in Ca-alginate beads: 1 glass vessel, 2 UV analyser, 3 pump 4,5 magnetic stirrer.

Typical curves obtained from the experiments conducted for particle size of radius $R$=2mm and two initial concentrations of the acetone ($C_{in}$ =1.54% and $C_{in}$ =3.08%) are shown in Fig.(8.2). These were fitted to equation (8.1) using least squares regression and the value of the diffusion coefficient, $D_{AB}$, was determined to be $1.2 \cdot 10^{-5}$ cm$^2$/s. Similar results were obtained for the particle radius of $R$=1mm. This uniformity indicates that for the particle sizes and concentrations considered, transport of acetone within the Ca-alginate immobilisation beads is not affected by bead size or by the concentration of acetone.

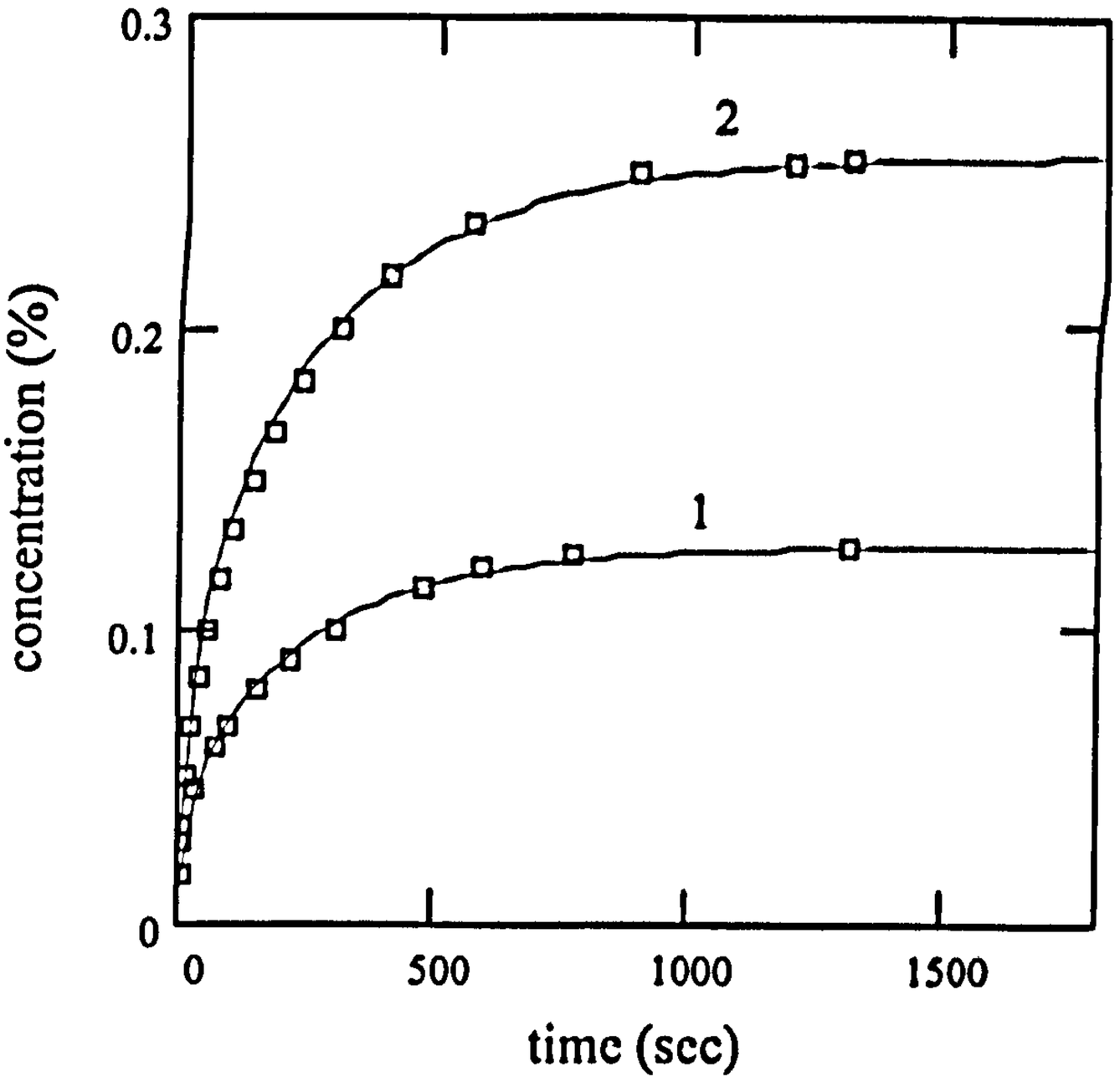


**Figure 8.2** Concentration vs. time profiles obtained during acetone desorption experiments from Ca-alginate beads of diameter R=2mm. Initial concentration of acetone in the beads: 1 $C_{in}$=1.54%, 2 $C_{in}$=3.08%.

### *8.1.3 Dynamic Tracer Experiments in Fixed Bed Columns*

A schematic diagram of the system used in all tracer experiments is shown in Fig.(8.3). This includes the acetone solution reservoir (1), the peristaltic pump (2), two magnetic valves (3,6) which can be switched on simultaneously at the same time activating the recorder (8) connected to the UV analyser (7), the flowmeter (9) and the fixed-bed column (4,5). The lower section of the latter is packed with glass beads, which act as a distributor, whereas the rest (active section) is filled either with porous (Ca-alginate) or impermeable (glass ballotini) beads. The column height is 22cm, while its diameter is 5cm.

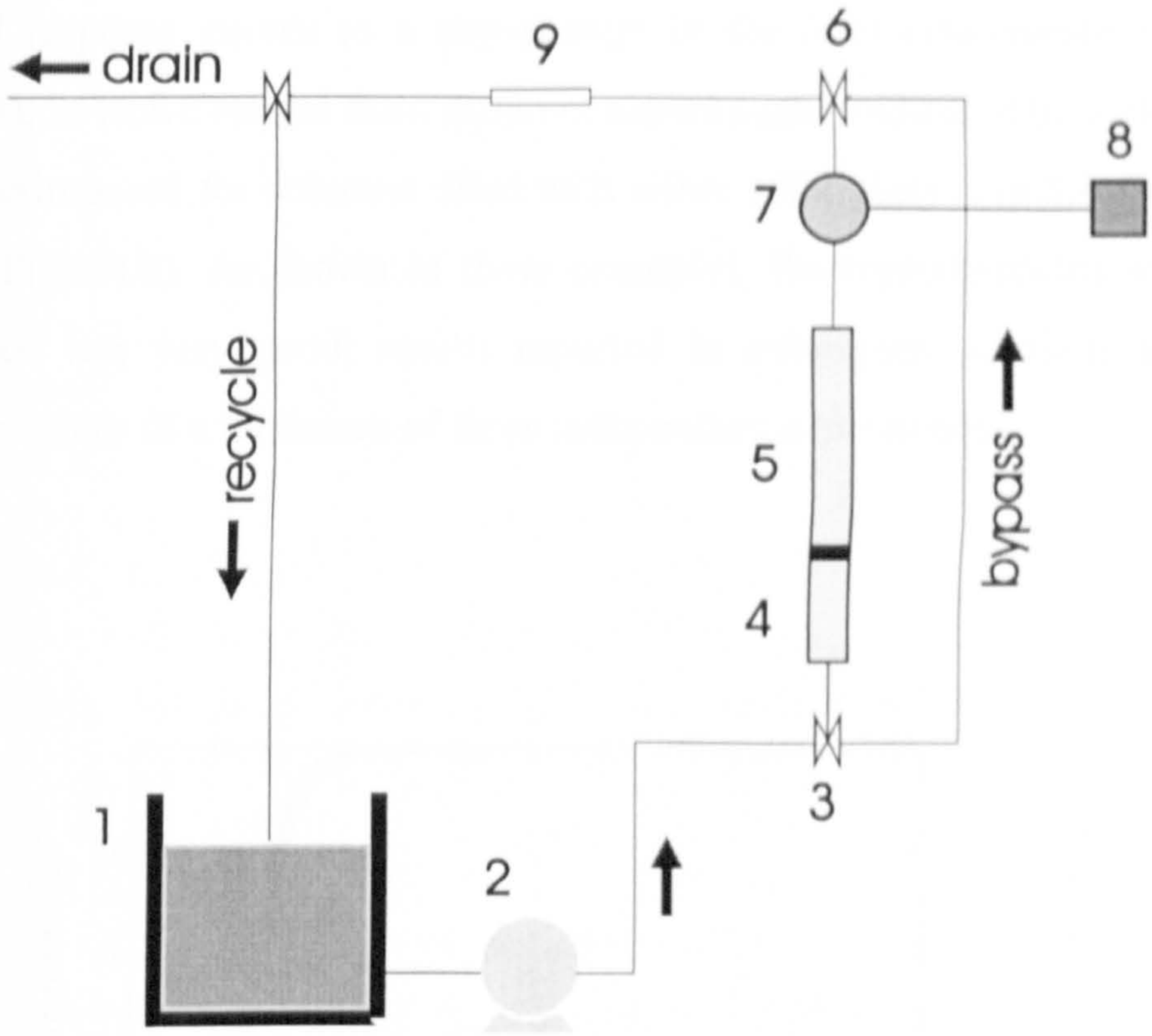


**Figure 8.3** Schematic diagram of the system used for the dynamic response experiment: 1 reservoir with acetone solution, 2 pump, 3,6 magnetic valves, 4 distributor, 5 column, 7 UV analyser, 8 chart recorder, 9 rotameter.

The system, including the tubing and the column, is initially filled with acetone-free demineralised water. Prior to conducting a tracer experiment, the column is isolated by switching-off valves (3) and (6) and 0.2% acetone solution is circulated from the reservoir (total volume 10l) through the by-pass for 20 minutes, thus allowing the stabilisation of the acetone concentration in the system. At time zero, the magnetic valves (3) and (4) are switched open, acetone solution is passed at fixed flowrate, $F$, through the column and the change in acetone concentration at its exit is measured with the UV analyser and recorded. A flowrate of 1.4 l/min was used in all experiments reported in this section. This flowrate results in the particle Reynolds numbers ($Re_p = \frac{u_s d_p \rho}{\mu}$) of 25 and 50, for particle radii $R$ of 1 and 2 mm respectively. The corresponding particle Sherwood numbers of 67 and 101, were obtained using the Thoenes and Kramers correlation from [88]).

Typical response curves to a step-change in the inlet concentration are shown in Fig.(8.4), in which results from different experiments (indicated by different symbols) are superimposed for columns filled with either solid glass (Fig.8.4.a) or Ca-alginate beads (Fig.8.4.b). As shown in these examples, the reproducibility of the recorded responses was very good; results reported in subsequent sections are always the average values of a minimum of three independent experiments.

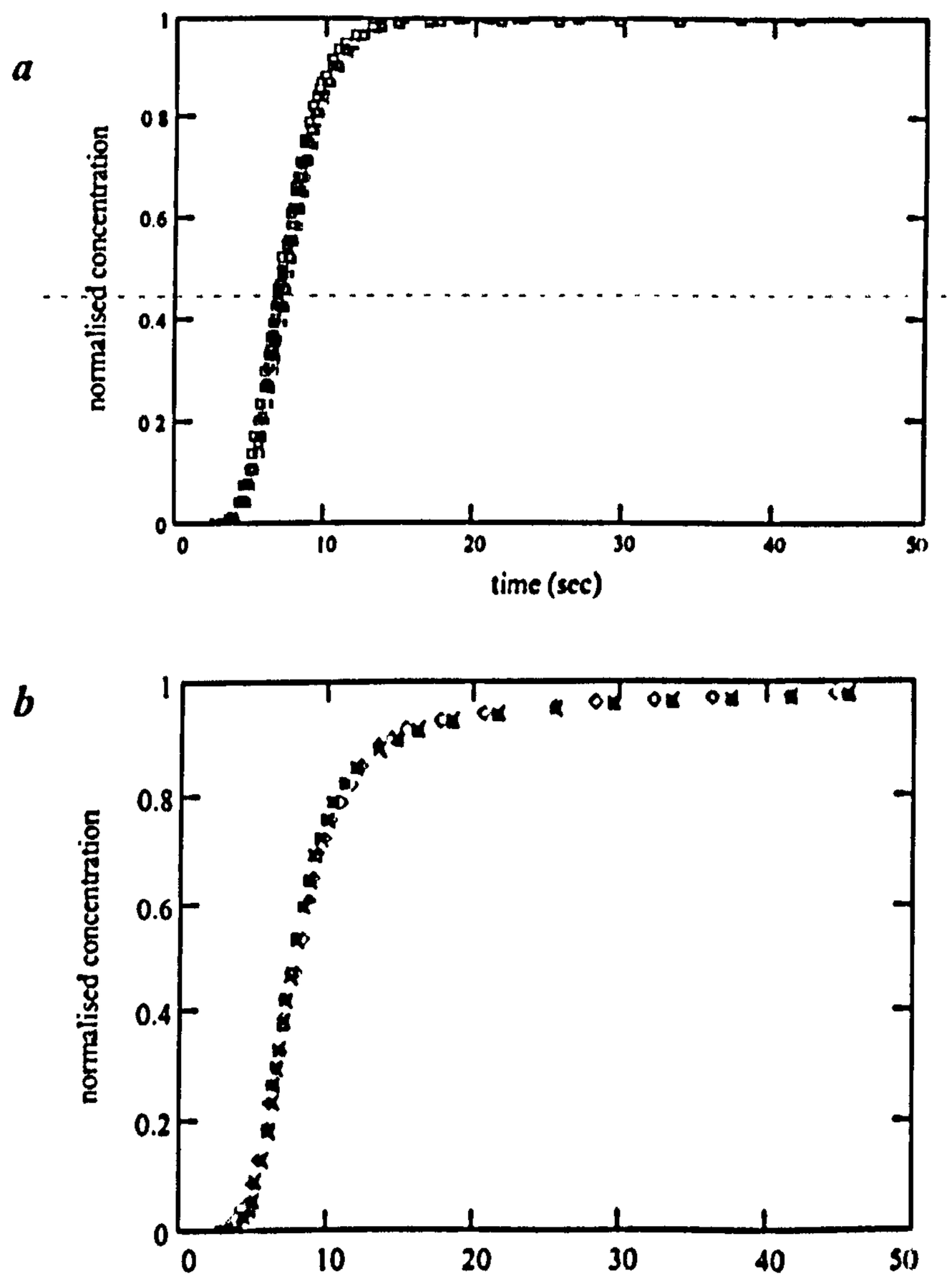


**Figure 8.4a,b** Reproducibility of tracer experiments for solid glass (*a)* and Ca-alginate beads (*b)*. The crosses (×), squares ( □) and diamonds (◊) are experimental points obtained by conducting three independent experiments.

## *8.2 The Effect of Intraparticle Diffusion on the Dynamic Responses of the Columns Containing Solid Non-Porous and Porous Beads*

In the following, the dynamic response of columns packed with solid glass or Ca-alginate beads to a step change in the inlet tracer concentration is obtained experimentally using the apparatus described in Section (8.1.3). These are compared to each other (in order to ascertain the relative effect of intra-particle diffusion on the dynamic response) as well as to the predictions of the model outlined in Section (7.2.1) (in order to evaluate its predictive capability and also comment on the mechanism responsible for tracer transport). In the model, all required parameters take values determined experimentally; the intraparticle diffusivity determined as outlined in Section (8.1.2) while the volumetric flowrate was measured on-line (Fig.(8.3)).

It should be pointed out that it is very difficult to generate experimentally a perfect step signal. In reality, some tracer dispersion will occur in both the distributor and in the tubing leading from valve (3) (Fig.(8.3)) to the column. The concentration of tracer in the inlet of the column is therefore more likely to be described by a modified error function than by the ideal step signal. In the following, the effect that such a deviation might have on the response of a column is investigated computationally. For this equations (7.11) and (7.12) were solved, subject to the initial condition:

$$C_{in} = erf(\kappa t),\ t > 0, \kappa > 0 \qquad (8.4)$$

Cascades of 3 and 10 CSTRs are used for this purpose, and the conditions are typical of experiments carried out in the column using glass or Ca-alginate beads. The effect of the characteristics of various error functions on the predicted response is shown in Fig.(8.5a,b).

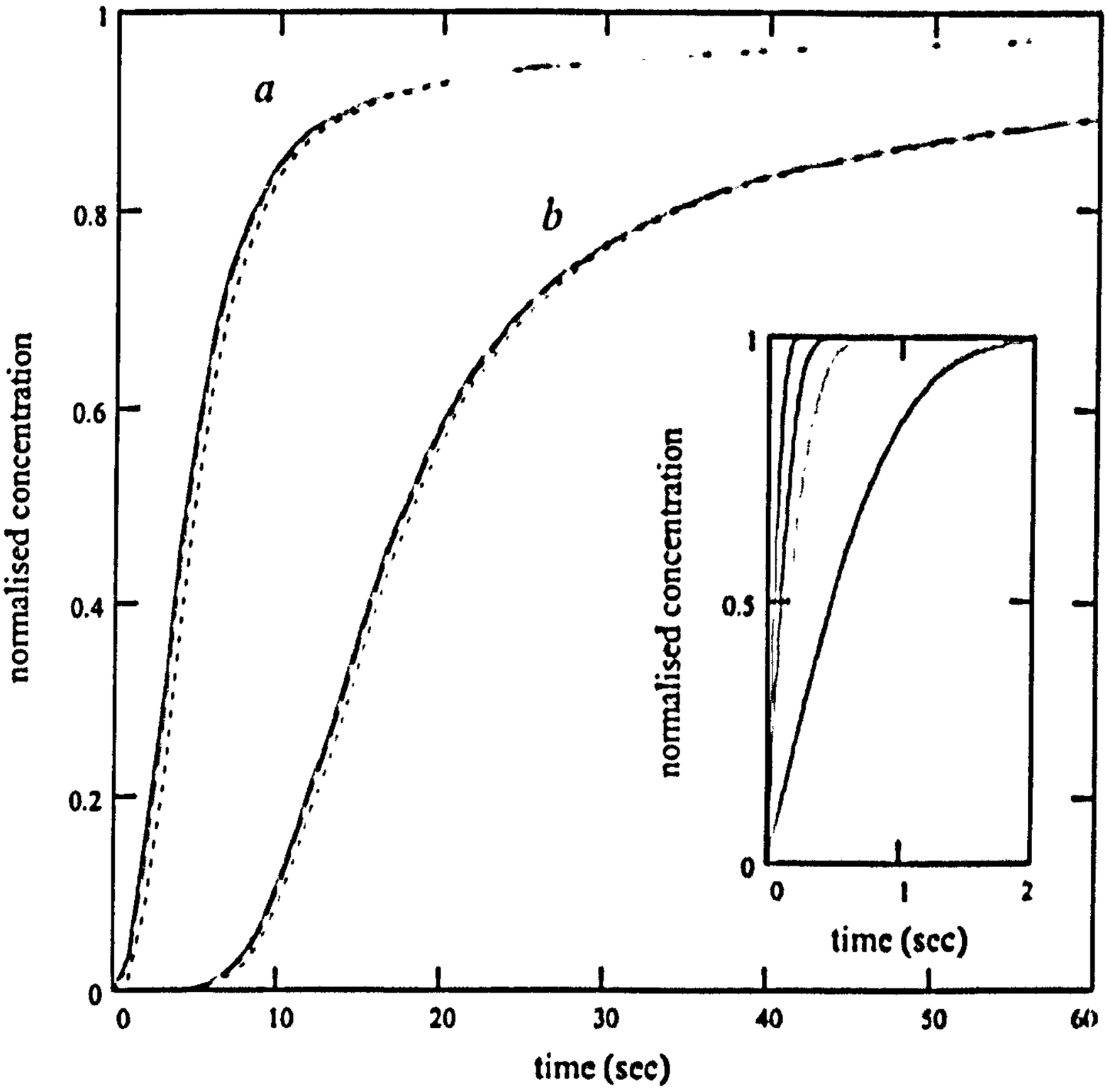


**Figure 8.5:** Effect of the shape of the inlet concentration profile on the response of a cascade of 3 CSTRs (*a*) and 10 CSTRs (*b*). The form of the error function used in each case is shown in the insert (error functions corresponding, from right to left, to $\kappa$=1,3,5,10).

It is seen that the effect of deviation from the ideal step signal is smaller when a large number of CSTRs in series is used (compare the curves *a* obtained for 3 CSTRs and the curves *b* obtained for 10 CSTRs). The insert to this figure is the inlet concentration profile obtained from equation (8.4) for various values of the parameter ($\kappa$). The experimentally measured inlet concentration profile was found to resemble equation (6.8) with $\kappa$=2.83. Since the dispersion in the actual columns corresponded to either $N$=13-15 (for $R$=2mm) or $N$=20 (for $R$=1mm), it was concluded that this small deviation of the input signal from the perfect step change will not have any significant effect on the conclusions drawn from this study.

### *8.2.1 The Effect of Intraparticle Tracer Diffusion*

The effect of tracer diffusion into the spherical beads on the observed response was investigated by comparing the experimental response of columns packed with non-porous ballotini glass beads (case (i)) and permeable Ca-alginate beads (case (ii)) of the same size. Flow conditions and particle sizes were identical ($Re_p$=50, $R$=2 mm) in the two experiments. Fig.(8.6) is a comparison between responses obtained in cases (i) and (ii), with the insert showing in detail the two responses at small times.

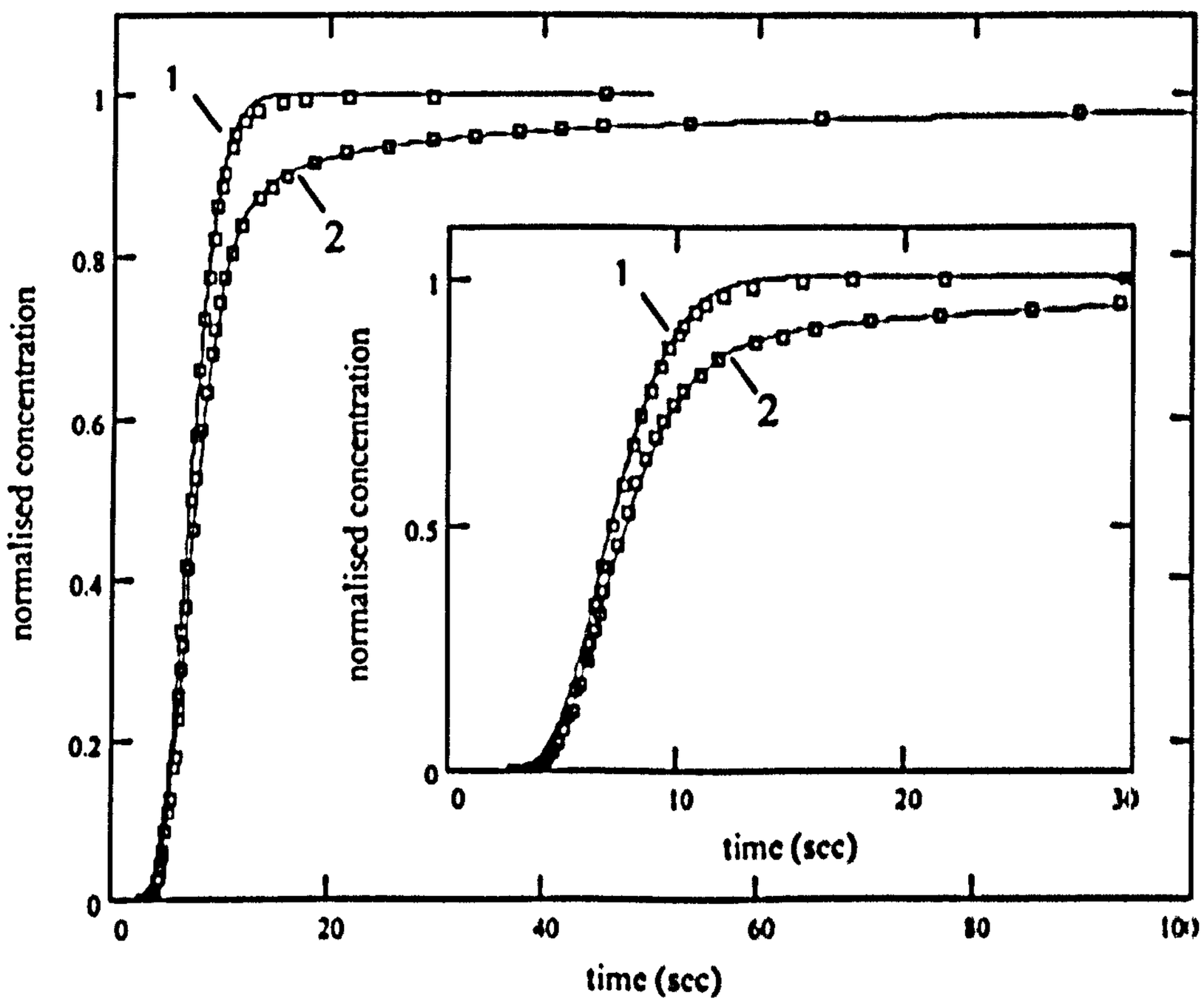


**Figure 8.6 Comparison of the responses of columns containing glass (curve 1) and Ca-alginate (curve 2) beads of 2mm radius for $Re_p$=50. Model predictions for $N$=15 are shown as solid lines. The insert is a detail of the two responses at shorter times.**

The number of CSTRs required to match the experimental response of the column filled with solid-glass beads was estimated to be $N$=15. This experimental response of impermeable packed bed is not affected by intra-particle tracer mass transfer and

characterises the amount of hydrodynamic dispersion in the column. In the model analysis of the experimental responses of Ca-alginate beads, the same number of CSTRs ($N$=15) was used to account for hydrodynamic dispersion, whilst the value for the intraparticle diffusivity was as obtained experimentally (Section (8.1.2). A first observation from Fig.(8.6) is that the presence of Ca-alginate beads alters substantially the transient behaviour of the column. The obtained response is qualitatively different from the one obtained for solid particles, the main difference being a substantial trailing of the response curve towards longer times. This is in agreement with the results of De Backer and Baron [100]. The predictions of the tanks-in-series model of Section (7.2.1), obtained for $N$=15, are also shown as solid lines in both cases.

In Figs.(8.7) and (8.8) the experimental data are plotted for case (ii) along with model predictions which were obtained by ignoring intra-particle diffusion and considering either higher bed voidage (Fig.(8.7)) or different numbers of CSTRs (Fig.(8.8)). Evidently, the experimental response cannot be adequately described by either approach. The good agreement between the predictions of the model presented in Section (7.2.1) and the experiment for the dynamic response of Ca-alginate beads (Fig.(8.6)) and the fact that the model assumes that tracer transport into the beads is caused solely by diffusion, supports the idea that the difference in the response characteristics of the two columns is due to tracer diffusion into the beads. Intra-particle diffusion is a slow process (the relevant dimensionless time scale is $D_{eff}t/R^2$), much slower than convection through the interstitial spaces in the column, and this explains the trailing observed in the response curves of the Ca-alginate column.

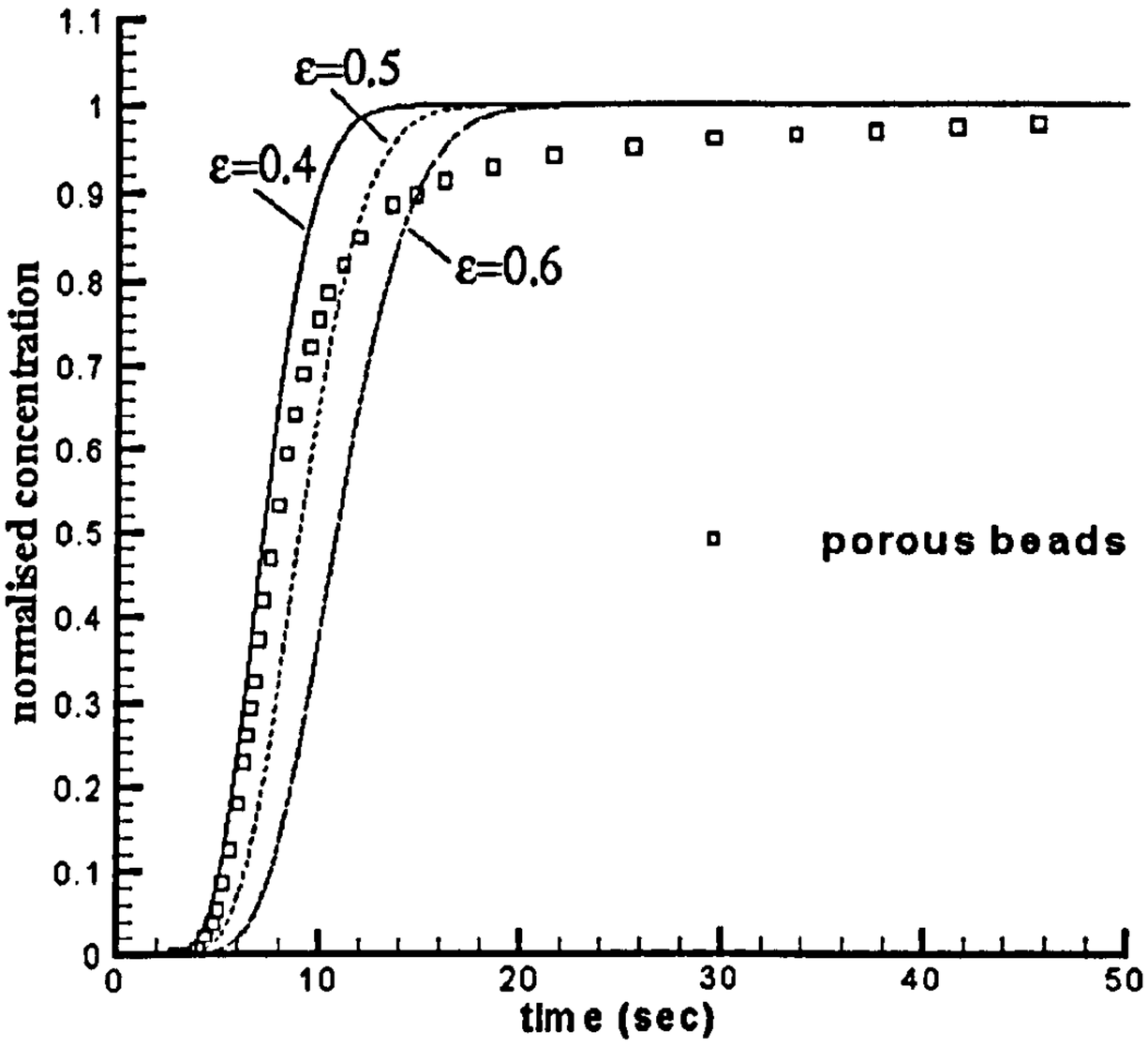


**Figure 8.7** Comparison of the experimental response (points) of the column containing Ca-alginate beads ($R$=2mm, $Re_p$=50) and model predictions at various levels of the bed voidage: $\varepsilon$=0.4 (solid line); $\varepsilon$=0.5 (dashed line); $\varepsilon$=0.6 (long dashed line).

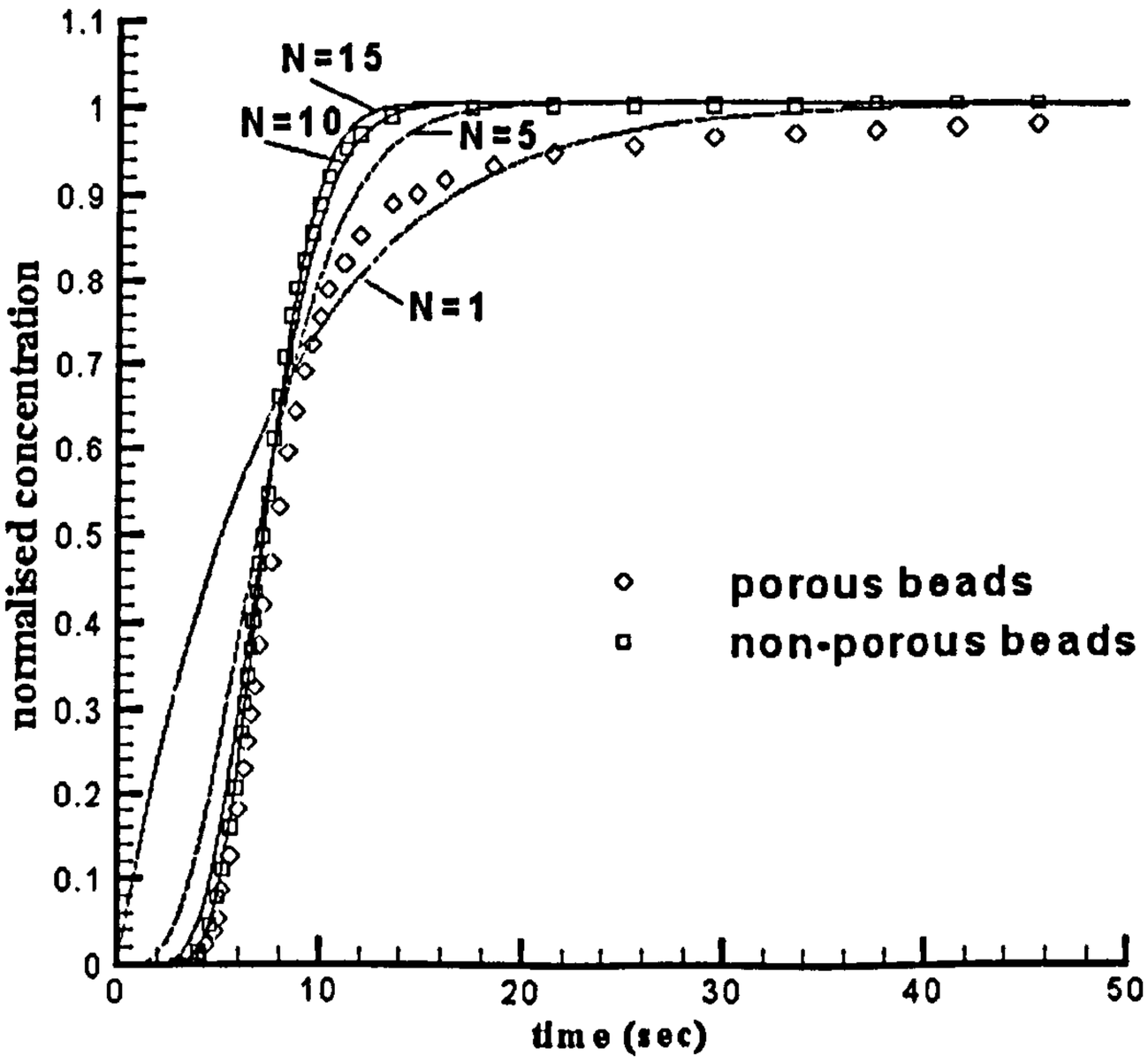


**Figure 8.8** Comparison of the experimental response of columns containing glass non-porous and Ca-alginate porous beads ($R$=2mm, $Re_p$=50). Model predictions corresponding to various numbers of CSTRs ($N$=1,5,10,15) are also shown.

### *8.2.2 The Effect of Particle Size*

The effect of particle size on the observed differences is shown in Fig.(8.9), which, in a manner similar to Fig. (8.6), presents the experimental responses of both glass impermeable and Ca-alginate porous beads of $R$=1 mm along with the model predictions. The best fit of the response of the glass-particle case (i) was achieved for $N$=20 in this case, which indicates a decrease in hydrodynamic dispersion at lower particle size. The agreement between model predictions and experimental response for case (ii) is slightly worse than in Fig.(8.6) (which corresponded to larger particles); this is due to lower value of the particle Sherwood number which implies a small but not negligible effect of the external mass transfer resistance.

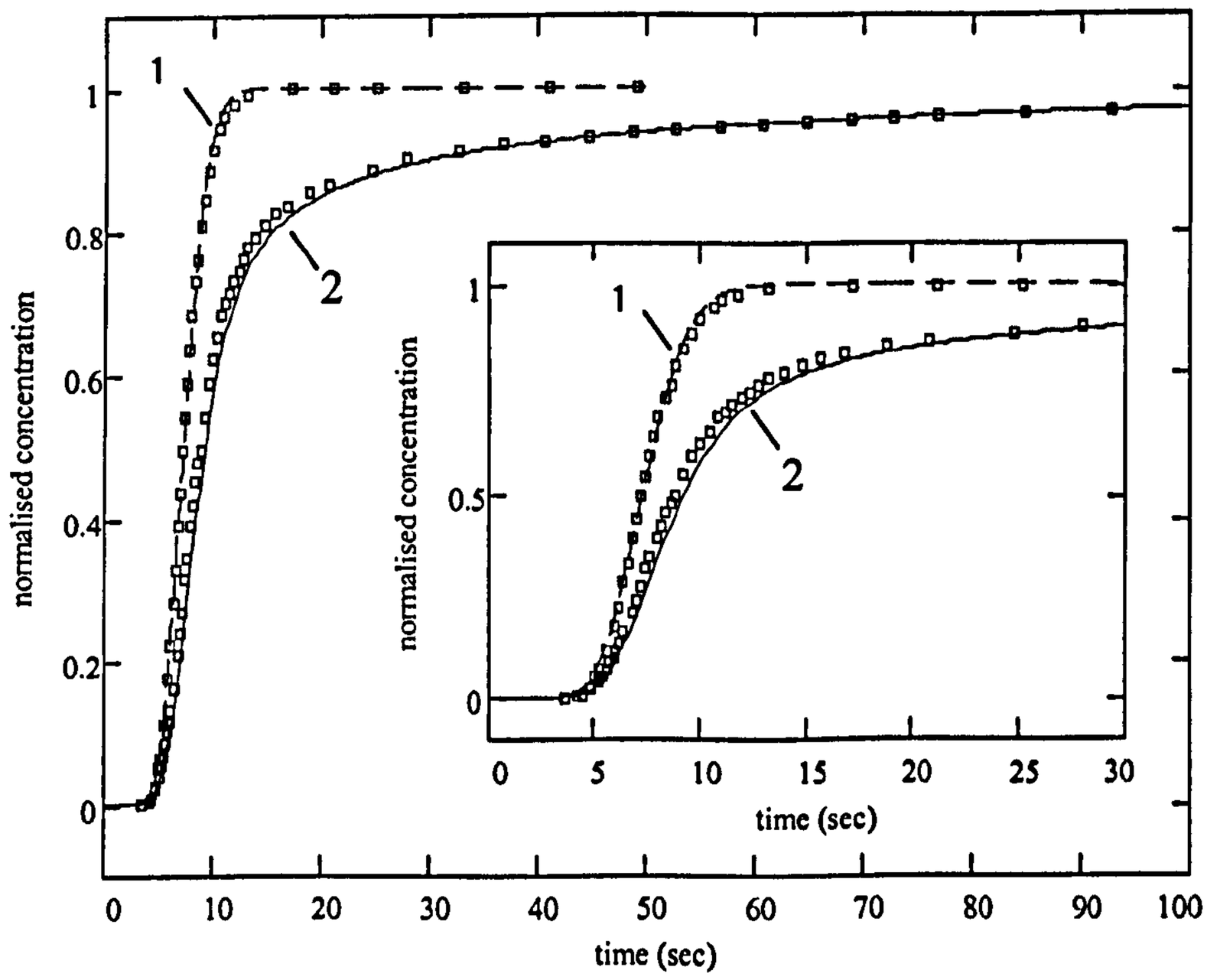


**Figure 8.9** Experimental responses (points) of columns containing glass (curve 1) and Ca-alginate (curve 2) beads of 1mm radius for $Re_p$=25. Model predictions for $N$=20 are shown as solid and broken lines. The insert is a detail of the two responses at shorter times.

In order to confirm that the observed decrease in axial dispersion when the particle radius is reduced from 2 to 1 mm is indeed due to the smaller particle size, the experimentally determined column Peclet numbers (*Pe*, as defined by equation (7.23) in Chapter 7) were compared to the predictions of existing correlations for the effect of particle size on the longitudinal dispersion in packed beds. The column Peclet numbers were first obtained by fitting the experimental response of a glass-bead filled column to the axial dispersion model and were found to be 38 and 25 for particle radii of 1 and 2mm respectively. The corresponding particle-based Peclet numbers ($Pe_p$) were found to be 0.345 and 0.445 respectively.

From previous experimental studies [75], $Pe_p$ is expected to range from 0.225 to 0.95 for 1mm particle radius (corresponding to $Re_p$=25) and from 0.240 to 1.15 for 2mm particle radius (corresponding to $Re_p$=50; values for $\rho$ and $\mu$ were taken as 1g/cm$^3$ and 1cP in the above calculation since the solution of acetone is very diluted). For comparison, the correlation of Chung and Wen [75], adopted by Dueck *et al.* [68] in the analysis of axial dispersion in a fluidised-bed microencapsulated urease column, gives values of 0.616 and 0.662 for $Pe_p$. The obtained values for $Pe_p$ of 0.345 and 0.445 for particle radii 1 and 2mm respectively are in agreement with the predictions of equation (7.27), within the range of the scatter of the data on which equation (7.27) is based.

The previously obtained values of the column Peclet number, *Pe* (from the dispersion model) were compared with the corresponding number of CSTRs (from tanks-in-series model). It can be seen by substituting into equation (7.29) that the values $N$=20 and $Pe=(u_i L/D_{ax})$=38 for particle radius of 1mm and $N$=15, $Pe$=25 for particle radius of 2mm are in excellent agreement.

### 8.2.3 Conclusions

The dynamic response of fixed beds filled with typical cell or enzyme immobilisation matrices, namely Ca-alginate in the form of spherical beads of two sizes, was studied experimentally using acetone solution as tracer at $Re_p$=50 and $Re_p$=25 respectively. These were compared to the breakthrough curves of the same column in the absence of intra-particle diffusion; this was achieved by replacing the Ca-alginate beads by solid glass particles of the same size. It was found that the presence of the (porous) Ca-alginate beads alters the response characteristics of the system significantly compared to a bed filled with impermeable particles. The measured response curves are compared with model predictions, where all required physical parameters are determined experimentally. The agreement is remarkably good, and points to the conclusion that the observed modified response is due to tracer diffusion inside the immobilisation beads. Small differences between model and experiment could be ascribed to external mass transfer resistance, which have not been considered in the model.

## 8.3 The Effect of Superficial Velocity on the Dynamic Responses of the Columns Containing Solid non-Porous and Porous Beads

The objective of the second part of the experimental program was to ascertain the influence of fluid to particle mass transfer resistance on the dynamic response of fixed beds in the low to moderate particle Reynolds numbers regime (ranging from 0.3 to 39.3) and high particle Peclet number regime (ranging from 250 to 40000). For that purpose, the dynamic response of columns packed either with impermeable glass or porous Ca-alginate beads to a step change in the inlet tracer concentration were obtained experimentally using the set-up described in the previous section. These are compared to each other as well as to the predictions of the models outlined in Section (7.2.1).

### *8.3.1 Hydrodynamic Dispersion*

The first step in the analysis was to determine the hydrodynamic characteristics of the glass column. Fig.(8.10) shows the experimental responses of a fixed bed packed with ballotini glass beads versus dimensionless time ($t_R = t\frac{F}{\varepsilon V}$) for all Reynolds numbers investigated including $Re_p$=50 from Section (8.2).

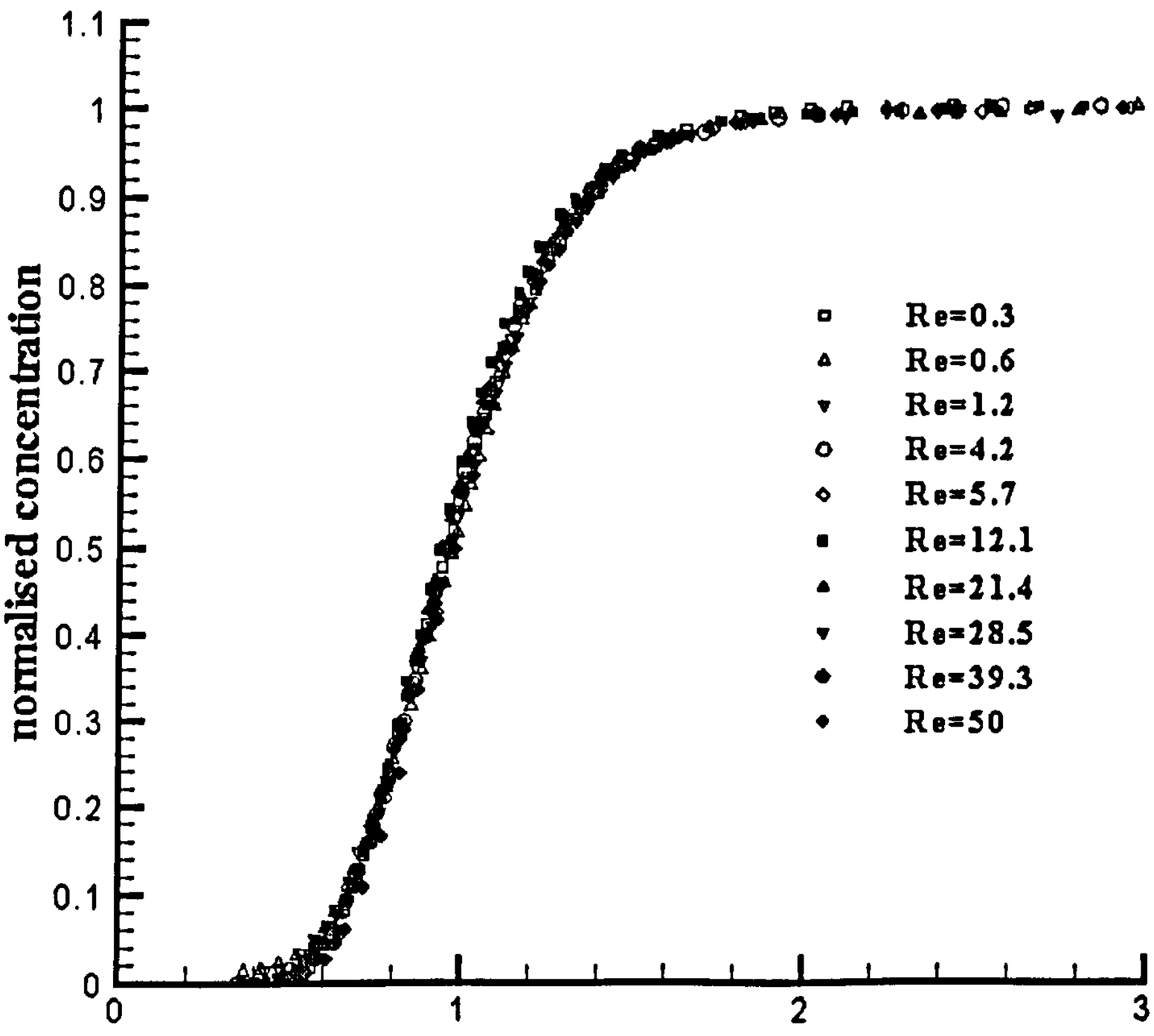


**Figure 8.10** The master curve of the dynamic responses on the step signal of acetone of the column packed with non-porous glass beads versus the dimensionless time $t_R$. All the observed responses were fitted with $N$=13 to $N$=15.

The experimental data fall on a single master curve. This master curve was used to determine *N*, the number of CSTRs in the tank-in-series model in Section (7.2.1) (with no mass flux term considered), that best fits the experimental data. Values of *N* from 13 to 15 were found to best fit the experimental breakthrough curves. This implies no significant effect of particle Reynolds number on the dispersion characteristics of the column. This result is in agreement with the experimental findings of Levenspiel and Bischoff [106], Chung and Wen [75] and Leitao *et al.* [78]. These authors propose correlations that give a small increase in the axial dispersion (smaller *N*) in column when $Re_p$ decreases for the range of $Re_p$ examined in our experiment. Since the fitted values of *N* slightly decreased with the decrease of $Re_p$ it was concluded that hydrodynamic dispersion does not alter significantly with decrease of $Re_p$.

The next step in the model analysis is to determine the fluid to particle mass transfer coefficient from the breakthrough curves of the column filled with porous Ca-alginate beads of the same size as the glass beads. As in the analysis in Section (8.2), it was assumed that *N*, which characterises the hydrodynamic dispersion in the column, is unaffected by the change from glass to porous particles. For this range of the particle Reynolds numbers, no noticeable change of the bed structure was observed, as there was no compressibility of the beads. Hence, it was assumed that the same *N* would describe the hydrodynamic dispersion in the column with Ca-alginate beads, and this number was used in the subsequent analysis.

### *8.3.2 The Effect of the Mass Transfer Resistance in the Inter-Particle Space*

Typical comparisons of the observed experimental breakthrough curves of fixed beds of glass beads and Ca-alginate beads of the same size (*R*=2mm) are presented in Fig.(8.11a,b) for the lowest $Re_p$=0.3 (8.11a) and a moderate $Re_p$=4.2 (8.11b) examined.

(a)

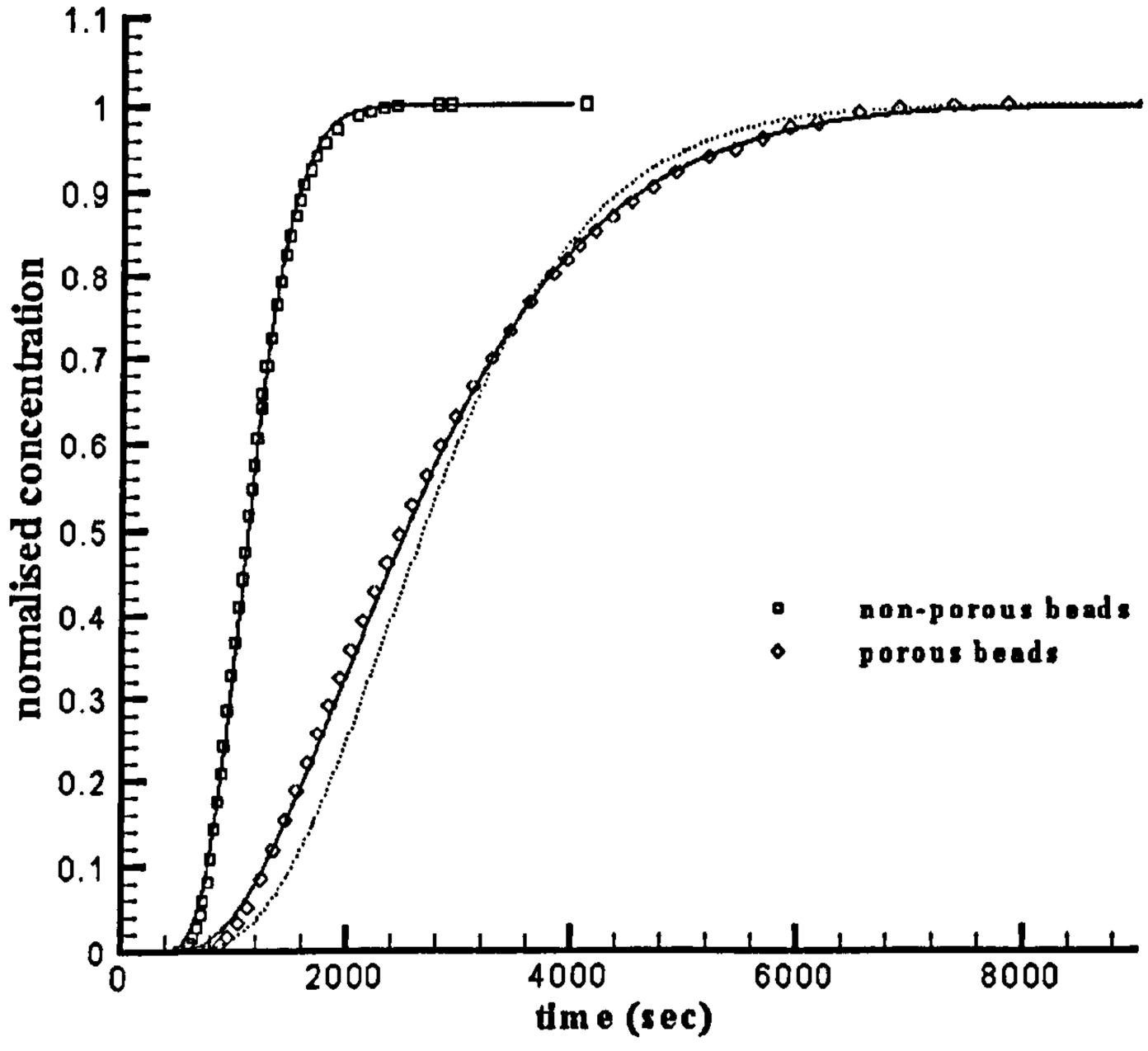


(b)

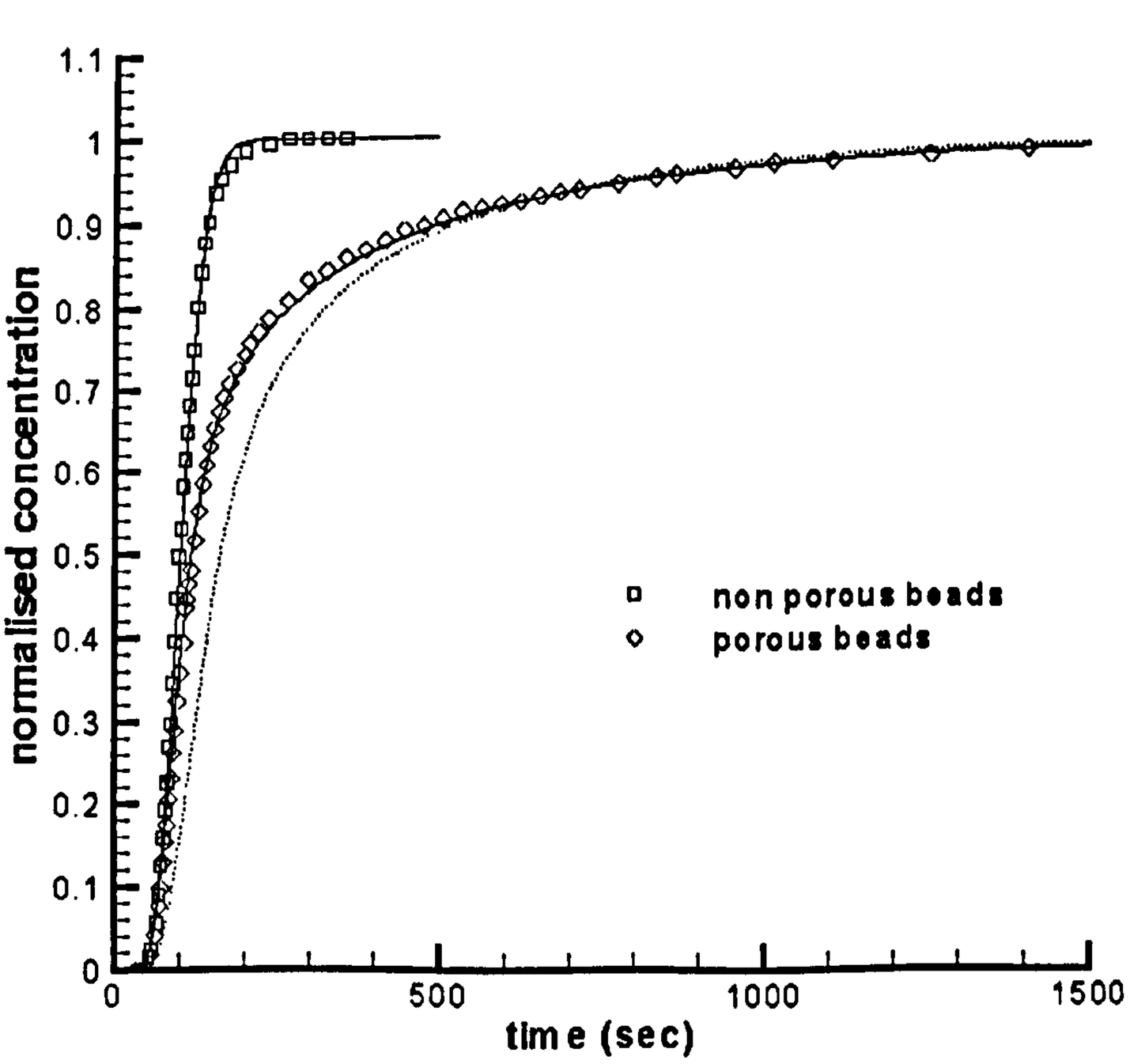


**Figure 8.11a,b** Comparison of the responses of columns containing glass (non-porous) beads and Ca-alginate (porous) beads of 2mm radius for $Re_p$=0.3 (a) and $Re_p$=4.2 (b). Model predictions for $N$=13 (glass beads) and $N$=13 and $Bi$=0.3 (alginate beads) are shown as solid lines. The dotted line shows model prediction where no mass transfer resistance is considered.

As expected, at all particle Reynolds numbers, the transient behaviour of the column with porous beads differs substantially from the response of the column filled with glass beads. When the column is filled with porous beads mass transfer from the bulk liquid into the beads occurs and the system takes longer time to reach the steady state. As a result, the response curves of the Ca-alginate column are shifted to the right side of the diagrams.

*A model based on the assumption that there is no fluid to particle mass transfer resistance in the system (obtained by setting $C_i(t) = C_s(t)$ in equation (7.14)) was not able to fit the experimental Ca-alginate responses well, particularly at lower $Re_p$* (Fig.8.11a,b). This is understandable, since at the corresponding low fluid superficial velocities the fluid to particle mass transfer resistance will not be negligible. The observed difference between model and experiment is appreciable for both moderate $Re_p$=4.2 and low $Re_p$=0.3 but, recalling from Fig.(8.6) almost negligible for $Re_p$=50.

Consideration of external mass transfer resistance in the model, as outlined in the Section (7.2.1) earlier, allows for the response of a bed of Ca-alginate beads to be properly modelled. The value of the external mass transfer coefficient $k_c$ (and, in turn, Biot number, *Bi*) is a quantitative measure of the external mass transfer resistance. By a trial-and-error procedure, *Bi* corresponding to a particular flowrate was determined as the one giving the best fit between model predictions and experiments. This is shown in Fig.(8.12) where comparisons are made for $Re_p$ =21.4 and the optimal *Bi*=20.

The predicted response curves corresponding to the values for *Bi* of ±20% around the mean (optimal) *Bi* value are also shown in Fig.(8.12). Simulation results were found to be in a reasonable agreement with the experimental curves for values of *Bi* ±20% around a mean value for all particle Reynolds numbers investigated.

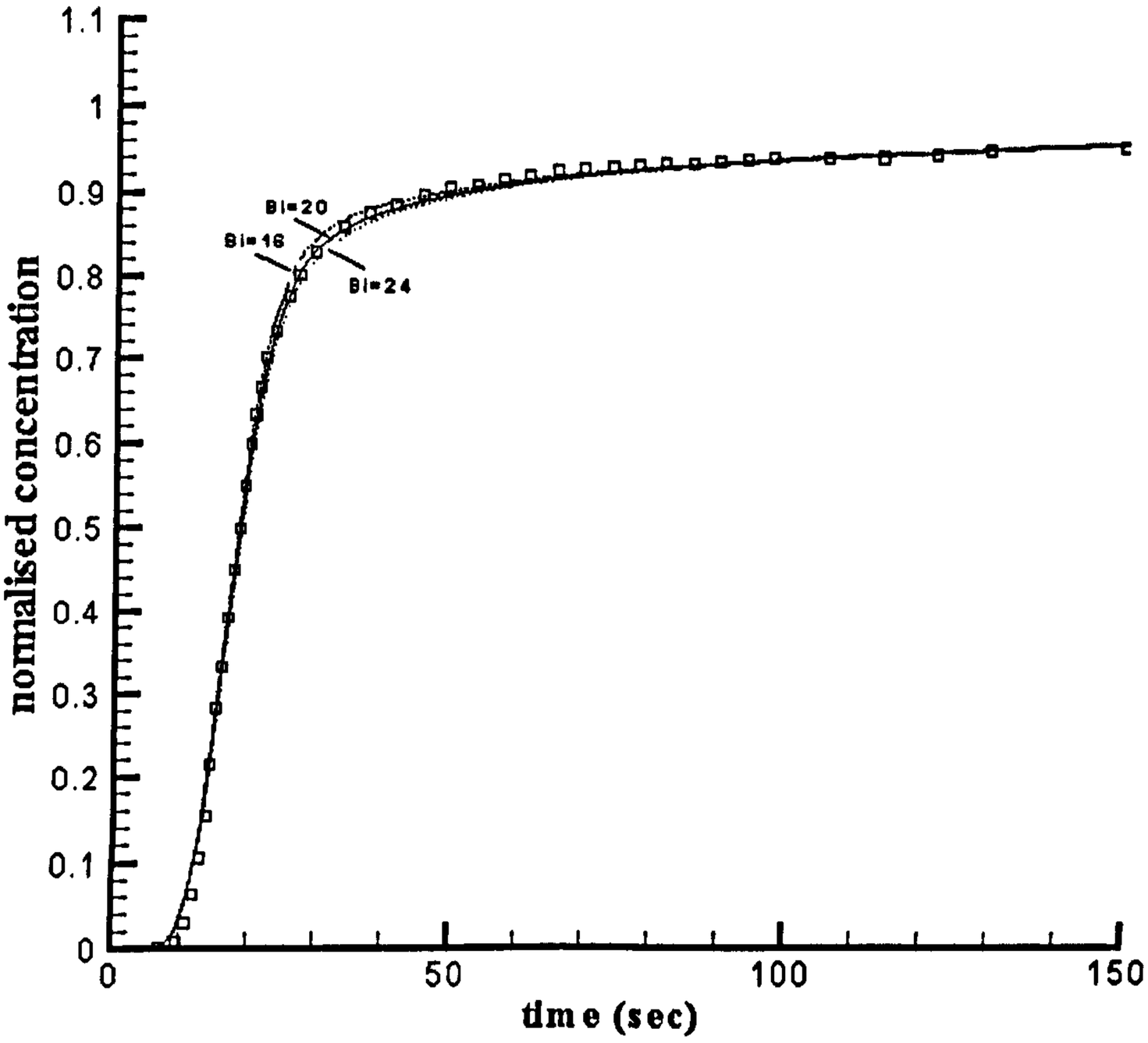


**Figure 8.12** Determination of the Biot number that gives the best fit of the experimental porous beads response (points) for $Re_p$=21.4. Model predictions with different values of $Bi$=16, $Bi$=20 (best fit) and $Bi$=24 are shown as dotted, solid and dashed lines respectively.

### *8.3.3 Comparisons with Models and Correlations from the Literature*

After the values of the external mass coefficients, $k_e$, were extracted from the experimental response curves for given Reynolds numbers, the values of the particle Sherwood numbers are obtained from $Sh_p = k_e \frac{d_p}{D}$, where $D$ is the diffusion coefficient of acetone in water ($1.22 \cdot 10^{-5}$ cm$^2$/s) [114] and $d_p$ is the particle diameter. These are used for the comparisons with the values for the particle Sherwood number taken from the literature for mass transfer in beds packed with spherical particles. The general way of presenting experimental data for mass transfer in packed beds is by the empirical correlations of type:

$$Sh_p = \alpha Re_p^{\beta} Sc^{\gamma} \tag{8.5}$$

where $Re_p = \frac{ud_p\rho}{\mu}$ is particle Reynolds number, $Sc = \frac{\mu}{\rho D}$ is Schmidt number and parameters $u$ and $D$ are determined experimentally. Several such correlations are listed in Table 1.

| Reference | Correlation | Validity |
|---|---|---|
| Gnielinski [115] | $Sh_p = f_a(2+\sqrt{Sh_{lam}^2 + Sh_{tur}^2}$ where: $f_a = 1+1.5(1-\varepsilon)$ $Sh_{lam} = 0.644\sqrt{Re_{p,int}}\sqrt[3]{Sc}$ $Sh_{tur} = \frac{0.037Re_{p,int}^{0.8}Sc}{1+2.443Re_{p,int}^{-0.1}(Sc^{2/3}-1)}$ $Re_{p,int} = \frac{Re_p}{\varepsilon}$ | All $Re_p$ |
| Thoenes and Kramers [88] | $Sh_p = 1.17Re_p^{0.585}Sc^{1/3}$ | $Re_p$>5 |
| Coeuret [116] | $Sh_p = 5.4Re_p^{1/3}Sc^{1/3}$ | 0.04< $Re_p$ <30 |
| Kasaoka and Nita [117] | $Sh_p = 0.7Re_p^{0.39}Sc^{0.50}$ | 1 < $Re_p$ <100 |
| Wilson and Geankoplis [118] | $Sh_p = 2.5Re_p^{1/3}Sc^{1/3}$ | 0.016< $Re_p$ <55 |
| Wiliamson *et al.*[119] | $Sh_p = 2.4Re_p^{0.34}Sc^{1/3}$ | 0.04< $Re_p$ <52 |
| Gaunand and Coeuret [120] | $Sh_p = 3.28Re_p^{0.326}Sc^{1/3}$ | 0.2< $Re_p$ <7 |
| Dwivedi and Upadhyay [121] | $Sh_p = \frac{1.11}{\varepsilon}Re_p^{0.326}Sc^{1/3}$ | $Re_p$ <10 |

**Table 1.** Literature mass-transfer correlations for beds of spherical particles used for comparison with the data obtained in this study.

Pfeffer [84] and Nelson and Galloway [85] proposed the theoretical models for the particle Sherwood number in beds of spherical particles in the low Reynolds number-high Peclet numbers regime (Pfeffer) and low Reynolds numbers regime (Nelson and Galloway, $0.1< Re_p <100$). Their expression for $Sh_p$ are given in Chapter 7.

The coefficient $\alpha$ in Nelson and Galloway in equations (6.3) and (6.3a) is an adjustable parameter that the authors suggested to take as 0.6 from the original paper. This value was used in the subsequent comparisons.

Plotted on Figs. (8.13-8.15) are the experimental responses of the column packed with Ca-alginate beads along with model predictions for $Re_p$ =0.3, $Re_p$=5.7 and $Re_p$=50. The latter were obtained by calculating the fluid to particle mass transfer coefficient $k_e$ (which is required for $Bi$ in the model) from $Sh_p$ obtained from the correlations of Table 1 and from the Pfeffer and the Nelson-Galloway models. The response curves with optimal value of $Bi$ ($Sh_p$) obtained by fitting the experimental data with model predictions are also plotted in each case.

For $Re_p$ =0.3 (Fig.(8.13)) the experimental data are in good agreement with the predictions of the Pfeiffers model (PF) and of virtually all the correlations of Table1. The discrepancy with the correlation of Thoenes and Kramers (TK) has been also shown to illustrate the limits of its usage ($Re_p$>5) as pointed out by the authors. In Fig.(8.14) for a moderate particle Reynolds number, $Re_p$=5.7, the experimental data fall slightly above the predictions of Pfeiffers model and all the correlations of Table 1. The overall discrepancies are small, being most pronounced for Coeuret and Gaunand and Coeuret correlations.

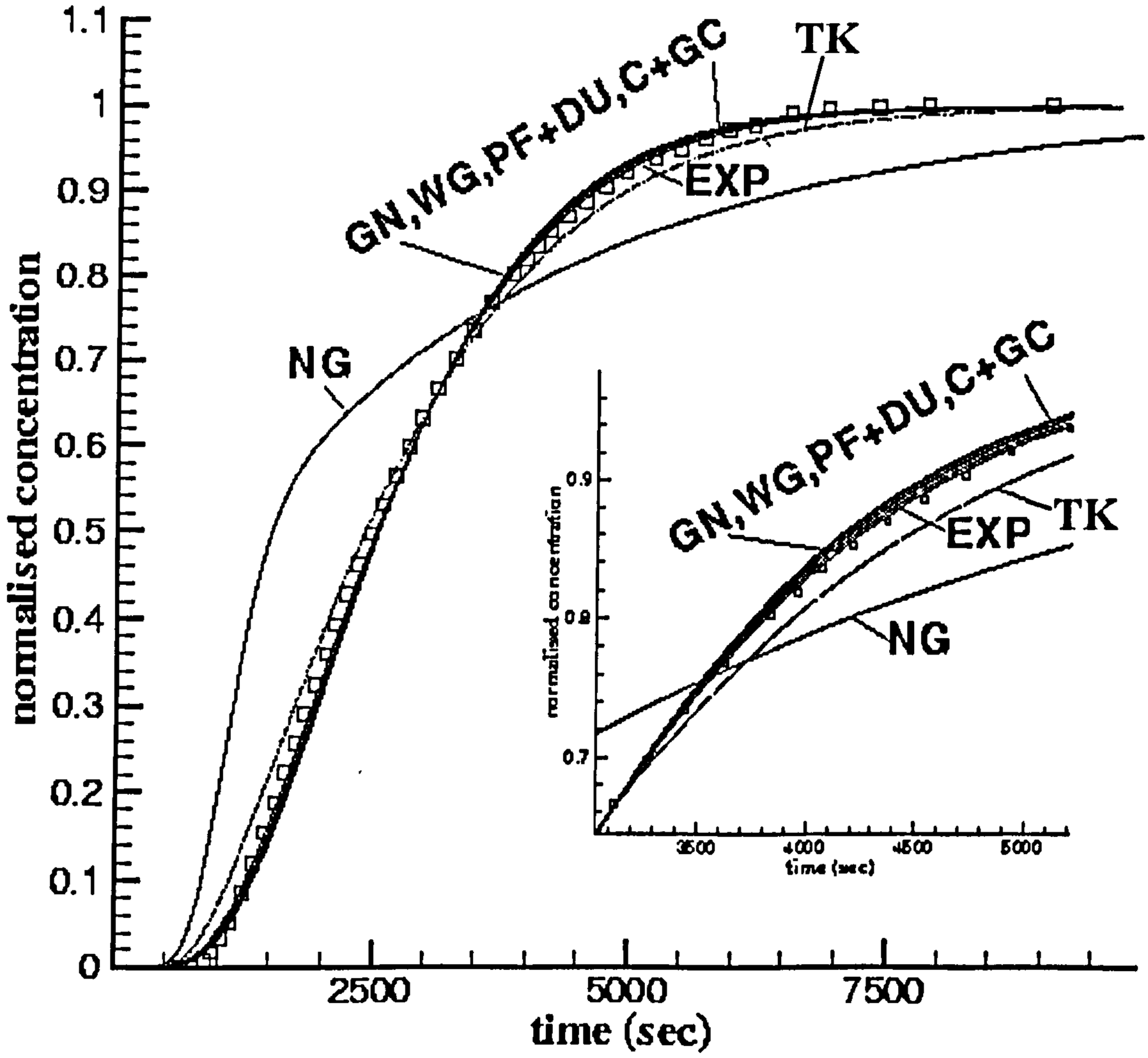


**Figure 8.13** Comparisons of the experimental responses of the column packed with Ca-alginate beads with the tanks-in-series model predictions based on the empirical correlations from Table 1and Pfeiffer and Nelson and Galloway models: $Re_p$=0.3, experimental data (points), best fit from the tanks-in-series model (equations (7.11), (7.12) and (7.14)) (EXP), Pfeiffer (PF), Nelson and Galloway model (NG), Thoenes and Kramers (TK), Gniellinski (GN), Wilson and Geankoplis (WG) Dwivedi and Upadhay (DU) Coeuret (C) and Gaunand and Coeuret (GC).

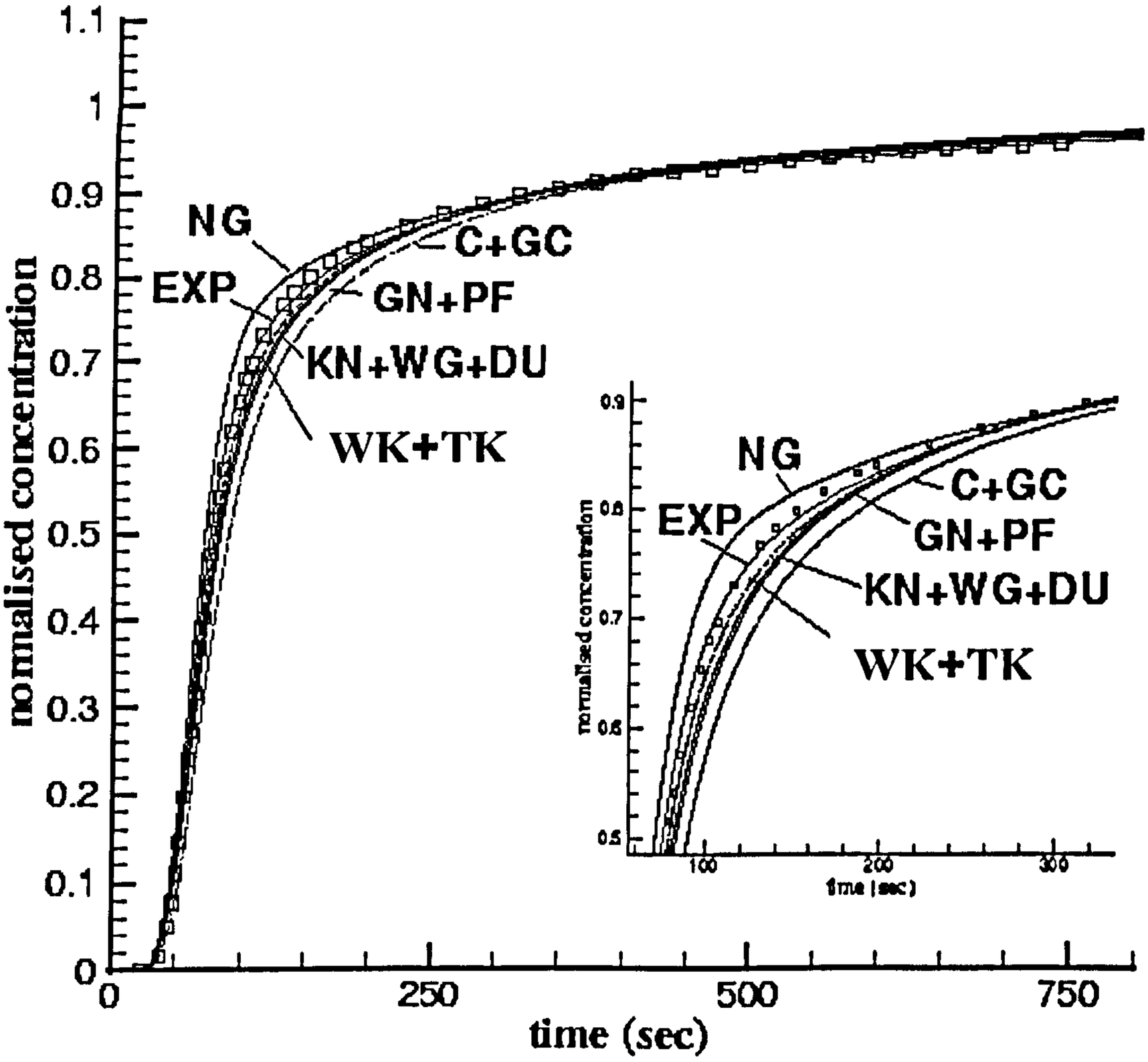


**Figure 8.14** Comparisons of the experimental responses of the column packed with Ca-alginate beads with the tanks-in-series model predictions based on the empirical correlations from Table 1and Pfeiffer and Nelson and Galloway models: $Re_p$=5.7, experimental data (points), best fit from the tanks-in-series model (equations (7.11), (7.12) and (7.14)) (EXP), Pfeiffer (PF), Nelson and Galloway model (NG), Thoenes and Kramers (TK), Gniellinski (GN), Wilson and Geankoplis (WG) Dwivedi and Upadhay (DU) Coeuret (C) and Gaunand and Coeuret (GC).

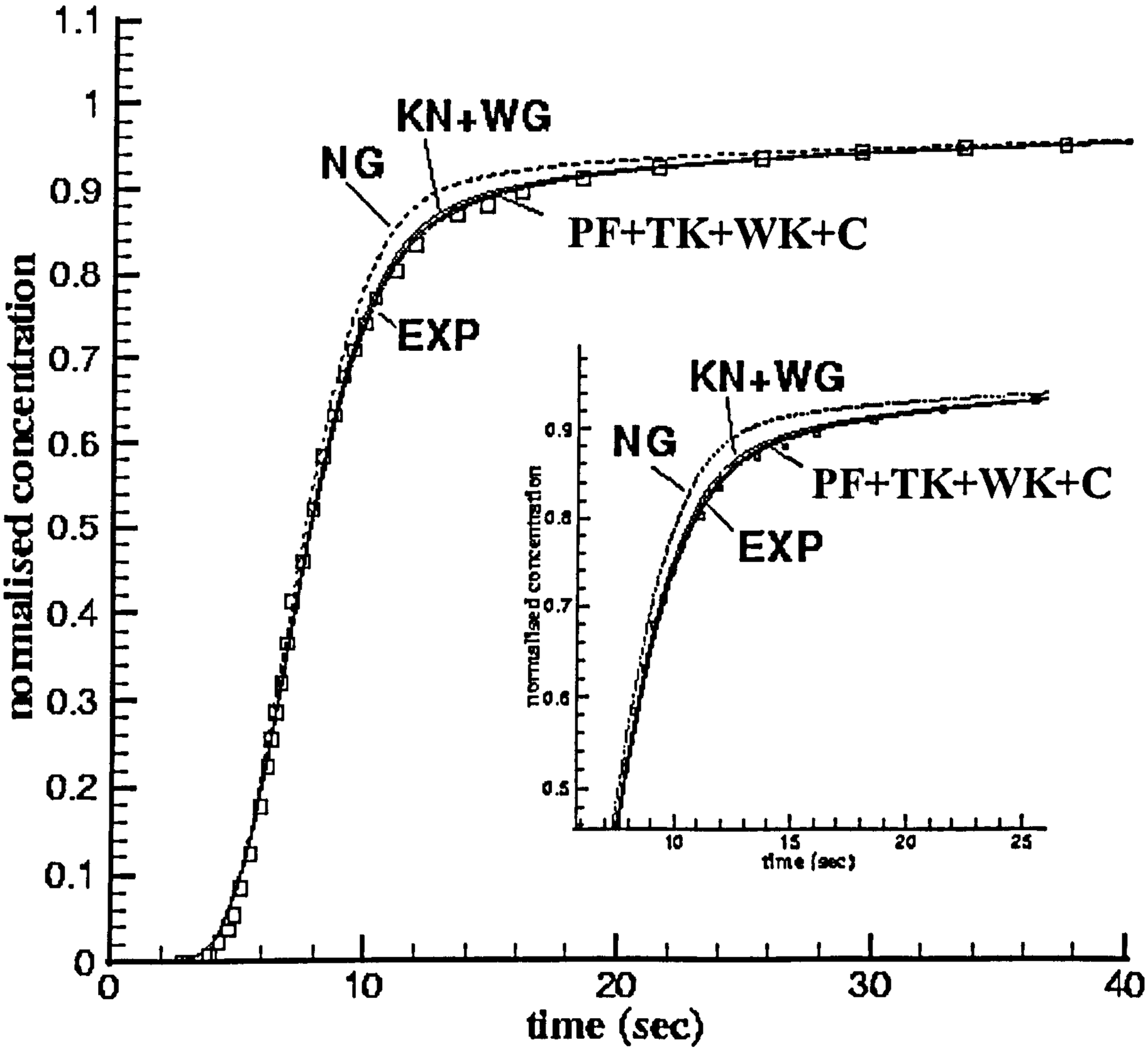


**Figure 8.15** Comparisons of the experimental responses of the column packed with Ca-alginate beads with the tanks-in-series model predictions based on the empirical correlations from Table 1and Pfeiffer and Nelson and Galloway models: $Re_p$=50, experimental data (points), best fit from the tanks-in-series model (equations (7.11), (7.12) and (7.14)) (EXP), Pfeiffer (PF), Nelson and Galloway model (NG), Thoenes and Kramers (TK), Gniellinski (GN), Wilson and Geankoplis (WG) Dwivedi and Upadhay (DU) Coeuret (C) and Gaunand and Coeuret (GC).

At the highest $Re_p$=50 (Fig.(8.15)) the agreement between model predictions and experimental data is very good. This is expected since this is the flow regime for

packed beds where fluid to particle mass transfer resistance can be neglected. The Nelson and Galloway model (with $\alpha$=0.6) resulted in external mass transfer coefficients that gave responses very different to the experimental data. In order to fit the experimental data the parameter α had to be readjusted in all cases. The reason for this discrepancy can lie in the way that Nelson and Galloway defined mass transfer coefficient, as pointed out by the authors in [95,96,122]. In their model mass transfer coefficient (and thus $Sh_p$) is related to the initial concentration difference between the fluid concentration at the bead surface and the fluid concentration in the bulk ($C_i$- $C_s$) instead of the time averaged concentration difference of the same term. In the model applied in this study this concentration difference is time dependent which is essential in the analysis of transient systems where the driving force for mass transfer is changing with time.

### *8.3.4 Conclusions*

The dynamic responses of columns made up of non-porous and porous beads were studied experimentally using acetone solution as the tracer at low and moderate particle Reynolds number regime (0.3< $Re_p$ <50) and high particle Peclet number regime (250< $Pe_p$ <40000). In order to assess the importance of mass transfer hindrance in the system the measured response curves are compared with model predictions, where all required physical parameters are determined experimentally.

In the investigated flow regime, the effect of the hydrodynamic dispersion on dynamic responses of the column was shown to be of small extent. It was found that at low Reynolds numbers ($Re_p \leq 5$) mass transfer resistance in the external film of liquid plays a significant role and should not be neglected in the dynamic analysis of these systems. At higher Reynolds numbers with moderate effect of turbulence this effect is less appreciable but still could be distinguished. For the highest $Re_p$=50 the effect of turbulence on flow patterns is intense and we have not observed any resistance to mass transfer. Apart from the predictions from Nelson-Galloway model the

experimental findings and model results in this study for the particle Sherwood numbers showed reasonably good agreement with other correlations from the literature.

## *8.4 Notation*

| | |
|---|---|
| A | tracer |
| B | particles |
| $C(t)$ | tracer concentration in the bulk liquid |
| $C_i(t)$ | tracer concentration in the bulk liquid in the *i-th* CSTR |
| $C_{in}$ | initial concentration of the tracer in the particles |
| $C_s(t)$ | tracer concentration at the particle surface in the *i-th* CSTR |
| $D$ | molecular diffusivity of the tracer A in water |
| $D_{ax}$ | axial dispersion coefficient |
| $D_{AB}$ | molecular diffusivity of the tracer A into the particles B |
| $D_{eff} = \varepsilon_p D_{AB}$ | effective diffusivity of the tracer A into the particles B |
| $d_p$ | bead diameter |
| $F$ | volumetric flowrate |
| $k_e$ | external mass transfer coefficient |
| $L$ | column length |
| $M$ | number of the beads |
| $N$ | number of continuously stirred tank reactors (CSTR) modelling back mixing in the column |
| $q_n$ | non-zero positive roots of equation: $\tan(q_n) = \frac{3q_n}{3+\alpha(q_n)^2}$ |
| $R$ | bead radius |
| $t$ | time |
| $t_R = t\frac{F}{\varepsilon V}$ | dimensionless time |
| $u_i$ | fluid interstitial velocity |
| $u_s$ | fluid superficial velocity |
| $V_{blk}$ | bulk liquid volume |
| $V$ | bed volume |

*Greek letters*

$\alpha$ the ratio of the bulk liquid volume ($V_{blk}$) over the volume occupied by the beads

$\varepsilon$ interparticle porosity (bed voidage)

$\varepsilon_p$ intraparticle porosity

$\kappa$ parameter defining the shape of the error function

$\rho$ fluid density

$\mu$ fluid dynamic viscosity

*Dimensionless Numbers*

$Bi = \frac{k_e R}{D_{eff}}$ mass Biot number

$Pe = \frac{u_i L}{D_{ax}}$ column Peclet number

$Pe_p = Pe\,(d_p/L)$ particle Peclet number

$Re_p = \frac{u_s d_p \rho}{\mu}$ particle Reynolds number

$Sc = \frac{\mu}{\rho D}$ Schmidt number

$Sh_p = k_e \frac{d_p}{D}$ particle Sherwood number

## Bibliography

[62] **Mazid, M.A.:** Biocatalysis and Immobilized Enzyme/Cell, *Bio. Biotech*,. **11** (1993) 690-695.

[63] **Cheryan, M.; Mehaia, M.:** *Membrane bioreactors.* In: McGregor, W.C. (Ed.): Membrane Separations in Biotechnology, pp. 255-301. New York : Marcel Dekker, Inc. (1986).

[64] **Bailey, J.E.; Ollis, D.F.:** *Biochemical Engineering Fundamentals.* New York: McGraw-Hill, Inc. 2nd edition (1986).

[65] **Ishimura, F.; Suga, K.:** New bioreactor for fibrous support and hydrolysis of penicillin G, *J. Chem. Eng. Jap.*, **28** (1995) 443-448.

[66] **Gilson, C.D; Thomas, A:** Ethanol production by alginate immobilised yeast in a fluidized bed reactor, *J. Chem. Tech. Biotechnol.*, **62** (1995) 38-45.

[67] **Gupta, S.K.; Chand, S:** Bioconversion of sugars to ethanol in an immobilised cell packed bed bioreactor-Dynamic response to perturbations in process parameters, *Chem. Eng. Journ.*, **43** (1990) B1-B12.

[68] **Dueck, C.L.; Neufeld, R.J.:** Hydrodynamics and urea hydrolysis in a microcapsulated urease, fluidised bed reactor, *Can. J. Chem. Eng.*, **64** (1986) 540-546.

[69] **Godia, F.; Casas, C.; Sola, C.:** A survey of continous ethanol fermentation systems using immobilised cells, *Proc. Biochem.*, **22** (1987) 43-48.

[70] **Taylor, G.I.:** Dispersion of soluble matter in solvent flowing slowly through a tube, *Proc. Roy. Soc.*, **219A** (1953) 186-203.

[71] **Taylor, G.I.:** Conditions under which dispersion of solute in a stream of solvent can be used to measure molecular diffusion, *Proc. Roy. Soc.*, **225A** (1954) 473 –477.

[72] **Aris, R.**: On the dispersion of a solute in a fluid flowing through a tube, *Proc. Roy. Soc.*, **A235** (1954) 67-77.

[73] **Bischoff, K.B.**: PhD. Thesis, Chemical Engineering Department, Illinois Institute of Technology (1961).

[74] **Levenspiel, O.:** Chemical Reaction Engineering. New York: John Wiley & Sons, Inc. 2nd edition (1999), pp.311

[75] **Chung, S.F.; Wen C.Y.:** Longitudinal dispersion of liquid flowing through fixed and fluidized beds, *AIChE Journal*, **14** (1968) 857-866.

[76] **Moulijn; J.A.**: Thesis, University of Amsterdam, Amsterdam.

[77] **Westerterp, K.R.; Van Swaaij, W.P.M.; Beenackers, A.A.C.M.**: *Chemical Reactor Design and Operation.* New York: John Wiley & Sons, Inc. 2nd edition (1983) pp. 214.

[78] **Leitao,A.; Carlos,P; Santos,S.; Rodrigues,A.:** Tracer experiments in fixed beds: effect of flow maldistribution on the estimation of transport kinetic parameters, *Chem. Eng. Journ.*, **53** (1994) 193-199.

[79] **Papathanasiou, T.D.; Kalogerakis, N.; Behie L.A.; Gaucher, G.M.; Thibault, J.:** Modelling the dynamic behaviour of immobilized cell/enzyme bioreactors: The tanks-in series model. In: Ho, C.S and Oldshue, J.(Eds): Biotechnology processes: Scale-up and Mixing pp.238-248. New York: (1987).

[80] **Froessling, N.**: Über die Verdunstung fallender. Tropfen, *Gerlands Beitr. Geophys.*, **52** (1938) 170-216.

[81] **Ranz W.E.**: Friction and transfer coefficients for single particles and packed beds, *Chem. Eng. Prog.*, **48** (1952) 247-253.

[82] **Cornish, A.R.H.**: Note on minimum possible rate of heat transfer from a sphere when other spheres are adjacent to it, *Trans. Inst. Chem. Engrs.*, **43** (1965) T332-T333.

[83] **Happel, J.**: Viscous flow in multiparticle systems: slow motion of fluids relative to beds of spherical particles, *AIChE Journal*, **4** (1958) 197-201.

[84] **Pfeffer,R.; Happel, J.:** An analytical study of heat and mass transfer in multiparticle systems at low Reynolds numbers, *AIChE Journal*, **10** (1964) 605-611.

[85] **Nelson, P.A.; Galloway, T.R.:** Particle-to fluid heat and mass transfer in dense systems of fine particles, *Chem. Eng. Sci.* **30** (1975) 1-6.

[86] **Danckwerts, P.V.:** Significance of liquid-film coefficients in gas absorption, *Ind. Eng. Chem.*, **43** (1951) 1460-1467.

[87] **Rowe, P.N.:** Particle-to-liquid mass transfer in fluidised beds, *Chem. Eng. Sci.*, **30** (1975) 7-9.

[88] **Thoenes, D. Jr.; Kramers, H.:** Mass transfer from spheres in various regular packings to a flowing fluid, *Chem. Eng. Sci.*, **8** (1958) 271-283.

[89] **Kunii, D.; Suzuki, M.:** Particle-to-fluid heat and mass transfer in packed beds of fine particles, *Int. J. Heat Mass Transfer*, **10** (1967) 845-852.

[90] **Wakao, N.; Funazkri, T.:** Effect of fluid dispersion coefficients on particle-to-fluid mass transfer coefficients in packed beds: Correlation of Sherwood numbers, *Chem. Eng. Sci.*, **33** (1978) 1375-1384.

[91] **Dwivedi, P. N.;Upadhyay, S. N.:** Particle-fluid mass transfer in fixed and fluidized beds, *Ind. Eng. Chem. Process. Des. Dev.*, **16** (1977) 157-165.

[92] **Wakao, N. and Kaguei S.:** *Heat and mass transfer in packed beds.* New York, London : Gordon and Breach Science, (1982).

[93] **Gunn, D. J.:** Transfer of heat or mass to particles in fixed and fluidised beds, *Int. J. Heat Mass Transfer*, **21** (1978) 467-476.

[94] **Fedkiew, P.; Newman, J.:** Low Peclet number behaviour of the transfer rate in packed beds, *Chem. Eng. Sci.*, **33** (1978) 1043-1048.

[95] **Glicksman,L. R.;Joos F. M.:** Heat and mass transfer in fixed beds at low Reynolds numbers, *J. Heat Transfer*, **102** (1980) 736-741.

[96] **Tsotsas, E.:** Low Peclet number transient heat transfer in packed beds: re-evaluation of the data of Donnadieu, *Chem. Eng. Sci.*, **48** (1993) 3434-3437.

[97] **Rexwinkel,G.; Heesink, A.B.M.; Van Swaaij,W.P.M.:** Mass transfer in packed beds at low Peclet numbers-wrong experiments or wrong interpretations?, *Chem. Eng. Sci.*, **52** (1997) 3995-4003.

[98] **Schlünder E.U.:** On the mechanism of mass transfer in heterogeneous systems-in particular in fixed beds, fluidized beds and on bubble trays, *Chem. Eng. Sci.*, **32** (1977) 845-851.

[99] **Westerterp, K.R.; Van Swaaij, W.P.M.; Beenackers, A.A.C.M.:** *Chemical Reactor Design and Operation.* New York: John Wiley & Sons, Inc. 2nd edition (1983) pp. 481.

[100] **De Backer, L.; Baron G.:** Residence time distribution in a packed bed bioreactor containing porous glass particles: influence of the presence of immobilized cells, *J. Chem. Tech. Biotech.*, **59** (1994) 297-302.

[101] **Siso, M.I.G.; Graber, M.; Condoret, J.; Combes, D.:** Effect of diffusional resistances on the action pattern of immobilised α-amilase, *J. Chem. Tech. Biotech.* **48** (1990) 185-200.

[102] **Axelsson, A.; Zacchi, G.:** Simulation of batch and continuous reactors with co-immobilised yeast and β-galactosidase, *J. Chem. Tech. Biotechnol.*, **52** (1991) 481-497.

[103] **Hassan, M.M.; Atiqullah, M.; Beg S.A.; Chowdhury, M.H.M.:** Analysis of non-isothermal tubular reactor packed with immobilised enzyme systems, Chem. Eng. Journ., **58** (1995) 275-283.

[104] **Nath, S.; Chand S.:** Mass transfer and biochemical reaction in immobilized cell packed bed reactors: correlation of experiment with theory, *J. Chem. Tech. Biotechnol.*, **66** (1996) 286-292.

[105] **Papathanasiou, T.D.; Kalogerakis, N.; Behie, L.A.:** Dynamic modelling of mass transfer phenomena with chemical reaction in immobilized-enzyme bioreactors, *Chem. Eng. Sci.*, **43** (1988) 1489-1498.

[106] **Levenspiel, O.:** *Chemical Reaction Engineering*. New York: John Wiley & Sons, Inc. 2nd edition (1999) 293.

[107] **Carslaw, H.S.; Jaeger J.C.:** *Conducton of heat in solids.* London: Oxford University Press, 2nd edition (1959).

[108] **Crank J.:** *The Mathematics of Diffusion*. London: Oxford university press, 3rd edition (1983).

[109] **Papathanasiou, T. D.; Bijeljic, B.:** Intraparticle diffusion alters the dynamic response of immobilized cell/enzyme columns. *Biop. Eng.*, **18** (1998) 419-426.

[110] **Gear, C.W.:** *Numerical Initial Value Problems in Ordinary Differential Equations.* London: Prentice Hall (1971).

[111] **Cramers, H.; Alberd, G.:** Frequency response analysis of continuous flow systems. *Chem. Eng. Sci.* **2** (1953) 173.

[112] **Tanaka, H.; Matsumura, M.; Veliky, I.A.:** Diffusion characteristics of substrates in Ca-alginate beads, *Biotechn. Bioeng.*, **26** (1984) 53-58.

[113] **Berk, D.; Behie, L.A.:** The production of the antibiotic patulin in a three phase fluidized bed reactor I. Effect of medium composition, *Can. J. Chem. Eng.*, **62** (1984) 112-119.

[114] **Wilke, C. R.; Chang, P.:** Correlation of Diffusion Coefficients in Dilute Solutions, *AIChE Journal*, **1** (1955) 264-270.

[115] **Gnielinski.V.:** In *VDI –Wärmeatlas*, VDI Verlag, Düsseldorf, 6th edition. (1991) Sect.Gh.

[116] **Coeuret,F.:** *Electrochim.Acta.*, **24** (1979) 109.

[117] **Kasaoka,S.;Nitta,K.:** *Kagaku Kogaku.*, **33** (1969) 1231-1236.

[118] **Wilson,E.J.; Geankoplis C.J.:** Liquid mass transfer at very low Reynolds numbers in packed beds, *Ind. Eng. Chem. Fundam.*, **5** (1966) 9-14.

[119] **Wiliamson,J.E.; Bazaire K.E.;Geankoplis C.J.:** Liquid-phase mass transfer at low Reynolds numbers, *Ind. Eng. Chem. Fundam.*, **2** (1963) 126-133.

[120] **Gaunand,A.; Coeuret,F.:** Influence of the relative electric conductivity of the two phases on the potential distribution in flow through porous electrodes under limiting current conditions, *Electrochim. Acta.*, **23** (1978) 1197-1203.

[121] **Dwivedi,P.N.;Upadhyay,S.N.:** Particle-fluid mass transfer in fixed and fluidized beds, *Ind. Eng. Chem. Process. Des. Dev.*, **16** (1977) 157-165.

[122] **Tsotsas, E.:** On mass transfer, dispersion and macroscopical flow maldistribution in packed tubes, *Chem. Eng. Proc.*, **31** (1992) 181-190.

[123] **Hewitt, G. F.; Shires, G. L.; Polezhaev, Y. V.:** *International Encyclopedia of Heat and Mass Transfer*, 1st edition, CRC (1997).

[124] **Massey, B. S.:** *Mechanics of Fluids*, 6st edition, London: Van Nostrand Reinhold (International), (1989).

[125] **Astarita, G.:** Dimensional analysis, scaling and Orders of Magnitude, *Chem. Eng. Sci.*, **52** (1997) 4681-4698.

[126] **Froment, G. F.; Bischoff K. B.:** *Chemical Reactor Analysis and Design*, 2nd edition, John Wiley & Sons (1990).

# Chapter 9

# Conclusions

The work reported in this thesis sought to elucidate the local physics of the flow and mass transfer in fibrous and granular heterogeneous porous media characterised by multiple length scales. The aim was to study transport phenomena in two fundamental classes of static porous media: (i) a porous medium surrounded by a free flow fluid region (including fore, aft and open channel region) and (ii) two porous media of different porosities. The formulation of the problems at a fundamental level served to broaden the applicability of the obtained results. On the other hand, the objective was to focus on model and/or real systems of substantial theoretical and experimental interest, which are directly applicable in many engineering disciplines, currently requiring a better understanding.

## *9.1 Coupled Slow Flow in a Fibrous Porous Medium and an Adjacent Free Flow Region*

The first part of the thesis concerned coupled slow flow of a Newtonian fluid (glycerol) in a fibrous porous medium and an adjacent free flow region in bounded systems. Namely, Magnetic Resonance Imaging velocimetry, as a powerful tool to study viscous flow in porous media, was employed to experimentally quantify the 2D flow fields in Hele-Shaw cells in which arrangements of single and multiple fibre lattices, formed by circular cylindrical rods, were placed. This strategy of experimental design, first of all, enabled determination of the global flow fields in a fibrous porous medium and a free flow region. Moreover, at the local level, it allowed further insights into the interrelation of fluid velocities between the two regions at the

*interface of the two flow regions. Finally, this made it possible to obtain the flow* distribution within the interstitial spaces of the fibre lattices.

The experimental concept is particularised by studying parameters defining macroscopic and microscopic geometry, pore size, porosity and number of the fibre lattices, whilst, with respect to the free flow region, the width of the open channel was kept constant or varied in a simple or more complex way.

A full knowledge of the global and local aspects of the viscous 2D flow field in the *lattice-channel arrangements* investigated has been provided. It proved extremely useful to be able to monitor the velocity component which *is transverse to the flow* direction in both porous and the free flow regions.

### *9.1.1 Coupled Slow Flow in a Macroscopically Rectangular Single Fibre Lattices and an Adjacent Open Channel Region of Constant Width*

From the study of macroscopically rectangular single fibre lattices adjacent to the open channel region of constant width, the most illuminating results are termed:

(i) 'edge' effects in the fore and aft part of the free flow region; they are a result of significant, but gradual, flow rearrangement as the fluid is offered less resistance by the open channel region than by the fibre lattice (the fore part) or as the fluid exits from the open channel into a region free of obstructions (the aft part).

(ii) 'entrance/exit' effects within the rectangular single fibre lattices. The local flow enhancements are observed at the corners of the lattices, as opposed to the regions with regular patterns of very low fluid velocities identified between the cylinder in the flow direction. These *local flow* enhancements are a result of the additional velocity gradients, caused by the proximity of the macroscopic flow rearrangements *in the* entrance/exit region of the lattice-channel arrangements. The 'entrance/exit'effects are

experimentally shown to depend on the channel width, the fibre lattice porosity and the fibre diameter.

An illustrative example of both 'edge' and 'entrance/exit' effects is given in Fig.(9.1) on a velocity image is obtained by NMR velocimetry. Shown is the contour map of the velocity component transverse to the flow direction in the cell formed by the macroscopically rectangular fibre lattice based on hexagonal unit cells.

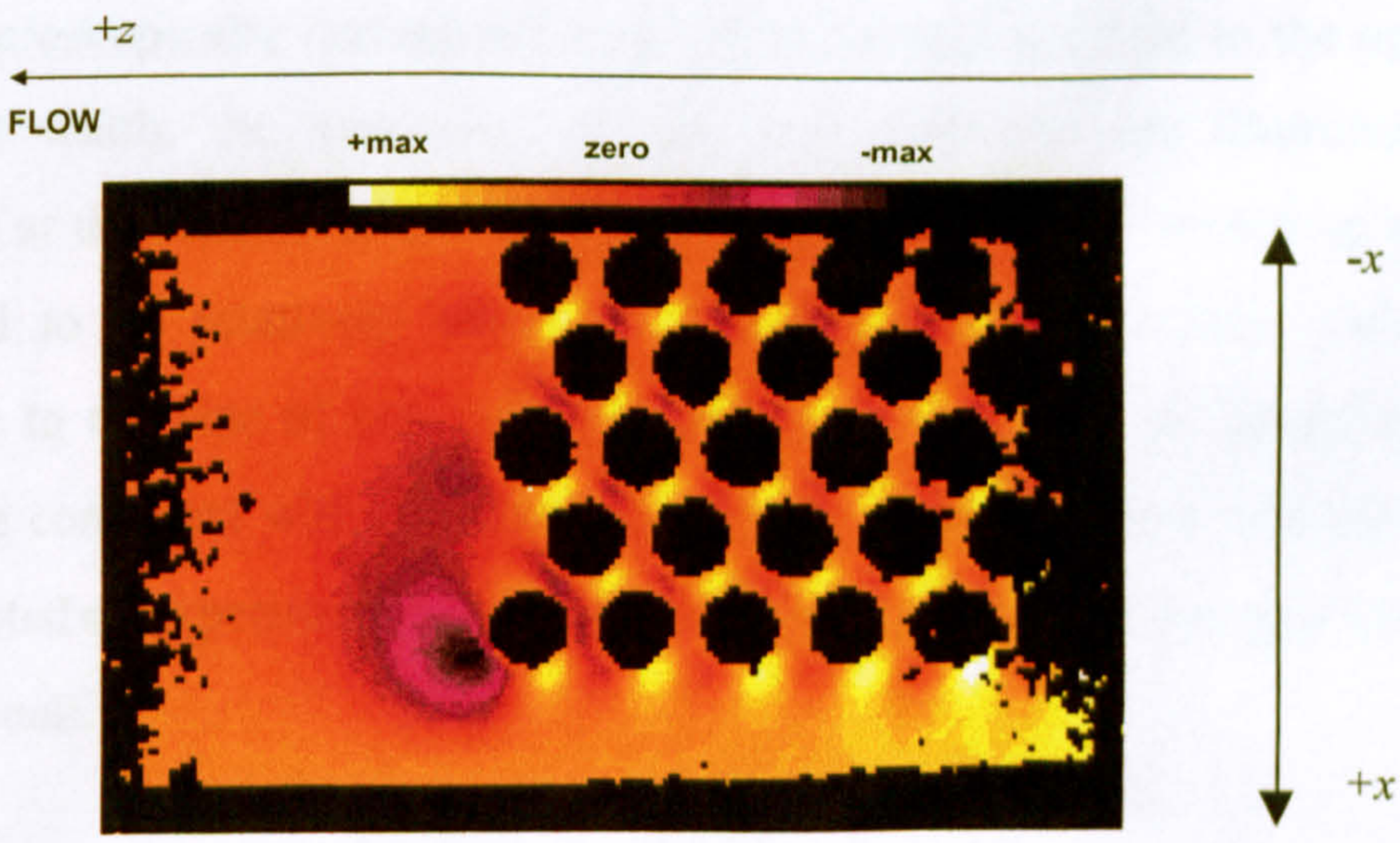


**Figure 9.1:** Flow of a Newtonian fluid (glycerol) in the direction *x* transverse to the direction of bulk flow, *z*, across a half of the macroscopically rectangular fibre lattice based on hexagonal unit cells. The velocities range from a negative value when the flow turns in the -*x* direction to a positive value when the flow turns in the +*x* direction. The maximum negative value is represented by the black colour, whilst the maximum positive value is represented by the white colour. Both 'edge' effect and, in this half of the cell, 'exit' effect are present at the edge and the corner of the lattice.

The experimental results were evaluated against numerical models, namely lattice-Boltzmann model and Boundary elements method, which both solved the Stokes equations for the creeping flow. The extent of both 'edge' effect and 'entrance/exit' effect phenomena, which had been fully quantified experimentally, was independently confirmed by the predictions of the lattice-Boltzmann model. A good agreement with the lattice-Boltzmann model is found on the magnitude of the 'edge effect' and on both the magnitude and the penetration depth of 'entrance/exit' effect. The available

boundary element code, by providing a solution for the average velocities for the infinite-length lattice-channel arrangements in the gap direction (unbounded flow), made it possible to clearly differentiate between these solutions and the experimental data and the solutions for flow across the finite-length lattice-channel arrangements in the gap direction (bounded flow). Hence, the two effects, namely 'edge' effect and 'entrance/exit' effects have been established as the local phenomena of critical importance for an accurate description of creeping flow in fibrous media of dual porosity.

For the macroscopically rectangular single fibre lattices adjacent to the open channel of constant width, the transitions of the fluid velocities are illuminated in two dimensions at the channel-lattice interface. The depths of this 'screening effect' zone were found to be relatively small. In fact, the scale of velocity variations was comparable to the size of one cylinder radius at either side of the interface. These findings are consistent with references [33,41,42], in which these velocity transitions were predicted or experimentally found to occur at the scale of the gap thickness of a Hele-Shaw cell.

### *9.1.2 Coupled Slow Flow in a Macroscopically Semi-Circular Single Fibre Lattices and an Adjacent Open Channel Region of Variable Width*

From the study of macroscopically semi-circular single fibre lattices adjacent to the open channel region of the variable width, the most remarkable findings were the presence of the local velocity enhancements in many of the places between the cylinders in the flow direction within the fibre lattices. A typical example of these local velocity enhancements is the contour plot of the velocity component transverse to the flow direction in the cell formed by the macroscopically semi-circular square unit cell fibre lattice (Fig.9.2).

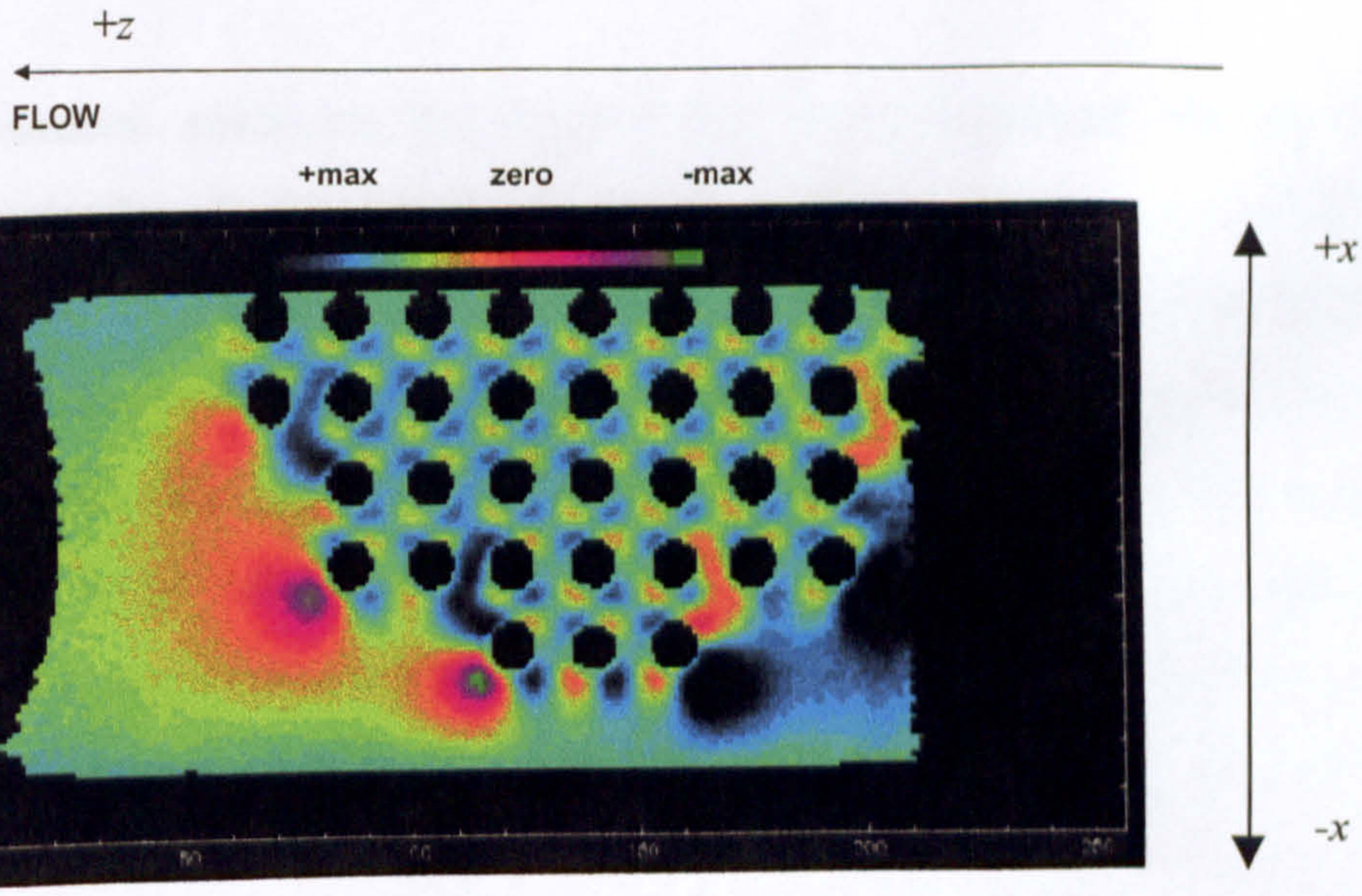


**Figure 9.2:** Flow of a Newtonian fluid (glycerol) in the direction *x* transverse to the direction of bulk flow, *z*, across a half of the macroscopically semi-circular fibre lattice. The velocities range from a negative value when the flow turns in the *-x* direction to a positive value when the flow turns in the *+x* direction. The maximum negative value is represented by the black colour, whilst the maximum positive value is represented by the white colour. The local velocity enhancements are directed in or out of the lattice, depending on the contraction or expansion of the flow in the adjacent open channel.

These enhancements, in turn, produce local velocity enhancements in the flow direction, which are present deeper within the lattice, and may even be extended to the lattice centre. The local flow enhancements are formed according to 'the least resistance to flow', i.e. are strongly dependent on the local macroscopic configuration of the fibre lattice and the variable width of the adjacent open channel. Hence, the flow within the fibre lattice must be treated in terms of its necessary connection with the flow in the free flow region.

The predictions of the lattice-Boltzmann model corroborate, qualitatively and quantitatively, the existence and the concatenation of the local velocity enhancements in the two examined directions. By controlling the macroscopic shape of the single fibre lattice and the width of the free flow region, the stagnant or recirculation regions within the fibre lattice could be either avoided (in heat and mass transfer applications) or facilitated (in filtration). Hence, it is shown that the local flow enhancements within

the fibre lattices are indispensable in the flow analysis in the fibrous media of dual porosity.

The experimental evidence has shown that the penetration depths of the local transverse velocity enhancements are of comparable length within the fibre lattices of different porosities with the cylinder diameters D=4mm and D=3mm. The magnitudes of the local transverse velocity enhancements in these lattices are different, subject to the local internal configuration of the lattices. When the cylinder size was reduced to D=2mm, the local transverse velocity enhancements within the lattice, although present, were considerably smaller in relation to the previous two fibre lattices due to increased surface area of the cylinders within the lattice offered for fluid friction.

It has explicitly been demonstrated (by MRI experiments and the lattice-Boltzmann model) that slow flow over single symmetrical lattice-channel arrangements conforms to the laws of symmetry.

### *9.1.3 Coupled Slow Flow in an Assembly of Macroscopically Rectangular Fibre Lattices and an Adjacent Open Channel Region of Variable Width*

The most complex geometry of the free flow region examined was adjacent to the fibre lattice assembly and designed to be affected by the surface macroscopic irregularities of the neighbouring lattices, with well-defined places in which fluid undergoes contraction or expansion. These places were a good indicator of the local velocity enhancements, which occurred within a lattice entirely surrounded by the assembly. Remarkably, these local velocity enhancements were directed in or out of the lattices, depending on the contraction or expansion of the flow in the adjacent part of the free fluid region.

From these findings it follows that the local flow details in the vicinity of the lattice-channel interface of the more complex fibrous media of dual porosity (the lattice

assembly) clearly discriminate this type of flow from the flows where the adjacent free flow regions are bounded by the walls or, from any other heterogeneous porous systems in which the fibre lattices are sufficiently far apart from one another that they do not influence the flow pathways in the free flow region. Yet, the local features of flow in the interior of a lattice that constitutes the lattice assembly hinge on the local configuration of the adjacent free flow region, which is a fact common to all above mentioned types of flows. Hence, with knowledge of the shape of the free flow region and an understanding of the interrelation between the flows in the porous and free flow regions at the local and macroscopic levels presented here, the transport processes in porous systems of dual porosity are better understood.

From the distributions of the velocities observed it is seen that all longitudinal velocity component maps, i.e. the component in the direction of the superficial flow, have only positive values which yields the conclusion that, for the low Reynolds number investigated, back-mixing is non-existent in the system. These results corroborated experimental findings from [39]. Within the fibre lattices no recirculation zones are present between the cylinders in the flow direction.

The experimental and theoretical comparisons of the global characteristics of flows within the fibre lattices of different porosities and/or fibre diameters (gap sizes) and adjacent free flow regions have shown that the ratio of the maximum open channel velocities to the maximum fibre lattice velocities increase with decreased porosity of the fibre lattices and decreased size of the cylinders (gap between the cylinders). When the total volumetric flowrates were compared for the fibre lattices and the free flow regions, the agreement between the experimental findings and theoretical predictions was remarkably good, thus further establishing both MRI velocimetry and the lattice-Boltzmann model as powerful tools for the flow analysis in heterogeneous fibrous porous media.

Further investigations of the coupled flow in a fibrous porous medium and an adjacent free flow region should include flow of Non-Newtonian fluids as well as the effects of flow inertia. It should also focus on the studies of more complex fibrous structures, including the random ones.

## *9.2 Coupled Flow and Mass Transfer in a Fixed Bed Granular Column*

In the second part of this study, the focus was to investigate the mechanisms governing the coupled flow and mass transfer in a fixed-bed granular column with a porous packing. This was achieved by comparing the transient experimental responses of the columns containing porous and non-porous beads; in the latter no mass transfer within the particles occurs. Hence, the difference in the responses can be quantified by the use of a suitable observational model.

For this study, the dynamic experiments are well utilised, since they permit the simultaneous determination of several mechanisms (hydrodynamic dispersion, mass transfer) constants. Experiments were carried out at low to moderate particle Reynolds numbers – high particle Peclet numbers. The presence of porous packing alters the response signal of the column significantly, as compared to a packed bed of impermeable particles. From comparisons with the predictions of a macro-scale (centimetres) tanks-in series model for beds packed with impermeable and porous particles, this change in column dynamics was ascribed to the effect of mass transfer from bed voidage to porous particles. The tanks-in series model employed the method of curve fitting, giving a remarkably good agreement with the experimental responses when the observed modified response in the model was due to tracer diffusion inside the porous beads. The alternative mechanisms that may cause the shift in the experimental response of the column with a porous packing, such as an increase in the hydrodynamic dispersion or an increase in the column effective porosity, were ruled out by an adequate analysis from the model. Hence, it was inferred that the mechanism principally responsible for the mass transfer to the porous beads is intraparticle diffusion. By this analysis, it was shown that the column with a porous packing has to be analysed as the two separate inter- and intraparticle regions with the intrinsically different mechanisms for flow and mass transfer.

The moderate Reynolds number flow regime, at which no significant mass transfer limitations to porous particles exist, was initially identified. Following that finding, an

experimental investigation of mass transfer in packed beds in the region of low Reynolds numbers where equivocal experimental results in the literature lead to controversial conclusions on the factors governing mass transfer, have shown that the mass transfer of the tracer from the bulk liquid to the intraparticle space started to be profoundly hindered at $Re_p \leq 5$. This fact is explained by the mass transfer limitations in the external liquid film surrounding the beads. The effect was quantified by comparing the experimental responses of the column to the predictions of the tanks-in series model for which the inclusion of mass transfer resistance proved to be essential in the analysis; otherwise the model would not be able to fit the experimental data. A typical comparison of the dynamic responses of the columns filled with non-porous and porous beads for $Re_p$ =4.2 with the models with and without intraparticle mass transfer included is shown in Fig.(9.3).

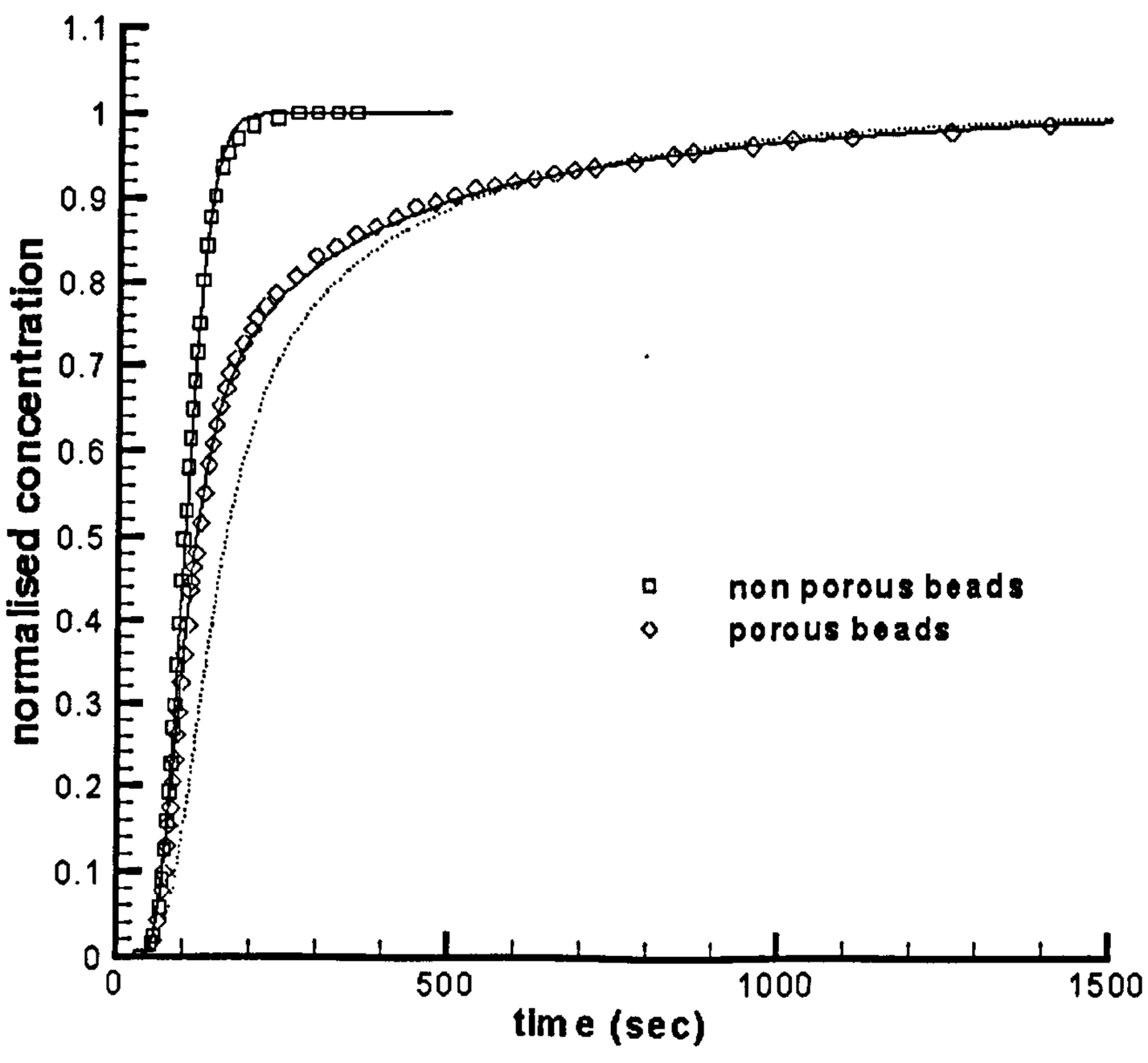


**Figure 9.3:** Comparison of the responses of columns containing non-porous beads and porous beads of 4mm diameter for $Re_p$=4.2. Model predictions for $N$=13 (glass beads with no mass transfer in the intraparticle space) and $N$=13 and $Bi$=0.3 (porous beads with mass transfer in the intraparticle space with the mass transfer resistance included) are shown as solid lines. The dotted line shows model prediction where only mass transfer in the intraparticle space is considered, but no effect of mass transfer resistance is included.

At higher Reynolds numbers with moderate effect of turbulence this effect is less appreciable but still could be distinguished. These findings have also been compared with a large number of relevant experimental and theoretical studies on mass transfer in packed beds. Apart from the predictions from Nelson-Galloway model the experimental findings and model results in this study for the particle Sherwood numbers showed reasonably good agreement with other correlations from the literature. Hence, the knowledge of the mechanisms of flow and mass transfer in the inter- and intarparticle space of a column filled with porous packing has been broadened.

The above analysis was based on the use of average values of the fluid and flow parameters at meso-scale. Further investigations on mass transfer in packed beds should concentrate on the mass transfer effects at the local scale.

# Appendix 1 Conservation Equations

## *A) Conservation of Mass*

Consider fluid in a control volume $V$ located in a body which is fixed with respect to the selected inertial frame of reference (as opposed to a material volume that contains fixed amount of material but moves with material). The control volume is bounded by a double-sided surface and the outward unit normal $\boldsymbol{n}$ is defined, as in Fig.(A1.1).

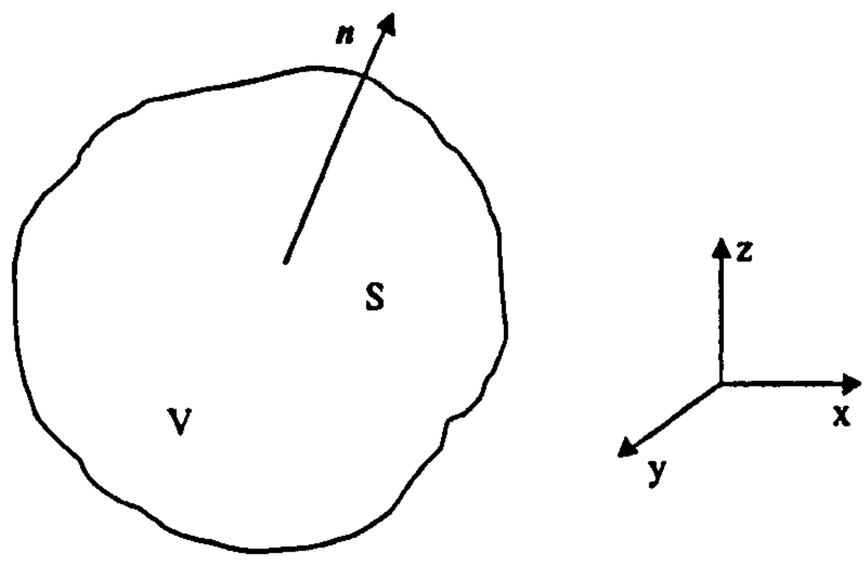


**Figure A1.1** Control volume $V$ located in a body bounded by a double-sided surface with the outward unit normal $\boldsymbol{n}$ defined.

The integral mass balance for the single phase follows from the following considerations [123].

The net mass flux of fluid of density $\rho$ moving with velocity $\boldsymbol{u}$ through the surface $S$ added to the rate of accumulation of fluid mass $m$ in the volume $V$ must be equal to zero:

$$\int_S \rho \boldsymbol{u}\cdot\boldsymbol{n}\, dS + \frac{\partial}{\partial t}\int_V \rho dV = 0. \qquad \textbf{(A1.1)}$$

Noting that the volume $V$ is not a function of time, we obtain:

$$\int_S \rho u \cdot n \, dS + \int_V \frac{\partial \rho}{\partial} dV = 0 . \qquad \textbf{(A1.2)}$$

Making use of the Gauss divergence theorem (see part *C*) to the first term on the left-hand side of equation (A1.2) results in:

$$\int_V (\frac{\partial \rho}{\partial} + \nabla \cdot (\rho u)) dV = 0 , \qquad \textbf{(A1.3)}$$

where $\nabla = \frac{\partial}{\partial x} i + \frac{\partial}{\partial y} j + \frac{\partial}{\partial z} z$ is the gradient operator expressed in Cartesian coordinate system along the axis *x, y, z* with the corresponding unit vectors ***i, j***, and ***z***. The vector dot product of mass velocity $\rho u$ and $\nabla$ is referred to as divergence of $\rho u$ (div $\rho u$). Since *V* is arbitrary, from equation (A1.3) follows:

$$\frac{\partial \rho}{\partial} + \nabla \cdot (\rho u) = 0 . \qquad \textbf{(A1.4)}$$

This equation is referred to as continuity equation. For an incompressible fluid $\rho$=const., and equation (A1.4) simplifies to:

$$\nabla \cdot u = 0 . \qquad \textbf{(A1.5)}$$

*B) Conservation of Linear Momentum*

The linear momentum balance in the form of integral equations is analysed in a defined control volume *V* bounded by a double-sided surface *S* and the outward unit normal ***n*** from Fig.(A1.1). The rate of accumulation of fluid momentum $\rho u$ in the volume *V* added to the net momentum flux $\rho uu$ of fluid through the surface *S* must be equal to the rates of gains of momentum due to volume (body) forces (i.e. gravity force, *mg*) and surface forces (stress vector ***t*** acting on the surface *S*). The governing equations are:

$$\frac{\partial}{\partial} \int_V \rho u \, dV + \int_S \rho uu \cdot n \, dS = \int_V \rho g \, dV + \int_S t \, dS . \qquad \textbf{(A1.6)}$$

Applying Cauchy's fundamental theorem for stress vector - stress tensor relationship and subsequently Gauss' divergence theorem on the second term on the right-hand side of the equation (A1.6) one can write:

$$\int_S \boldsymbol{t}\, dS = \int_S \boldsymbol{n}\cdot \tau dS = \int_V \nabla \cdot \tau dV\,, \qquad \textbf{(A1.7)}$$

where $\tau$ is a tensor quantity.

Application of Gauss' divergence theorem on the second term of the left-hand side of equation (A1.6) results in:

$$\int_S \rho \boldsymbol{uu}\cdot \boldsymbol{n}\, dS = \int_V \nabla \cdot (\rho \boldsymbol{uu}) dV\,. \qquad \textbf{(A1.8)}$$

Hence, equation (A1.6) can be rewritten as:

$$\int_V (\frac{\partial}{\partial}(\rho \boldsymbol{u}) + \nabla \cdot (\rho \boldsymbol{uu}) - \rho \boldsymbol{g} - \nabla \cdot \tau) dV = 0\,, \qquad \textbf{(A1.9)}$$

and, as the volume $V$ is arbitrary:

$$\frac{\partial}{\partial}(\rho \boldsymbol{u}) + \nabla \cdot (\rho \boldsymbol{uu}) - \rho \boldsymbol{g} - \nabla \cdot \tau = 0. \qquad \textbf{(A1.10)}$$

It can be shown that [124]:

$$\nabla \cdot (\rho \boldsymbol{uu}) = \rho \boldsymbol{u}\cdot \nabla \boldsymbol{u} + \boldsymbol{u}(\nabla \cdot \rho \boldsymbol{u})\,. \qquad \textbf{(A1.11)}$$

Upon substitution this equation in the equation (A1.10) one obtains:

$$\boldsymbol{u}\frac{\partial \rho}{\partial} + \rho \frac{\partial \boldsymbol{u}}{\partial} + \rho \boldsymbol{u}\cdot \nabla \boldsymbol{u} + \boldsymbol{u}\nabla \cdot (\rho \boldsymbol{u}) = \rho \boldsymbol{g} + \nabla \cdot \tau\,. \qquad \textbf{(A1.12)}$$

Grouping the first and the fourth term on the left-hand side of equation (A1.12) and recognising this new expression to contain conservation of mass equation (A1.4), equation (A1.12) simplifies to:

$$\rho \frac{\partial \boldsymbol{u}}{\partial} + \rho \boldsymbol{u}\cdot \nabla \boldsymbol{u} = \rho \boldsymbol{g} + \nabla \cdot \tau\,, \qquad \textbf{(A1.13)}$$

or, using the substantial derivative notation:

$$\rho\frac{D\boldsymbol{u}}{Dt}=\rho\boldsymbol{g}+\nabla\cdot\boldsymbol{\tau}\,. \qquad \textbf{(A1.14)}$$

Decomposing the stress tensor field from equation (A1.16) into a scalar field $p$, which is related to the static pressure, and the deviatoric stress tensor $\tau_D$, which is related to the tangential (shear) stresses, the equation of conservation of linear momentum becomes:

$$\rho\frac{D\boldsymbol{u}}{Dt}=\rho\boldsymbol{g}-\nabla p+\nabla\cdot\boldsymbol{\tau}_D\,. \qquad \textbf{(A1.15)}$$

For an incompressible fluid, the gravity force of magnitude $g$ which acts in the negative $x$ direction can be absorbed into the modified pressure $P = p + \rho g x$. For a Newtonian fluid the simple constitutive relation between stress $\tau$ and the rate of strain tensor $e=\nabla\boldsymbol{u}+\nabla\boldsymbol{u}^{\mathrm{T}}$ is:

$$\boldsymbol{\tau}_D=\mu\boldsymbol{e}\quad. \qquad \textbf{(A1.16)}$$

It can be shown that for an incompressible (and Newtonian) fluid holds [124]:

$$\nabla\cdot\boldsymbol{e}=\nabla^2\boldsymbol{u} \qquad \textbf{(A1.17)}$$

where $\nabla^2\boldsymbol{u}=\nabla\cdot\nabla\boldsymbol{u}$ is the Laplacian operator representing divergence of the velocity gradient. By substitution of equations (A1.16) and (A1.17) into equation (A1.15), Navier Stokes equations are obtained:

$$\rho\frac{D\boldsymbol{u}}{Dt}=-\nabla P+\mu\nabla^2\boldsymbol{u}\quad. \qquad \textbf{(A1.18)}$$

This equation states that momentum transfer due to pressure and viscous forces are counterbalanced by momentum transfer resulting from inertia forces. If viscous forces dominate over inertial forces (the reciprocal ratio between the two forces is given by a dimensionless group Reynolds number defined in Appendix 2), the latter forces can be neglected and equation (A1.18) simplifies to:

$$0 = -\nabla P + \mu \nabla^2 \boldsymbol{u} \quad . \tag{A1.19}$$

These equations are referred to as Stokes equations. Derivation of Reynolds number is described in detail in Appendix 2.

*C) Gauss Divergence Theorem*

Consider a material volume $V$ bounded by a double-sided area $S$ and having an outward normal vector $\boldsymbol{n}$, as in Fig.(A1.1). For a continuously differentiable vector field $\boldsymbol{u}=\boldsymbol{u}(\boldsymbol{x})$, the volume integral of its divergence is related to the corresponding surface integral by the equation:

$$\int_V (\nabla \cdot \boldsymbol{u})\, dV = \int_S (\boldsymbol{n} \cdot \boldsymbol{u}) dS \, . \tag{A1.20}$$

# Appendix 2 Dimensionless Numbers

Physical systems can be analysed and compared by a technique termed dimensional analysis. In dimensional analysis, a physical system is described in the form of mathematical relations relating the relevant variables. In mathematical relations, the primary magnitudes of some quantities, which are specified as independent of any others, define the secondary magnitudes of quantities. The magnitude of quantity is expressed as a dimensional formula. Any magnitude which has only numerical value is said to be dimensionless.

Dimensional analysis is based on the principle of dimensional homogeneity i.e. all terms equated, added or subtracted in the analysis must have identical dimensional formulae. Thus, the law (with a physical meaning) that is described in an equation does not depend on the size of units used in expressing the various magnitudes [124, 125].

The dimensional analysis concerning flow and mass transfer is based on similarity of forces, which is referred to as dynamic similarity. In two dynamically similar systems, the magnitude ratio of any two forces is fixed. The dimensionless groups formed from secondary magnitudes used in this study were:

a) Reynolds number, defined as the ratio of the inertia force of magnitude $F_{in}=ma$, which represents the resistance of the particle of mass $m$ (or density $\rho$) to be accelerated with acceleration $a$, and the net force due to fluid viscosity $\mu$ acting on a particle surface $A$, $F_{vis}=A\mu\, du/dl$, where $du/dl$ is the shear rate $u$ is velocity and $l$ is the linear dimension in the system. The former force scales as $\rho l^3u^2/l=\rho l^2u^2$, whilst the latter force is proportional to $l^2\mu\, u/l=\mu\, ul$. Hence the ratio between the two forces is

$$Re=\frac{ul\rho}{\mu} \qquad \textbf{(A2.1)}$$

In physical terms, Reynolds number expresses total momentum transfer over viscous momentum transfer. The length $l$ in the expression for Reynolds number may be any length that is significant for a given system. Since the mass transfer in packed bed occurs to spherical particles, logical choice the characteristic length is selected to be diameter of the particle, $d_p$ so that:

$$Re_p = \frac{u_s d_p \rho}{\mu} \quad , \tag{A2.2}$$

where $Re_p$ is termed now the particle Reynolds number and $u_s=F/A$ is the fluid superficial velocity, defined as the ratio between the volumetric flowrate $F$ and $A$ is the cross section of an empty column, imagined to be without packing.

b) Schmidt number, $Sc$ is defined as the ratio between viscous effects (molecular momentum transfer) and diffusion effects (molecular mass transfer):

$$Sc = \frac{\mu}{\rho D} \tag{A2.3}$$

where $D$ is molecular diffusivity.

c) Particle Sherwood number, $Sh_p$ is defined as the ratio between total mass transfer (by advection and diffusion) to mass transfer by diffusion

$$Sh_p = k_e \frac{d_p}{D} \quad , \tag{A2.4}$$

where $d_p$ is the particle diameter.

d) Biot number, $Bi$ (or modified Sherwood number [126]) is defined as the ratio between the internal to external mass transfer resistances:

$$Bi = \frac{k_e R}{D_{eff}} \quad , \tag{A2.5}$$

and is expressed with respect to particle radius and effective diffusivity in porous particle.

e) Column Peclet number, $Pe$ is defined as the ratio between the bulk flow movement and fluid movement by longitudinal dispersion:

$$Pe = \frac{u_i L}{D_{ax}}, \qquad \textbf{(A2.6)}$$

where $L$ is the length of the column.

f) Particle Peclet number, $Pe_p$ is defined as the ratio between the bulk flow movement and fluid movement by longitudinal dispersion, but the selected linear dimension is the particle diameter:

$$Pe_p = \frac{u_i d_p}{D_{ax}}. \qquad \textbf{(A2.7)}$$